

Group IV element-based luminescent nanoparticles: synthesis, environmental impact  
evaluation and bio-imaging applications

A DISSERTATION

SUBMITTED TO THE FACULTY OF THE

UNIVERSITY OF MINNESOTA

BY

Bo Zhi

IN PARTIAL FULFILLMENT OF THE REQUIREMENTS

FOR THE DEGREE OF

DOCTOR OF PHILOSOPHY

Christy L. Haynes, Adviser

August 2019



## Acknowledgements

Throughout the preparation of my dissertation, I have received a great number of support and assistance. I would like to express my gratitude to my advisor Prof. Christy Haynes for the generous support of my Ph.D. research. Her guidance helped me in all the time of research and writing of this thesis.

In addition, I would like to thank the rest of my doctoral final exam committee: Prof. Andreas Stein, Prof. Renee Frontiera, and Prof. Uwe Kortshagen, for their encouragement, insightful comments, and inspiring questions.

I would also like to acknowledge my collaborators from the Center for Sustainable Nanotechnology and University of Minnesota MRSEC program for the past collaborations. Specifically, my sincere thanks go to Prof. Robert Hamers, Prof. Howard Fairbrother, Prof. Zeev Rosenzweig, Prof. Galya Orr, Prof. Qiang Cui, Prof. Uwe Kortshagen and their past and current students: Dr. Arielle Mensch, Dr. Miranda Gallagher, Benjamin Frank, Richard Brown, Denise Williams, Dr. Yi Cui, Sadhana Mishra and Yueke Yang.

Last but not the least, I am also grateful to my fellow labmates in Haynes Group. I would particularly like to single out my mentees, Xiaoxiao Yao and Elaine Kappel. It was my great pleasure to work with them on the carbon dot projects.

What follows present specific acknowledgements for funding sources and technical supports for each chapter.

## **Chapter One**

This work was supported by the National Science Foundation through Chemical Innovation Program, under grant CHE-1503408 for the Center for Sustainable Nanotechnology. Part of this work was done at the Environmental Molecular Sciences Laboratory, a national scientific user facility sponsored by DOE's Office of Biological and Environmental Research and located at Pacific Northwest National Laboratory.

## **Chapter Two**

This work was supported by the National Science Foundation Center for Chemical Innovation Program Grant No. CHE-1503408 under the Center for Sustainable Nanotechnology. Parts of this work, including XPS and TEM characterization, were carried out in the Characterization Facility, University of Minnesota, which receives partial support from the MRSEC program. We would like to thank the Materials Characterization Facility at Johns Hopkins University Whiting School of Engineering for use of their facilities.

## **Chapter Three**

This work was supported by the National Science Foundation Center for Chemical Innovation Program Grant No. CHE-1503408 under the Center for Sustainable Nanotechnology. We thank Dr. Christopher J. Douglas (University of Minnesota) for carbon dot separation supplies and equipment. Part of this work, including super-resolution cell imaging and fluorescence characterization of single dots, was performed using the Environmental Molecular Sciences Laboratory, a national scientific user facility

sponsored by the Department of Energy's Office of Biological and Environmental Research and located at Pacific Northwest National Laboratory. Parts of this work, including XPS and TEM characterization, were carried out in the Characterization Facility, University of Minnesota, which receives partial support from the MRSEC program (DMR-1420013).

#### **Chapter Four**

This work was supported primarily by National Science Foundation through the University of Minnesota MRSEC under Award Number DMR-1420013. Part of this work was carried out in the College of Science and Engineering Characterization Facility, University of Minnesota, which has received capital equipment funding from the NSF through the UMN MRSEC program under Award Number DMR-1420013. NVH acknowledges support through the National Science Foundation Graduate Research Fellowship Program. The authors would like to thank Fang Zhou for microtoming the biological TEM samples. We thank Dr. Tian (Autumn) Qiu for providing ROS assay protocol and advice.

#### **Chapter Five**

This work was supported primarily by National Science Foundation through the University of Minnesota MRSEC under Award Number DMR-1420013. Part of this work was carried out in the College of Science and Engineering Characterization Facility, University of Minnesota, which has received capital equipment funding from the NSF through the UMN MRSEC program under Award Number DMR-1420013. Portions of

this work were conducted in the Minnesota Nano Center, which is supported by the National Science Foundation through the National Nano Coordinated Infrastructure Network (NNCI) under Award Number ECCS-1542202. N.V.H.-S. acknowledges support through the National Science Foundation Graduate Research Fellowship Program (00039202). The authors thank Fang Zhou for microtoming the biological TEM samples.

## **Chapter Six**

This work was supported by the National Science Foundation Center for Chemical Innovation Program Grant No. CHE-1503408 under the Center for Sustainable Nanotechnology. Part of this work, including cell imaging and cell viability tests, were performed using the Environmental Molecular Sciences Laboratory, a national scientific user facility sponsored by the Department of Energy's Office of Biological and Environmental Research and located at Pacific Northwest National Laboratory. Parts of this work, including TEM characterization, were carried out in the Characterization Facility, University of Minnesota, which receives partial support from the MRSEC program (DMR-1420013). We thank Kelly Zhang for the assistance on EEM measurements, and Prof. Vivian Feng for lending us the CombiFlash system.

## **Dedication**

I would like to dedicate my thesis to my father, Zhi Yuhua, whose continual support and encouragement are always with me to pursue my next dream.

This thesis is also dedicated to my beloved girlfriend, Wang Shengyang, whose considerate companionship backs me to walk through the journey of grad school.

## Abstract

Optically emissive nanoparticles have begun to find applications in fields ranging from domestic flat screen displays to clinical biomedical treatment, spurring the development of luminescent nanomaterials. Due to their tunable optical and electrical properties via the quantum confinement effect, traditional QDs have stimulated a significant amount of fundamental research into nanoscale luminescence phenomena as well as a rapid growth of consumer products that are made of QDs. However, the commercialization of QD-based products has aroused safety concerns towards the ecosystem as well as human health, considering the potential leakage of heavy metal contents, such as cadmium, into the environment. Therefore, it is desirable to design and prepare eco-friendly luminescent nanomaterials with comparable, or even improved, performance to replace traditional QDs.

In recent years, group IV elements (*e.g.*, C, Si, and Ge) based fluorescent materials, such as carbon dots, Si or Ge semiconductor nanocrystals, are finding favor in researchers' eyes as they are conventionally considered as non-toxic elements and pose negligible influence on both the environment and human health. Under such context, this thesis work is focused on the preparation and bio-imaging applications of polymeric carbon dots as well as the bacterial toxicity assessment of CDs as well as Si and Ge nanocrystals using an environment-related bacterium, *Shewanella oneidensis* MR-1.

Specifically, Chapter 1 summarizes recent progress in the syntheses and applications of multicolor CDs. Chapter 2 discusses how the doping with phosphorus influences the optical properties of citric acid-based CDs. Chapter 3 represents how photoblinking malic acid-based CDs are applied for super-resolution bio-imaging experiments and how as-

made CDs are separated into different colored fractions efficiently. Chapter 4 and 5 assess how the doping of Group IV nanocrystals with boron and phosphorus induces the generation of ROS and as such, induces toxicity to bacteria. Finally, in Chapter 6, an automatic separation method is developed to purify as-made citric acid-based CDs and obtain multicolor CD fractions.

In summary, by carefully examining the influence induced by doped phosphorus, this work has revealed that the doping with P did not improve the photoluminescence properties of polymeric carbon dots but may enhanced their photostability. In addition, undoped or lightly doped carbon dots were non-toxic in most cases. Moreover, one of the carbon products, malic acid carbon dots were tested to be suitable for super-resolution localization microscopy and after a reversed-phase separation, it was confirmed that the particle size influenced the optical properties of individual carbon dot components. On the other hand, via a complete materials characterization and toxicity measurements, it has been revealed that the doping with boron and phosphorus did not lead to structural variation to silicon and germanium nanocrystals but result in bacterial toxic effects.

## Table of Contents

<b>Acknowledgements</b> .....	<b>i</b>
<b>Dedication</b> .....	<b>v</b>
<b>Abstract</b> .....	<b>vi</b>
<b>Table of Contents</b> .....	<b>viii</b>
<b>List of Tables</b> .....	<b>xii</b>
<b>List of Figures</b> .....	<b>xiii</b>
<b>List of Abbreviations</b> .....	<b>xx</b>
<b>Chapter 1</b> .....	<b>1</b>
1.1 Overview .....	2
1.2 Introduction.....	2
1.3. Hypotheses for the photoluminescence mechanism of CDs .....	4
1.3.1 Size-dependent emission.....	4
1.3.2 Surface state-derived luminescence .....	6
1.3.3 Molecular luminophores .....	7
1.4 Syntheses of multicolor CDs.....	8
1.4.1 Precursor screening for multicolor CDs.....	9
1.4.2 Solvent engineering for multicolor CDs .....	13
1.4.3 Separation or purification methods for as-synthesized CD mixtures.....	15
1.5 Applications of multicolor CDs .....	18
1.5.1 Selected sensing with CDs.....	19
1.5.2 High-resolution bioimaging with CDs .....	21
1.6 Perspective and future directions .....	26
<b>Chapter 2</b> .....	<b>28</b>
2.1 Overview .....	29
2.2 Introduction.....	29
2.3 Experimental .....	33
2.3.1 Chemicals.....	33
2.3.2 Synthesis of amorphous polymeric carbon dots.....	33
2.3.3 Material characterization.....	35
2.3.4 Photostability testing.....	36
2.3.5 QY and $\tau_{\text{avg}}$ measurement.....	37

2.3.6 Bacterial culture and polymeric carbon dot exposure .....	38
2.3.7 Colony counting assays (drop plate method) .....	39
2.4 Results and discussion .....	40
2.4.1 Characterization of polymeric CDs .....	40
2.4.2 Photostability tests of polymeric CDs .....	53
2.4.3 Optical properties after phosphorus doping .....	55
2.4.4 Bacterial toxicity of polymeric CDs .....	56
2.5 Conclusions .....	59
<b>Chapter 3 .....</b>	<b>61</b>
3.1 Overview .....	62
3.2 Introduction .....	62
3.3 Experimental .....	66
3.3.1 Chemicals .....	66
3.3.2 MACD synthesis .....	67
3.3.3 Characterization of the MACD photoblinking .....	67
3.3.4 Cell imaging and cytotoxicity analysis .....	69
3.3.5 MACD separation by C <sub>18</sub> reversed phase silica gel column chromatography .....	70
3.3.6 Material characterization of MACDs .....	71
3.4 Results and discussion .....	73
3.4.1 The photoblinking property of MACDs .....	73
3.4.2 Application of MACDs in super-resolution localization imaging .....	76
3.4.3 MACD separation and characterization of MACD fractions .....	80
3.4.4 Optical properties of MACD fractions .....	86
3.5 Conclusions .....	90
<b>Chapter 4 .....</b>	<b>91</b>
4.1 Overview .....	92
4.2 Introduction .....	92
4.3 Experimental .....	95
4.3.1 Si NC synthesis .....	95
4.3.2 TEM analysis .....	96
4.3.3 Powder XRD .....	97
4.3.4 Bacterial culture and Si NC exposure .....	97
4.3.5 Colony counting assays .....	98

4.3.6 CytoViva analysis .....	98
4.3.7 Detection of total ROS generation .....	99
4.4 Results and discussion .....	99
4.4.1 Characterization of Si NCs .....	100
4.4.2 Abiotic assessment of total ROS generation .....	105
4.4.3 Bacterial toxicity evaluation of doped Si NCs .....	107
4.4.4 Si NC association with <i>S. oneidensis</i> MR-1 cells .....	109
4.5 Conclusions .....	125
<b>Chapter 5 .....</b>	<b>126</b>
5.1 Overview .....	127
5.2 Introduction .....	127
5.3 Experimental .....	130
5.3.1 Ge NC synthesis .....	130
5.3.2 TEM imaging .....	132
5.3.3 Powder XRD .....	133
5.3.4 FTIR and XPS analyses .....	133
5.3.5 Bacterial culture and Ge NC exposure .....	133
5.3.6 Colony counting assays .....	134
5.3.7 Curcumin method and ascorbic acid method .....	135
5.3.8 Measurement of total ROS generation .....	136
5.3.9 Hyperspectral imaging analysis .....	137
5.4 Results and discussion .....	138
5.4.1 Materials characterization of Ge NCs .....	139
5.4.2 Bacterial toxicity assessment of Ge NCs .....	147
5.4.3 Investigation of the microbial toxicity mechanism(s) of Ge NCs .....	149
5.4.4 Potential toxic chemicals released during transformation of doped Ge NCs .....	150
5.4.5 Abiotic measurement of total ROS production .....	154
5.4.6 Ge NC association with <i>S. oneidensis</i> MR-1 cells .....	157
5.5 Conclusions .....	172
<b>Chapter 6 .....</b>	<b>174</b>
6.1 Overview .....	175
6.2 Introduction .....	175
6.3 Experimental .....	177

6.3.1 Synthesis and separation of as-made CDs .....	177
6.3.2 Material characterization of CDs .....	178
6.3.3 Cell Imaging and Cell Viability Analysis .....	178
6.4 Results and discussion .....	179
6.4.1 Screening of synthesis conditions for as-made CDs .....	179
6.4.2 Separation for as-made CDs and characterization of CD fractions.....	181
6.4.3 Cellular toxicity experiments and bio-imaging experiments .....	187
6.5 Conclusions.....	195
<b>Concluding remarks .....</b>	<b>197</b>
<b>Bibliography .....</b>	<b>198</b>
<b>Appendix I: Curriculum Vitae.....</b>	<b>237</b>

## List of Tables

<b>Table 1.1.</b> Carbon dot application in sensing ions and other molecules .....	21
<b>Table 1.2.</b> Application of CDs in SRM.....	25
<b>Table 2.1.</b> XPS element analysis results of all of samples.....	50
<b>Table 2.2.</b> $\tau_{avg}$ and QY data of citric acid CDs series (left) and malic acid CDs series (right). .....	54
<b>Table 3.1.</b> Oligonucleotide sequences used as probes for p53 smFISH. Each probe was labeled with Alexa647. ....	70
<b>Table 4.1.</b> Size and surface chemistry characteristics of Si NCs .....	101
<b>Table 4.2.</b> Grain sizes of Si NCs calculated based on the Scherrer equation.....	104
<b>Table 5.1.</b> <i>d</i> -spacing values of undoped Ge NCs (calculated using the SAED pattern). .....	140
<b>Table 5.2.</b> <i>d</i> -spacing values of 10% B-doped Ge NCs (calculated using the SAED pattern). .....	140
<b>Table 5.3.</b> <i>d</i> -spacing values of 30% B-doped Ge NCs (calculated using the SAED pattern). .....	140
<b>Table 5.4.</b> <i>d</i> -spacing values of 10% P-doped Ge NCs (calculated using the SAED pattern). .....	141
<b>Table 5.5.</b> <i>d</i> -spacing values of 30% P-doped Ge NCs (calculated using the SAED pattern). .....	141
<b>Table 5.6.</b> Atomic percentage summary of Ge NCs.....	146
<b>Table 5.7.</b> PSD and $\zeta$ -potential summary for undoped and doped Ge NCs. ....	146
<b>Table 6.1.</b> Fluorescence properties of obtained CD fractions. ....	183

## List of Figures

<b>Figure 1.1.</b> The summary of carbon dot publication since 2005, analyzed via Web of Science up to April 25 <sup>th</sup> , 2019. Search criteria: TOPIC: (carbon dots) OR TOPIC: ("carbon quantum dots") OR TOPIC: ("graphene quantum dots") OR TOPIC: ("carbon nanodots") OR TOPIC: ("non-conjugated polymer dots") NOT TITLE: ("quantum dots").....	3
<b>Figure 1.2.</b> (a) blue, yellow, and orange emitting CDs prepared from phenylenediamine derivatives. Adapted with permission from Ref <sup>76</sup> ; (b) multicolor CQDs obtained by the assembly of phloroglucinol molecules. Adapted permission from Ref <sup>42</sup> ; (c) the emissions of CDs were tuned from the blue (482 nm) to the near-infrared (680 nm) region by adjusting the ratios of polythiophene derivatives. Adapted with permission from Ref <sup>77</sup> ..	9
<b>Figure 1.3.</b> (a) Multicolor CQDs synthesized by tuning the composition and ratios of reaction solvents (water, DMF, ethanol, and acetic acid). Adapted with permission from Ref <sup>104</sup> ; (b) The solvatochromism of CDs induced by the polarity difference of solvents: CCl <sub>4</sub> , toluene, CHCl <sub>3</sub> , acetone, dimethylformamide, CH <sub>3</sub> OH and H <sub>2</sub> O. Adapted with permission from Ref <sup>110</sup> .....	14
<b>Figure 1.4.</b> Multicolor CD application in metal ion sensing. (a) Fluorescence emission of CDs at 466, 555, and 637 nm when excited at 360 nm, 450 nm, and 540 nm to 13 metal ions. (b) Principle component analysis of the discrimination of the 13 metal ions based on the fluorescence emission of the CDs. (reprinted from ref. <sup>128</sup> ).....	19
<b>Figure 1.5.</b> Diverse applications of CDs in bioimaging. (A) Two-photon fluorescence imaging of CDs internalized by human breast cancer cells (reprinted from ref. <sup>154</sup> ). (B) Super-resolution single-molecule localization microscopy (SMLM) enabled by photoblinking CDs. The substantially improved spatial resolution helps resolve closely aligned fine structures within a diffraction-limited area (reprinted from ref. <sup>20</sup> ). (C) In vivo tumor imaging with NIR CDs: <i> bright-field image, <ii> fluorescence image, <iii> color-coded image of a nude mouse bearing papillary thyroid carcinoma cells. After 30 min post-intravenous injection, CDs primarily accumulated in bladder and the xenograft tumor site (pointed by arrow) (reprinted from ref. <sup>155</sup> ). (D) CDs used for siRNA delivery. HeLa cells were incubated with passivated CDs (blue) loaded with Cy5-labeled siRNA (red) for 2 h. The co-localization of CDs and Cy5 signals implicate successful delivery (reprinted from ref. <sup>156</sup> ).....	22
<b>Figure 2.1.</b> TEM images of (a) CACDs and (b) MACDs (scale bar: 20 nm; inset scale: 10 nm) and particle size distributions of (c) CACDs and (d) MACDs.....	40
<b>Figure 2.2.</b> Optical (UV-vis absorbance and fluorescence) spectra of (a) CACDs and (b) MACDs and fluorescence lifetime traces of (c) CACDs and (d) MACDs.....	42
<b>Figure 2.3.</b> EEM of (a) CACDs, (b) MACDs, (c) CA-P-CDs-4 and (d) MA-P-CDs-4..	44
<b>Figure 2.4.</b> FTIR spectra of (a) citric acid polymeric CDs series, and (b) malic acid polymeric CDs series with a detailed spectral identification of phosphorylated peaks in	

citric acid polymeric CD series ((c) & (d)), and in malic acid polymeric CD series ((e) & (f)).	45
<b>Figure 2.5.</b> $^{13}\text{C}$ NMR spectra of (a) CACDs (b) CA-P-CDs-4, (c) MACDs and (d) MA-P-CDs-4.	47
<b>Figure 2.6.</b> XPS of CDs: (Left hand side) Comparison of the C(1s) regions for CACDs and MACDs, prepared with and without phosphorous doping. (Right hand side) N(1s), O(1s) and P(2p) regions of phosphorous-doped CDs (CA-P-CDs-4 and MA-P-CDs-4).	48
<b>Figure 2.7.</b> EDAX element analysis of citric acid polymeric CD series (left), and malic acid polymeric CD series (right).	51
<b>Figure 2.8.</b> Photostability of the CACDs, CA-P-CDs-4, MACDs and MA-P-CDs-4. Photostability was determined by measuring the change in the absorbance ( $A/A_0$ ) at 350nm as a function of CD exposure to the intense visible light generated in a Rayonet reactor.	52
<b>Figure 2.9.</b> Comparison of $\tau_{\text{avg}}$ among (a) citric acid carbon dots, and (b) malic acid carbon dots using one-way ANOVA.	55
<b>Figure 2.10.</b> Colony counting assay results of citric acid polymeric CDs after (a) 15-min exposure and (b) 1-hour exposure, and results of malic acid polymeric CDs after (c) 15-min exposure and (d) 1-hour exposure (Error bars indicate standard deviation, and for simplicity, only the positive half of each error bar is shown).	56
<b>Figure 2.11.</b> (a) 15-min and (b) 1-hour exposure results of MA-P-CDs-4 (5 mg/mL) in dark condition and under lab light condition.	59
<b>Figure 3.1.</b> Characterization of individual MACDs. (a) Time-lapse fluorescence imaging of MACDs on glass coverslip shows stochastic on and off fluorescence emission. (b) A representative fluorescence trace of an individual MACD. (c) Histogram of MACD on-time distribution. (d) The average duty cycle of MACDs, determined by summarizing a large number of single-particle blinking traces (>5,000 particle traces). (e) Characterization of fluorescence emission over 400 s green excitation shows the survival fraction of MACD particles (error bars indicate the standard deviation of five independent replicates).	74
<b>Figure 3.2.</b> Characterization of the MACD SNR under different conditions. (a) Representative emission traces of MACDs in response to different excitation wavelengths. (b) SNR of MACDs under different excitation wavelengths in comparison with commonly used organic dyes under their optimal excitation wavelengths. (c) Characterization of MACD photoblinking in a variety of imaging solutions. (d) Comparison of MACD SNRs in different imaging solutions.	75
<b>Figure 3.3.</b> SRLM of MACDs in fixed trout epithelial gill cells. The spontaneous photoblinking of MACDs enables a significant improvement of the spatial resolution as demonstrated by the fluorescence emission profiles (right panel) of the region of interest (ROI) marked by the small rectangle in the fluorescence images.	77

**Figure 3.4.** Distribution of MACDs in live trout gill epithelial cells. (a) MACDs with different sizes, corresponding to excitation wavelengths 488 nm, 514 nm and 561 nm, were found to localize at the same intracellular compartments, while MACDs that were excited with 405 nm were found to localize at different compartments. (b) The green-to-yellow MACDs (with excitation wavelength  $\geq$  488 nm), were found to be present mainly in mitochondria, as determined by their co-localization with MitoTracker. .... 78

**Figure 3.5.** Photographic images of MACD fractions #2, #10, and #14 under (a) room light condition and (b) 365 nm UV illumination. TEM images of MACD fractions (c) #2, (d) #10, and (e) #14 (inset scale bar: 5nm, 5nm, and 20nm, respectively). Corresponding PSD for MACD fractions (f) #2, (g) #10, and (h) #14, determined by ImageJ analysis of TEM images. .... 81

**Figure 3.6.** Significance test of the MACD fraction TEM PSDs. .... 83

**Figure 3.7.** MACD fraction DLS: PSD of fraction (A) #2, (B) #10, and (C) #14. .... 83

**Figure 3.8.** (a) FTIR and (b) XPS spectra of unseparated MACDs (black) and MACD fraction #2 (red), #10 (green), and #14 (blue). UV-vis extinction spectra of MACD fraction: (C) #2, (D) #10, and (E) #14. .... 84

**Figure 3.9.** Fluorescence properties of MACD fractions. Upper panel, fraction #2: (A) fluorescence emission under varied excitation, with normalized spectrum embedded, (B) 2D EEM, and (C) CIE 1931 color coordinates; middle panel, fraction #10: (D) fluorescence emission under varied excitation, with normalized spectrum embedded, (E) 2D EEM, and (F) CIE 1931 color coordinates; lower panel, fraction #14: (G) fluorescence emission under varied excitation, with normalized spectrum embedded, (H) 2D EEM, and (I) CIE 1931 color coordinates. .... 86

**Figure 3.10.** Upper panel: (A) 3D EEM and (B) fluorescence decay traces of MACD fraction #2; middle panel: (C) 3D EEM and (D) fluorescence decay traces of MACD fraction #10; lower panel: (E) 3D EEM and (F) fluorescence decay traces of MACD fraction #14. .... 89

**Figure 4.1.** Morphology and size analysis of Si NCs. TEM images of (a) undoped Si NCs, (b) 5% B-doped Si NCs, and (c) 5% P-doped Si NCs. Corresponding particle size distribution of (d) undoped Si NCs, (e) 5% B-doped Si NCs, and (f) 5% P-doped Si NCs (c.a. 500 counts based on TEM data). .... 100

**Figure 4.2.** HRTEM images and SAED patterns (inset) of Si NCs: (a) undoped Si NCs, (b) 5% B-doped Si NCs, (c) 30% B-doped Si NCs, (d) 5% P-doped Si NCs, and (e) 30% P-doped Si NCs. .... 102

**Figure 4.3.** XRD patterns of Si NCs. .... 104

**Figure 4.4.** (a) Abiotic induction of ROS by Si NCs determined by the DCFDA assay (incubation time: 2.5 hours, n = 3), (b) enlarged view for low intensity data. .... 105

**Figure 4.5.** Bacterial viability of *S. oneidensis* MR-1 evaluated by colony counting assay (drop plate method). The asterisk indicates significance level: \*p<0.05, \*\*p<0.01, \*\*\*p<0.001, \*\*\*\*p<0.0001 (examined by one-way ANOVA, followed by Dunnett's multiple comparisons test, n = 4 or 5). .... 107

<b>Figure 4.6.</b> TEM image (left) and SAED pattern (right) of 30% B-doped Si NCs after 2-hr bacteria exposure. Bacteria exposure has no influence on particle morphology, size, and crystallinity (scale bar: 20nm, inset: 5 nm). .....	109
<b>Figure 4.7.</b> CytoViva-enhanced dark-field analysis of the interaction between 5% P-doped Si NCs with <i>S. oneidensis</i> MR-1. (a) dark-field image of bacteria exposure solution, (b) hyperspectral image of boxed area in A. Mapping (c) bacteria cells alone and (d) 5% P-doped Si NCs alone in the hyperspectral data. (e) Merged mapping results of (c) and (d) where bacteria cells are false-colored yellow while 5% P-doped Si NCs with red. ....	110
<b>Figure 4.8.</b> CytoViva analysis of <i>S. oneidensis</i> MR-1 cells: (a) dark field image, (b) hyperspectral image, and (c) spectral library of <i>S. oneidensis</i> MR-1 cells, generated by ROI tool.....	113
<b>Figure 4.9.</b> CytoViva analysis of undoped Si NCs: (a) dark field image, (b) hyperspectral image, and (c) spectral library of undoped Si NCs, generated by ROI tool. ....	114
<b>Figure 4.10.</b> CytoViva analysis of 5% B-doped Si NCs: (a) dark field image, (b) hyperspectral image, and (c) spectral library of 5% B-doped Si NCs, generated by ROI tool. ....	115
<b>Figure 4.11.</b> CytoViva analysis of 30% B-doped Si NCs: (a) dark field image, (b) hyperspectral image, and (c) spectral library of 30% B-doped Si NCs, generated by ROI tool. ....	116
<b>Figure 4.12.</b> CytoViva analysis of 5% P-doped Si NCs: (a) dark field image, (b) hyperspectral image, and (c) spectral library of 5% P-doped Si NCs, generated by ROI tool. ....	117
<b>Figure 4.13.</b> CytoViva analysis of 30% P-doped Si NCs: (a) dark field image, (b) hyperspectral image, and (c) spectral library of 30% P-doped Si NCs, generated by ROI tool. ....	118
<b>Figure 4.14.</b> CytoViva enhanced darkfield analysis of the interaction between undoped Si NCs with <i>S. oneidensis</i> MR-1. (a) darkfield image of bacteria exposure solution, (b) hyperspectral image of bacteria exposure solution. Mapping (c) bacteria cells alone and (d) undoped Si NCs alone in the hyperspectral data. (e) The merge of mapping results (c) and (d) (bacteria cells are false colored with yellow while undoped Si NCs with red). ....	119
<b>Figure 4.15.</b> CytoViva enhanced darkfield analysis of the interaction between 5% B-doped Si NCs with <i>S. oneidensis</i> MR-1. (a) darkfield image of bacteria exposure solution, (b) hyperspectral image of bacteria exposure solution. Mapping (c) bacteria cells alone and (d) 5%B doped Si NCs alone in the hyperspectral data. (e) The merge of mapping results (c) and (d) (bacteria cells are false colored with yellow while 5% B-doped Si NCs with red). ....	120
<b>Figure 4.16.</b> CytoViva enhanced darkfield analysis of the interaction between 30% B-doped Si NCs with <i>S. oneidensis</i> MR-1. (a) darkfield image of bacteria exposure	

<p>solution, (b) hyperspectral image of bacteria exposure solution. Mapping (c) bacteria cells alone and (d) 30%B doped Si NCs alone in the hyperspectral data. (e) The merge of mapping results (c) and (d) (bacteria cells are false colored with yellow while 30% B-doped Si NCs with red). .....</p> <p><b>Figure 4.17.</b> CytoViva enhanced darkfield analysis of the interaction between 30% P-doped Si NCs with <i>S. oneidensis</i> MR-1. (a) darkfield image of bacteria exposure solution, (b) hyperspectral image of bacteria exposure solution. Mapping (c) bacteria cells alone and (d) 30%P doped Si NCs alone in the hyperspectral data. (e) The merge of mapping results (c) and (d) (bacteria cells are false colored with yellow while 30% P-doped Si NCs with red). .....</p> <p><b>Figure 4.18.</b> Bio-TEM images of <i>S. oneidensis</i> MR-1 cells alone (a), and <i>S. oneidensis</i> MR-1 cells exposed to undoped Si NCs (b), 5% B-doped Si NCs (c), and 5% P-doped Si NCs (d). The right column in each section displays corresponding magnified view in both bright field mode (upper panel) and dark field mode (lower panel). The dark field TEM diffraction angle was set to reveal the crystalline Si NCs. ....</p> <p><b>Figure 4.19.</b> TEM images of <i>S. oneidensis</i> MR-1 exposed to 30% B-doped Si NCs: (a) bright field image, (b) zoom-in view of (a), and (c) corresponding dark field image. TEM images of <i>S. oneidensis</i> MR-1 exposed to 30% P-doped Si NCs: (d) bright field image, (e) zoom-in view of (d), and (f) corresponding dark field image. ....</p> <p><b>Figure 5.1.</b> TEM, high-resolution TEM (inset: SAED patterns), and PSDs of (a-c) undoped Ge NCs, (d-f) 10% B-doped Ge NCs, and (g-i) 10% P-doped Ge NCs. The PSDs are fit to log-normal distributions with geometric mean <math>\mu</math> and geometric standard deviation <math>\sigma</math>; the number of counts (N) is approximately 500. ....</p> <p><b>Figure 5.2.</b> (a) XRD and (b) FTIR spectra for Ge NCs; high-resolution (c) Ge 3d and (d) Ge 2p XPS spectra for undoped Ge NCs. ....</p> <p><b>Figure 5.3.</b> FTIR spectra for freshly synthesized Ge NCs. ....</p> <p><b>Figure 5.4.</b> XPS survey spectrum for undoped Ge NCs. ....</p> <p><b>Figure 5.5.</b> Comparison of doping levels of Ge NCs. ....</p> <p><b>Figure 5.6.</b> Bacterial viability of <i>S. oneidensis</i> exposed to Ge NCs, evaluated by the colony counting assay (drop plate method). The asterisks indicate statistical significance level: *<math>p &lt; 0.05</math>, **<math>p &lt; 0.01</math>, ***<math>p &lt; 0.001</math>, ****<math>p &lt; 0.0001</math> (examined by one-way ANOVA, followed by Dunnett's multiple comparison tests, <math>n = 4</math> or <math>5</math> biological replicates). ....</p> <p><b>Figure 5.7.</b> (a) Calibration curve to determine the concentration of boron. (<math>n = 3</math>) (b) Calibration curve to determine the concentration of phosphorus. (<math>n = 3</math>) .....</p> <p><b>Figure 5.8.</b> Colony counting experiments using the supernatants of Ge NCs. There are no significant differences among the different experimental conditions. ....</p> <p><b>Figure 5.9.</b> Abiotic assessment of ROS generation by DCFDA assay (incubation time = 75 minutes, <math>n = 3</math>): (A) undoped Ge NCs, (B) 10%B Ge NCs, (C) 30%B Ge NCs, (D) 10%P Ge NCs, and (E) 30%P Ge NCs. ....</p> <p><b>Figure 5.10.</b> Enlarged views for the abiotic ROS generation of varied Ge NCs. ....</p>	<p>121</p> <p>122</p> <p>123</p> <p>123</p> <p>139</p> <p>141</p> <p>143</p> <p>144</p> <p>145</p> <p>148</p> <p>151</p> <p>152</p> <p>153</p> <p>153</p>
--	---

**Figure 5.11.** Hydroxyl radical generation at 15-minute and 1-hour time intervals, as measured by cell-free HPF assays. The asterisks indicate statistical significance level: \* $p < 0.05$ , \*\* $p < 0.01$ , \*\*\* $p < 0.001$ , \*\*\*\* $p < 0.0001$  (examined by two-way ANOVA, followed by Sidak’s multiple comparison tests,  $n = 3$ ). ..... 155

**Figure 5.12.** Superoxide radical generation at 15-minute and 1-hour time intervals, as measured by DHE assays. The asterisks indicate statistical significance level: \* $p < 0.05$ , \*\* $p < 0.01$ , \*\*\* $p < 0.001$ , \*\*\*\* $p < 0.0001$  (examined by two-way ANOVA, followed by Sidak’s multiple comparison tests,  $n = 3$ ). ..... 156

**Figure 5.13.** CytoViva analysis of *S. oneidensis* cells: DF image, HSI image, and spectral library for *S. oneidensis* MR-1 cells, generated using the ROI tool. .... 158

**Figure 5.14.** CytoViva analysis of undoped Ge NCs: DF image, HSI image, and spectral library for undoped Ge NCs, generated using the ROI tool. .... 159

**Figure 5.15.** CytoViva analysis of 10% B-doped Ge NCs: DF image, HSI image, and spectral library for 10% B-doped Ge NCs, generated using the ROI tool. .... 160

**Figure 5.16.** CytoViva analysis of 30% B-doped Ge NCs: DF image, HSI image, and spectral library for 30% B-doped Ge NCs, generated using the ROI tool. .... 161

**Figure 5.17.** CytoViva analysis of 10% P-doped Ge NCs: DF image, HSI image, and spectral library for 10% P-doped Ge NCs, generated using the ROI tool. .... 162

**Figure 5.18.** CytoViva analysis of 30% P-doped Ge NCs: DF image, HSI image, and spectral library for 30% P-doped Ge NCs, generated using the ROI tool. .... 163

**Figure 5.19.** Enhanced DF analysis of the association between *S. oneidensis* MR-1 cells with undoped Ge NCs: (a) DF image of bacteria exposure solution, (b) HSI image of ROI in a. Mapping (c) undoped Ge NCs alone and (d) *S. oneidensis* MR-1 cells alone in the HSI data. (e) Merged mapping results of (c) and (d) where bacteria cells are false-colored red while undoped Ge NCs with green. .... 164

**Figure 5.20.** Enhanced DF analysis of the association between *S. oneidensis* MR-1 cells with 10% B-doped Ge NCs: (a) DF image of bacteria exposure solution, (b) HSI image of ROI in a. Mapping (c) 10% B-doped Ge NCs alone and (d) *S. oneidensis* MR-1 cells alone in the HSI data. (e) Merged mapping results of (c) and (d) where bacteria cells are false-colored red while 10% B-doped Ge NCs with green. .... 165

**Figure 5.21.** Enhanced DF analysis of the association between *S. oneidensis* MR-1 cells with 30% B-doped Ge NCs: (a) DF image of bacteria exposure solution, (b) HSI image of ROI in a. Mapping (c) 30% B-doped Ge NCs alone and (d) *S. oneidensis* MR-1 cells alone in the HSI data. (e) Merged mapping results of (c) and (d) where bacteria cells are false-colored red while 30% B-doped Ge NCs with green. .... 166

**Figure 5.22.** Enhanced DF analysis of the association between *S. oneidensis* MR-1 cells with 10% P-doped Ge NCs: (a) DF image of bacteria exposure solution, (b) HSI image of ROI in a. Mapping (c) 10% P-doped Ge NCs alone and (d) *S. oneidensis* MR-1 cells alone in the HSI data. (e) Merged mapping results of (c) and (d) where bacteria cells are false-colored red while 10% P-doped Ge NCs with green. .... 167

<b>Figure 5.23.</b> Enhanced DF analysis of the association between <i>S. oneidensis</i> MR-1 cells with 30% P-doped Ge NCs: (a) DF image of bacteria exposure solution, (b) HSI image of ROI in a. Mapping (c) 30% P-doped Ge NCs alone and (d) <i>S. oneidensis</i> MR-1 cells alone in the HSI data. (e) Merged mapping results of (c) and (d) where bacteria cells are false-colored red while 30% P-doped Ge NCs with green. ....	168
<b>Figure 5.24.</b> (upper level) BF TEM images for (a) <i>S. oneidensis</i> MR-1 cells and bacteria cells exposed to (b) 30% B-doped Ge NCs and (c) 30% P-doped Ge NCs; (lower level) DF TEM images for bacteria cells exposed to (b) 30% B-doped Ge NCs and (c) 30% P-doped Ge NCs. ....	170
<b>Figure 5.25.</b> BF (upper) and DF (lower) bio-TEM images of <i>S. oneidensis</i> MR-1 cells exposed to (a) undoped, (b) 10% B-doped, and (c) 10% P-doped Ge NCs. For the DF images, Ge NC diffraction angles were chosen so that Ge NCs would appear bright compared to other features. ....	171
<b>Figure 6.1.</b> Representative UV-vis (left) and FL (right) spectra of as-made CD reactions. Citric acid to urea molar ratio was kept at 0.7 and the reaction temperature was 200 °C. ....	181
<b>Figure 6.2.</b> (a) Photographic image of obtained CD fractions, (b)-(d) UV-vis extinction spectra and (e)-(g) 2D EEM of representative blue, green, and red fractions, (h) the normalized FL spectra and (i) the chromaticity diagram of CD fractions. ....	182
<b>Figure 6.3.</b> TEM images of (a) as-made CDs, (b) CACD-B, (c) CACD-G, and (d) CACD-R fractions. ....	184
<b>Figure 6.4.</b> DLS measurements for (a) as-made CDs, (b) CACD-B, (c) CACD-G, and (d) CACD-R fractions. ....	185
<b>Figure 6.5.</b> ATR-IR spectra of CACD-B (blue), G (green), and R (red) compared to the as-made CDs (black). ....	187
<b>Figure 6.6.</b> Impact of fractionated carbon dots on cell viability. (a) Red, blue and green carbon dots caused no significant decrease in trout gill epithelial cell viability following 1 h exposure to 1, 10, 50, or 100 µg/mL of carbon dots. (b) Red and green carbon dots caused no significant decrease in cell viability following exposure for 24 h at all concentrations studied. Blue carbon dots did cause a significant decrease in cell viability following exposure to 100 µg/mL. **, p < 0.01. ....	189
<b>Figure 6.7.</b> Comparison of fractionated and unfractionated carbon dots on cell viability following 2 h exposure to 100 µg/mL of carbon dots. The blue carbon dots caused a significant decrease in viability compared to control cells. ***, p < 0.001. ....	190
<b>Figure 6.8.</b> Distribution of unseparated CACDs in living gill cells. ....	191
<b>Figure 6.9.</b> Red CACDs mainly localizes in lysosomes upon uptake. ....	192
<b>Figure 6.10.</b> Some blue CACDs could localize in lysosomes upon uptake. ....	193
<b>Figure 6.11.</b> Some blue CACDs could localize in mitochondria upon uptake. ....	194
<b>Figure 6.12.</b> MACDs mainly localize in mitochondria upon uptake. ....	195

## List of Abbreviations

lifetime ( $\tau_{\text{avg}}$ )	2',7'-dichlorofluorescein diacetate (DCFDA)
geometric standard deviation ( $\sigma_g$ )	dark field (DF)
adenosine diphosphate (ADP)	dilution fold (DF)
anion-exchange HPLC (AE-HPLC)	density functional theory (DFT)
atomic force microscopy (AFM)	dihydroethidium (DHE)
adenosine monophosphate (AMP)	dynamic light scattering (DLS)
adenosine triphosphate (ATP)	dimethyl fumarate (DMF)
attenuated total reflection-Fourier transform infrared spectroscopy (ATR-FTIR)	dimethyl Sulfoxide (DMSO)
bright field (BF)	Dulbecco's phosphate-buffered saline (DPBS)
citric acid (CA)	energy dispersive X-ray analysis (EDAX)
carbon dots (CDs)	energy-dispersive X-ray spectroscopy (EDS)
Commission International de l'Eclairage (CIE)	excitation emission matrix (EEM)
colony-forming unit (CFU)	enhanced permeability and retention (EPR)
carbon quantum dots (CQDs)	4-(2-hydroxyethyl)-1-piperazineethanesulfonic acid (HEPES)
carbon nanodots (CNDs)	highest occupied molecular orbital (HOMO)
carbon nanotubes (CNTs)	
4',6-diamidino-2-phenylindole (DAPI)	

glucose oxidase-containing solution (GLOX)	3-(4,5-dimethylthiazol-2-yl)-5-(3-carboxymethoxyphenyl)-2-(4-sulfophenyl)-2H-tetrazolium (MTS)
graphene quantum dots (GQDs)	messenger RNA (mRNA)
fluorescence in-situ hybridization (FISH)	molecular weight (MW)
hydroxyphenyl fluorescein (HPF)	numerical aperture (NA)
high resolution TEM (HRTEM)	nanocrystal (NC)
hyperspectral (HSI)	nanodiamond (ND)
full width at half maximum (FWHM)	near infrared (NIR)
high-performance liquid chromatography (HPLC)	nanoparticle (NP)
Luria-Bertani (LB)	optical density at wavelength of 600 nm (OD <sub>600</sub> )
light-emitting diodes (LED)	photo-activated localization microscopy (PALM)
liquid/liquid extraction (LLE)	polymeric dot (PD)
lipopolysaccharides (LPS)	polydispersity index (PDI)
localized surface plasmon resonance (LSPR)	inorganic phosphate (Pi)
lowest unoccupied molecular orbital (LUMO)	photoluminescence (PL)
malic acid (MA)	proton-pump inhibitor (PPi)
methanol (MeOH)	particle size distributions (PSD)
millisecond (ms)	point spread function (PSF)
	quantum dot (QD)
	quantum yields (QY)

region-of-interest (ROI)

reactive oxygen species (ROS)

ribonucleic acid (RNA)

reversed-phase HPLC (RP-HPLC)

selected area electron diffraction (SAED)

spectral angle mapper (SAM)

structured illumination microscopy (SIM)

single-molecule fluorescence in-situ hybridization (smFISH)

single-molecule localization-based microscopy (SMLM)

signal-to-noise ratio (SNR)

*Shewanella oneidensis* MR-1 (*S. oneidensis* MR-1)

super-resolution optical fluctuation imaging (SOFI)

solid-phase extraction (SPE)

super-resolution localization microscopy (SRLM)

saline-sodium citrate (SSC)

stimulated emission depletion (STED)

stochastic optical reconstruction microscopy (STORM)

single-walled carbon nanotube (SWCNT)

carboxytetramethylrhodamine (TAMRA)

transmission electron microscopy (TEM)

time-correlated single-photon counting (TCSPC)

thin layer chromatography (TLC)

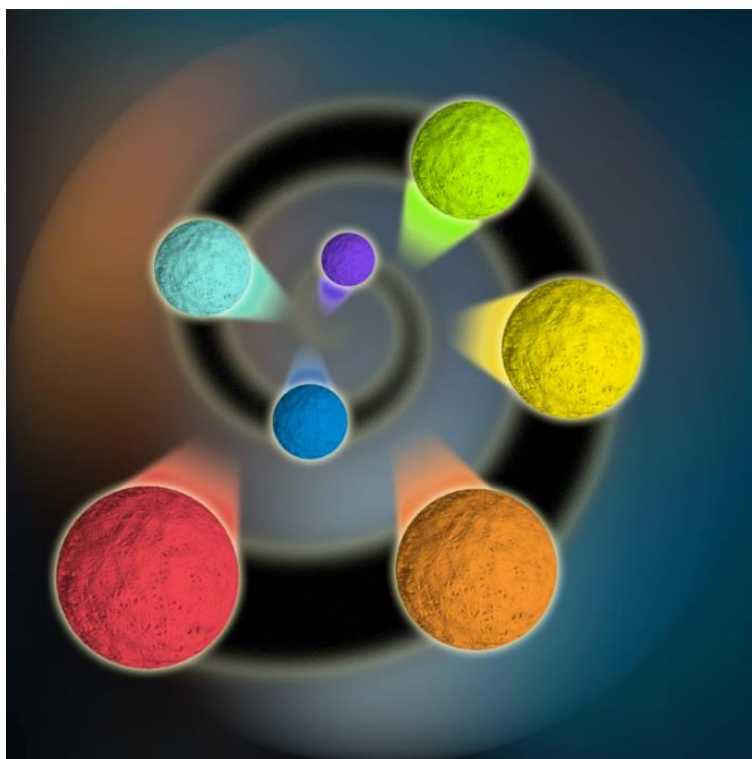
ultraviolet (UV)

X-ray photoelectron spectroscopy (XPS)

X-ray diffraction (XRD)

## Chapter 1

Syntheses and applications of multicolor carbon-based luminescent dots



Reproduced from: Zhi, B.; Yao, X.; Cui, Y.; Orr, G.; Haynes, C.L., Syntheses and applications of multicolour carbon-based luminescent dots. *Nanoscale*, *In revision*.

Copyright 2019, with permission from the Royal Society of Chemistry.

Bo Zhi is responsible for the drafting of the overview, introduction, hypotheses, syntheses, perspective and future directions.

## **1.1 Overview**

Due to the prominent characteristics of carbon-based luminescent nanostructures (known colloquially as CDs), such as inexpensive precursors, excellent hydrophilicity, low toxicity, and intrinsic fluorescence, these nanomaterials are regarded as potential candidates to replace traditional QDs in some applications. As such, research in the field of CDs has been increasing in recent years. In this mini-review, we summarize recent progress in studies of multicolor CDs focusing on potential photoluminescence mechanisms, strategies for effective syntheses, and applications in ion/molecule and temperature sensing, and high-resolution bioimaging techniques.

## **1.2 Introduction**

The first report on the discovery of “fluorescent carbon fragments” in 2004 triggered research interest in carbon-based luminescent dots, namely, CDs.<sup>1</sup> Typically, CD refers to zero-dimensional fluorescent or phosphorescent carbon nanostructures, where the particle size is typically around 10 nm.<sup>2-5</sup> Up to now, there has not been a well-defined categorization among CDs, but conventionally, CDs with discernible crystalline lattices are named as GQDs (with a single graphene layer) or CQDs (with multi graphene layers) while CDs with an amorphous nature are named as CNDs or non-conjugated PDs; specifically, GQDs or CQDs can be synthesized via top-down methods, such as acid treatments of bulk carbon sources (e.g., anthracite coal or carbon black)<sup>6,7</sup> while a bottom-up approach is usually applied to prepare CNDs or PDs using small organic molecules such as citric acid and dopamine.<sup>8-10</sup>

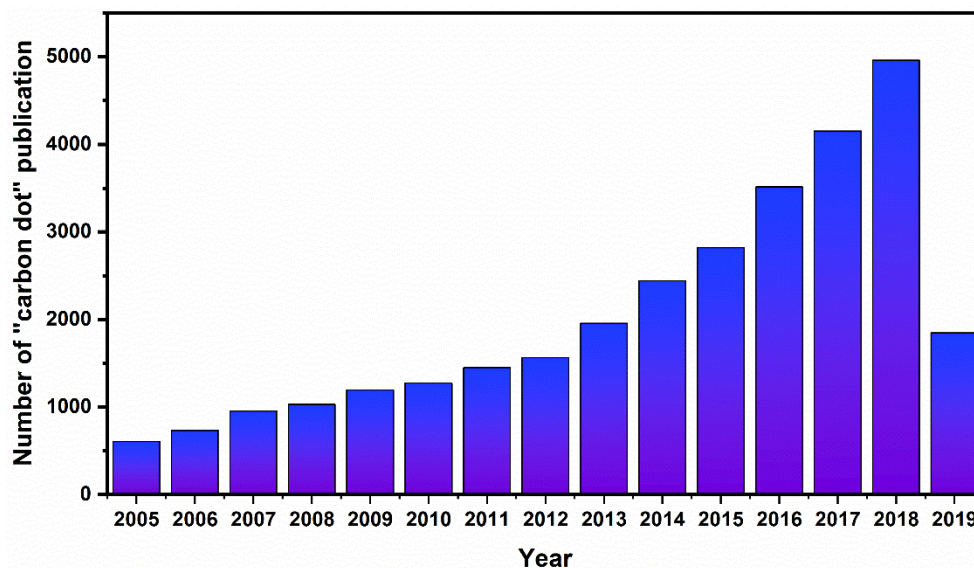


**Figure 1.1.** The summary of carbon dot publication since 2005, analyzed via Web of Science up to April 25<sup>th</sup>, 2019. Search criteria: TOPIC: (carbon dots) OR TOPIC: ("carbon quantum dots") OR TOPIC: ("graphene quantum dots") OR TOPIC: ("carbon nanodots") OR TOPIC: ("non-conjugated polymer dots") NOT TITLE: ("quantum dots").

Typically, CDs are characterized by broad choices of inexpensive precursors, ease of synthesis and surface functionalization, bright luminescence, excellent photostability, and superior biocompatibility.<sup>3, 8, 11, 12</sup> Hence, CDs have the potential to replace traditional semiconductor nanocrystals QDs, which are usually high-cost and raise environmental concerns due to their heavy metal content.<sup>13, 14</sup> Consequently, CDs have become a fast-growing field, attracting an increasing number of researchers to refine synthesis strategies, improve optical and optoelectronic properties, and develop CD-based applications, such as selective sensing,<sup>15-19</sup> target-specific bioimaging,<sup>12, 20-22</sup> environmental remediation,<sup>23</sup> LED,<sup>24-28</sup> energy conversion devices,<sup>29-32</sup> and photocatalysis<sup>10, 33, 34</sup>. As shown in the publication analysis (Figure 1.1), in recent decades, publication efforts on CDs are robust, especially after 2012, making CDs a hot research topic in nanoscience.

However, most of the reported CDs only emit intense blue or green luminescence, especially for popular citric-acid based CDs.<sup>4, 35-39</sup> Compared to traditional QDs, such a narrow emission window and short emission range (~450 to 560 nm) limits the development of CD-based applications, such as color-coded sensing systems and full-color LED devices. Therefore, to make the most of the potential of CDs, it is necessary to seek CDs covering more of the visible/IR spectrum, as is possible with traditional QDs. Fortunately, in recent years, publications on multicolor emitting CDs or long-wavelength-emitting CDs have increased, and quite a few inspiring studies have been reported. Herein, this review will provide a summary of several prevalent hypotheses regarding the origin of the CD photoluminescence and synthesis success of multicolor CDs as well as related applications, all topics that are active challenges in the field. The overall goal of this mini-review is to present a clear overview of current achievements and challenges in the field of multicolor CDs.

### **1.3. Hypotheses for the photoluminescence mechanism of CDs**

It is necessary to gain a thorough understanding of the CD luminescence phenomenon before these optical properties can be readily tuned as is possible with traditional QDs. Unfortunately, due to the diversity and complexity of CDs, there is not an accurate description of the CD structure, let alone their photoluminescence mechanism. Up to now, several hypotheses have been proposed to explain the origins of the emission from CDs, such as size-dependent emission (the quantum confinement effect), surface state-derived luminescence, and embedded molecular luminophores.

#### **1.3.1 Size-dependent emission**

As the particle size distribution of typical CDs (~10 nm) is comparable to the quantum size range, some research groups believe that, similar to the traditional QDs, the size-dependent quantum confinement effect, contributes to the luminescence emission of CDs.<sup>40-45</sup> Yuan and co-workers generated a series of nitrogen-doped, surface-passivated, and highly crystalline CQDs by tuning the fusion and carbonization of citric acid and diamionaphthalene via a bottom-up solvothermal method.<sup>25</sup> Interestingly, by carefully controlling the synthesis conditions, the emission of the five CQD products were adjusted from blue (430 nm) to red (604 nm). In addition, as the maximum excitation wavelengths were in line with the corresponding excitonic absorption peaks, the authors claimed that the emission should be attributed to band-edge exciton-state decay rather than surface/defect states. Moreover, by carefully examining the particle size and height distribution via TEM and AFM, respectively, it was observed that along with the emission red-shift, the average CD diameters increased from 1.95 nm (blue CDs) to 6.68 nm (red CDs). As such, authors deduced that the red-shifting emission revealed the bandgap transitions in CDs derived from the quantum confinement effect. In our previous work on malic acid-based CDs, we applied reversed-phase column chromatography to separate as-synthesized polymeric CD products (of which the emission was excitation dependent).<sup>20</sup> Three main CD fractions were obtained after the chromatographic purification, emitting blue, turquoise green, and greenish yellow. The size distributions of these CDs were observed to increase from  $6.2 \pm 2.0$  to  $9.2 \pm 1.7$  to  $15.6 \pm 6.0$  nm, corresponding to decreasing optical bandgap energies from 2.97 eV to 2.91 eV to 2.21 eV. Even though the size-dependent emission mechanism is supported in some cases, other studies were unable

to find a correlation between size and emission wavelength.<sup>46, 47</sup> Thus, other photoluminescence mechanisms are being explored, such as surface state and molecular luminophore.

### 1.3.2 Surface state-derived luminescence

Using either top-down or bottom-up synthesis routes, a high temperature (typically 100-200 °C) is necessary to break down carbon precursors or polymerize/carbonize molecular precursors. Therefore, CD reactions are highly reactive (e.g., subject to oxidation and localized carbonization) and consequently, the chemical environments on the CD surfaces are potentially diverse and complicated. One can expect  $sp^2/sp^3$  hybridised carbons, surface defects, and other functional groups.<sup>48-52</sup> As these surface moieties possess different energy levels, some researchers agree that the surface states of CDs should influence the multicolor emissions.<sup>35, 47, 48</sup> Ding and co-workers applied a one-pot hydrothermal method to prepare CD mixtures, and after a thorough chromatographic separation, luminescent CD fractions were obtained covering almost the entire visible range.<sup>53</sup> TEM was used to determine the CD size ranges as well but it was found that the particle size distributions were quite broad. Thus, the authors did not attribute the variable emission properties to the quantum size effect. On the other hand, after carefully comparing the oxygen atom percentages among four representative CD samples, they observed that an increase of carboxyl content and degree of oxidation corresponded with the red shift of CD emissions. As LUMO is influenced by oxygen species,<sup>47</sup> they claimed that the band gaps between HOMO and LUMO should decrease corresponding to the

intensifying surface oxidation of CD samples, leading to a red shift in the photoluminescence emission.

### 1.3.3 Molecular luminophores

Molecular luminophore-derived emission or molecular state emission is another prevalent hypothesis for CD emission upon preparation by bottom-up methods.<sup>54-59</sup> Considering the existence of active functional groups (e.g., carboxyl and amine groups) within the structures of molecular precursors (e.g., citric acid and *p*-phenylenediamine), these carbon precursors can readily react with one another and undergo further condensation, polymerization, and carbonization, forming the final CD products. However, as bottom-up methods support highly reactive conditions (e.g., a high reaction temperature, high pressure, and/or a long reaction time),<sup>55, 60-62</sup> it is reasonable to expect other side reactions as well. In other words, small molecules or even oligomeric luminophores can be produced during CD synthesis and as such, these luminophores can be covalently attached to the surface of CD backbones, granting CDs bright emission characteristics. Recently, Rogach and coworkers hydrothermally synthesized three different CDs by reacting citric acid with three different amine precursors (e.g., ethylenediamine, hexamethylenetetramine, and triethanolamine).<sup>36, 55</sup> They carefully characterized the chemical environments of carbon and nitrogen species within the CDs via X-ray photoelectron spectroscopy, and compared their optical performance with that of citrazinic acid, a molecular fluorophore belonging to the pyridine family. This study confirmed the presence of the derivatives of citrazinic acid and as such, their contribution to the blue fluorescence of ethylenediamine-CDs (e-CDs) and hexamethylenetetramine-

CDs (h-CDs). Moreover, they claimed that fluorescent citrazinic acid derivatives were attached to e-CDs and h-CDs by comparing their photoluminescence lifetimes to that of pure citrazinic acid. Zhang and co-workers also proposed an intriguing mechanism that the hydrogen bond effect between CD molecular states and solvents may be responsible for the red emission observed from their five CD samples.<sup>63</sup> They prepared five red-emitting CDs by reacting *p*-phenylenediamine in five different polar solvents, that is, water, ethanol, dimethylformamide, cyclohexane, and toluene. Interestingly, due to solvation effects, the CD emission can be adjusted from green to red (540–614 nm). Furthermore, by applying a variety of theoretical models, they thoroughly evaluated the influence of polarization and hydrogen bonding effects on the expected emission variations for the CDs. With these data, they argued that hydrogen bond-dominated molecular state emission was the main mechanism responsible for the spectral shifts.

#### **1.4 Syntheses of multicolor CDs**

Because there is not a decisive understanding about how the CD structure contributes to their luminescence, it remains a challenge to fine-tune the emission wavelengths of the final CD products via adjusting synthesis conditions. In the past decades, most of the reported as-synthesized CDs emit blue or green;<sup>64-67</sup> however, it is desirable that CDs can luminesce across and beyond the visible spectrum comparable to their QD counterparts; specifically, long-wavelength emission (e.g., red or even near infrared regions) can provide deeper penetration depths for biological microscopy applications.<sup>64, 68</sup> In fact, quite a number of synthesis successes for multicolor- and long-wavelength-emitting CDs

have been reported; this section summarizes these achievements based on the critical synthesis element: precursor screening, solvent engineering, or refining via separation.

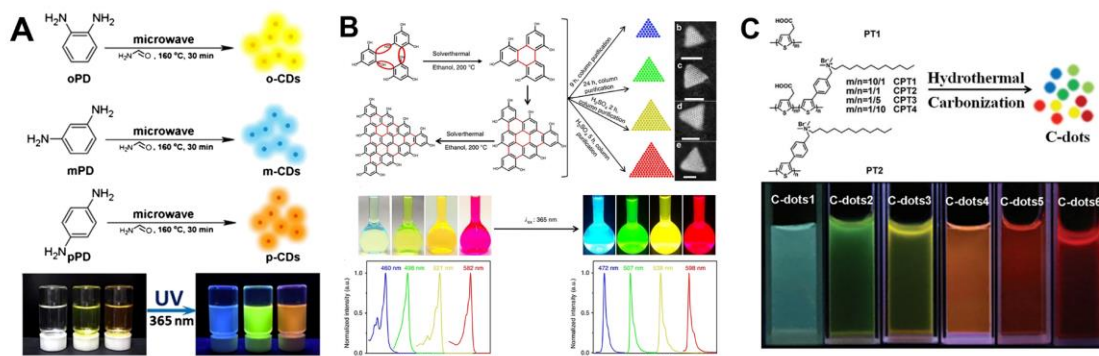


**Figure 1.2.** (a) blue, yellow, and orange emitting CDs prepared from phenylenediamine derivatives. Adapted with permission from Ref<sup>76</sup>; (b) multicolor CQDs obtained by the assembly of phloroglucinol molecules. Adapted permission from Ref<sup>42</sup>; (c) the emissions of CDs were tuned from the blue (482 nm) to the near-infrared (680 nm) region by adjusting the ratios of polythiophene derivatives. Adapted with permission from Ref<sup>77</sup>

#### 1.4.1 Precursor screening for multicolor CDs

The choice of carbon precursors plays a critical role in the generation of multicolor CDs. Typically, in top-down approaches, bulk carbon sources with crystalline character are chemically or physically “broken down” to obtain GQDs or CQDs. Common precursors include carbon fibers,<sup>69</sup> single/multi-wall carbon nanotubes,<sup>70, 71</sup> and other carbon-rich chemicals.<sup>72, 73</sup> Yuan and co-workers synthesized single-layer and single-crystalline GQDs by refluxing C<sub>96</sub>H<sub>30</sub> with fuming nitric acid, followed by hydrothermal treatment at 200 °C.<sup>64</sup> These GQD products exhibited a uniform particle size distribution and more importantly, their optical properties, such as absorption, photoluminescence, and two-photon photoluminescence, were highly dependent on the size of GQDs; that is, redshifts in emission were observed as the size increased. It is worth noting that an oxidation

treatment using phosphoric acid during CD synthesis is nearly a universal component when obtaining long-wavelength-emitting CDs. For example, Gong and co-workers produced N, P-codoped CDs using a one-step acidic oxidation of pumpkin by  $\text{H}_3\text{PO}_4$ .<sup>74</sup> These CDs emitted at 550 nm (yellow fluorescence), corresponding to an optimized excitation of 425 nm. In recent work by Jiang and co-workers, red-emitting CDs were obtained by carbonizing sugar cane bagasse with concentrated  $\text{H}_2\text{SO}_4$  and  $\text{H}_3\text{PO}_4$  at 100 °C. Moreover, these CDs can be coated onto polyvinyl fluoride membranes for the fabrication of a solid-state fluorescent vapor sensor, which could selectively detect and quantify the level of toxic ammonia gas.<sup>75</sup>

Compared to these top-down synthesis, bottom-up methods are typically accomplished using a high-temperature solvothermal environment to assemble molecular or polymer precursors, such as small organic acids, aniline derivatives, phenol derivatives, and polythiophene derivatives, into CD structures.

The most common small organic acid used for the syntheses of CDs is citric acid, originally characterized by emission of intense blue fluorescence,<sup>45, 78-80</sup> however, in recent years, several break-throughs have been reported where citric acid-based CDs can fluoresce in other spectral regions.<sup>26, 81-84</sup> For example, Hola and co-workers reacted citric acid with urea in formamide at 180 °C for 12 hours and then the obtained as-synthesized mixture underwent a chromatographic separation in an anion-exchange column.<sup>81</sup> CD eluents were collected using water and hydrochloric acid as the mobile phase, and the resulting emissions covered the entire visible range. Based on theoretical models, the authors ascribed the multicolor luminescence to the presence of graphitic nitrogen.

In addition to citric acid, aniline derivatives, such as phenylenediamine (PD), are another common molecular precursor that is gaining increasing attention in the last decade.<sup>25, 46, 53, 63, 76, 85-87</sup> Chen and coworkers reported their synthesis work of three different luminescent CDs using *o*-phenylenediamine, *m*-phenylenediamine, and *p*-phenylenediamine as carbon sources.<sup>76</sup> The PD precursors were dissolved in formamide and heated in a microwave reactor at 160 °C for 30 minutes, after which the as-prepared mixtures were further purified by silica column chromatography and dialysis against ethanol. The obtained CD products fluoresced independently of excitation wavelengths, in the blue (444 nm), yellow (533 nm), and orange (574 nm) ranges upon optimized excitations. Based on the facts that the quantum yield was enhanced with increased nitrogen content and that the emission red-shifted with increased C=O/-CONH- content, the authors posit that the luminescence properties are impacted significantly by the surface states, that is, nitrogen-containing functional groups and the degree of oxidation. Liu et.al. chose *o*-phenylenediamine and phthalic acid as precursors and applied a one-pot solvothermal method to prepare as-synthesized CD mixtures.<sup>86</sup> A subsequent chromatographic purification was conducted to precisely separate them into three different colored products (green, yellow, and orange). After a systematic analysis, the authors suggest that the emission from the green and yellow CDs can be attributed to the quantum size effect while the surface defects induced by oxidation is responsible for the orange-emitting CDs.

In addition to aromatic phenylenediamines, phenol derivatives are also finding increased use in the synthesis of multicolor-emitting CDs.<sup>42, 88-93</sup> Yang and coworkers published

their inspiring design of the assembly of phloroglucinol molecules into multicolor triangular CQDs via a six-membered ring cyclization.<sup>42</sup> They skillfully controlled the propagation of the ring cyclization by applying varied amounts of the catalyst, concentrated sulfuric acid, and as such, fine-tuned the sizes of CQDs from 1.9 to 3.9 nm. Along with the increase of the CQD sizes, the emissions red-shifted from 472 to 598 nm and fluoresced four different colors (i.e. blue, green, yellow, and red) corresponding to a decrease in optical bandgap energies from 2.63 to 2.07 eV, which was ascribed to the quantum confinement effect. In addition, as revealed by X-ray powder diffraction, high-angle annular dark field scanning TEM, and high-resolution TEM, the entire set of CQDs exhibited sharp (002) diffraction peaks and well-defined crystalline lattice fringes of the (100) plane, indicative of the highly crystalline nature of these CQD products. Furthermore, DFT simulation studies provided insight that electron-donating hydroxyl groups on the surface of highly crystalline CQD reinforce the charge delocalization and restrain the coupling of electrons and photons, contributing to the high color-purity and narrow emission bandwidth (FWHM of 29-30 nm).

Polymers consisting of aromatic monomers, such as polythiophene derivatives, can also be used to synthesize multicolored CDs.<sup>77, 94-97</sup> Wang and coworkers are taking the lead in designing tunable multicolor-emitting CDs using polythiophene derivatives as starting agents.<sup>77</sup> In this work, they hydrothermally reacted mixtures of two polythiophene derivatives and, by adjusting the ratios of polythiophene derivatives, the emission of final CD products were tuned from the blue (482 nm) to the near-infrared (680 nm) region while using a single excitation wavelength of 400 nm. Additionally, as these

polychromatic CDs exhibited similar size distributions, the authors deduced that the size effect is not responsible for the luminescence. Instead they suggest that differences in CD surface states induced by doping with heteroatoms, such as nitrogen and sulfur, may be responsible and require further investigation.

Overall, though small organic compounds, such as citric acid, used to be the dominating precursors for the preparation of highly luminescent CDs, they tend to yield as-synthesized CD mixtures with extremely complicated compositions, due to their relatively high chemical reactivity and various reaction pathways under high-temperature hydrothermal or solvothermal synthetic conditions. On the other hand, with the goal of achieving some control over the structure of colloidal particles to design multicolor emitting CDs, researchers are more often turning to carbon sources with well-defined molecular structures and relatively predictable reaction routes, such as aromatic compounds that are known to form graphene-like CD structures via controllable syntheses. However, beyond the relatively high expenses of these aromatic chemicals, CD researchers should also be aware of their high toxicity and their potential hazardous influence on the environment and humans.<sup>98-101</sup> Moreover, aniline and phenol derivatives are subject to oxidation in ambient environments<sup>102, 103</sup> and as such, they demand air-free and low-temperature storage conditions, which may eventually increase the synthesis or application cost. Therefore, it remains a challenge and requires further exploration to understand how to prepare these "aromatic" multicolor CDs in an eco-friendly and economical manner as those traditional CDs, such as citric acid-based CDs.

#### 1.4.2 Solvent engineering for multicolor CDs

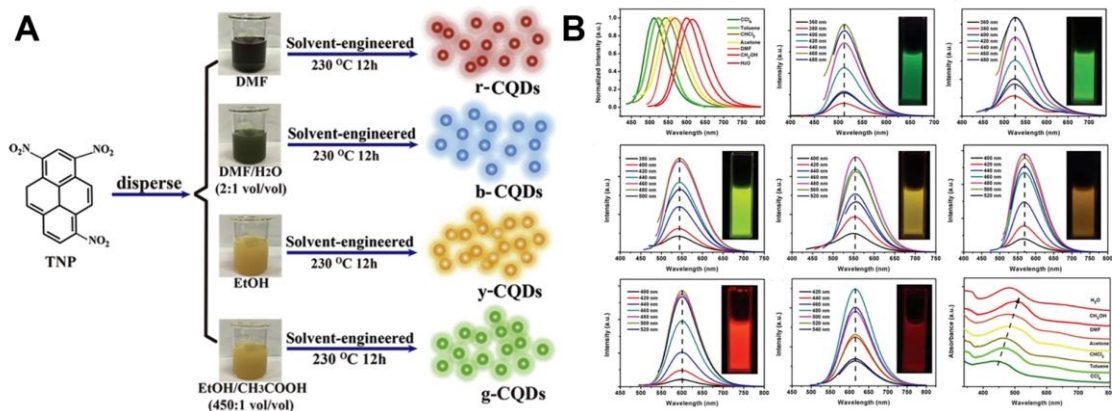


**Figure 1.3.** (a) Multicolor CQDs synthesized by tuning the composition and ratios of reaction solvents (water, DMF, ethanol, and acetic acid). Adapted with permission from Ref<sup>104</sup>; (b) The solvatochromism of CDs induced by the polarity difference of solvents: CCl<sub>4</sub>, toluene, CHCl<sub>3</sub>, acetone, dimethylformamide, CH<sub>3</sub>OH and H<sub>2</sub>O. Adapted with permission from Ref<sup>10</sup>

In the case of the “solvent cocktail” approach, Wu and coworkers recently applied a distinguished molecular fusion strategy and synthesized multicolor CQDs via tuning the composition and ratio of reaction solvents, including water, DMF, ethanol, and acetic acid.<sup>104</sup> In this way, the bandgaps of CQDs were solvent-engineered from 2.89 down to 2.15 eV, covering the spectral emission range from 460 to 620 nm (Figure 1.3a). In addition, their optical properties were tested in nonpolar solvents as well to rule out the solvatochromism of CDs induced by the solvent polarity and the spectral characteristics were similar to those of quantum dots. Solvents were found to alter the elemental composition and functionalization of CDs. Thus they claimed that the mechanism of their multicolor emission should be ascribed to the quantum size effect and surface functional groups. In contrast, though solvatochromism achieved by post-treatment may not be considered a true synthesis approach, it can serve as a convenient and temporary method to tune the emission of CDs in specific solvents.<sup>51, 110-112</sup> The *p*-phenylenediamine-based

CDs prepared by Wang and co-workers exhibited solvent-dependent but excitation-independent emissions from 511 to 615 nm (e.g., from dark green to red) upon the dissolution in CCl<sub>4</sub>, toluene, CHCl<sub>3</sub>, acetone, dimethylformamide, CH<sub>3</sub>OH and H<sub>2</sub>O, respectively (Figure 1.3b).<sup>110</sup> In addition, based on their X-ray photoelectron spectroscopy and FTIR results, they qualitatively demonstrated that the heteroatoms that are attached to the CD structures, such as nitrogen and oxygen, contribute to an increased charge carrier density, promoting charge transfer of electrons. Therefore, they deduced that these CDs behave like organic dyes, where the arrangement of electrons on the CD surfaces can be affected by the dipole moment of solvents; that is, alongside the increase of solvent polarity, the bandgaps gradually decrease, leading to emission redshifts.

#### 1.4.3 Separation or purification methods for as-synthesized CD mixtures

In general, the syntheses for CDs requires a high-temperature (~100 to 250 °C) for either the break-down of bulk carbon (the top-down method) or the carbonization of precursors (the bottom-up method) and so, under such a highly active reaction condition, it is challenging to carefully control of the formation of CDs. As a result, most as-synthesized CD mixtures are composed of unreacted precursors, molecular compounds that are luminescent or not, oligomers or polymers that are carbonized or not, graphene or graphene oxides of varied layers, and amorphous carbons that are doped with heteroatoms or not, depending on the types of carbon sources and reactions.<sup>4, 113-116</sup> Some of these components are photoluminescent while the rest are not and moreover, the fluorescent components can emit distinctive colors upon varied excitation. Thus, even though in recent years, reports about CDs with excitation-independent emission are increasing,<sup>117,</sup>

<sup>118</sup> as-synthesized CDs are still well-known for their excitation-dependent emission.<sup>48, 51,</sup>  
<sup>119, 120</sup> Under such circumstance, it is necessary to purify or separate CD blends before well-defined CD samples are available for studies of luminescence mechanism or the development of CD-based applications.

Typically, CD researchers perform a two-step post-treatment to refine CD mixtures: 1) a rough purification by dialysis, filtration or centrifugation and 2) a thorough chromatographic separation, such as LLE and SPE.<sup>4, 34, 121</sup>

In most cases, step one is used to remove unreacted starting chemicals, by-products of low MW, and bulk residuals induced by over carbonization. While this first step is usually intended for preparation for the more thorough separation, there are a few reports where multicolor CDs were obtained in this first step. For example, the as-prepared CDs by Bao and co-workers were synthesized by oxidizing carbon fibers with nitric acid, followed by an effective ultrafiltration of CD.<sup>43</sup> Specifically, multicolor CD fractions (from blue fluorescence to red) were obtained via applying ultrafiltration membranes with an increasing MW equivalents, that is, < 3, 3-10, and 10-30 kDa. And interestingly, the obtained CD particle diameters also showed an increasing tendency:  $2.7 \pm 0.4$ ,  $3.3 \pm 0.6$ , and  $4.1 \pm 0.6$  nm. In addition, the authors carefully examined the influence of reaction time and the concentration of nitric acid, and it turned out that these two factors could lead to emission variation as well. As such, they concluded that both the size effect and the surface oxidation are important for determining the optical properties of their CDs.

For the second step, the separation of CDs via column chromatography often involves LLE or SPE. With the LLE approach, successful separation cases for crude CDs take

advantage of normal or reverse phase silica column chromatography, anion-exchange column chromatography, or HPLC.<sup>20, 53, 122, 123</sup> Lin and coworkers recently utilized o-/m-phenylenediamine and tartaric acid as precursors for CD syntheses.<sup>46</sup> The as-synthesized CDs were further purified with a silica column using methylene chloride and methanol as mobile phases, leading to multicolor CD fractions emitting blue, green, yellowish green, and red. Additionally, it was observed that the addition of tartaric acid could induce a red-shifted emission but the size distributions of blue (6.0 nm) and yellowish green (8.2 nm) fractions were larger than those of the green (3.6 nm) and red (4.8 nm) counterparts, as revealed by transmission electron microscopy and atomic force microscopy. As such, the authors inferred that the quantum size effect was not responsible for the luminescent properties, but rather the surface oxidation and carboxylation caused by the addition of tartaric acid. Though LLE methods have become a prevalent strategy for CD post-treatments, the use of a significant amount of organic solvents and the high cost of separation apparatus such as HPLC instruments hamper the scale-up of LLE-based separation techniques. On the other hand, as SPE approaches are less costly and easier to scale-up, they can be another promising option worthy of consideration. Georgakilas and coworkers recently reported their work on the solid-phase separation of as-synthesized CDs using their self-developed aluminium column.<sup>124</sup> To prepare the CDs, citric acid and diamines (e.g., triethylenetetramine and o-phenylenediamine) were chosen as precursors, and their solution in water or ethanol underwent hydrothermal treatment, resulting in the as-prepared mixture. Then, these crude CDs were examined by TLC to distinguish CDs from undesired organic compounds such as by-products or unreacted precursors.

Meanwhile, based on the TLC results, the compositions of mobile phases were optimized for the follow-on SPE operation, leading to a simple and effective purification for violet-, blue-, green-, and yellow-emitting CDs.

As mentioned above, the CD field has largely come to a consensus that it is essential to purify or separate the as-synthesized CDs to achieve refined multicolor CD fractions for further studies. However, due to the complexity of as-synthesized CD mixtures and the lack of understanding the structural details of desired CD fractions, information regarding MW, particle size distributions, particle densities, and particle solubilities are limited. As such, when the first batch of as-synthesized CDs is obtained, researchers face a dilemma: it is difficult to adjust the specifications of their purification apparatus, such as MW cut-off of dialysis membranes, membrane filter pore sizes, centrifugation speed, and suitable mobile phases, until the purification process and subsequent analyses of CD fractions are completed. Accordingly, these purification and analysis have to be repeated many times until the characteristics of the CD fractions can be completely elucidated, which eventually increases the cost of syntheses and hinders large-scale syntheses. Therefore, it is desirable that the syntheses for multicolor CDs should be free of labour-intensive and time-consuming post treatments.<sup>125, 126</sup> Fortunately, up to now, a few pioneering studies have been published, presenting inspiring work on the separation-free syntheses of multicolor CDs with a high color purity.<sup>42, 127</sup>

### **1.5 Applications of multicolor CDs**

Akin to other luminescent materials, the emission behaviour of CDs, in essence, refers to the energy transfer between photons and electrons. A variety of CD-based applications

have been designed and developed, especially in the areas of sensing and imaging. This review will provide a summary of recent progress using multicolor CD-based applications for ion/molecule and temperature sensing and modern bioimaging.

### 1.5.1 Selected sensing with CDs

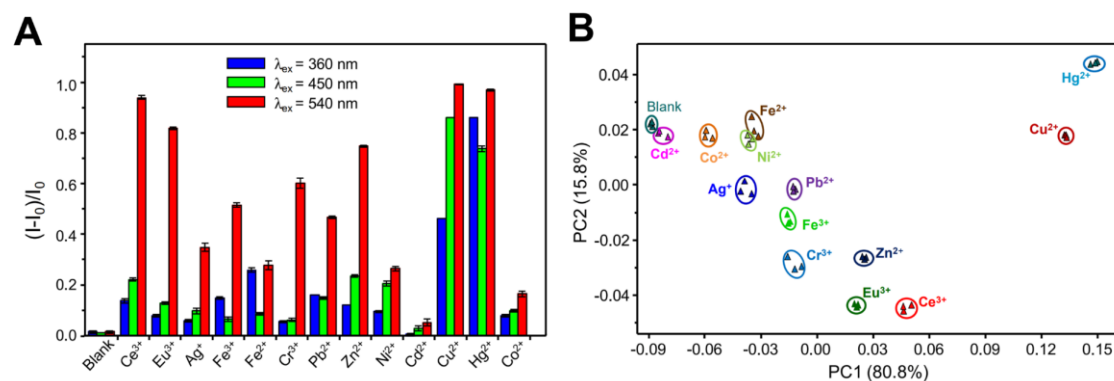


**Figure 1.4.** Multicolor CD application in metal ion sensing. (a) Fluorescence emission of CDs at 466, 555, and 637 nm when excited at 360 nm, 450 nm, and 540 nm to 13 metal ions. (b) Principle component analysis of the discrimination of the 13 metal ions based on the fluorescence emission of the CDs. (reprinted from ref. <sup>128</sup>).

Due to their intrinsic fluorescence, CDs have been developed as sensors for a variety of targets, including pH,<sup>74, 129-131</sup> temperature,<sup>56, 132, 133</sup> metal ions,<sup>128, 132, 134-137</sup> and others.<sup>137-143</sup> Most detection approaches rely on fluorescence intensity change while a smaller number depends on fluorescence lifetime. Multicolor CDs with a broad range of emission wavelengths are especially suitable for ratiometric sensing and target discrimination. For example, a CD based ratiometric pH sensor was developed which shows dual fluorescence emissions where the ratio of emission at 475 nm / 545 nm shows a linear response to pH from 5.2 to 8.8. This label-free pH nanosensor was used to test intracellular pH in HeLa cells.<sup>130</sup> Ratiometric sensing avoids many factors that influence measurement of the

absolute fluorescence intensity such as the stability of light source and the concentration of CDs.<sup>130</sup>

Carbon dot emission can also be temperature sensitive. CDs synthesized from acrylic acid and methionine have emission between the wavelengths of 440 nm to 555 nm, and the fluorescence intensity correlates linearly to changes in temperature between 25 – 75 °C.<sup>144</sup> In another case, the fluorescence lifetime of N,S co-doped CDs was found to be temperature-dependent and was applied to monitor intracellular temperature.<sup>56</sup>

Fluorescence lifetime has advantages over fluorescence intensity in that it is intrinsically referenced. In the same CDs used above, the lifetime of the CDs is not influenced by CD concentration ( $1.5 \times 10^{-5}$  to 0.5 mg / mL) or pH (5-12) and is stable for at least 40 h of continuous excitation. An increase in temperature leads to lifetime shortening, and this can be fitted to a 3rd order polynomial calibration curve, where this CD nanothermometer could be used to sense intracellular temperature of HeLa cells.<sup>56</sup>

CDs are also known to be sensitive to various metal ions, including  $\text{Fe}^{3+}$ ,<sup>144</sup>  $\text{Ag}^+$ ,<sup>134</sup>  $\text{Hg}^+$ ,<sup>136</sup>  $\text{Cu}^{2+}$ ,<sup>135</sup>  $\text{Co}^{2+}$ ,<sup>145</sup>  $\text{Pb}^{2+}$ ,<sup>146</sup> and others.<sup>147-149</sup> Lin and coworkers used CDs synthesized from citric acid and formamide as a multidimensional sensor for metal ions. The emissions of the CDs covered the entire visible range with dominant emissions at 466, 555, and 637 nm. As shown in Figure 1.4, CDs showed different emission intensities in the presence of different metal ions, and these ions can be differentiated properly using principle component analysis.<sup>128</sup> These multicolor CDs could be built into a platform for simultaneous discrimination of multiple metal ions. In another study by Lin and coworkers where multicolor CDs were also made from citric acid and formamide, CDs formed

ensembles with the metal ions:  $Ce^{3+}$ ,  $Fe^{3+}$  and  $Cu^{2+}$ . These CD-metal ion complexes could effectively distinguish various phosphate anions, such as ATP, ADP AMP, PPI and Pi.<sup>150</sup> This example demonstrates that multicolor CDs could be developed into a platform for sensing and distinguishing different ions as their fluorescence emission at different wavelengths responds differently to presented ions. Other recent representative works are listed in Table 1.1. Despite these early successes, further clarity on CD structure and emission mechanisms would facilitate more advanced design of environmental sensing applications.

**Table 1.1.** Carbon dot application in sensing ions and other molecules

CD emission wavelength	Sensing target	Detection range	Reference
408 nm	glucose	9 - 900 $\mu$ M	138
450 nm	ascorbic acid	24 - 40 $\mu$ g/mL	140
455 nm	2, 4, 6-trinitrotoluene	10 nM - 1.5 $\mu$ M	139
510 nm	alkaline phosphate	0.01 to 25 U/L	141
550 nm	$H^+$	pH 4.7 - 7.4	74
568 nm	$Ag^+$ and cysteine	1 - 7 $\mu$ M and 2 - 10 $\mu$ M	134
594 nm	$Fe^{3+}$	9.7 nM - 4 $\mu$ M	151
632 nm	$Pt^{2+}$ , $Au^{3+}$ and $Pd^{2+}$	0.886, 3.03 and 3.29 $\mu$ M - 160 $\mu$ M	152
440 nm and 615 nm	$Cu^{2+}$	8.82 nM – 225 nM	153

### 1.5.2 High-resolution bioimaging with CDs

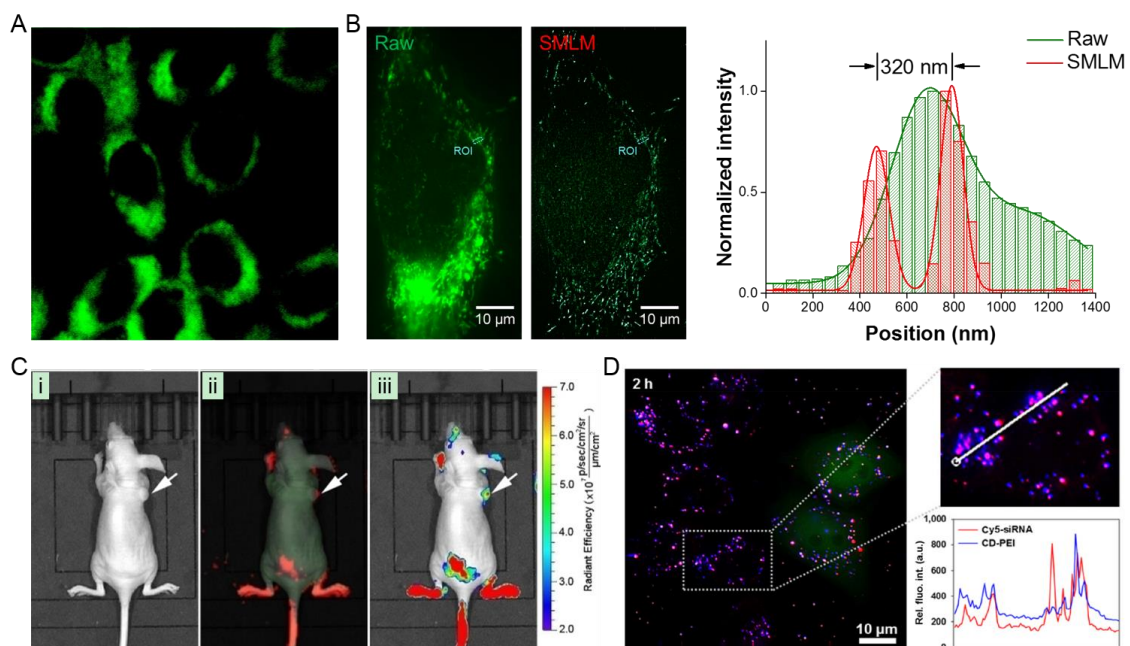


**Figure 1.5.** Diverse applications of CDs in bioimaging. (A) Two-photon fluorescence imaging of CDs internalized by human breast cancer cells (reprinted from ref. <sup>154</sup>). (B) Super-resolution single-molecule localization microscopy (SMLM) enabled by photoblinking CDs. The substantially improved spatial resolution helps resolve closely aligned fine structures within a diffraction-limited area (reprinted from ref. <sup>20</sup>). (C) In vivo tumor imaging with NIR CDs: <i>i</i> bright-field image, <i>ii</i> fluorescence image, <i>iii</i> color-coded image of a nude mouse bearing papillary thyroid carcinoma cells. After 30 min post-intravenous injection, CDs primarily accumulated in bladder and the xenograft tumor site (pointed by arrow) (reprinted from ref. <sup>155</sup>). (D) CDs used for siRNA delivery. HeLa cells were incubated with passivated CDs (blue) loaded with Cy5-labeled siRNA (red) for 2 h. The co-localization of CDs and Cy5 signals implicate successful delivery (reprinted from ref. <sup>156</sup>).

With about two decades' development and optimization, modern carbon dots (CDs) feature excellent water solubility, tunable fluorescence emission, sub-10-nm size, superior biocompatibility, and photostability, making them ideal for a broad range of bioimaging applications.<sup>157, 158</sup> Without specific surface modifications, CDs can be readily internalized by different cell types (*e.g.*, plant, bacterial, fungal and cancer cells) (Figure 1.5a)<sup>159-162</sup> and have been found to localize in various intracellular compartments (*e.g.*,

cell membrane, cytoplasm, mitochondria, endosomes and lysosomes),<sup>20, 154, 163, 164</sup> possibly dependent on the different synthesis strategies used to produce the CDs. One prominent advantage of using CDs for bioimaging is their highly efficient uptake by live cells, without apparent toxicity. In addition, the CD surface is often covered with abundant functional groups, such as –COOH and –OH, which can be conveniently modified or conjugated to realize a diversity of sensing/imaging tasks. For example, by covalently binding the CD surface to 4'-(aminomethylphenyl)-2,2':6',2''-terpyridine (AE-TPY) molecules, Tian and coworkers produced integrated CD-TPY particles that exhibited pH-dependent fluorescence emission where increasing  $[H^+]$  potentially increases the fluorescence intensity.<sup>165</sup> In another case, *m*-phenylenediamines derived CDs (*m*-CDs) with surface isoquinoline and amines specifically interacted with the major groove of RNA through strong electrostatic force and  $\pi$ – $\pi$  stacking, which enabled long-term imaging of cellular RNA.<sup>166</sup> To date, surface-modified CDs have also been explored for cancer detection and have shown great promise when cancer-specific markers were targeted, such as the folate receptor.<sup>167-170</sup> Of particular note is the facile production of multicolor CDs from the same precursor, suggesting that similar surface modification chemistry could be exploited to facilitate targeted imaging of more than one target simultaneously.<sup>171-173</sup> All the synthesis and fundamental efforts with CDs facilitate a variety of next-generation biosensing and medical applications.

One inherent challenge constraining conventional optical microscopy is the diffraction-limited spatial resolution ( $> 200$ - $250$  nm). Over the past decade, super-resolution fluorescence microscopy (SRM) has experienced rapid advancement due to the continued

development of new instruments and labeling materials.<sup>174</sup> According to their distinct working principles, current super-resolution techniques can be classified into two major groups: patterned illumination-based microscopy (*e.g.*, STED and SIM), and SMLM (*i.e.*, STORM, PALM, or SOFI). The first demonstration of SRM using biocompatible CDs was achieved by Pompa and coworkers with the STED technique.<sup>175</sup> In this study, CDs were synthesized by laser ablation and had a peak emission at 490 nm. With the depletion wavelength of 592 nm, a spatial resolution of about 30 nm was achieved both in fixed and live cells. Initially it was thought that the fluorescence emission of CDs was non-intermittent and non-photoblinking.<sup>169</sup> However, a growing body of evidence has revealed that the photoluminescence properties of CDs are subject to a large number of factors, and the fluorescence intensity of certain CDs do actively fluctuate in time-lapse experiments.<sup>176-178</sup> The photoblinking of CDs makes them suitable for applications in single-molecule localization-based SRM. Recently, two studies have characterized the photoblinking properties of as-synthesized CDs.<sup>20, 179</sup> As determined in these studies, as-synthesized CDs exhibited a low on-off duty-cycle (< 1%), high photon output per burst emission (> 6,000), and robust resistance to photobleaching. Taking advantage of these unique properties, SMLM was performed, achieving 25-30 nm spatial resolution (Figure 1.5b). Moreover, with super-resolution capability, the cellular uptake and transport processes of CDs were better resolved. Representative applications of CDs in SRM are summarized in Table 1.2.

**Table 1.2.** Application of CDs in SRM.

Particle size	Imaging method	Cellular localization	Resolution achieved	Ref.
5 nm	STED	lysosome	30 nm (lateral)	<sup>175</sup>
4 nm	SOFI	nucleus (blue dots); endosomes/lysosomes (green dots)	1.4-fold improvement over wide-field imaging (lateral)	<sup>164</sup>
4.5 nm	SMLM	microtubule, CCR3 membrane receptor (antibody-based)	25 nm (lateral)	<sup>179</sup>
5.4 nm	SMLM	nucleolus	4-fold improvement over wide-field imaging (lateral)	<sup>188</sup>
5 – 15 nm	SMLM	mitochondria	30 nm (lateral)	<sup>20</sup>

In addition to the demonstrated potential imaging in cultured cells, CDs have proven to be versatile for *in vivo* imaging as well.<sup>180</sup> By tuning the emission to the NIR range, the biodistribution and toxicology profile of CDs prepared from acid oxidation of carbon nanotubes and graphite has been studied.<sup>181</sup> Moreover, it was found that different injection routes resulted in distinct body distribution and clearance rate.<sup>182</sup> In general, CDs are nontoxic and mainly excreted from the body through the urinary system. Furthermore, CDs have shown strong EPR effect in tumor sites and therefore have been explored as an effective *in vivo* tumor imaging agent (Figure 1.5c).<sup>155, 169, 183, 184</sup> In light of these findings, CDs can be further functionalized for multimodal *in vivo* applications in conjunction with imaging, considering the abundant reactive groups on their surface. So far, a variety of ideas have been attempted, including targeted chemotherapy, photodynamic therapy, radiation therapy, and gene therapy (Figure 1.5d).<sup>156, 185-187</sup> Owing to the intrinsic *in vivo* imaging capacity, CD-dependent drug delivery and nanomedicine have the potential to enable real-time tracking, which will greatly facilitate effective drug discovery.

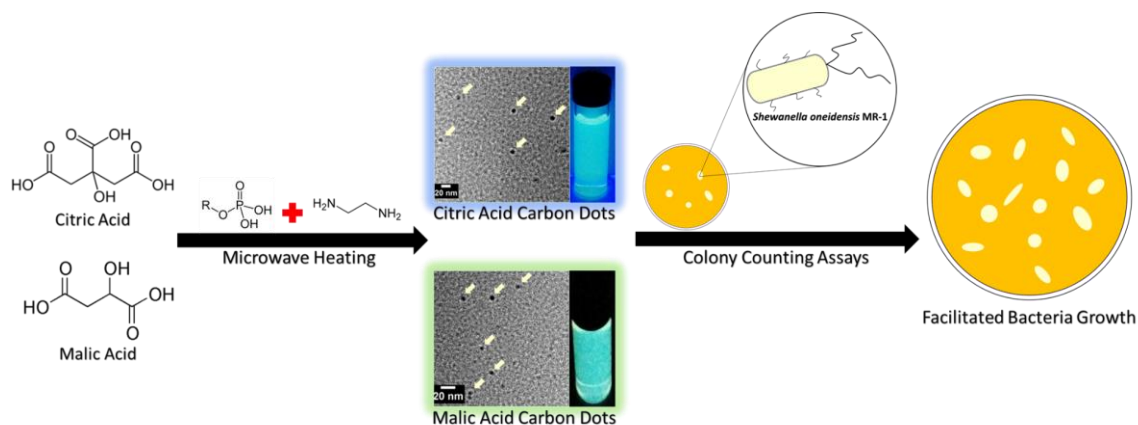
## 1.6 Perspective and future directions

It has been fifteen years since the break-through discovery of carbon-based fluorescent nanostructures in 2004. Due to their fascinating luminescent features, CDs have been attracting an increasing number of researchers that are dedicated to exploration of the photoluminescence mechanisms behind their bright emission, preparation of distinct multicolor products independent of excitation, and use in creative applications exploiting their prominent luminescent properties. Many challenges remain, including the lack of thorough interpretation of CD structures and luminescence origins, the difficulty in controlling CD reactions, time-consuming post-treatment procedures, and relatively low quantum yields that limit further applications. However, it is possible that in the near future, studies on mechanisms, optimization of syntheses, and development of applications will benefit from one another and bring about inspiring progress. Accordingly, critical next directions for CD researchers include: 1) approaching the luminescence mechanism mystery based on direct observations of CD structure, making use of state-of-the-art characterization techniques and accurate computational simulations that construct theoretical CD models, 2) refining synthesis conditions that are suitable for scaled-up preparation of highly pure multicolor CDs, and 3) designing and fabricating CD-based applications to address urgent issues, such as medical or biological devices, environmental monitoring platforms, and conversion/storage appliances for sustainable energy. Therefore, to cope with these technological gaps, this thesis work is featured by the pioneering work on the purification and applications of CDs, such as applying automated

technique to separate as-made CD crudes as well as utilizing CD products for super-resolution microscopy imaging technique.

## Chapter 2

Investigation of phosphorous doping effect on polymeric carbon dots: fluorescence, photo stability and environmental impact



Reprinted from: Zhi, B.; Gallagher, M. J.; Frank, B. P.; Lyons, T. Y.; Qiu, T. A.; Mensch, A. C.; Rosenzweig, Z.; Fairbrother, D. H.; Hamers, R. J.; Haynes, C. L., Investigation of Phosphorous Doping Effect on Polymeric Carbon Dots: Fluorescence, Photostability and Environmental Impact. *Carbon* **2018**, 129, 438-449. Copyright 2018, with permission from Elsevier.

Bo Zhi is responsible for the design of this research as well as carbon dot synthesis, TEM analysis, bacterial toxicity assays and the drafting of manuscript.

## 2.1 Overview

Carbon dots have arisen as a potential alternative to traditional quantum dots since they fluoresce but are synthesized from sustainably sourced green chemicals. Herein, fluorescent nitrogen-doped polymeric CDs were synthesized by using CA or MA as carbon precursors and ethylenediamine as the nitrogen precursor. Additionally, phosphoric acid was used as a doping agent for each type of CDs to evaluate the impact of incorporating phosphorus into the nanoparticles. Thus, four kinds of doped CDs (N-doped or N, P co-doped) were obtained and named as CA-CDs, CA-P-CDs, MA-CDs, and MA-P-CDs. QY and fluorescence lifetime analysis indicate that phosphorus doping of up to *c.a.* 10 wt.% does not induce a remarkable influence in CD photoluminescence. The photostability of the N, P co-doped MACDs (MA-P-CDs), however, was observed to increase compared to the N-doped MACDs under 350 nm UV exposure. Lastly, to assess the impact of this emerging nanoparticle on prokaryotes, the bacterial toxicity of these CDs was tested using *Shewanella oneidensis* MR-1 as a model microorganism. Interestingly, the CDs exhibited no toxicity in most cases, and in fact facilitated bacteria growth. Hence, this work suggests that CDs are potentially eco-friendly fluorescent materials.

## 2.2 Introduction

Since the discovery of CDs during the purification of arc-discharged SWCNTs in 2004<sup>1</sup>, they have become a carbon nanoallotrope of great interest<sup>2, 3</sup>. Generally, CDs are zero-dimensional carbon nanoparticles of 2 to 10 nm diameter with quasi-spherical morphology. The majority of the carbon within the CDs is sp<sup>3</sup>-hybridized and usually exists as

amorphous carbon, different from the other 0D carbon nanoallotrope, NDs, which consist of highly crystalline domains<sup>2-5</sup>. Due to their excellent photoluminescence, stability, low cost, and easy preparation<sup>4, 6-8</sup>, CDs have been under intense investigation for their potential applications in sensing<sup>9-14</sup>, bioimaging or cell labelling<sup>3, 15-17</sup>, drug delivery<sup>16, 17</sup>, white light-emitting device<sup>7, 18</sup>, and energy conversion<sup>19-21</sup>.

A variety of methods have been developed to generate fluorescent CDs in the past decade. Roughly, these synthesis approaches can be classified as either “top-down” or “bottom-up”<sup>4, 22</sup>. Generally, the “top-down” route involves breaking down bulk carbon sources, like graphite<sup>19, 23</sup>, carbon fibers<sup>24, 25</sup>, or carbon nanotubes<sup>1, 26</sup>, into tiny carbon nanoparticles, namely, carbon dots. Available “top-down” synthetic techniques exploit electrochemistry, arc discharge, laser ablation or plasma treatment<sup>27, 28</sup>. Conversely, the “bottom-up” route refers to the construction of amorphous carbon nanostructures from molecular precursors such as saccharides<sup>29</sup>, organic acids<sup>8, 13</sup>, or amino acids<sup>30, 31</sup> via combustion methods, hydrothermal/solvothermal treatment, or microwave irradiation<sup>4, 27</sup>. To be more specific, microwave heating-based synthesis capitalizes on internal precursor molecular rotation transitions coupling with external electromagnetic irradiation<sup>32</sup>. Thus, the heating efficiency is not related to the thermal conductivity of the precursors, realizing an immediate on/off switching in heating<sup>32, 33</sup>. Hence, compared to other methods, microwave-assisted thermal treatment conserves both time and energy, and might even avoid undesirable side reactions or facilitate new reaction routes<sup>32-34</sup>. Thus, microwave heating has been broadly used as a promising method to prepare stable and highly photoluminescent CDs<sup>7, 8, 35-39</sup>.

Doping heteroatoms into CDs has been a popular concept for potentially improving the performance of carbon nanomaterials<sup>40-42</sup>. A significant number of doped CD studies have been reported, most of them doped with non-metal heteroatoms, such as N<sup>43-45</sup>, S<sup>44, 46</sup>, B<sup>47-49</sup>, or P<sup>49-51</sup>; there are also rare cases of metal atom dopants such as Cu<sup>52</sup>, Mg<sup>53</sup> and Gd<sup>54</sup>. In general, doped CDs have exhibited improved optical properties compared to non-doped CDs, such as higher QYs and longer fluorescence lifetimes, especially when a functionalization route is used. The chemical identity of the doped heteroatom influences the electron distribution within the CDs, altering the band-gap energy and thus improving the CD photoluminescence<sup>55, 56</sup>. Currently, there is a lack of systematic investigations on the effects of doping on the properties of CDs. To address this issue, a series of polymeric CDs with different levels of doping was synthesized herein to compare the fluorescence properties of these polymeric CDs, and to elucidate whether doping is an effective strategy for polymeric CD performance improvement. It is important to mention here that there is a range of definitions are used for carbon dots nanomaterials, including carbon quantum dots, graphene quantum dots, and polymer dots. To avoid confusion, the products made in this work will be identified as polymeric CDs because they are generated by carbonizing polymerized intermediates.

CDs have exhibited comparable QYs to traditional semiconductor QDs and they are free of toxic heavy metal ions<sup>2, 4</sup>. Thus, they are assumed to be of low toxicity and may serve as a green alternative to QDs<sup>57-59</sup>. Up to now, most CD research has been heavily focused on their synthesis and applications, while only a few reports have addressed their potential environmental consequences, let alone the comparative impact of modified/doped CDs<sup>60</sup>.

<sup>61</sup>. To assess their true potential, it is necessary to characterize CD photoluminescence in parallel with a toxicity assessment relevant to the potential release of CDs into the ecosystem -- a specific goal of this study. Microorganisms, located at the bottom of the food web, are ubiquitous<sup>62</sup> and thus likely to first interact with and respond to nanomaterials released into environment. *S. oneidensis* MR-1, first discovered in Lake Oneida, NY<sup>63</sup>, is a species of Gram-negative bacteria important in the ecosystem based on their notable ability to reduce metal oxides via dissimilatory reduction under anaerobic conditions<sup>64</sup>. In addition, *S. oneidensis* MR-1 has been widely applied in nanomaterial toxicity screening, including studies of silver NPs<sup>65</sup>, gold NPs<sup>66</sup>, and Li-ion battery materials<sup>67</sup>. Thus, *S. oneidensis* MR-1 has been chosen herein as the model microorganism to evaluate the potential environmental impact of N- and P-doped polymeric CDs.

In this manuscript, we will demonstrate the synthesis, materials characterization, photostability tests, and bacterial toxicity screening of nitrogen and phosphorous-doped polymeric carbon dots. This is the first effort in a larger set of experiments, and future work will further explore the underlying chemical or physical properties of the polymeric carbon dots that result in the exciting photoluminescent properties.

Specifically, this work explores the impact of phosphorous doping on nitrogen-doped polymeric CDs. Based on quantitative analysis, we find that doping phosphorus into the polymeric CD structure using a phosphorous-containing precursor does not significantly impact polymeric CD fluorescence behavior, including QY and lifetime. The phosphorus-doped polymeric CDs, however, do demonstrate enhanced photostability during UV-B exposure (350nm) compared to undoped polymeric CDs. Interestingly, comparing the

photoluminescence performance of nitrogen-doped polymeric CDs generated from citric acid, containing three carboxylic acid groups versus the two carboxylic acid groups in malic acid show significant differences, likely due to their different crosslinking patterns with ethylenediamine. Furthermore, the bacterial toxicity results indicate that phosphorous doping did not increase toxic effects on the bacteria but potentially stimulated bacteria growth in most cases, highlighting the potential of polymeric CDs as an emerging fluorescent nanomaterial with minimal adverse environmental effects.

## **2.3 Experimental**

### 2.3.1 Chemicals

Citric acid (ACS reagent,  $\geq 99.5\%$ ), DL-malic acid (ReagentPlus®,  $\geq 99\%$ ), phosphoric acid (ACS reagent,  $\geq 85\%$  H<sub>3</sub>PO<sub>4</sub>) and ethylenediamine (ReagentPlus®,  $\geq 99\%$ ) were purchased from Sigma Aldrich. Quinine sulfate dihydrate (99+%, ACROS Organics™) was obtained from Fisher Scientific. The Biotech cellulose ester membrane (MWCO 100-500 D) was obtained from Spectrum Labs. Deionized water was produced by a Millipore Milli-Q system (Billerica, MA), and used through all experiments. All other reagents were of analytical grade and used without further purification. Difco™ LB broth (Miller) and Difco™ agar (granulated) were purchased from Becton, Dickinson, and Company. DPBS was purchased from Mediatech, Inc. NaCl and HEPES were purchased from Sigma Aldrich.

### 2.3.2 Synthesis of amorphous polymeric carbon dots

The synthesis was adopted from previous reports<sup>8</sup> with minor modifications. To synthesize the CACDs, a 4 M aqueous citric acid stock solution was prepared in advance. 2 mL of this stock solution was transferred into a 100-mL beaker, and then 540  $\mu$ L of ethylenediamine was added. The reaction was completed within one minute as heat was released and a homogenous solution was formed. The mixture was stirred for 30 min and allowed to cool. Then, the colorless transparent mixture was transferred to a domestic microwave oven and heated under 360 W for 3 minutes. The resultant orange-yellow foamy solid was cooled in a fume hood for 20 minutes before 10 mL of MQ water was added into the beaker. The obtained reddish-brown transparent solution was dialyzed for 24 hours to remove unreacted precursors. Then, rotary evaporation was used to remove most of the water in the solution, leaving behind a brown solid product at the bottom. Further drying was completed in an oven at 40 °C for one day.

To generate varied phosphorus-doped citric acid polymeric carbon dots (the CA-P-CDs series), 2 mL of citric acid stock solution was poured into a beaker, and then, 34  $\mu$ L of phosphoric acid was added. After mixing for 10 minutes, 540  $\mu$ L ethylenediamine was added. The subsequent procedure was the same as followed for the CACDs. Thus, CA-P-CDs-1 were obtained. To synthesize CA-P-CDs-2, 3 and 4, phosphoric acid was added in quantities of 68, 136 and 272  $\mu$ L, respectively. The final products of the CACDs and CA-P-CDs series were all yellow powders with gradually darker yellow color with increasing amount of doped phosphorus.

For the synthesis of MACDs and the MA-P-CDs series (phosphorus-doped malic acid polymeric carbon dots), malic acid was used as carbon source instead of citric acid. The

synthesis procedure was otherwise the same. All the final products in this series appeared as dark brown powders.

### 2.3.3 Material characterization

Extensive characterization was performed to learn as much about the chemical and structural characteristics of the CDs as possible UV-vis extinction spectra were obtained using a Mikropack DH-2000 UV-Vis-NIR spectrometer. Fluorescence spectra were measured with a PTI QuantaMaster™ 400. EEMs were collected on a Thermo Scientific Lumina fluorescence spectrometer (Waltham, MA USA) with the 3D Scan Module using a 1 cm path length cell, 2.5 nm slit width, and internal correction for the lifetime of the photomultiplier tube with excitation from 200-600 nm (5 nm step size) and resultant emission collected from 300-750 nm (1 nm step size). Inner filter effects were avoided by using a dilute polymeric CD solution with an absorbance of 0.1 at the peak absorbance (*c.a.* 350 nm). The morphology and size distribution of polymeric CDs were examined using a FEI Tecnai G<sup>2</sup> F30 TEM at 300 kV. The TEM samples were prepared by dropping an aqueous suspension of polymeric CDs onto a 300-mesh gold grid coated with an ultra-thin lacey carbon film. Wide-angle XRD data were collected by a Bruker-AXS (Siemens) D5005 XRD using Cu K $\alpha$  as the radiation source ( $\lambda = 0.15418$  nm), with a step of 0.02° in the range from 10° to 70°. The ATR-FTIR spectra were recorded with a Nicolet Magna-IR 750 spectrometer. The XPS spectra were analyzed by a Surface Science SSX-100 using a monochromatic Al K $\alpha$  X-ray source (50 eV pass energy, and 0.9 eV energy resolution by the full width at half maximum of Au 4<sub>f7/2</sub> peak) and a PHI 5600 XPS (58.7 eV pass energy, 0.125 eV/step, Mg K $\alpha$  X-rays) and processed with CasaXPS software

(Teignmouth, UK). EDAX was performed on a JEOL 6700F SEM using a 20-kV electron beam using an EDAX Genesis 4000 X-ray analysis system as a detector. AFM images were collected in tapping mode using a Dimension FastScan AFM (Bruker, Santa Barbara, CA, USA). Si nitride cantilevers with nominal spring constants of  $18 \text{ N m}^{-1}$  were used for imaging samples in air at room temperature. A Bruker Avance III HD nanobay AX-400 spectrometer equipped with SampleXpress autosampler (Billerica, MA, USA) was used to obtain  $^{13}\text{C}$ -NMR spectra of suspensions of nanoparticles in  $\text{D}_2\text{O}$ . The ACD/Spectrus processor (ACD/Labs, Toronto, Ontario, Canada) was used for manual phase correction and peak assignment.

#### 2.3.4 Photostability testing

A 300-ppm polymeric CD stock solution was made by dissolving 15 mg of polymeric CDs in 50 mL of water. Dilutions to 7.5, 18, and 30 ppm were then made, and a UV-vis extinction spectrum from 250-800 nm was obtained for each sample using a Varian, Inc. Cary® 50 UV-vis spectrometer (Agilent Technologies, Santa Clara, CA USA). Before each UV-vis measurement the quartz cuvette was rinsed with 500  $\mu\text{L}$  of the polymeric CD-containing solution before 2 mL was pipetted in for analysis. Five technical replicates were recorded for each polymeric CD dilution to obtain an average spectrum and to verify that the colloidal suspension remained stable throughout measurement. The linear calibration curve was used to generate a 100-mL polymeric CD-containing solution that exhibited an extinction of 0.1 at the  $\sim 345 \text{ nm}$  peak. Once this solution was obtained, 6 mL aliquots were placed into either quartz or glass test tubes for photostability measurements. Both the pH and emission spectrum of the polymeric CDs remaining were measured using

a Orion™ 9103BNWP SemiMicro Combination Ag/AgCl pH probe (Thermo Scientific, Waltham, MA USA) and Lumina fluorescence spectrometer (Thermo Scientific, Waltham, MA USA), respectively. The polymeric CD-containing solutions in the glass test tubes were exposed in an RPR-100 Photochemical Rayonet Reactor© (SNEUVCo Branford, CT, USA) equipped with sixteen RMR-3500A Black Light Bulbs (>90% emission, 350 nm,  $1.76 \times 10^{17}$  quanta/s as measured with actinometry, *vide infra*). The extinction spectra for each set of polymeric CD-containing solutions were measured after 5, 10, 20, 30, 40, and 60 minutes of irradiation to determine the photostability. Because photodegradation is possible during the EEM experiment, separate replicate samples were used for each irradiation time.

### 2.3.5 QY and $\tau_{\text{avg}}$ measurement

The QY of CACDs, the CA-P-CDs series, MACDs, and the MA-P-CDs series were determined based on protocols described in previous reports<sup>68, 69</sup>. The extinction of each CD sample was measured with a PTI QuantaMaster 400 and then diluted to achieve an extinction value of  $\sim 0.1$  as measured by measurements at 340 nm. Quinine sulfate was dissolved in 0.1 M H<sub>2</sub>SO<sub>4</sub> ( $\phi = 0.54$ )<sup>69</sup> and used as the standard for the QY measurements (fluorimeter settings: 340 nm excitation, emission range: 350 nm – 700 nm, 1.5 nm slit width). The QY of CDs were calculated by the following equation:

$$Q_x = Q_{STD} (I_x / I_{STD}) ((1 - 10^{-OD_{STD}}) / (1 - 10^{-OD_x})) (\eta_x^2 / \eta_{STD}^2)$$

where Q stands for QY, I is the integral value of emission intensity at the excitation maximum, OD means optical density (lower than 0.1 to avoid inner filter effects), and  $\eta$

is the refractive index. The value of the subscript  $x$  identifies the polymeric CD sample while STD indicates the standard<sup>69</sup>.

Lifetime measurements were performed three times in parallel on the same samples (extinction ~0.1) with a 375-nm laser as the excitation source (Becker&Hickl GmbH BDL 375-SMN Picosecond Diode Laser, operated at 1MHz), slit width of 1 nm for excitation and emission, and detection at the peak wavelength of the sample. Lifetime plots were fitted with multi-exponential decay kinetics:

$$I(t) = \sum_{i=1}^{\infty} \alpha_i \exp(-t/\tau_i)$$

And the amplitude average  $\tau_{avg}$  of each replicate is given by:

$$\tau_{avg} = \frac{\sum_{i=1}^{\infty} \alpha_i \tau_i^2}{\sum_{i=1}^{\infty} \alpha_i}$$

where  $\alpha_i$  is the pre-exponential factor,  $\tau_i$  is the lifetime of each decay<sup>69</sup>.

### 2.3.6 Bacterial culture and polymeric carbon dot exposure

*S. oneidensis* MR-1 stock was a generous gift from the Gralnick Lab at the University of Minnesota. *S. oneidensis* MR-1 were stored at -80 °C before being inoculated onto LB agar plates. The plates were incubated at 30 °C until discernible colonies were obtained. About 2-3 colonies were transferred into 10 mL LB broth. The bacterial suspension was incubated in an orbital shaker for 3 to 5 hours and harvested before entering stationary phase, as determined by the OD<sub>600</sub>. Bacteria cells were pelleted by centrifugation at 750 × g for 10 minutes, re-suspended in DPBS buffer, and dispersed into HEPES buffer (2

mM HEPES and 25 mM NaCl, at pH = 7.4). The bacterial suspension was then diluted to ~0.05 OD<sub>600</sub> so that the cell density was ~10<sup>7</sup> cells/mL. The concentration of the polymeric CD working solution was 50 mg/mL. The subsequent nanoparticle exposure was performed by mixing the bacterial suspension with carbon dot suspension (volume ratio was 10:1, thus, the exposure concentration was 5 mg/mL), and incubated for 15 minutes or 1 hour.

### 2.3.7 Colony counting assays (drop plate method)

To examine the possible toxic effect of phosphorus-doping into polymeric CDs (that is, comparing N-doped polymeric CDs and N, P co-doped polymeric CDs), an adapted colony counting assay (drop plate methods) was used for the bacterium *S. oneidensis* MR-1<sup>70</sup>. A bacterial suspension of about 10<sup>7</sup> cells/mL (~0.05 OD<sub>600</sub>) was exposed to 5 mg/mL of polymeric CDs, followed by a 10-fold serial dilution to dilute the bacterial suspension to a proper cell density. Aliquots of 10 μL from three DFs of the exposed bacterial suspension, *i.e.* 10<sup>-3</sup>, 10<sup>-4</sup> and 10<sup>-5</sup>, were dropped onto the surface of LB agar plates, and the agar plates were incubated at 30 °C overnight until observable colonies formed; a representative plate is shown in Fig. S10. Data from the dilution fold of 10<sup>-4</sup> was used for further analysis as the colonies formed at this dilution fold were countable. Colony counts were transformed into the CFUs, and normalized to the negative control by dividing CFUs of a treated sample by the average CFUs from control groups in the same experimental run. This calculation is done using the following equation:

$$\text{Cell Density} = \frac{\frac{1}{n} \sum_{i=1}^n x_i \text{ (CFU)}}{0.01 \text{ (mL)} / \text{DF}},$$

$$\text{Normalized CFUs} = \frac{\text{Cell Density}_{TG}}{\text{Average of Cell density}_{NC}}$$

where NC means negative control, TG means treated group,  $x_i$  is the number of colonies counted,  $n$  indicates the number of aliquots from the same sample that were dropped onto plates, 0.01 is the volume of each aliquot (0.01 mL), and DF is the dilution fold.

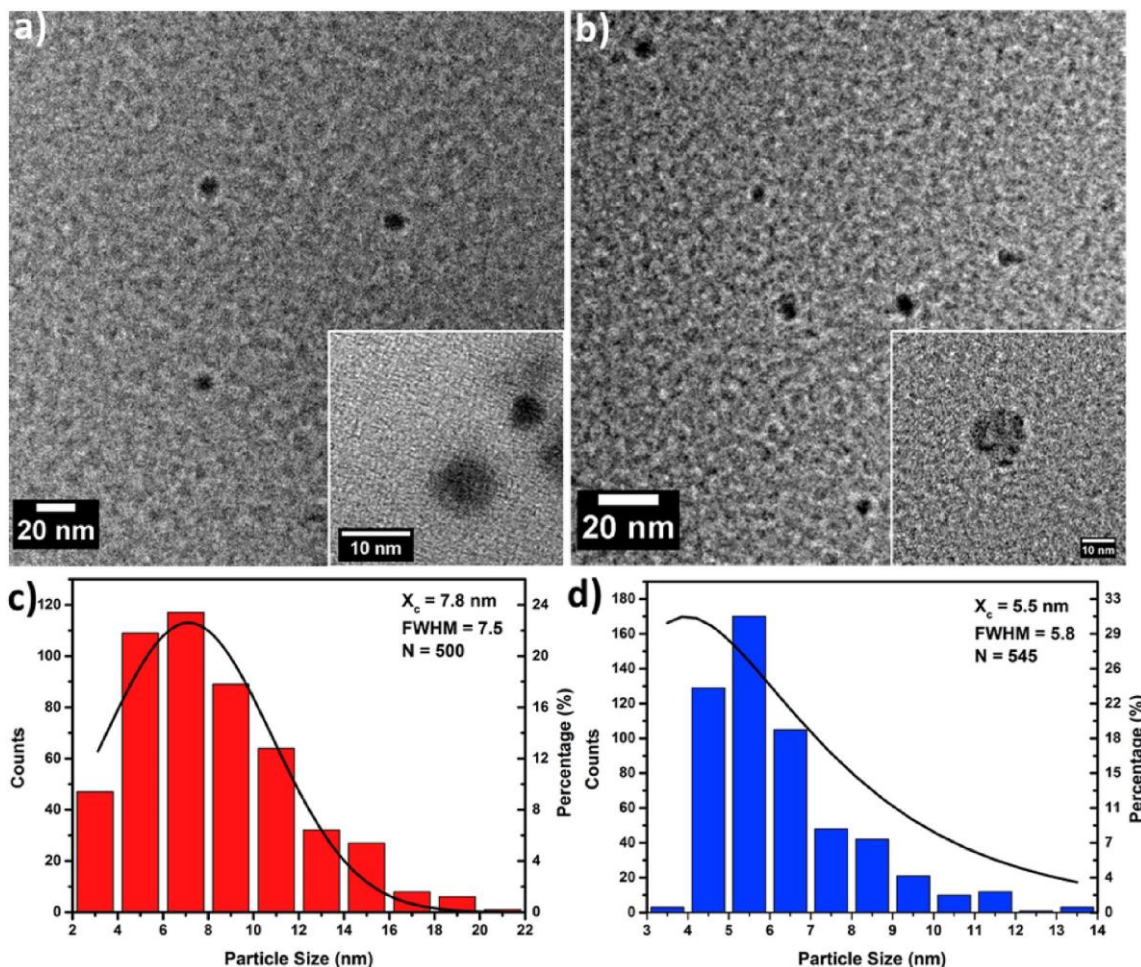


**Figure 2.1.** TEM images of (a) CACDs and (b) MACDs (scale bar: 20 nm; inset scale: 10 nm) and particle size distributions of (c) CACDs and (d) MACDs.

## 2.4 Results and discussion

### 2.4.1 Characterization of polymeric CDs

While it is currently not possible to characterize the specific atomic structure of carbon dots, this study includes an extensive array of characterization that reveals many aspects of the polymeric carbon dot structure. TEM was used to reveal the morphology of both CACDs and MACDs, as shown in Figure 2.1.

Both types of polymeric CDs exhibit a uniform circular shape without significant aggregation. No discernible crystal lattice was visible in either case, suggesting an amorphous nature for these polymeric CDs. Such amorphous carbon character was further confirmed by the broad peaks around  $20^\circ$  in their XRD patterns<sup>71, 72</sup>. There may be a small amount of graphene inside, but any resulting weak diffraction signals are overwhelmed by those from amorphous carbon, so no crystalline carbon was detected via TEM or XRD. In addition, particle size analysis was performed based on CD Feret diameter from TEM images (counting  $\geq 500$  nanoparticles).<sup>73</sup> Assuming polymeric CD are normally distributed in size, the polymeric CD size peaks were fitted with a normal log function to calculate the average polymeric CD size. For CACDs, the peak diameter was  $\sim 7.8$  nm, and for MACDs, it was  $\sim 5.5$  nm. Both are smaller than 10 nm, which is the typical size range of CDs<sup>2, 3</sup>. Since TEM is only two-dimensional, AFM was used as well to determine the particle height distribution (z-profile). The height of CACDs and MACDs were  $\sim 3.7$  nm and  $\sim 3.5$  nm by AFM, respectively. Both are smaller than their lateral diameter, thus, it is possible that these polymeric CDs are not perfect spheres but rather ellipsoids.

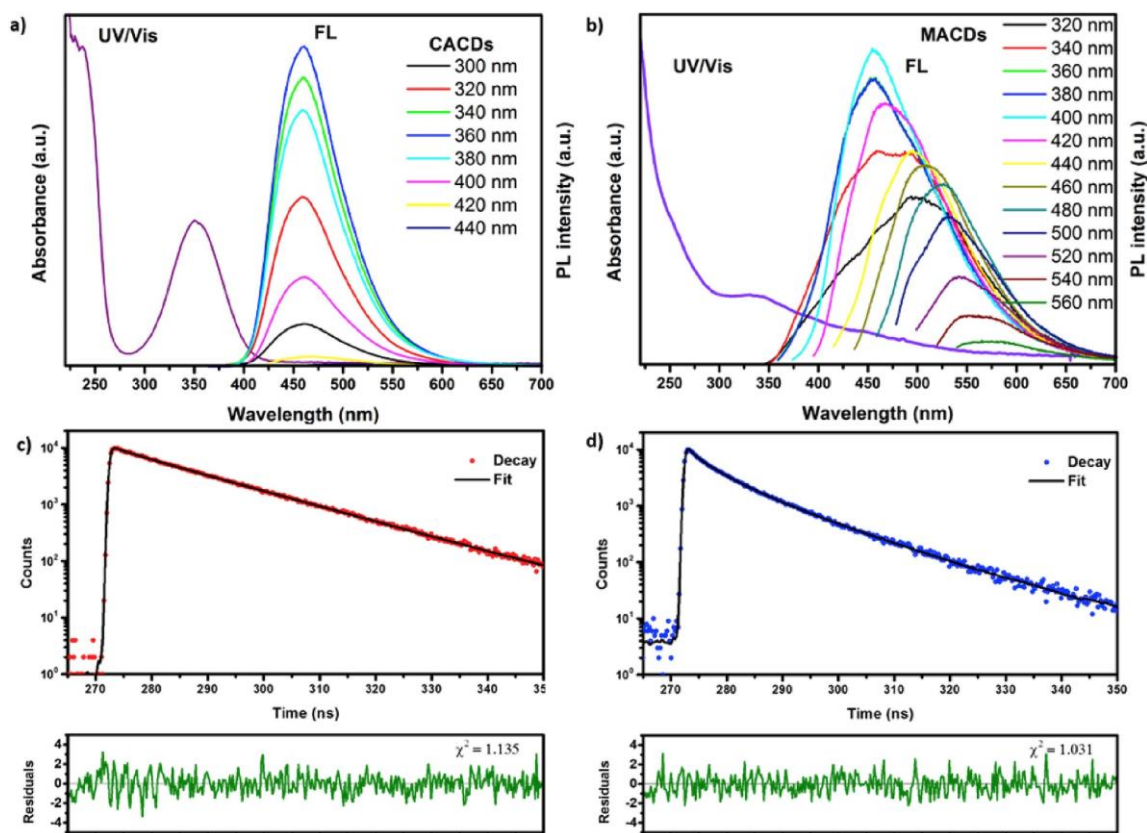


**Figure 2.2.** Optical (UV-vis absorbance and fluorescence) spectra of (a) CACDs and (b) MACDs and fluorescence lifetime traces of (c) CACDs and (d) MACDs.

The optical properties of both polymeric CDs were examined, as shown in Figure 2.2a, there are two peaks in the UV-vis spectrum of the CACDs with  $\lambda_{\text{max}}$  values of  $\sim 230$  nm and  $\sim 350$  nm. The first peak can be assigned to a  $\pi\text{-}\pi^*$  transition (aromatic C=C), and the second one can be assigned to a  $n\text{-}\pi^*$  transition (C-N or carboxyl)<sup>74</sup>. The fluorescence emission does not shift as the excitation wavelength shifts, remaining at  $\sim 460$  nm. Unlike most reported polymeric CDs, these CACDs do not demonstrate excitation-dependent emission. The fluorescence lifetime for the CACDs was measured three times in parallel using a 375-nm laser as excitation source, as shown in Figure 2.2c. The lifetime trace was fitted with a multi-exponential decay function, to minimize deviation from the exponential

fit function of the fluorescence lifetime of the polymeric CDs. The acceptable reduced Chi-square value ( $0.9 < \chi^2 < 1.2$ ) and the symmetrical distribution of residuals around zero indicate a good fit. Therefore, the overall fluorescence lifetime of CACDs is revealed by the mean value of three replicate results ( $\tau_{\text{avg}}$ ), that is,  $11.17 \pm 0.65$  ns. In contrast, MACDs only showed a weak absorption near 350 nm (Figure 2.2b), but interestingly, they exhibited excitation-dependent emission. When the excitation wavelength was adjusted from 320 nm to 400 nm, the peak of the emission spectra blue shifts from ~500 nm and reaches a maximum intensity at ~450 nm with 400 nm excitation, followed by a red shifting emission with decreasing intensity. The fluorescence decay kinetics for MACDs are shown in Figure 2.2d. The overall lifetime of MACDs was  $4.77 \pm 0.34$  ns, shorter than that of CACDs.

Furthermore, non-Raman corrected EEM reveal information about the excited state transitions of fluorescent molecules. The CACD excitation:emission pairs, visualized in Figure 2.3, were easily identified as ( $\lambda_{\text{ex}}=250$  nm: $\lambda_{\text{em}}=456.8$  nm) and ( $\lambda_{\text{ex}}=350$  nm: $\lambda_{\text{em}}=453.9$  nm), indicating the typical excitation independence. The MACD excitation:emission pairs in Figure 2.3b are not as easily isolated and have been assigned the following excitation:emission pairs: ( $\lambda_{\text{ex}}=255$  nm: $\lambda_{\text{em}}=454.9$  nm), ( $\lambda_{\text{ex}}=340$  nm: $\lambda_{\text{em}}=453.9$  nm), ( $\lambda_{\text{ex}}=385$  nm: $\lambda_{\text{em}}=468.6$  nm) and ( $\lambda_{\text{ex}}=450$  nm: $\lambda_{\text{em}}=514.5$  nm), visualizing the excitation-dependent emission. Considering the different numbers and positions of carboxyl groups within citric acid and malic acid molecules, their crosslinking patterns with ethylenediamine should be different during polymerization, and as a result, the final carbonized products, that is, the polymeric CDs, likely possess distinct structures,

and thus, behave differently in terms of optical behavior. The structures of these polymeric CDs will be explored by our further theoretical studies.

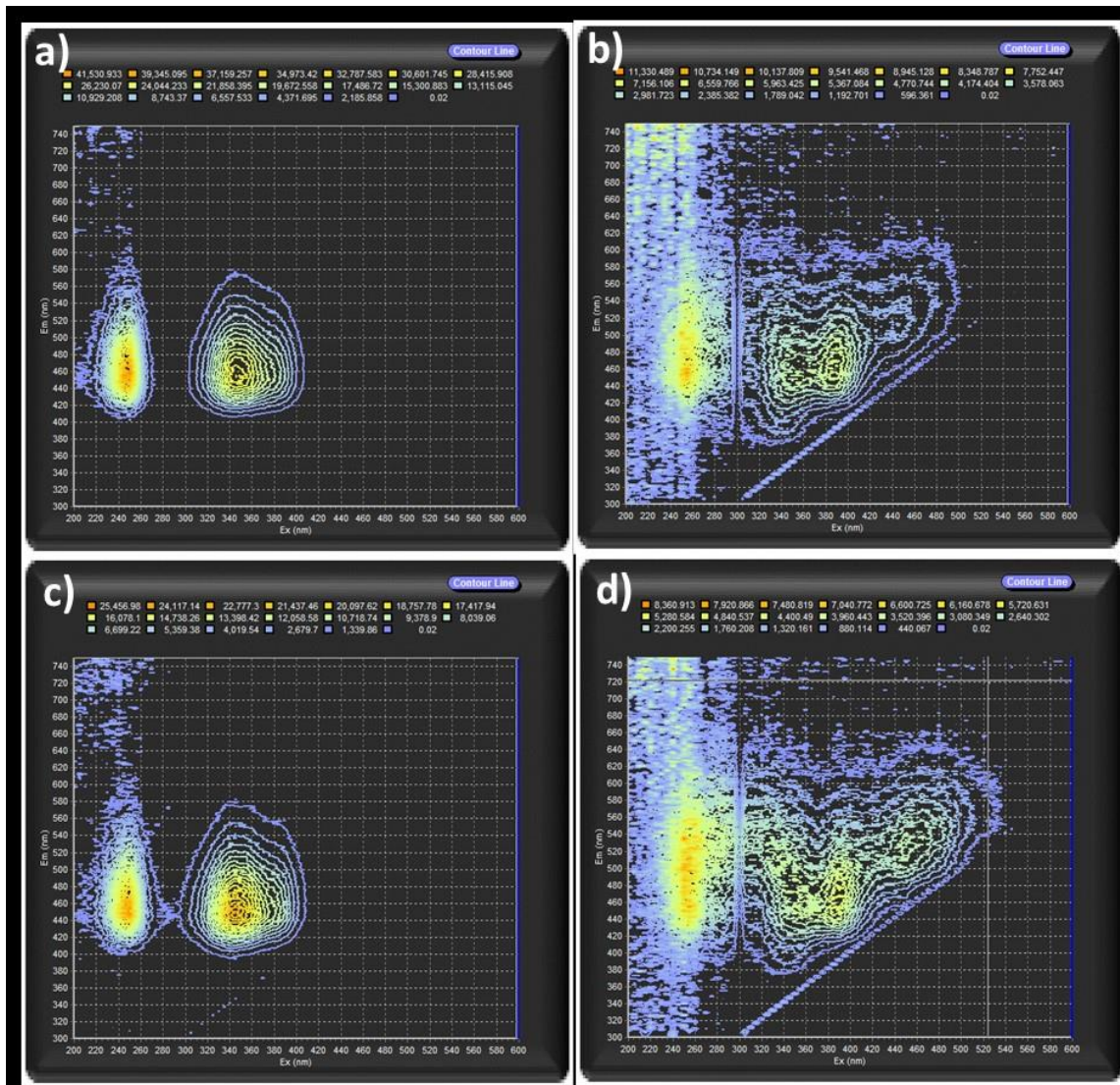


**Figure 2.3.** EEM of (a) CACDs, (b) MACDs, (c) CA-P-CDs-4 and (d) MA-P-CDs-4.

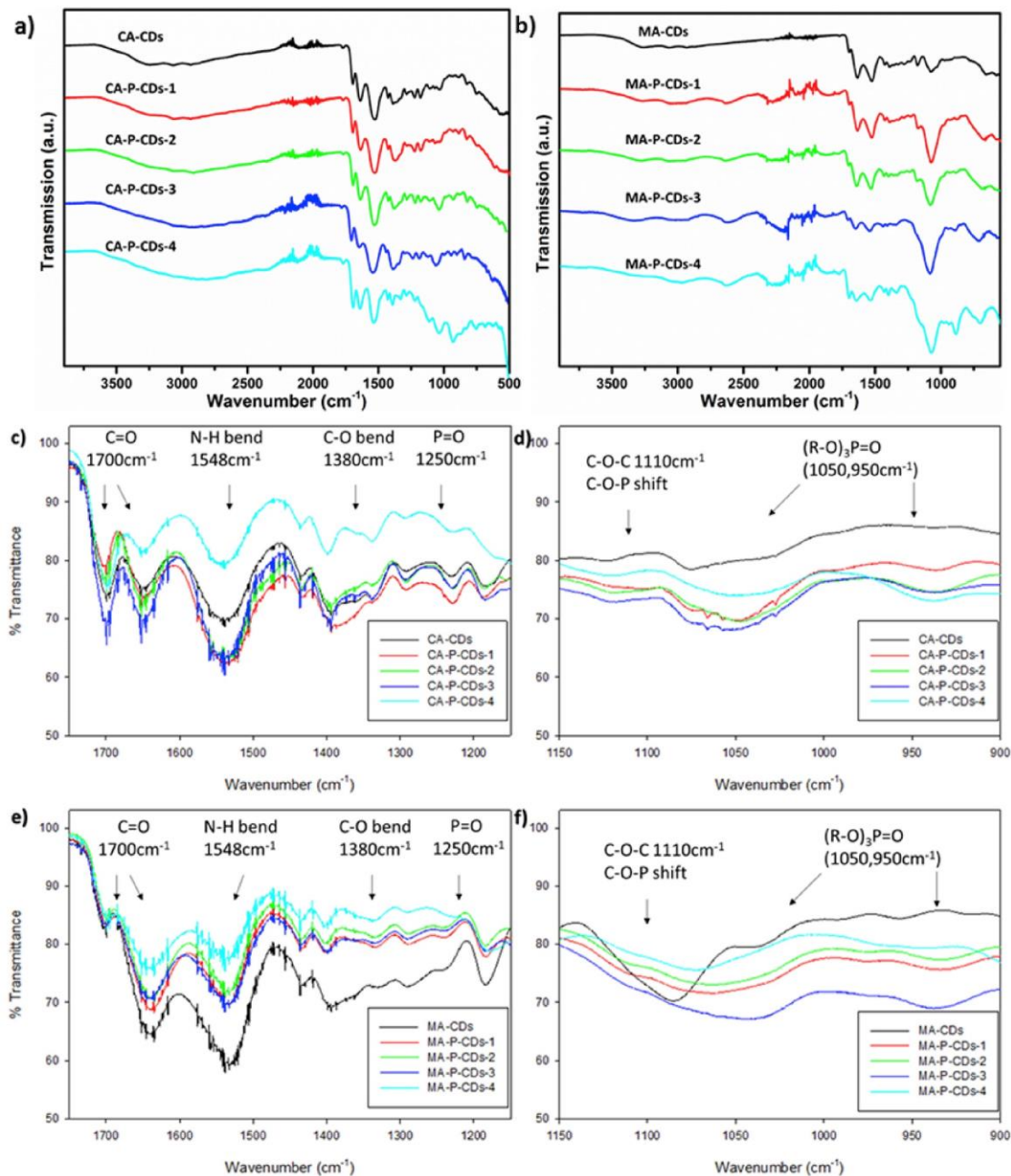


**Figure 2.4.** FTIR spectra of (a) citric acid polymeric CDs series, and (b) malic acid polymeric CDs series with a detailed spectral identification of phosphorylated peaks in citric acid polymeric CD series ((c) & (d)), and in malic acid polymeric CD series ((e) & (f)).

To delve deeper into the molecular character of these polymeric CDs, FTIR analysis was performed to characterize the functional groups within both polymeric CDs; these spectra

are shown in Figure 2.4. The FTIR spectra of the two polymeric CDs were similar. The broad peaks at  $\sim 3200\text{ cm}^{-1}$  and  $\sim 3000\text{ cm}^{-1}$  can be assigned to N-H and O-H stretching vibrations, respectively<sup>75</sup>. The  $\sim 2900\text{ cm}^{-1}$  peak is the alkyl stretch, the main component of the carbon network. The two IR absorption bands at  $\sim 1700\text{ cm}^{-1}$  and  $\sim 1640\text{ cm}^{-1}$  confirm the presence of carbonyl groups<sup>76</sup>. Specifically, the  $\sim 1700\text{ cm}^{-1}$  peak can be attributed to carboxyl carbonyl (-COOH) character, and the  $\sim 1640\text{ cm}^{-1}$  peak to amide carbonyl (-CO-NH) character<sup>77</sup>. The  $\sim 1400\text{ cm}^{-1}$  peak confirms a C-N stretch.

Moreover,  $^{13}\text{C}$  NMR results provide a qualitative analysis of the carbon hybridization state inside both the CACDs and the MACDs (Figure 2.5). The  $^{13}\text{C}$  NMR spectra reveal groups of peaks at  $\sim 40\text{ ppm}$ ,  $\sim 70\text{ ppm}$  and  $\sim 180\text{ ppm}$ , respectively<sup>78</sup>. The  $\sim 40\text{ ppm}$  peaks can be assigned to saturated carbon ( $\text{sp}^3$ ), that is, alkyl groups,  $\text{R}_2\text{CH}_2$  and  $\text{NH}_2\text{RCH}_2$  groups<sup>74, 79</sup>. The  $\sim 70\text{ ppm}$  peaks also reveal  $\text{sp}^3$  carbon connected to an electron withdrawing O or N atom, such as C-OH and C-N (in these cases, the peaks shift towards low field due to the electronegative effect). The CACDs and CA-P-CDs-4 spectra indicated the presence of two electron-withdrawing functional groups whereas the MACDs have five different electron withdrawing functional groups. An increased number of functional groups indicates the initial hydroxyl group on the malic acid precursor molecule remains intact. The phosphorylated CACDs indicate an incorporation of C=C character into the nanoparticle due to characteristics shifts at 162.40, 154.86 and 148.48 ppm. The last group at  $\sim 180\text{ ppm}$  indicates an unsaturated carbon ( $\text{sp}^2$ ) present within carbonyl groups, like carboxyls (-CO-OH) and amides (-CO-NH) not all carbonyl groups were lost to dehydration of the precursor when crosslinked with ethylenediamine.

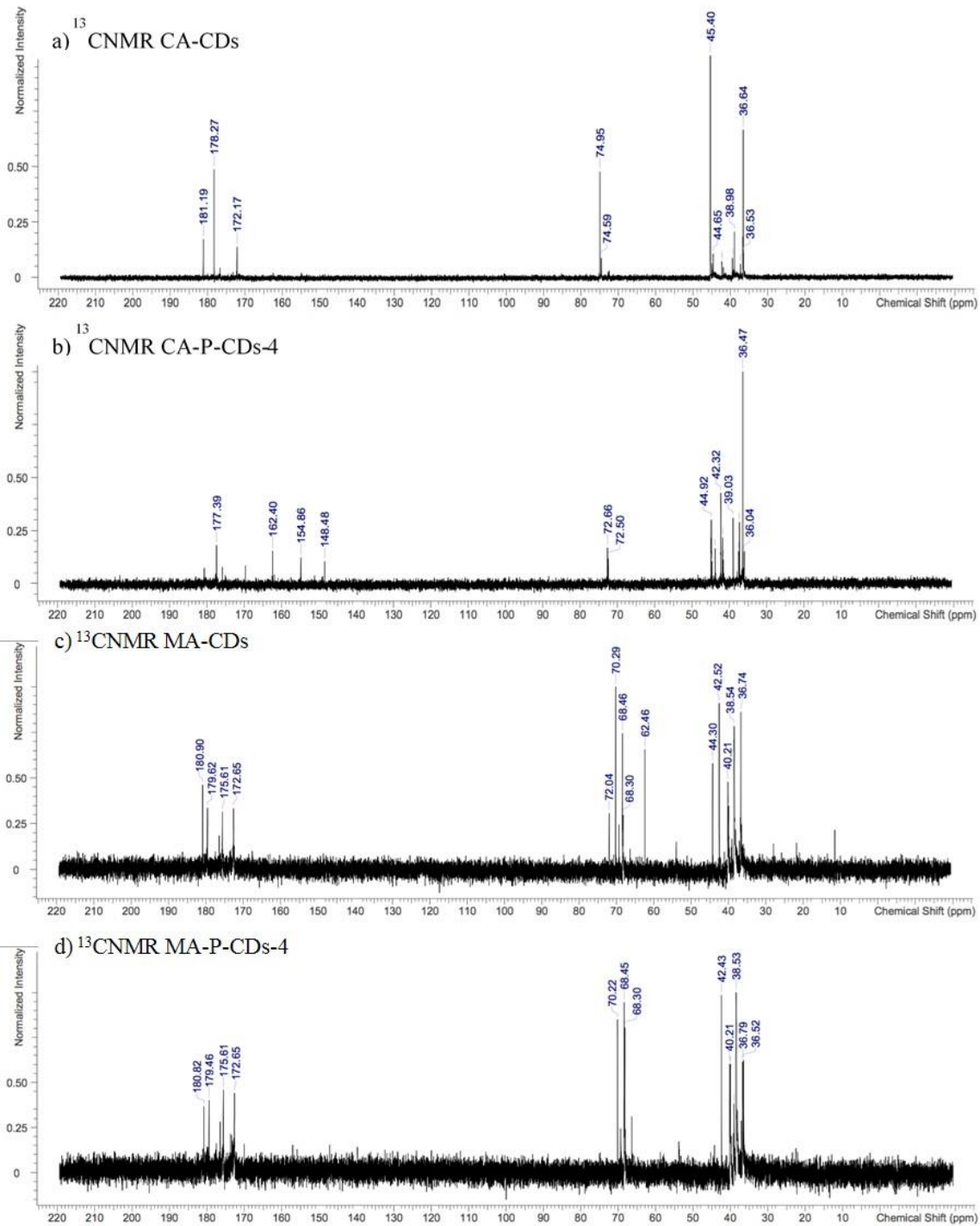


**Figure 2.5.**  $^{13}\text{C}$  NMR spectra of (a) CACDs (b) CA-P-CDs-4, (c) MACDs and (d) MA-P-CDs-4.

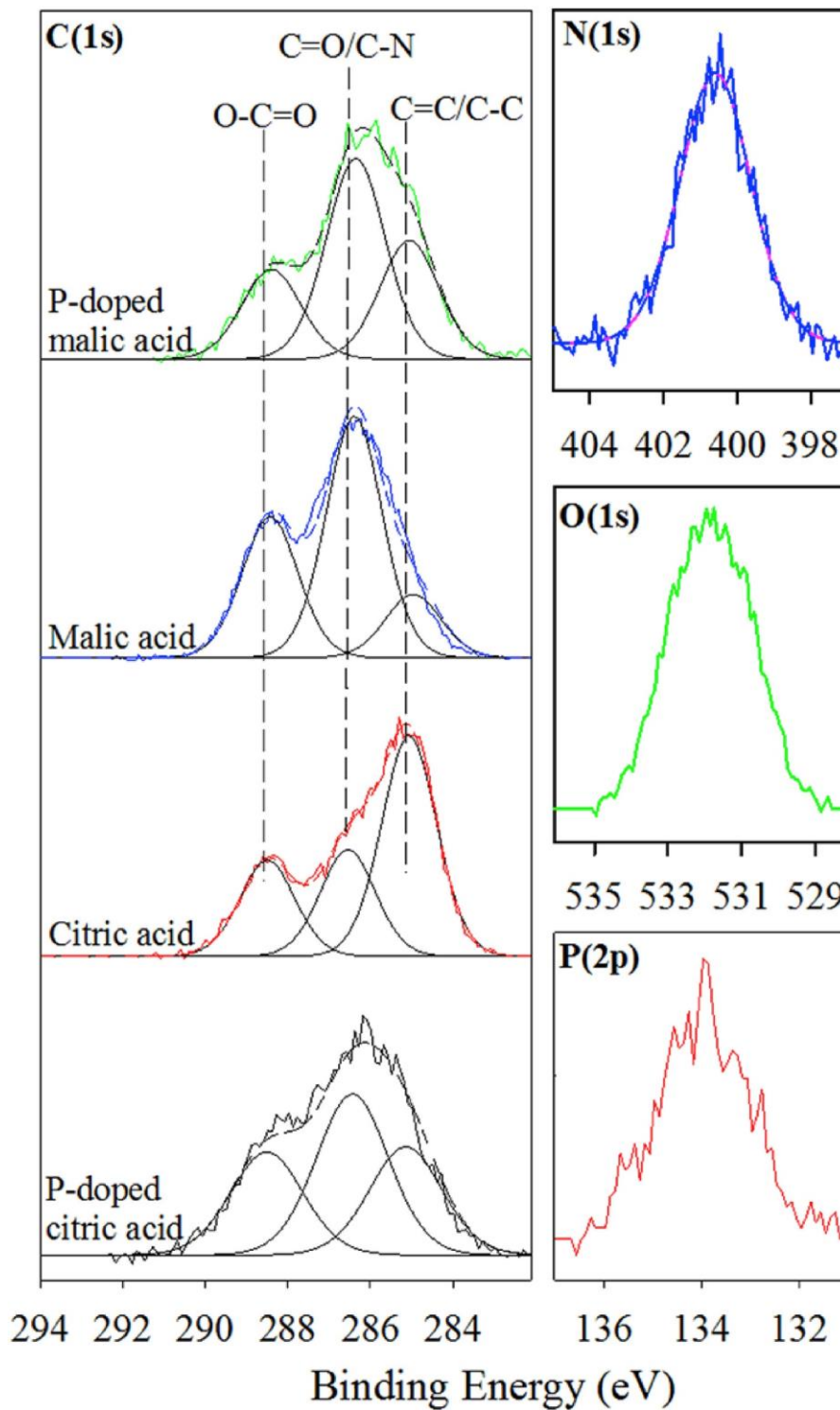


**Figure 2.6.** XPS of CDs: (Left hand side) Comparison of the C(1s) regions for CACDs and MACDs, prepared with and without phosphorous doping. (Right hand side) N(1s), O(1s) and P(2p) regions of phosphorous-doped CDs (CA-P-CDs-4 and MA-P-CDs-4).

XPS analysis of the polymeric CDs (Figure 2.6) revealed the presence of carbon, nitrogen and oxygen. For the polymeric CDs prepared in the presence of phosphoric acid, phosphorous was also detected. The C(1s) regions for each polymeric carbon dot could be fit well using the same set of three peaks, consistent with XPS data previously obtained on polymeric CDs<sup>44, 80-85</sup>. The peak positions of these three components are located at 288.5 eV, 286.5 eV, and 285 eV and correspond to O-C=O/O=C-N, C=O/C-N, and C=C/C-C species, respectively. These are the same species detected with IR (Figure 2.4). The C(1s) region is lacking a  $\pi-\pi^*$  shake-up peak at 292 eV, suggesting the absence of an extended conjugated pi-electron system. The C(1s) spectral envelopes of three of the four polymeric carbon dots (MACDs, CA-P-CDs-4, and MA-P-CDs-4) are similar; the C(1s) envelope of CACDs differs principally probably due to a higher concentration of C=C/C-C species. In previous work, the N(1s) XPS region of the nitrogen-containing polymeric CDs is often clearly asymmetric, indicative of a range of different nitrogen bonding environments<sup>86-88</sup>. In contrast, the N(1s) region of each of the four polymeric CDs analyzed in this study are very similar with a peak profile that can be fit well by a single Gaussian peak centered at  $\sim 400.7$  eV. Although the proximity of peak positions for different nitrogen bonding environments makes an unambiguous assignment difficult<sup>89</sup> the invariance of the N(1s) spectral envelope suggests that phosphorous incorporation does not lead to a significant perturbation in the chemical bonding environments of nitrogen atoms in the carbon dots. The O(1s) regions of each polymeric CD were also similar to one another, and no attempt was made to spectrally deconvolute the O(1s) regions due to the presence of a large number of bonding environments (*e.g.* O-C=O, C=O,

P-O) and the close proximity of the peak positions. For each of the two P-doped polymeric CDs, an additional peak in the P-region was observed with a peak position (~134 eV) indicative of oxidized phosphorous atoms. Moreover, the level of phosphorous incorporated into the polymeric CDs could be varied by changing the usage of phosphoric acid in the synthesis (see Table 2.1). Hence, based on the N<sub>1s</sub>, O<sub>1s</sub> and P<sub>2p</sub> XPS profiles, we confirm that the phosphorous doping is successful without inducing any turbulence into the original nitrogen and oxygen chemical environments of polymeric carbon dots. In addition, as XPS only reveals information of polymeric CD surface, EDAX was used to investigate the atom percentage of each element in bulk, as shown in Figure 2.7.

**Table 2.1.** XPS element analysis results of all of samples.

<b>Samples</b>	<b>%C</b>	<b>%O</b>	<b>%N</b>	<b>%P</b>
<b>CACDs (N=4)</b>	62.0 ± 3.0	24.3 ± 1.6	13.6 ± 1.6	0.02 ± 0.03
<b>CA-P-CDs-1</b>	64.8	18.5	16.7	0
<b>CA-P-CDs -2</b>	62.7	22.0	14.2	1.1
<b>CA-P-CDs -3</b>	63.1	22.2	13.8	0.9
<b>CA-P-CDs -4</b>	61.7	24.1	11.4	2.7
<b>MACDs (N=4)</b>	62.6 ± 1.8	22.0 ± 3.0	15.0 ± 2.0	0.0 ± 0.0
<b>MA-P-CDs-1</b>	60.5	22.0	16.4	1.1
<b>MA-P-CDs -2</b>	58.0	23.2	17.0	1.8
<b>MA-P-CDs -3</b>	58.0	23.3	15.9	2.8
<b>MA-P-CDs -4</b>	61.2	21.5	14.9	2.4

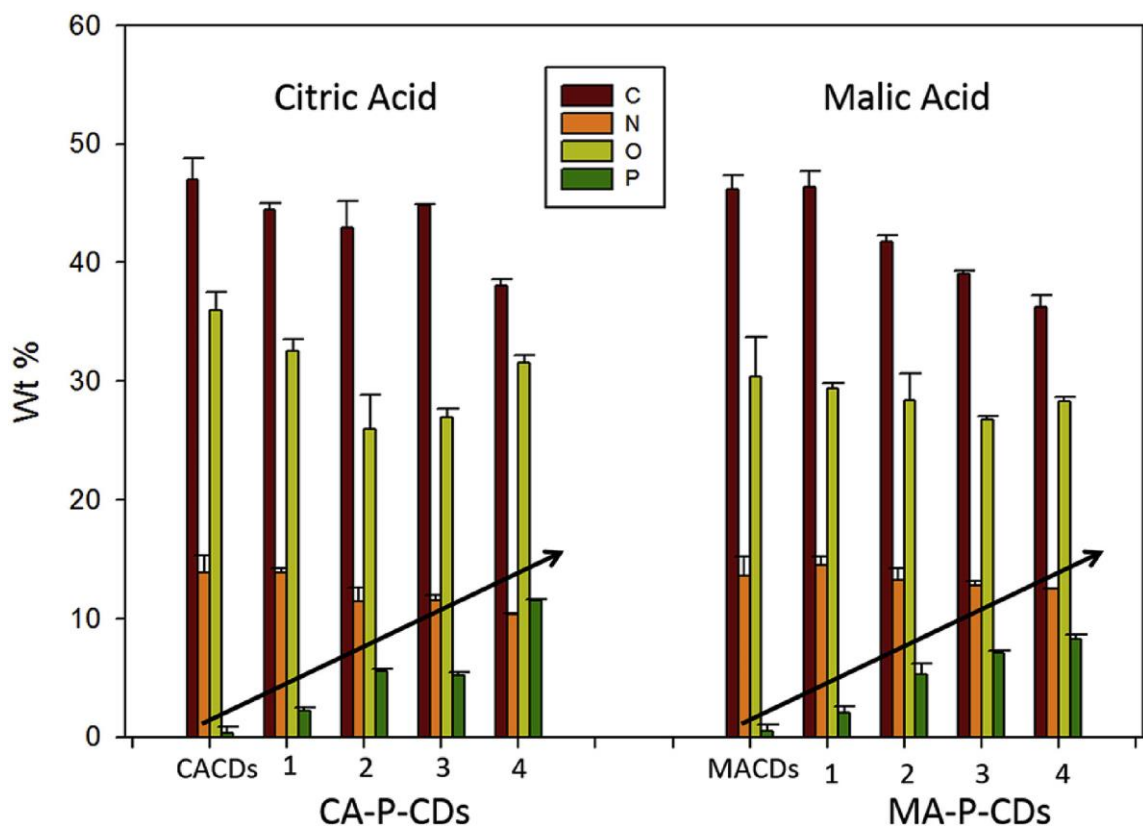


**Figure 2.7.** EDAX element analysis of citric acid polymeric CD series (left), and malic acid polymeric CD series (right).

Clearly, the phosphorus percentage gradually increased (indicated by the arrows), up to *c.a.* 10 wt.% for both polymeric carbon dots, if we used more and more phosphoric acid. Therefore, based on the XPS and EDAX data, we confirmed that the phosphorous doping was successful.

The morphology and diameter of the P-doped CACDS and MACDs were also analyzed by TEM. After doping with phosphorus, both types of N, P co-doped polymeric CDs retained the quasi-spherical morphology in 2D. The average values from the size distributions for the CA-P-CDs with increasing levels of P doping were ~6.5 nm, ~6.9 nm, ~6.3 nm and ~7.1 nm, respectively. For MA-P-CDs, they were ~8.1 nm, ~7.9 nm, ~5.8

nm and ~7.3 nm, respectively. Compared to the particle diameter of the original N-doped polymeric CDs, there was no remarkable difference after adjusting the precursors to incorporate phosphorus into the polymeric CDs.

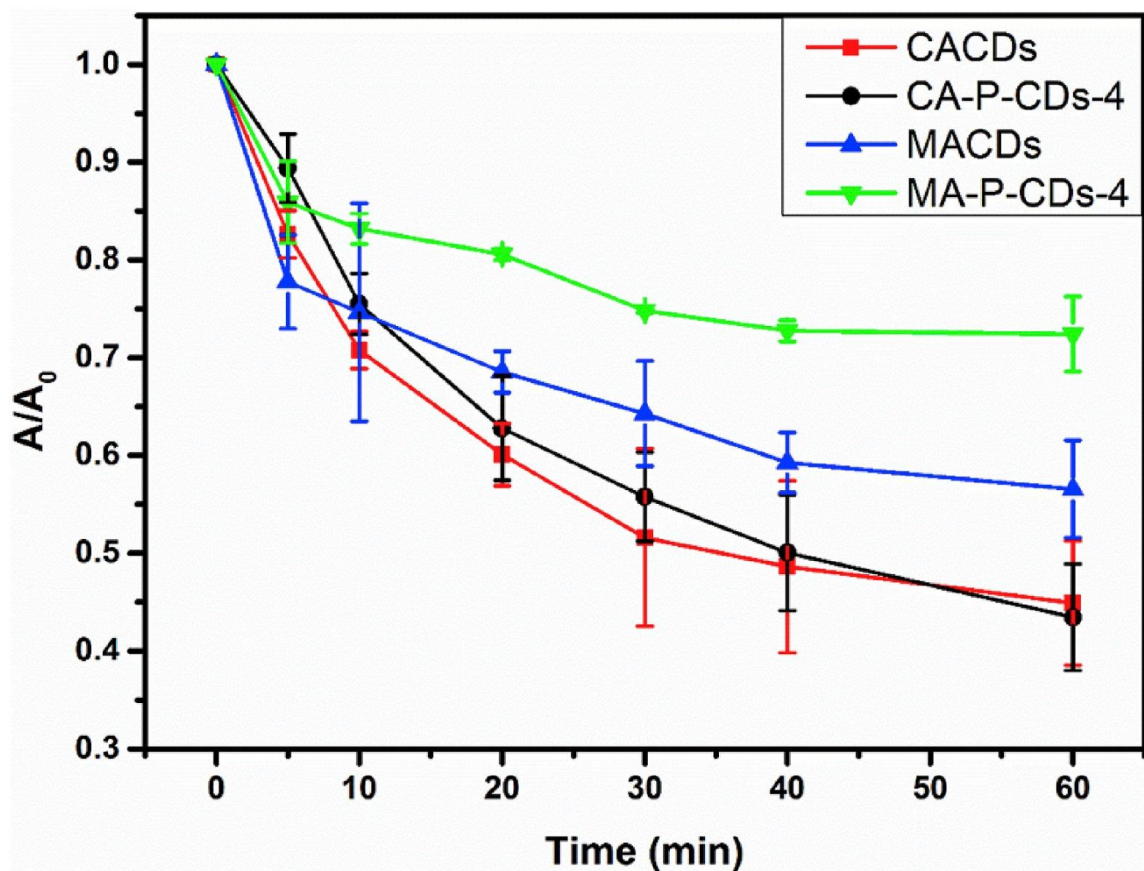


**Figure 2.8.** Photostability of the CACDs, CA-P-CDs-4, MACDs and MA-P-CDs-4. Photostability was determined by measuring the change in the absorbance ( $A/A_0$ ) at 350nm as a function of CD exposure to the intense visible light generated in a Rayonet reactor.

We attempted to determine the chemical features of N-doped polymeric CDs and N, P-co-doped polymeric CDs using ATR-FTIR (Figure 2.4). The incorporation of the phosphorous is indicated by the shift in the  $1110\text{ cm}^{-1}$  C-O-C vibration to a lower wavenumber due to the presence of C-O-P<sup>79</sup>. Furthermore, the phosphoryl (R-O)<sub>3</sub>P=O does not present in the citric acid is distinctly present in the phosphorylated samples

around  $950\text{ cm}^{-1}$  and  $1050\text{ cm}^{-1}$ . In addition, the IR absorption spectra for CA-P-CDs and MA-P-CDs resembled those of CACDs and MACDs, with features attributable to carboxyl, hydroxyl and amine groups. Hence, these N, P co-doped polymeric CDs exhibited high hydrophilicity, like their N-doped counterparts.

#### 2.4.2 Photostability tests of polymeric CDs

An ideal fluorophore should remain photostable for an extended period, so it is important to assess how doping polymeric CDs with phosphorous influences photostability. On the bench, under the influence of laboratory lighting, solutions of CDs and phosphorous-doped CDs were found to be stable over the course of at least six days, based on UV-vis analysis. To assess the effect (if any) of phosphorous doping on the photostability, it was therefore necessary to conduct accelerated photobleaching studies. This was accomplished by subjecting four of the polymeric CDs to intense visible light in a Rayonet reactor. Results from these studies, shown in Figure 2.8, demonstrate that there was a steady decrease in absorbance over one hour of exposure, which was accompanied by a blue shift in the peak emission. The pH of the solutions remained above 6 for the entirety of the experiments, ruling out acidic quenching<sup>90</sup>. The absorbance peaks were fit with a cubic baseline and subsequently a Gaussian function. For the first 40 min, CA-P-CDs-4 exhibited higher, but not statistically different, photostability than the CACDs. The MA-P-CDs-4 demonstrated a statistically significant ~25% increase in photostability compared to MACDs after 60-minute exposure. Thus Figure 2.8 demonstrates that distinct advantages in photostability are gained by doping the MACDs with phosphorous. The

overall stability trend with these four samples after one hour was determined to be: MA-P-CDs-4 > MACDs > CACDs  $\geq$  CA-P-CDs-4.

Previous accelerated photobleaching studies of CDs have typically been conducted by measuring changes in the QY under a wide range of different conditions (*e.g.* exposure to the white light from a Xe lamp, continuous irradiation at 360nm), where the incident photon flux is not reported.<sup>91-95</sup> Consequently, a direct quantitative comparison of the results from this investigation to previous photobleaching studies of CDs is not possible. However, in general photostability is found to depend on the synthetic route used to prepare the CDs. Specifically, crystalline CDs prepared by a “top-down” approach (*e.g.* by exfoliating carbon nitride using acid) are extremely photostable even when exposed to intense light sources (*e.g.* no change in PL after irradiation with a 365nm UV lamp for 12 hours).<sup>93</sup> In contrast, CDs prepared using a “bottom-up” approach (typically hydrothermally or by using microwaves) are more susceptible to photobleaching, an effect ascribed to the presence of a greater number of surface defects.<sup>92, 95</sup> Results from the present study are therefore in qualitative agreement with this general trend.

**Table 2.2.**  $\tau_{\text{avg}}$  and QY data of citric acid CDs series (left) and malic acid CDs series (right).

<b>Samples</b>	<b><math>\tau_{\text{avg}}</math> (ns)</b>	<b>QY (%)</b>	<b>Samples</b>	<b><math>\tau_{\text{avg}}</math> (ns)</b>	<b>QY (%)</b>
<b>CACDs</b>	11.17 $\pm$ 0.65	48.34	<b>MACDs</b>	4.77 $\pm$ 0.34	12.07
<b>CA-P-CDs-1</b>	9.11 $\pm$ 0.37	40.98	<b>MA-P-CDs-1</b>	5.43 $\pm$ 0.39	15.56
<b>CA-P-CDs-2</b>	9.12 $\pm$ 0.07	39.29	<b>MA-P-CDs-2</b>	4.45 $\pm$ 0.15	11.58
<b>CA-P-CDs-3</b>	8.88 $\pm$ 0.09	35.56	<b>MA-P-CDs-3</b>	5.63 $\pm$ 0.30	10.19
<b>CA-P-CDs-4</b>	9.72 $\pm$ 0.80	44.23	<b>MA-P-CDs-4</b>	4.32 $\pm$ 0.06	11.99

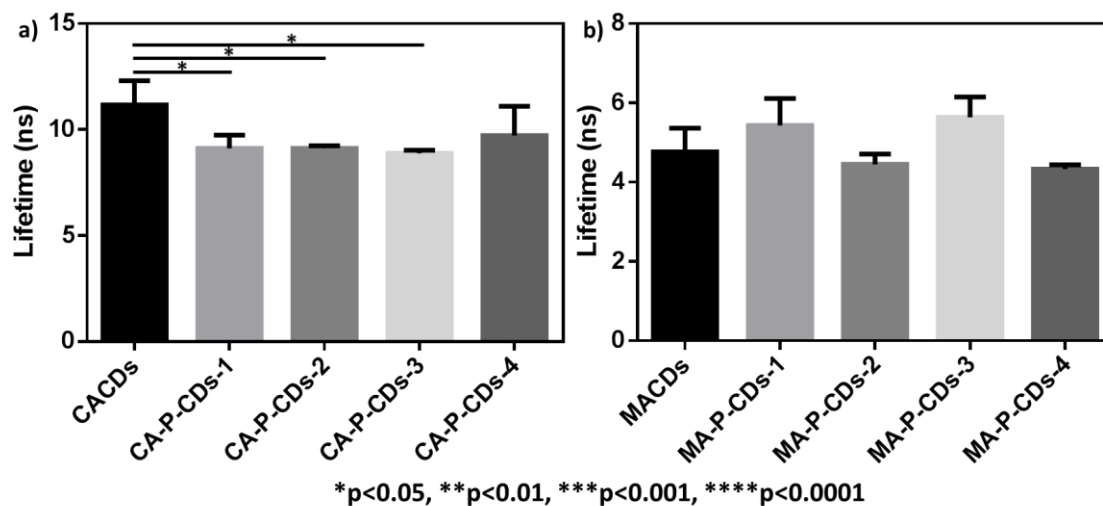


**Figure 2.9.** Comparison of  $\tau_{\text{avg}}$  among (a) citric acid carbon dots, and (b) malic acid carbon dots using one-way ANOVA.

### 2.4.3 Optical properties after phosphorus doping

The high QY of the CACDs was in concurrence with literature values<sup>6, 8, 46</sup>. After doping with different levels of phosphorous, the QY of doped CACDs was maintained around 40% (Table 2.2). Specifically, the QY is 40.98% for CA-P-CDs-1, 39.29% for CA-P-CDs-2, 35.56% for CA-P-CDs-3, and 44.23% for CA-P-CDs-4. The citric acid polymeric CDs are found to be much more efficient at conversion of absorbed photons with 340 nm laser excitation than the malic acid polymeric CDs. The most prominent excitation, however, occurs at 385 nm for the MACDs. The MACDs were found to have a QY closer to that of tryptophan (~14%)<sup>69</sup>. The QY of MACD series remained *c.a.* 10% after P-doping (Table 2.2), that is, 15.56% for MA-P-CDs-1, 11.58% for MA-P-CDs-2, 10.19% for MA-P-CDs-3, and 11.99% for MA-P-CDs-4. The MACD series may have lower QY due to the multiple pathways for relaxation shown in the EEM in Figure 2.3b and d. The  $\tau_{\text{avg}}$  of citric acid polymeric CDs is about two times longer than those of malic acid polymeric CDs

(Table 2.2). The lifetimes have decreased after doping phosphorus into CACDs, but there was no such an effect for P-doped MACDs (Figure 2.9).

#### 2.4.4 Bacterial toxicity of polymeric CDs

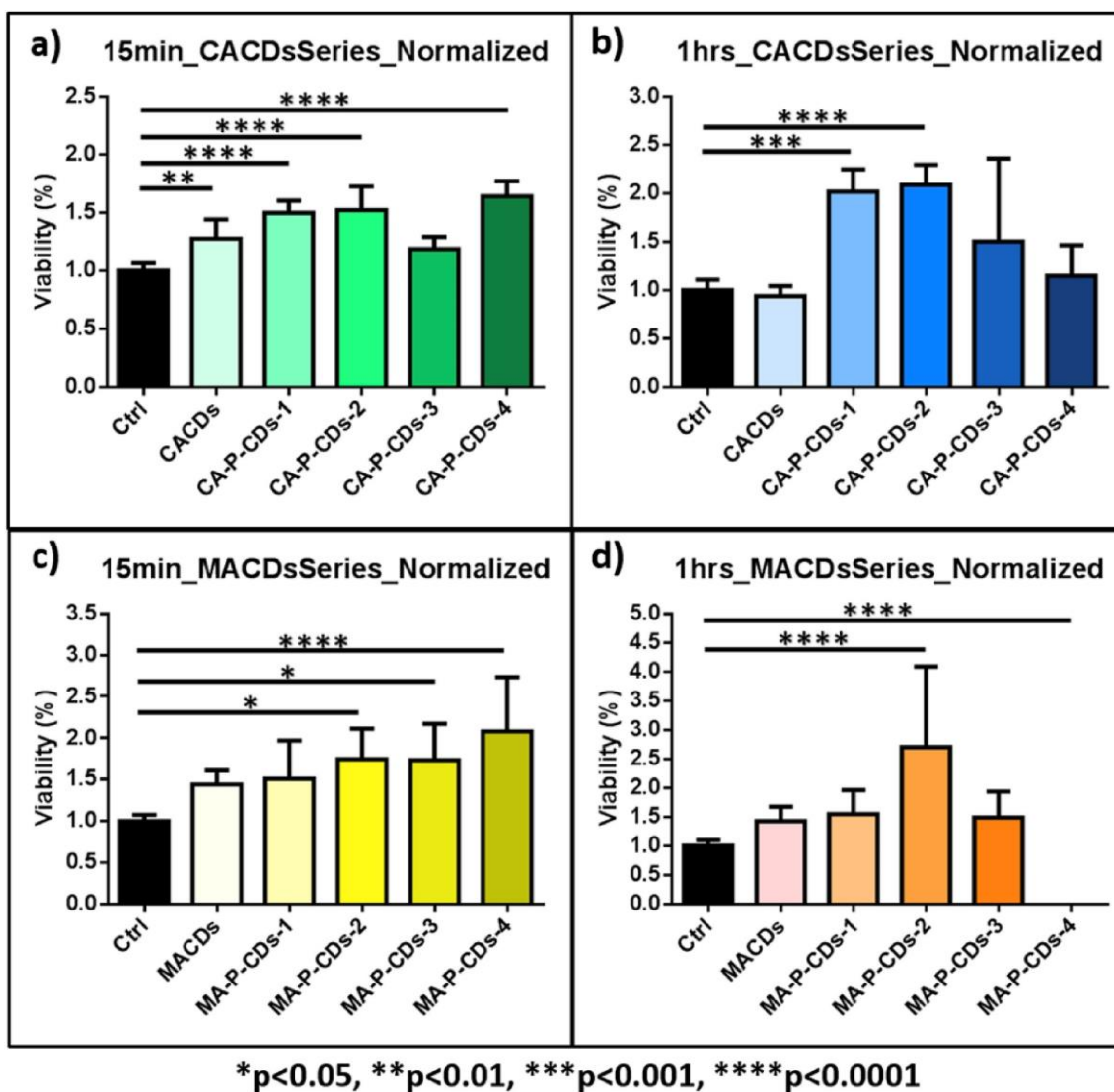


**Figure 2.10.** Colony counting assay results of citric acid polymeric CDs after (a) 15-min exposure and (b) 1-hour exposure, and results of malic acid polymeric CDs after (c) 15-min exposure and (d) 1-hour exposure (Error bars indicate standard deviation, and for simplicity, only the positive half of each error bar is shown).

With luminescence and photostability properties of the new polymeric CDs looking promising, nanoparticle toxicity was considered since one proposed advantage of polymeric CDs over traditional QDs lies in their likely biocompatibility. Figure 2.10 describes the toxicity results of polymeric CDs towards the model bacterium, *S. oneidensis* MR-1, as measured by a colony counting assay (drop plate method).

Statistical analysis was performed using one-way ANOVA, followed by post-hoc Tukey's multiple comparisons tests (GraphPad Prism software, La Jolla, CA). All values plotted are the mean  $\pm$  standard error of mean, and statistical significance is indicated using asterisks (\* $p < 0.05$ , \*\* $p < 0.01$ , \*\*\* $p < 0.001$  and \*\*\*\* $p < 0.0001$ ). The results show that, in most cases, neither N-doped polymeric CDs nor N, P co-doped polymeric CDs exhibit a toxic effect; on the contrary, the bacteria formed more colonies than the negative control (untreated) samples in some cases. This increased colony formation suggests that *S. oneidensis* MR-1 can potentially use polymeric CDs as their carbon nutrient source. In fact, it is known that *S. oneidensis* MR-1 performs a standard tricarboxylic acid cycle for carbon metabolism under aerobic growth<sup>96</sup> wherein citric acid and malate anion play a role. However, neither genomic prediction nor experimental evidence have previously demonstrated that this bacterium can utilize citric acid or malic acid as a carbon source<sup>97</sup>. It is possible that other components in the polymeric CDs, such as phosphorus or unknown by-products from the synthesis, promote bacterial colony formation. It is worth noting that the MA-P-CDs-4 (malic acid carbon dots doped with the highest amount of phosphorus) showed extremely high bacterial toxicity, eradicating almost the whole bacterial population. Recall from Figure 2.8, doping the malic acid samples with phosphorous

gained an advantage in photostability which may not be favorable when compared to the toxic response seen in the *S. oneidensis* MR-1 over one-hour exposure. It is worth noting, however, that the threshold to toxicity is quite high at 5000 mg/L in a concentrated (300  $\mu$ L) of solution. This high of a concentration would be too bright for a detector in a confocal scanning laser microscopy and would be an impractical working solution concentration for bio-imaging. It is important to note that the need for something to be illuminated over an hour in a microscope may be unnecessary. Notwithstanding, the gains in photostability and lower QY demonstrate phosphorous doping of malic acid might not be worth the acute toxicity exhibited by *S. oneidensis* MR-1. Future studies on metabolomics could provide insight into the stress imposed upon this organism by the high concentration of particles. Other model organisms would also give a well-rounded picture of acute toxicity. Finally, it may be important to look at the photodegraded polymeric carbon dots to assess if the photoproducts are, in and of themselves, toxic. It was initially suspected that such toxicity was a result of light-induced polymeric CD degradation, since the exposure was done under lab light, and the toxicity was only apparent after 1-hour exposure; thus, another two sets of experiments were set up to investigate this possibility. Results showed that lab light was not the mechanism responsible for the high toxicity of MA-P-CDs-4 (Figure 2.11). The source of this repeatable high toxicity after 1-hour exposure is the subject of ongoing investigation. In general, most of the polymeric CDs were not at all toxic towards the *S. oneidensis* MR-1 even at high doses (5 mg/mL), showing that polymeric CDs are quite benign. Thus, the non-toxic polymeric CDs are used for our further bio-imaging and bio-sensing studies.

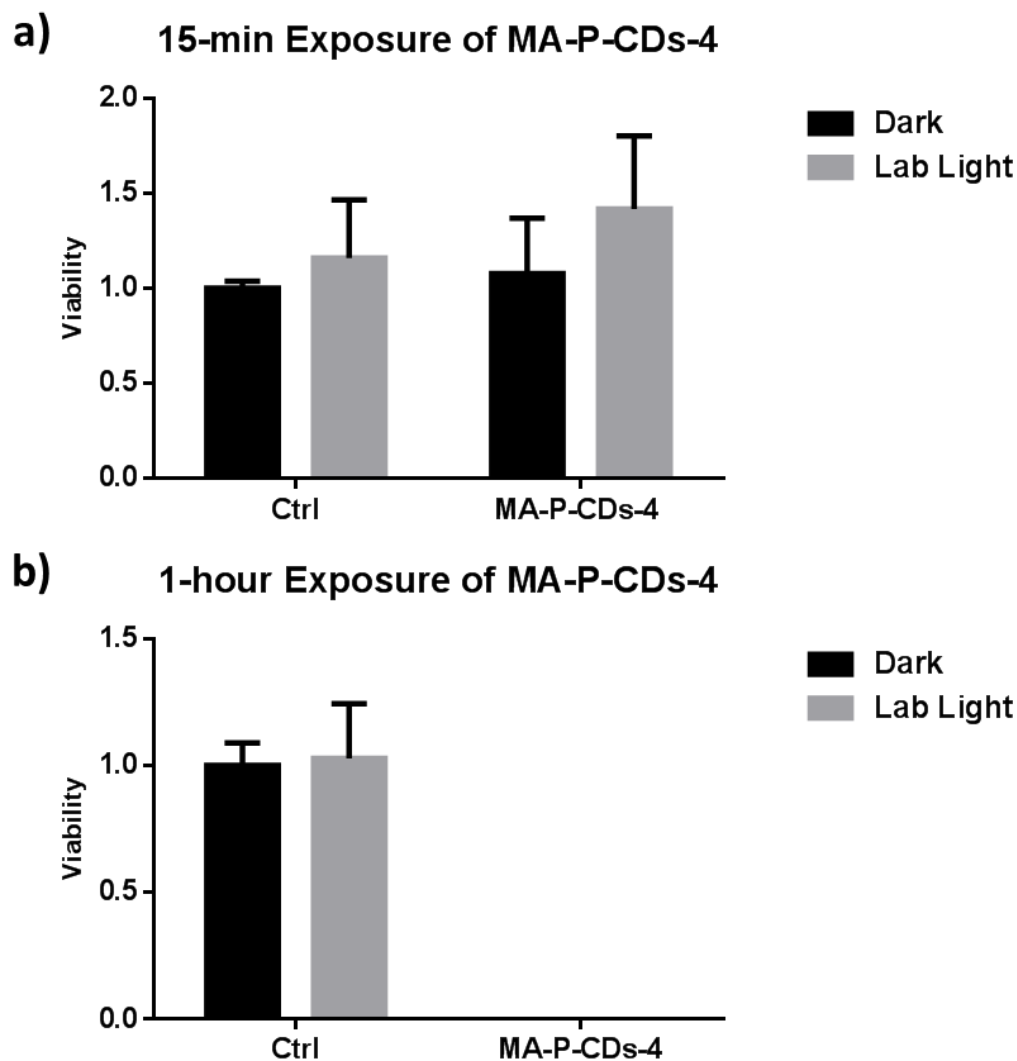


**Figure 2.11.** (a) 15-min and (b) 1-hour exposure results of MA-P-CDs-4 (5 mg/mL) in dark condition and under lab light condition.

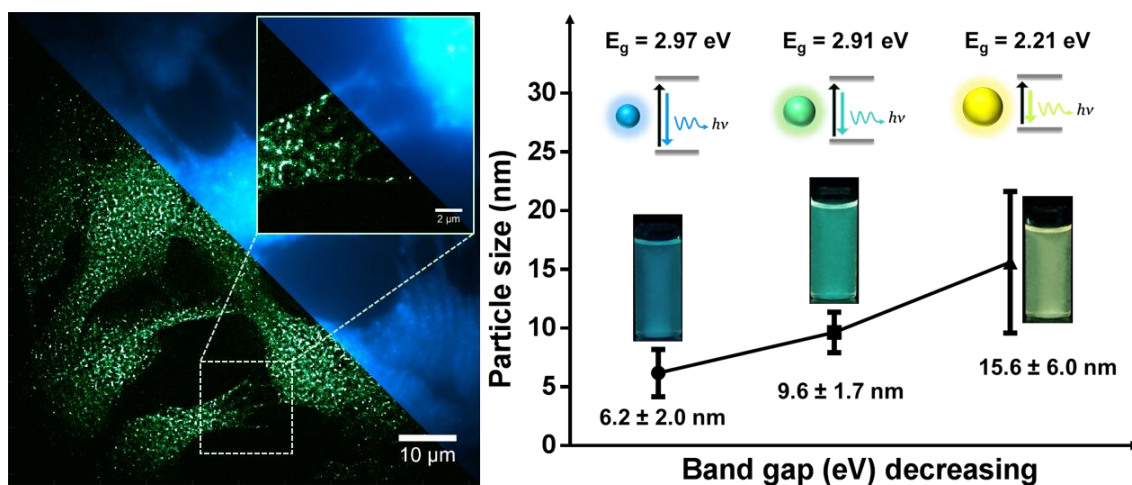
## 2.5 Conclusions

Polymeric CDs display reproducible, highly marketable luminescence properties that are influenced by chemical composition. In this work, citric acid and malic acid were used as carbon sources to generate N-doped polymeric CDs (using ethylenediamine as the nitrogen source). Furthermore, various amounts of phosphorus were introduced into these

polymeric CDs, resulting in N, P-co-doped polymeric CDs. These doped polymeric CDs were great candidates to systematically and quantitatively analyze the impact of phosphorus doping on emission properties, photostability, and toxicity; the results reveal that there is no remarkable influence after doping with phosphorus in terms of QY or lifetime. The starting material with three carboxylic acid groups was found to be a better performing polymeric carbon dot with higher QY and longer fluorescent lifetime compared to the starting material with two carboxylic acid groups. By contrast, the N, P-co-doped malic acid polymeric CDs may show an advantage over N, P-co-doped citric acid polymeric CDs and N-doped polymeric CDs in terms of photostability under 350 nm UV exposure. Any advantages accrued in photostability are diminished by the toxicity results. Lastly, to assess the possibility that luminescent CDs may be a viable replacement for toxic heavy metal-based quantum dots in a variety of applications, the bacterial toxicity of these doped polymeric CDs was evaluated using *S. oneidensis* MR-1 as a model microorganism. The polymeric CDs exhibited no inhibition in bacterial colony formation in most cases, and in some cases, even facilitated bacterial growth, making polymeric CDs a potentially eco-friendly fluorescent material with a wide range of potential applications.

## Chapter 3

Malic acid carbon dots: from super-resolution living cell imaging to highly efficient separation



Reprinted from: Zhi, B.; Cui, Y.; Wang, S.; Frank, B. P.; Williams, D. N.; Brown, R. P.; Melby, E. S.; Hamers, R. J.; Rosenzweig, Z.; Fairbrother, D. H.; Orr, G.; Haynes, C. L., Malic Acid Carbon Dots: From Super-resolution Live-Cell Imaging to Highly Efficient Separation. *ACS Nano* **2018**, *12* (6), 5741-5752. Copyright 2018, with permission from the American Chemical Society.

Bo Zhi is responsible for the design of this research as well as malic acid carbon dot synthesis, TEM analysis, optical property measurements and the drafting of manuscript.

### **3.1 Overview**

As-synthesized malic acid carbon dots are found to possess unique and superior photoblinking properties compared to conventional dyes. Considering their excellent biocompatibility, malic acid carbon dots are suitable for super-resolution fluorescence localization microscopy under a variety of conditions, as we demonstrate in fixed and live trout gill epithelial cells. In addition, during imaging experiments, the so-called “excitation wavelength-dependent” emission was not observed for individual as-made malic acid carbon dots, which motivated us to develop a time-saving and high-throughput separation technique to isolate malic acid carbon dots into fractions of different particle size distributions using C<sub>18</sub>-reversed phase silica gel column chromatography. This post-treatment allowed us to determine how particle size distribution influences the optical properties of malic acid carbon dot fractions, *i.e.*, optical band gap energies and photoluminescence behaviors.

### **3.2 Introduction**

Super-resolution fluorescence microscopy has become increasingly important for biomedical research and discovery.<sup>1-4</sup> Conventional fluorescence microscopy is limited by the diffraction limit of light, and imperfections in optical components further decrease spatial resolution. This results in a lateral resolution limit of 250-300 nm as determined by the Abbe criterion.<sup>5</sup> To obtain a resolution comparable to the size of most biomolecules (< 10 nm), two major approaches are extensively used to overcome the diffraction limit: the patterned illumination-based imaging, including STED microscopy and SIM, and the single-molecule localization-based imaging, including STORM and PALM.<sup>6</sup> For the latter

strategy, closely clustered fluorescent molecules are resolved by stochastically turning each molecule's signal on and off.<sup>7,8</sup> The centroid of on-state molecules is mathematically determined in each imaging frame. A "super-resolution" image can then be reconstructed via the combination of multiple iterations. To achieve high-quality super-resolution imaging, it is crucial that photoswitchable fluorophores possess high photon yield and low on-off duty cycle.<sup>9</sup> A variety of organic dyes can be tuned to photoblink for super-resolution localization microscopy, mostly requiring high-power excitation and special imaging solutions containing oxygen scavenger and high thiol content.<sup>10,11</sup> Even with that, few organic fluorophores have proven to be suitable for super-resolution localization microscopy under visible excitation and emission wavelengths. It is important to note that the high photobleaching rates of organic fluorophores severely limit the utility of these fluorophores in super-resolution applications, basically restricting their use to short duration applications. Hence, to advance single-molecule imaging, it is desirable to develop cost-effective and photostable fluorophores that combine spontaneous photoblinking properties with intense brightness and low photobleaching rates.

Photoluminescent zero-dimension carbon nanostructures, including CDs, graphene dots, polymer dots, and nitrogen-vacancy centered nanodiamonds, have generated great interest in many fields due to their unique optical properties, including their strong fluorescence, excellent water solubility, and high resistance to photobleaching.<sup>12-17</sup> Amongst these carbon-based luminescent materials, CDs have emerged as a particularly attractive option due to availability of inexpensive carbon precursors, ease of synthesis and functionalization, and large-scale production.<sup>18, 19</sup> CDs are characterized by broadband

optical absorption,<sup>16, 20</sup> high emission QY,<sup>20</sup> excellent biocompatibility,<sup>21</sup> and minimal environmental impact.<sup>22</sup> This unique combination of outstanding properties make CDs a highly promising, eco-friendly alternative to inorganic semiconductor quantum dots, which often contain toxic heavy metals,<sup>23, 24</sup> and traditional organic fluorophores. To date, CDs have been used in a broad range of applications including biosensing and bioimaging,<sup>16, 25</sup> drug delivery,<sup>26</sup> photocatalysis,<sup>27</sup> patterning,<sup>28</sup> and photoelectronic devices.<sup>20, 29</sup> Recently, CDs were found to be reversibly photoswitchable, which make them suitable as labeling agents for super-resolution localization microscopy.<sup>30-32</sup>

Generally, CDs exhibit a quasi-spherical morphology with dimensions on the scale of 10 nm,<sup>16, 33</sup> composed of crystalline or amorphous carbon nanostructures<sup>34</sup> depending on carbonization temperature.<sup>35, 36</sup> CDs can be generated via a so-called “top-down” synthetic route<sup>13, 37</sup> by breaking down bulk carbon sources such as active carbon,<sup>38</sup> graphite,<sup>18, 39</sup> graphite oxide,<sup>40, 41</sup>, and carbon soot.<sup>42, 43</sup> However, top-down methods are relatively expensive and generate less material, limiting the scale of CD production.<sup>34</sup> On the other hand, “bottom-up” approaches involving the assembly of the CD nanostructure using cheap molecular carbon precursors are more favorable for large-scale and high-yield production.<sup>34, 37</sup> The choices of these small organic molecules are quite broad, and include citric acid,<sup>44</sup> glucose,<sup>45</sup> chitosan,<sup>46</sup> vitamin C,<sup>47</sup> glycerol,<sup>48</sup> ethylenediaminetetraacetic acid,<sup>49</sup> and L-glutamic acid.<sup>50</sup> Bottom-up procedures mainly involve thermal dehydration, polymerization, and carbonization of these inexpensive organic molecules.<sup>14, 34</sup> A variety of synthesis strategies have been developed for CD fabrication, such as microwave irradiation,<sup>51</sup> hydrothermal carbonization,<sup>52</sup> pyrolysis, or thermal decomposition.<sup>53, 54</sup>

Microwave-based synthesis features advantages including strong interaction of carbon materials with electromagnetic irradiation, fast, localized heating, and energy-saving processes.<sup>55,56</sup> In our group, DL-malic acid (a green and inexpensive organic compound)<sup>57</sup> is utilized as the carbon source with ethylenediamine as the cross-linker and self-passivating agent to fabricate highly fluorescent MACDs via a rapid microwave-assisted heating treatment.<sup>22, 58</sup>

In recent years there has been an exponential increase in research interest related to CD preparation and applications.<sup>16</sup> Nevertheless, most of the as-prepared CDs exist as a relatively complex mixture of varied components with distinct optical properties.<sup>59-61</sup> Thus, the purification and/or separation of as-synthesized CDs is essential to probe the nature of single components.<sup>19, 59</sup> In this respect, chromatographic purification has been used as an effective method to separate carbon-based photoluminescent materials.<sup>52, 62</sup> For instance, Ding *et al.* employed silica column chromatography to fractionate as-made CDs based on their degree of oxidation. Though the separation results were quite impressive, the process took more than ten hours due to the high affinity of CDs towards commonly used silica gel.<sup>52, 62</sup> HPLC has also found favor with CD researchers as a highly efficient option for separation. Vinci *et al.* utilized AE-HPLC to separate as-synthesized CDs generated from graphite nanofibers and confirmed that the emission wavelength of CD fractions was dependent on the NP size but not on the excitation wavelength.<sup>60, 63</sup> However, AE-HPLC is more suitable to separate charged CDs produced by microwave synthesis from acidic rather than neutral small molecule precursors.<sup>22, 59</sup> AE-HPLC columns are also expensive. To overcome these drawbacks, Gong and co-workers applied RP-HPLC and achieved a

rapid and effective separation for hollow carbon nanoparticles.<sup>64</sup> The isolated fractions gave off blue, green, and red fluorescence emission which was related to the carbon shell thickness. Although RP-HPLC seems to be an ideal option, the low output that results from the limited HPLC injection volume (1  $\mu\text{L}$  to 20  $\mu\text{L}$ ) restricts the wide scale application of this method.<sup>59</sup> Therefore, there is an urgent need to develop a fast, low-cost and high-yield separation method to realize the efficient fractionation of as-prepared CD samples.

Here, we report on the photoblinking properties of our as-synthesized MACDs. With active photoblinking, burst-like photon emission, efficient cell uptake, and high biocompatibility, we show that MACDs can be an excellent nanomaterial for super-resolution localization microscopy. Interestingly, the well-known “wavelength-dependent emission” phenomenon was not observed in single particle imaging experiments. As such, to further explore the physiochemical properties of MACD components, we have developed a time-saving and high-throughput method to separate as-synthesized MACDs, utilizing  $\text{C}_{18}$  reverse-phased silica gel column chromatography. The MACD fractions obtained in this way exhibit wavelength-independent emission and distinct PSD. More interestingly, these MACD fractions exhibit distinct optical properties, namely, absorption, optical band gap energy, and photoluminescence behaviors.

### **3.3 Experimental**

#### 3.3.1 Chemicals

All materials were used as received, without further purification. DL-malic acid (ReagentPlus®, ≥99%), ethylenediamine (ReagentPlus®, ≥99%) and C<sub>18</sub>-reversed phase silica gel (for column chromatography, fully endcapped) were purchased from Sigma-Aldrich. The Biotech cellulose ester membrane (MWCO 100-500 D) was obtained from Spectrum Labs. Deionized water was produced by a Millipore Milli-Q system (Billerica, MA) and used for all experiments.

### 3.3.2 MACD synthesis

We synthesized the MACDs based on our previous work.<sup>22</sup> Briefly, a 4 mol/L aqueous malic acid stock solution was prepared in advance. 4 mL of this stock solution was transferred into a 100-mL beaker, and then 1080 μL of ethylenediamine was added. The reaction was completed within 1 min as heat was released, and a homogenous solution was formed. The mixture was stirred for 30 min and allowed to cool. Then, the colorless transparent mixture was transferred to a domestic microwave oven and heated at 360 W for 3 minutes. The resultant dark brown foamy solid was cooled in a fume hood for 20 minutes before 10 mL of water was added into the beaker. The dark brown transparent solution thus obtained was dialyzed for 24 hours to remove unreacted precursors. Then, rotary evaporation was used to remove most of the water from the solution, leaving behind a dark brown sticky solid product at the bottom. Further lyophilization was completed in a freeze dryer (Labconco FreeZone 4.5 L Benchtop Freeze-Dry System) for 16 hours.

### 3.3.3 Characterization of the MACD photoblinking

To characterize the photoblinking properties of MACDs, a low concentration solution (0.5  $\mu\text{g}$  MACD/mL, to avoid having multiple particles in a single imaging pixel) was used to achieve uniform dispersion of particles onto a clean #1.5 coverslip. The exposure experiments and SRLM were performed with a home-built single-molecule fluorescence imaging system based on an Olympus IX71 microscope. High-power solid-state laser sources ( $> 0.1 \text{ kW/cm}^2$ ) were used to excite MACDs at different wavelengths (405 nm, 488 nm, 542 nm, 642 nm). The emitted fluorescence was collected with a 100 $\times$  oil immersion objective (NA = 1.4) and imaged with an EMCCD camera (Andor iXon 897). The raw images were stored as 16-bit 512 $\times$ 512 files (pixel size 160 nm). In general, a 600 s time series was taken at the frame rate of 25 fps. The photoblinking of MACDs became stable after 200 s excitation, and so the subsequent 400 s data was used in post-processing. From such series of exposures, the duty cycle of a single particle was determined as the proportion of image frames with fluorescence emission events. The SNR was defined as the ratio of the mean emission intensity of single MACD to the background fluctuation:

$$\text{SNR} = \frac{I_s - I_b}{\sigma_b}$$

, where  $I_s$  is the emission intensity of single MACD,  $I_b$  is the mean intensity of background,  $\sigma_b$  is the standard deviation/fluctuation of background.  $I_b$  and  $\sigma_b$  were obtained from pixel traces without MACDs and  $I_s$  of MACD emission events was defined as five times the  $\sigma_b$  value over the  $I_b$  value in pixel traces with MACDs. Post-processing was conducted with MATLAB and OriginPro software. All imaging buffers were freshly prepared before each experiment. The GLOX solution contained 50 mM Tris (pH 8.0), 10 mM NaCl, 10% glucose, 560  $\mu\text{g/mL}$  glucose oxidase (Sigma, G2133), 34  $\mu\text{g/mL}$  catalase (Sigma, C3155), and 1% 2-mercaptoethanol.

### 3.3.4 Cell imaging and cytotoxicity analysis.

*Oncorhynchus mykiss* (rainbow trout) epithelial gill cells (ATCC, CRL-2523) were routinely cultured in Leibovitz's L-15 media supplemented with 10% FBS and 1% Penicillin-Streptomycin. Cells were grown at 19°C in ambient atmosphere. Before imaging, cells were incubated with 5 µg/mL MACDs for 2 h. Prior to live-cell imaging, culture media was replaced with phenol-red free imaging solution (Thermo Fisher Scientific, A14291DJ). In SRLM, a Gaussian mask function based single-molecule localization algorithm was used, for which a detailed description can be found in our previous studies.<sup>81, 82</sup> In brief, image stacks were taken under 542 nm excitation (50-100 W/cm<sup>2</sup>) and 25 Hz (8,000-10,000 frames). Raw images were first smoothed with a LoG filter, followed by identification of local maxima. Based on the local maxima, fluorescence emission was determined while a blinking event was defined as the signal above a threshold of five times the standard deviation of the background fluctuation. The localization error was calculated according to the equation:

$$\langle (\Delta x)^2 \rangle = \frac{s^2 + a^2 / 12}{N} + \frac{8\pi s^4 b^2}{a^2 N^2},$$

where  $s$  is the standard deviation of the Gaussian PSF,  $a$  is the pixel size,  $b$  is the background noise, and  $N$  is the collected photons.<sup>68</sup> For MACDs under 520-560 nm excitation, the localization error was determined to be ~15 nm and the resolution of reconstructed images was set to 30 nm. The intracellular localization experiments were performed on a Zeiss LSM 710 confocal system and using MitoTracker Deep Red (Thermo Fisher Scientific, M22426).

**Table 3.1.** Oligonucleotide sequences used as probes for p53 smFISH. Each probe was labeled with Alexa647.

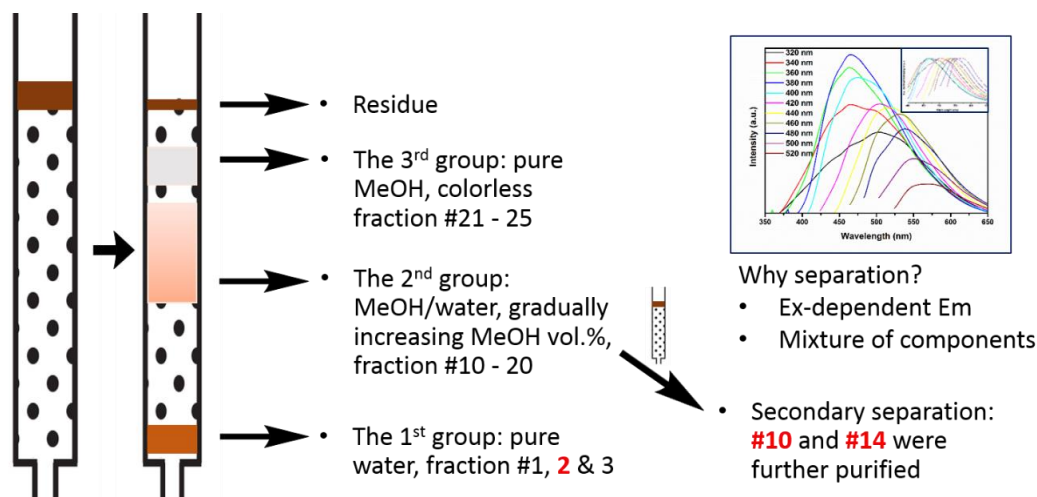
---

CCTCCTTCATAGCACGTTTG  
ACTTGGTCTTCTTACTGGCC  
TTCATCGTCACTCACAGCA  
CCTCGAATCTGAAGAGTGTA  
TCACTCAGTTCAAGACTGTC  
ATTTGTCAGCGTCGGCAACA  
TTGGTGAGGCATTTCTGACG  
CTTCACCAGTAGTTTCTTCC  
TCAGTCAGAGTCGCTCTTCT  
ATGGAACCGAATCTCGCTCT  
GTGTCATGGCTTGCTGAAAT  
CTACCGGTTTCCA ACTATAG

---

Upon different treatment conditions, the cell viability was determined with the MTS proliferation assay (Promega, G3580). smFISH was used to evaluate the impact of MACDs and CdSe quantum dots to the expression level of p53 gene. In brief, 80-90% confluent cells were exposed to 5  $\mu\text{g/mL}$  MACDs for 24 h, followed by fixation with 4% paraformaldehyde and permeabilization with 70% ethanol. The hybridization step was performed with 5 nM oligonucleotide probes, 10% dextran sulfate, 10% formamide, and  $2\times$  SSC at  $37^\circ\text{C}$  overnight. The cell nuclei were counterstained with DAPI. For each field of view, a z-stack spanning 7-10  $\mu\text{m}$  was taken and the location of each transcript was identified by maximum intensity projection. The quantification of RNA copies in each single cell was performed with customized MATLAB scripts. The sequence information of the FISH probes is provided in Table 3.1.

### 3.3.5 MACD separation by $\text{C}_{18}$ reversed phase silica gel column chromatography



**Scheme 3.1.** The general set-up and process of the MACD separation by C<sub>18</sub> reverse-phased silica gel column chromatography. The inset fluorescence spectra show the remarkable excitation-dependent emission of as-synthesized MACDs before separation.

As demonstrated by Scheme 3.1, 1 mL of highly concentrated carbon dots solution (200 mg/mL) was prepared for column chromatography. During the separation process, the fluorescence of each fraction was examined by a portable UV lamp (365 nm). Pure water was used as the first mobile phase until the blue fractions of carbon dots had completely eluted. Then, the MeOH/water mixture was used as the second mobile phase with the MeOH ratio gradually increasing until pure MeOH was used as the final mobile phase (volume ratio of MeOH/water starts from: 1:9, MeOH% was added by 20% per 30 mL). In this way, twenty-four MACD fractions were obtained after the first round of separation. A subset of these fractions still exhibited excitation-dependent emission. So, to further separate fraction #10 and #14, we applied the identical method once more. These twice purified fractions were dried by rotovap into powder form for further experiments.

### 3.3.6 Material characterization of MACDs

The PSD of carbon dots was determined by TEM (FEI Tecnai G<sup>2</sup> F30 TEM at 300 kV) and DLS (Microtrac NANO-flex<sup>®</sup> 180° DLS System). UV-vis extinction spectra were obtained using a Mikropack DH-2000 UV-Vis-NIR spectrometer. Fluorescence spectra and EEMs were measured with a PTI QuantaMaster<sup>™</sup> 400, equipped with a PicoMaster TCSPC steady-state and fluorescence lifetime spectrometer for lifetime analysis. ATR-FTIR were obtained using a Thermo Scientific Nicolet iS5 Fourier Transform Infrared Spectrometer with an iD5 Attenuated Total Reflectance attachment. Spectra were obtained with 64 scans using 0.8 cm<sup>-1</sup> resolution and a diamond crystal stage. X-ray photoelectron spectra of MACDs were obtained using a PHI 5600 instrument equipped with a Mg K $\alpha$  flood source (1253.6 eV) and a hemispherical energy analyzer. Survey scans were taken at a pass energy of 187.85 eV with a 1.6 eV/step size and 10 sweeps. High resolution multiplex scans of C (1s), O (1s), and N (1s) regions were taken at a source power of 300 W, with a pass energy of 5.85 eV, 0.025 eV/step, and 50 sweeps. All XPS data were analyzed using CASA XPS software. First, MACDs were suspended in water and subsequently centrifuged to remove silica. The supernatant was then separated and lyophilized to recover the MACDs. This significantly reduced the level of Si contamination. MACDs were attached as a powder to double sided copper adhesive tape which was attached to an XPS sample stage. Due to the smaller amount of available sample (<20 mg), MACD fractions were dried after filtration onto aluminum foil which was then adhered to the sample stage with double sided copper adhesive tape. In these cases, a small aperture size was used for XPS analysis to avoid detecting background aluminum from the foil.

### 3.4 Results and discussion

#### 3.4.1 The photoblinking property of MACDs

At the single-particle level, the fluorescence on-off activity of MACDs was found to be stochastic and intermittent. As shown in Figure 3.1a, the bright spots (MACDs in the on-state) were randomly distributed at different time points throughout the imaging session. In the time domain, the fluorescence trace of single MACDs further validates the stochastic nature of MACD emission (Figure 3.1b). The photon burst of single MACDs occurs on the ms-level timescale, facilitating clear identification of each emission event. Under green laser excitation, the on-time of MACD photon burst is highly uniform where over 95% of blinking events occur within 200 ms and ~75% of events occur within 100 ms (Figure 3.1c). The average duty cycle of the MACDs was determined to be 0.53% (Figure 3.1d), consistent with a previous report.<sup>31</sup> Moreover, MACDs exhibited excellent photostability, as more than 60% of the particles were still fluorescent after 400 s of high-power excitation ( $> 0.5 \text{ kW/cm}^2$ ) (Figure 3.1e). This set of results demonstrates the active photoblinking of the as-made MACDs and quantitatively characterizes their low duty-cycle and superior photostability, identifying them as promising materials for super-resolution localization microscopy.

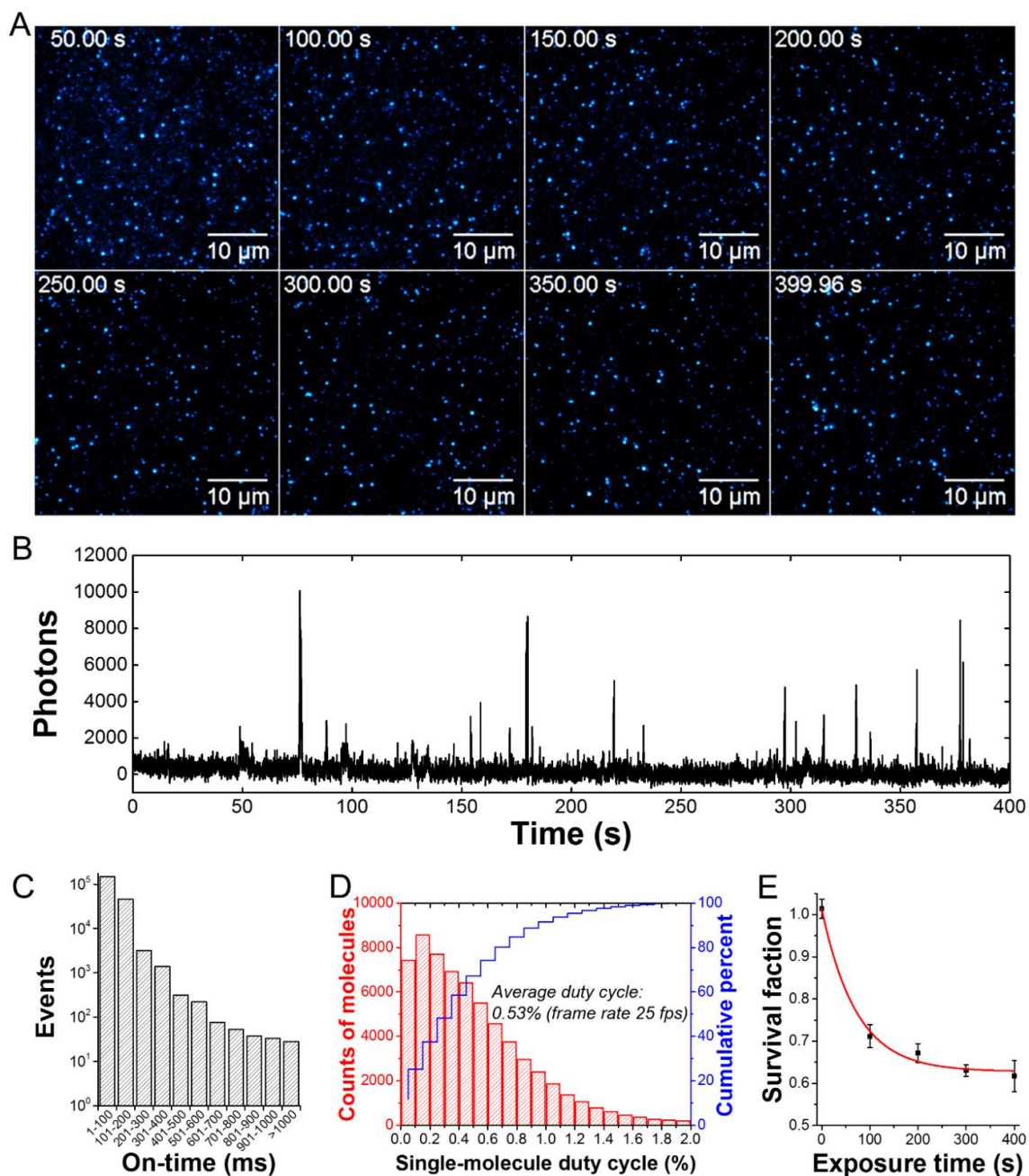


**Figure 3.1.** Characterization of individual MACDs. (a) Time-lapse fluorescence imaging of MACDs on glass coverslip shows stochastic on and off fluorescence emission. (b) A representative fluorescence trace of an individual MACD. (c) Histogram of MACD on-time distribution. (d) The average duty cycle of MACDs, determined by summarizing a large number of single-particle blinking traces (>5,000 particle traces). (e) Characterization of fluorescence emission over 400 s green excitation shows the survival fraction of MACD particles (error bars indicate the standard deviation of five independent replicates).

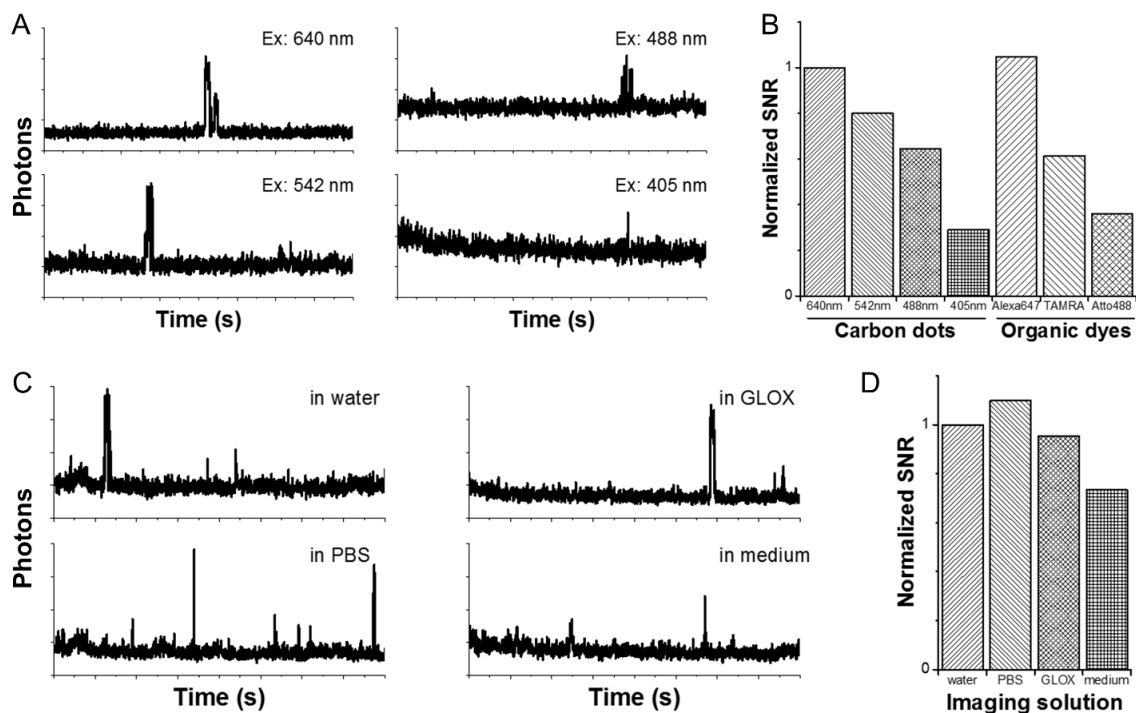


**Figure 3.2.** Characterization of the MACD SNR under different conditions. (a) Representative emission traces of MACDs in response to different excitation wavelengths. (b) SNR of MACDs under different excitation wavelengths in comparison with commonly used organic dyes under their optimal excitation wavelengths. (c) Characterization of MACD photoblinking in a variety of imaging solutions. (d) Comparison of MACD SNRs in different imaging solutions.

To better utilize MACDs as a novel class of imaging materials, we determined the SNR of MACDs under different conditions. First, we found that the original MACD samples responded to a broad range of excitation wavelengths, under which active photoblinking was universally observed (Figure 3.2a). Interestingly, a comparison of images taken from different emission channels (*e.g.*, the green and red channels) showed that the so-called “excitation wavelength-dependent” emission was not observed for individual MACDs, but originated from different particles, each emitting at a different excitation wavelength. Considering our synthesis strategy, the as-synthesized MACDs were a relatively complex mixture composed of non-uniformly sized MACD particles.<sup>22, 60, 65</sup> The single-particle

SNR values of these different components display a trend with higher values at the red-excitation wavelength (“red particles”) and lower values at the blue excitation wavelength (“blue particles”) (Figure 3.2b). Further, the SNR of MACDs with specific excitation wavelengths was compared with those of commonly used organic dyes in SRLM, such as Atto488 and TAMRA. The results demonstrate that MACDs have comparable, if not better, SNR over its counterparts in the chosen emission ranges (Figure 3.2b). The SNR of MACDs is slightly inferior to Alexa647 in the far-red emission range, which might be due to the low yield of red-emission MACDs and crosstalk emission from other MACD components. In addition, we measured the photoblinking SNR of MACDs within different imaging solutions at the single-particle level. In conventional SRLM, a special buffer (*e.g.*, GLOX) is often required to reduce the dissolved oxygen level and stabilize the excited electrons at the triplet state for a long dark-state time. In contrast, the MACD’s photoblinking was observed ubiquitously in a variety of imaging solutions (Figure 3.2c), indicating a unique photoblinking mechanism, different from commonly used organic dyes. Although the SNR of MACDs was negatively impacted by the complexity of the solution (a low value obtained from cell culture medium, Figure 3.2d), a sufficient SNR value (>15) could be achieved in all the tested solutions, making it possible to apply MACDs in various imaging environments, including live-cell imaging.

#### 3.4.2 Application of MACDs in super-resolution localization imaging

The MACD’s photoblinking properties (low duty cycle, high photostability, and buffer-independent blinking) make them an excellent candidate for biological imaging. In light of these findings, the biocompatibility of MACDs was examined in a rainbow trout gill

epithelial cell line. Cell viability was impacted only at a relatively high MACD dose (5 mg/mL), where an approximate 20% decrease in cell viability was detected 24 h post exposure, probably due to the impact of the overload of MACDs on cell proliferation through interaction with microtubules. In addition, smFISH was used to quantify gene expression at the single cell level, as particle uptake can be highly variable between cells, and substantial changes can occur at low uptake before irreversible cell death takes place.<sup>66</sup> In this set of experiments, we quantified mRNA copies of the stress-sensing protein p53 in response to MACDs as well as commercially available CdSe QDs for comparison. After exposure to 5  $\mu\text{g/mL}$  MACDs or QDs for 24 h, the gene expression level of p53 in the gill cells showed detectable increase compared to the control group. However, the expression level of p53 in cells exposed to MACDs was lower than the expression levels in cells exposed to CdSe QDs (~30% less in copy number per cell). Hence, MACDs exhibit an overall satisfactory biocompatibility and are a promising alternative to Cd-based QDs for bio-imaging experiments.

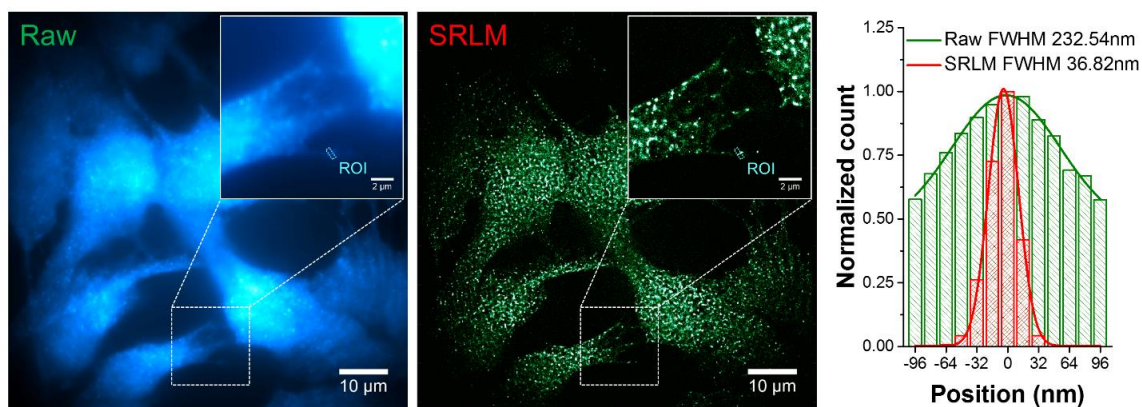


**Figure 3.3.** SRLM of MACDs in fixed trout epithelial gill cells. The spontaneous photoblinking of MACDs enables a significant improvement of the spatial resolution as demonstrated by the fluorescence emission profiles (right panel) of the region of interest (ROI) marked by the small rectangle in the fluorescence images.

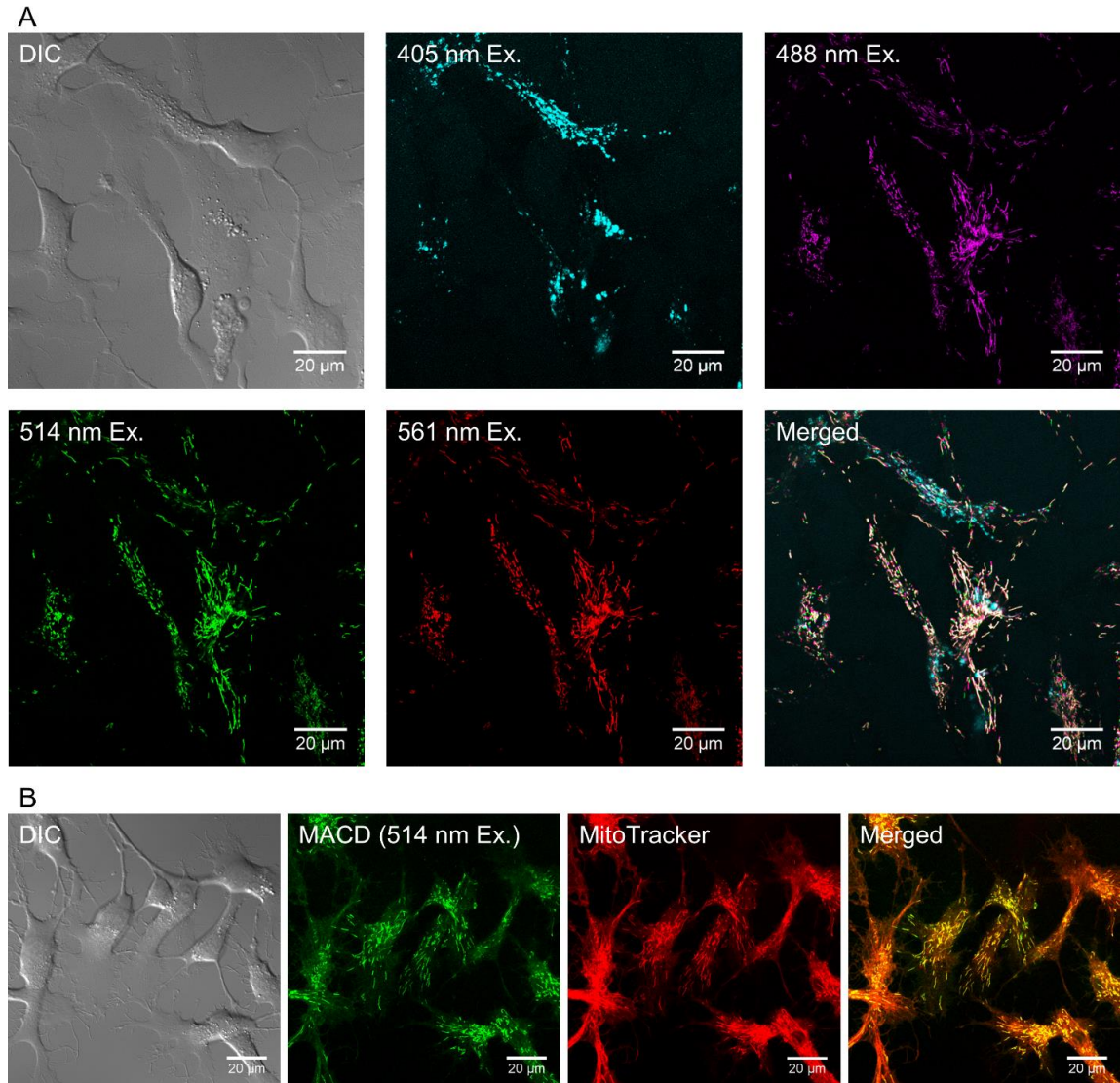


**Figure 3.4.** Distribution of MACDs in live trout gill epithelial cells. (a) MACDs with different sizes, corresponding to excitation wavelengths 488 nm, 514 nm and 561 nm, were found to localize at the same intracellular compartments, while MACDs that were excited with 405 nm were found to localize at different compartments. (b) The green-to-yellow MACDs (with excitation wavelength  $\geq 488$  nm), were found to be present mainly in mitochondria, as determined by their co-localization with MitoTracker.

According to the Nyquist-Shannon theorem,<sup>67</sup> the low on-off duty cycle of MACDs makes it possible to identify  $\sim 200$  particles within a diffraction limited area ( $\sim 250$  nm). However, the spatial resolution is also constrained by localization error. Based on the Gaussian

PSF,<sup>68</sup> the standard error of localization using MACDs was determined to be ~15 nm in cultured cells. Hence, the theoretical imaging resolution using green-to-yellow MACDs could reach 30 nm. SRLM was then performed both in fixed and live cells. As we demonstrate in fixed gill cells, the active photoblinking of MACDs enables a higher resolution imaging of the particles in the intracellular environment. As shown in Figure 3.3, an object with an apparent size of over 230 nm in the raw wide-field image was revealed to be around 36 nm by SRLM.

Because MACDs show sufficient blinking activity in different solutions and do not require a special buffer, the uptake and MACDs internalization by live gill cells could be imaged with SRLM as well. We observed a highly efficient uptake of MACDs by live cells. Interestingly, the as-synthesized MACDs exhibited two distinct intracellular distribution patterns under different excitation wavelengths. The green-to-yellow MACDs (Figure 3.4a, representative excitation by 488 nm, 514 nm and 561 nm) show a unique, filament-like distribution inside live cells, which is different than the distribution of blue-to-cyan MACDs (Figure 3.4a, representative excitation by 405 nm), as well as to the distribution of MACDs in fixed cells (Figure 3.3). To minimize phototoxicity to living cells and pave the way for future applications, we focused the subsequent live-cell imaging on the green-to-yellow MACDs. The diameter of these MACD-associated structures is no more than 100 nm. The improved spatial resolution also helps to distinguish closely aligned structures within a diffraction-limited area. After testing a number of organelle-specific dyes, the side-by-side comparison of live cells exposed to MACDs and MitoTracker showed a clear co-localization pattern that indicates the accumulation of MACDs in or on

mitochondria (Figure 3.4). Moreover, we observed directional movement of the MACD-associated mitochondria in live cells, suggesting the transport of mitochondria-associated MACDs along the cytoskeleton (*e.g.*, microtubules).<sup>69, 70</sup> These results prompt the idea that this class of MACDs could be further explored as an efficient live-cell delivery vector and mitochondria-targeting tool without further nanoparticle surface modification.

### 3.4.3 MACD separation and characterization of MACD fractions

As observed in previous experiments when we tried to determine the SNR values of as-synthesized MACDs, the fluorescence emission of individual MACD particles was found to be invariant as the excitation wavelength was changed. Carbon dots are often acclaimed for their so called “excitation-dependent emission”, so this unexpected phenomenon motivated us to separate the as-synthesized MACDs into distinct fluorescent components. To combine the advantages of the traditional silica gel column chromatography and RP-HPLC as mentioned before, we employed C<sub>18</sub> reversed phase column chromatography, as shown in Scheme 3.1. The general set-up is quite similar to that of a traditional silica gel column, but we utilized C<sub>18</sub> reversed phase silica gel as the stationary phase and a mixture of water and methanol as the mobile phase. The entire separation process was accomplished in less than three hours, a significant time-savings compared to the traditional silica column chromatography that took more than ten hours.<sup>52</sup> Besides, by virtue of the large sample loading capacity, we were able to separate at least 200 mg of as-synthesized MACDs in one single batch. As such, the output of each fraction was up to 5 mg, higher than HPLC separation yield (a few microliter, quantities of which are too small for characterization).<sup>59</sup> Taking advantage of this time-saving and higher throughput

separation method, we obtained twenty-four MACD fractions and three of them (i.e., fraction #2, #10, and #14) were chosen for further analysis because they were collected from three distinctive color regions visible following column chromatography. Also, their concentrations were high enough to give off bright fluorescence under 365 nm UV lamp, representing the most promising fluorescence properties among the 24 fractions.

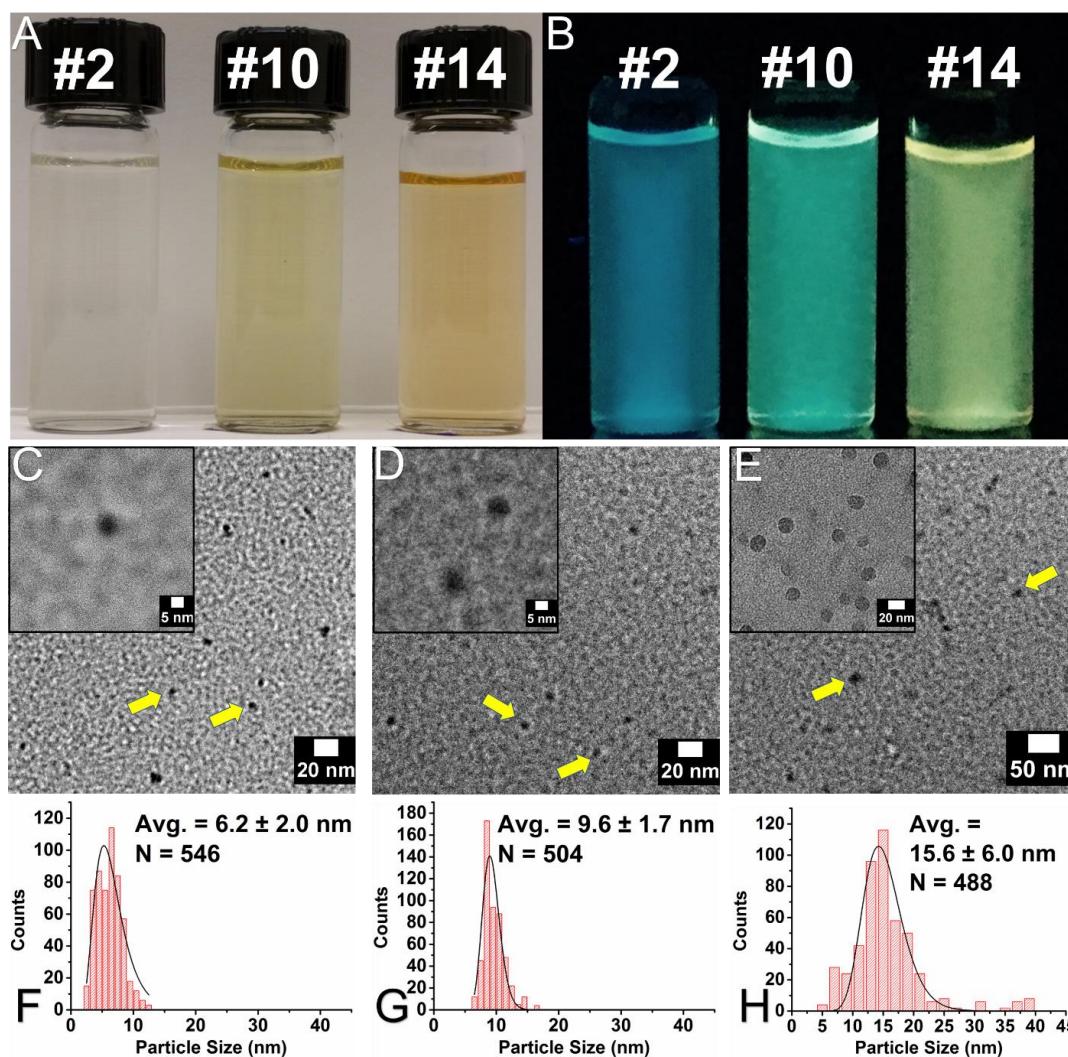


**Figure 3.5.** Photographic images of MACD fractions #2, #10, and #14 under (a) room light condition and (b) 365 nm UV illumination. TEM images of MACD fractions (c) #2, (d) #10, and (e) #14 (inset scale bar: 5nm, 5nm, and 20nm, respectively). Corresponding PSD for MACD fractions (f) #2, (g) #10, and (h) #14, determined by ImageJ analysis of TEM images.

As shown in Figure 3.5a, if exposed to room light, the aqueous solutions of these three fractions appear pale yellow, yellow, and brown, respectively. These same three fractions exposed to long-wavelength UV illumination (365 nm) fluoresced blue, cyan, and greenish yellow (Figure 3.5b). TEM was applied to probe the size and morphology of these three MACD fractions. In Figures 3.5c through e, these well-dispersed MACD fractions exhibit clear circular outlines without severe agglomeration. PSDs were obtained based on these TEM images (~500 particles counted). It was assumed that the sizes of each fraction were normally distributed, so the distribution histograms were fit with a log-normal function to estimate the mean size of each fraction, using the peak analyzer function in OriginPro 9.0. The results are displayed in Figures 3.5f through h, showing that MACD fraction #2 is  $\sim 6.2 \pm 2.0$  nm, #10 is  $\sim 9.2 \pm 1.7$  nm, and #14 is  $15.6 \pm 6.0$  nm. It is discernible that the log-normal peak is shifting to the right, indicating an increase in particle size. The PSDs of each fraction were also statistically analyzed using one-way ANOVA multi-comparison, processed by GraphPad Prism 6 (Figure 3.6), with significance level indicated by asterisks (\* $p < 0.05$ , \*\* $p < 0.01$ , \*\*\* $p < 0.001$  and \*\*\*\* $p < 0.0001$ ). Based on this analysis, the MACD fractions' PSDs were determined to be significantly different from one another. To confirm this finding, we used dynamic light scattering (DLS) to analyze the size of the MACDs in each fraction in aqueous suspension. As shown in Figure 3.7, the change in the PSDs between the three fractions are clear in the DLS data and are in agreement with the TEM results. We are therefore confident that the size of the MACD fractions is increasing when we gradually lowered

the water percentage, that is, decreased the polarity of mobile phase, in the C<sub>18</sub> reversed phase column chromatography.

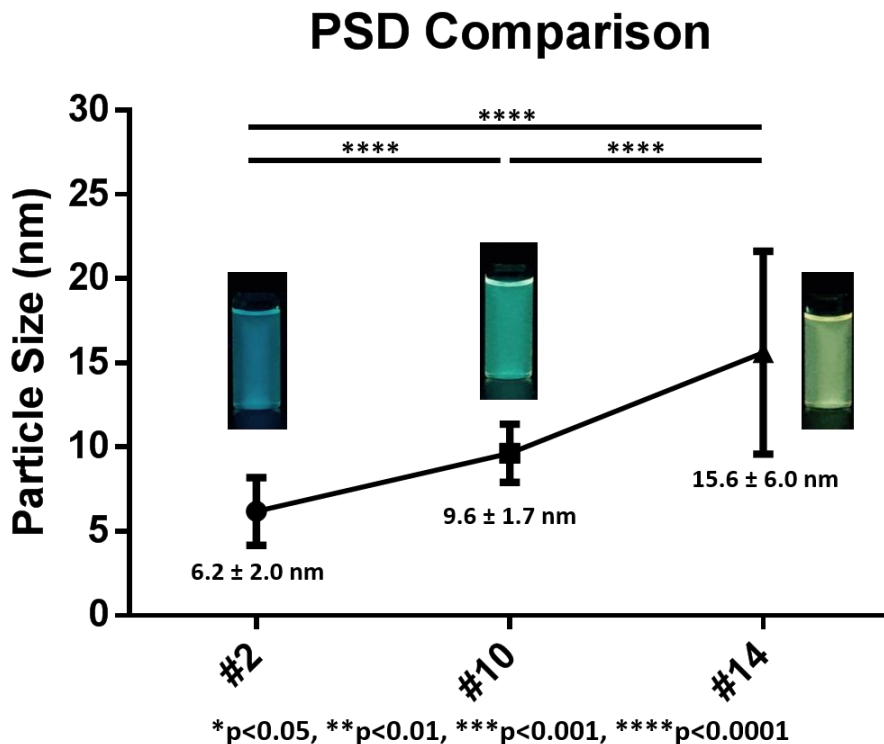


**Figure 3.6.** Significance test of the MACD fraction TEM PSDs.

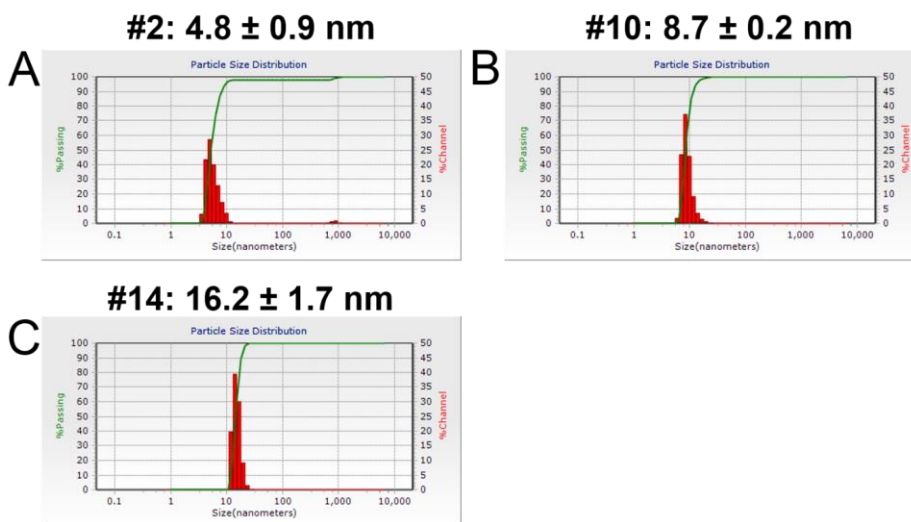


**Figure 3.7.** MACD fraction DLS: PSD of fraction (A) #2, (B) #10, and (C) #14.

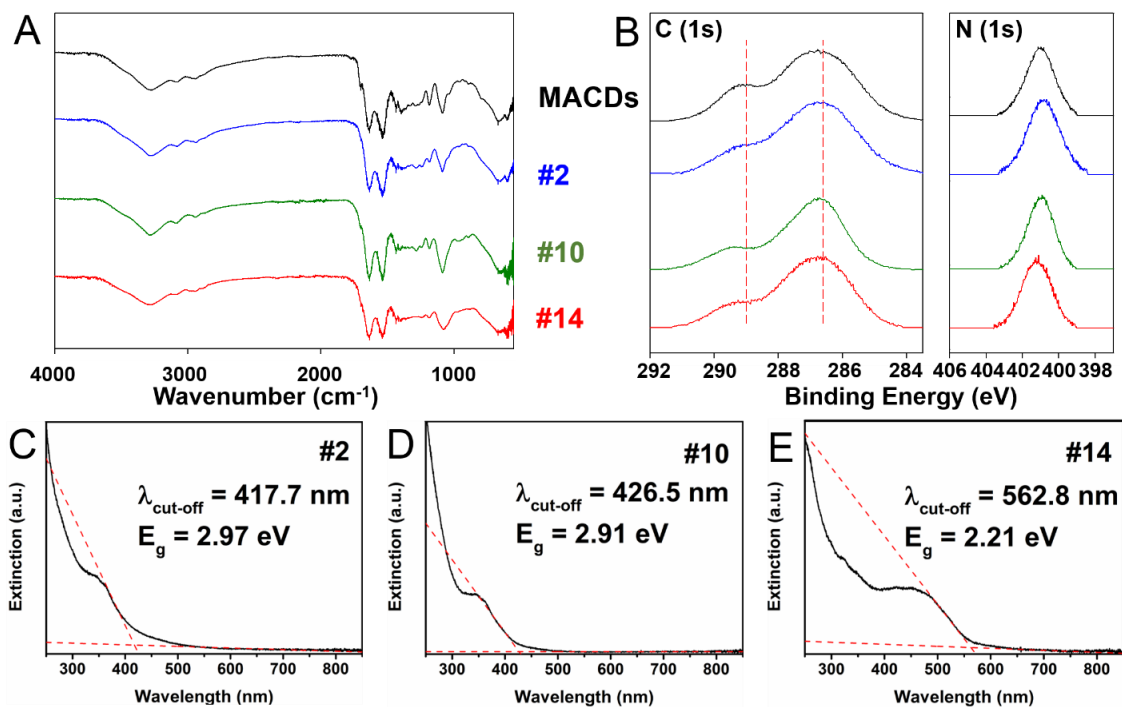


**Figure 3.8.** (a) FTIR and (b) XPS spectra of unseparated MACDs (black) and MACD fraction #2 (red), #10 (green), and #14 (blue). UV-vis extinction spectra of MACD fraction: (C) #2, (D) #10, and (E) #14.

To assess the chemical composition of the three MACD fractions, we employed ATR-FTIR and XPS. IR analysis of the as-synthesized MACDs and each of the fractions are shown in Figure 3.8a. Each CD exhibits an infrared spectrum characteristic of malic acid carbon dots. N-H, O-H, and C-H stretching bands are observed at 3280, 3080, and 2950 cm<sup>-1</sup>, respectively.<sup>71</sup> Peaks at 1702 and 1640 cm<sup>-1</sup> indicate C=O stretching modes,<sup>72</sup> with characteristic N-H bending and C-O stretching modes observed at 1540 and 1090 cm<sup>-1</sup>, respectively.<sup>71</sup> Moreover, the relative intensity of these various peaks in the ATR-FTIR are observed to be virtually identical amongst each of the three fractions, suggesting that the chemical bonding remains constant. XPS analysis of MACD parent batch and fractions revealed the presence of C, N, and O in all samples (Figure 3.8b). Si contamination was observed in some samples, which can reasonably be assumed to have been introduced

when the CD fractions were scraped off from the sides of glassware during synthesis, and for this reason the O (1s) regions are not shown. The C (1s) regions for the parent MACD and each one of the three CD fractions were found to be qualitatively similar, consisting of a broad peak at 286.7 eV, composed of contributions from C-C/C=C/C=O and C-N species as well as a lower intensity (roughly half) peak at 289.2 eV associated with O-C=O species.<sup>73, 74</sup> Component fitting of the C (1s) region was not deemed appropriate due to the multiple carbon bonding environments present in the C (1s) envelope. The N (1s) region of the parent MACD and each one of the three CD fractions is characterized by a single broad peak at  $\approx 401$  eV in all samples. The broad similarities observed for both the ATR-FTIR and XPS of the three fractions indicates that there are no significant differences in the nature or relative concentration of chemical functionality amongst the three MACD fractions.

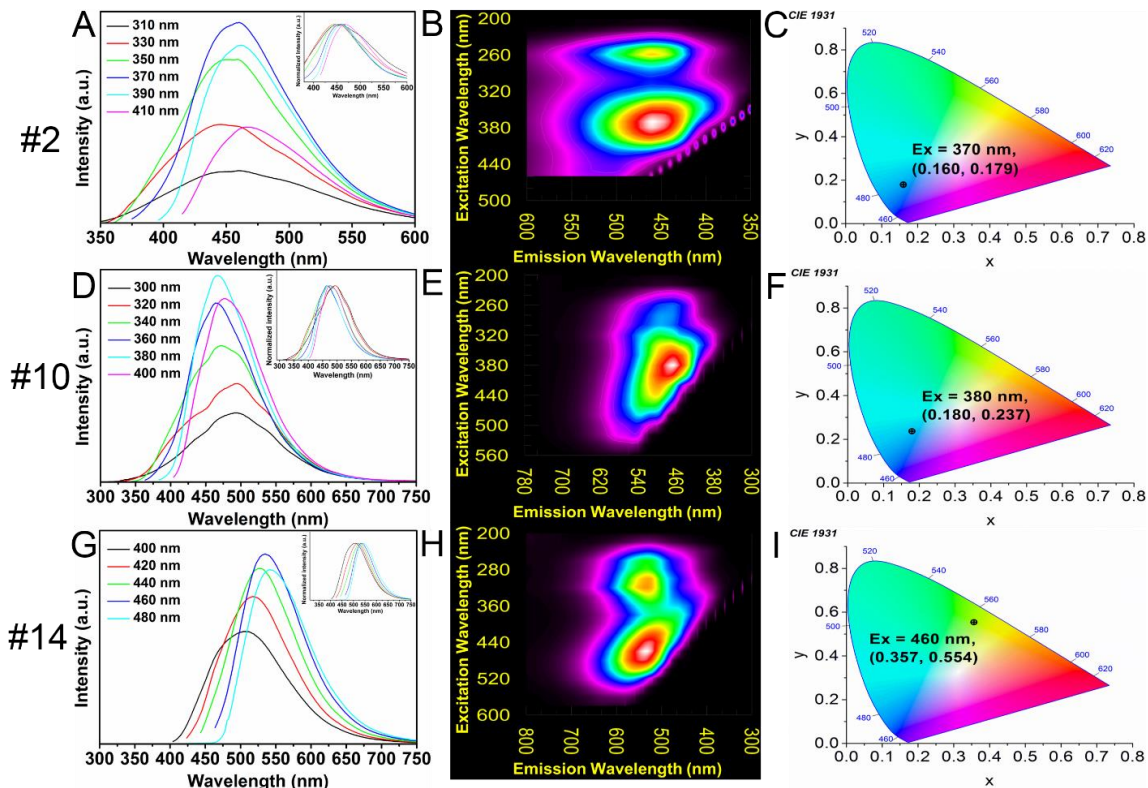


**Figure 3.9.** Fluorescence properties of MACD fractions. Upper panel, fraction #2: (A) fluorescence emission under varied excitation, with normalized spectrum embedded, (B) 2D EEM, and (C) CIE 1931 color coordinates; middle panel, fraction #10: (D) fluorescence emission under varied excitation, with normalized spectrum embedded, (E) 2D EEM, and (F) CIE 1931 color coordinates; lower panel, fraction #14: (G) fluorescence emission under varied excitation, with normalized spectrum embedded, (H) 2D EEM, and (I) CIE 1931 color coordinates.

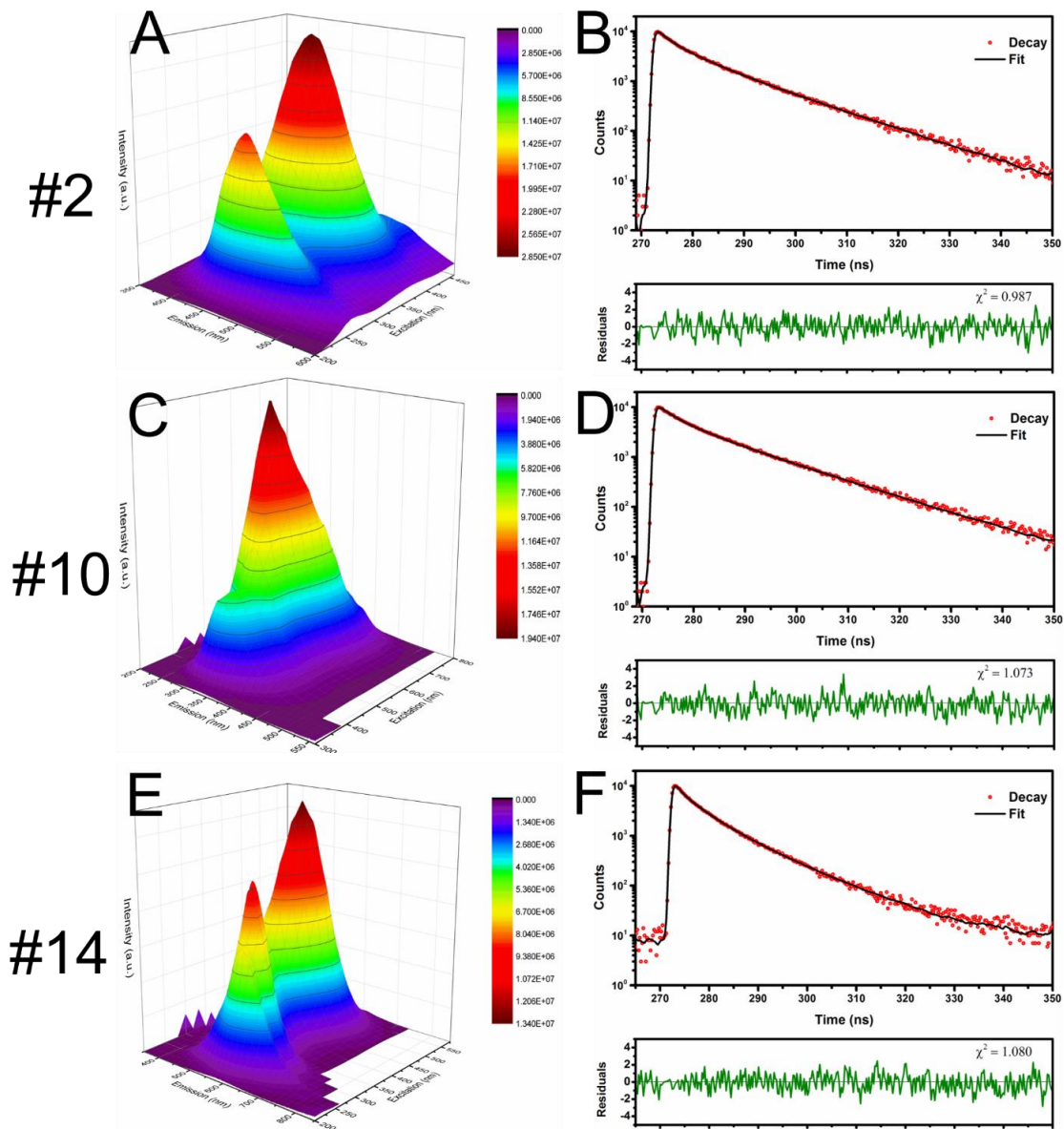
#### 3.4.4 Optical properties of MACD fractions

Figure 3.8c through e exhibits the UV-Vis extinction spectra of all separated MACD fractions. Both fractions #2 and #10 exhibit intense extinction features around 350 nm, usually assigned to  $n-\pi^*$  transitions for nitrogen-doped CDs.<sup>72</sup> Interestingly, a well-resolved extinction shoulder is observed at  $\sim 470$  nm in fraction #14. Such a red-shift is typically related to the narrowing of the electronic band gap and is often found for long wavelength emissive CDs.<sup>61, 72</sup> To confirm this, we calculated the optical band gap energy

( $E_g$ ) of the three fractions using the equation  $E_g = h*c/\lambda_{\text{cut-off}}$ , where  $h$  refers to the Plank constant ( $6.626 \times 10^{-34}$  Joules sec),  $c$  is the speed of light ( $3.0 \times 10^8$  meter/sec), and  $\lambda_{\text{cut-off}}$  (in  $\text{nm} \times 10^{-9}$  meters) indicates the onset value of the first excitonic absorption band, with the conversion factor of 1 eV equaling  $1.6 \times 10^{-19}$  Joules.<sup>75, 76</sup> The calculated  $E_g$  are 2.97 eV (#2), 2.91 eV (#10), and 2.21 eV (#14), respectively, along with the increasing fraction PSDs (namely,  $6.2 \pm 2.0$  nm,  $9.2 \pm 1.7$  nm, and  $15.6 \pm 6.0$  nm), which demonstrates how the PSD impacts the band gap energies of fractions. In addition, we systematically investigated the photoluminescent properties of MACD fractions, as illustrated by Figure 3.9 and 3.10. We excited fraction #2 with a series of wavelengths ranging from 310-410 nm in 20 nm increments. The resulting (normalized) fluorescence emission data is shown in Figure 3.9a. Compared to the spectra of crude MACDs (included in Scheme 3.1),<sup>22</sup> there is no remarkable shift in the emission peak position, which is around 460 nm. The maximum emission intensity was observed at  $\lambda_{\text{ex}} = 370$  nm, with a FWHM of 96 nm. A prominent luminescence center can be observed at *c.a.* (371.3 nm, 458.7 nm) in the 2D EEM (Figure 3.9b) and 3D EEM (Figure 3.10a), with a Stokes shift as large as  $16,822 \text{ cm}^{-1}$ . The corresponding color coordinates (under 370 nm excitation) were calculated to be (0.160, 0.179), located within the blue region of the CIE 1931 chromaticity diagram (Figure 3.9c). The QY of fraction #2 was measured to be as high as 30.0% using an integration sphere. For the analysis of the fluorescence lifetime, the fluorescence decay of MACD fraction #2 was fitted with multi-exponential function (Figure 3.10b) to minimize deviation from the exponential fit function. This fit was further examined by residual analysis. The reduced chi-square value ( $\chi^2$ ) of 0.987 is reasonable ( $0.9 < \chi^2 < 1.2$ ) and

residuals are distributed around zero almost symmetrically, indicative of a justifiable fitting.<sup>77,78</sup> Thus, the average fluorescence lifetime was extrapolated to be  $6.48 \pm 0.10$  ns, comparable to commercially available fluorophores (*e.g.* fluorescein and rhodamine).<sup>79</sup> The fluorescence properties of MACD fractions #10 and #14 were investigated in a similar manner. For fraction #10, the emission peak can be found at  $\sim 470$  nm, achieving maximum intensity if excited by 380 nm (Figure 3.9d, peak width at half max  $\sim 100$  nm), leading to a bright fluorescence center at *c.a.* (380.3 nm, 468.3 nm) in EEM (Figure 3.9e and 3.10c) and a Stokes shift of  $4959 \text{ cm}^{-1}$ . The CIE 1931 coordinates of (0.180, 0.237) achieve a position in the cyan region of the color space (Figure 3.9f). The QY is determined to be 24.0%, with a lifetime of  $7.14 \pm 0.63$  ns (Figure 3.10d). For fraction #14, the excitation-independent emission peak can be identified at 550 nm with a FWHM of *c.a.* 104 nm under excitation of 460 nm (Figure 3.9g). Thus, a global photoluminescence center can be observed about (460.0 nm, 523.7 nm) (Figure 3.9h and Figure 3.10e). Accordingly, the Stokes shift decreased to  $2644.3 \text{ cm}^{-1}$ . The color of MACD fraction #14 can be defined as greenish yellow (0.357, 0.554) by CIE 1931 colorimetry (Figure 3.9i). Correspondingly, the calculated QY is 27.6%, and the average lifetime is  $4.25 \pm 0.09$  ns (Figure 3.10f). So, MACD fractions don't exhibit wavelength-dependent emission, in contrast to unseparated MACDs.<sup>22</sup> This fraction is particularly important because it represents a carbon dot population that can be used with visible, rather than UV, excitation. It is noteworthy to mention that along with the increasing PSD, the corresponding emission of MACD fractions is red-shifted from blue, to cyan, and to greenish yellow,

indicating that the as-prepared MACD fluorescence properties are size-dependent, consistent with other published studies.<sup>19, 60, 80</sup>



**Figure 3.10.** Upper panel: (A) 3D EEM and (B) fluorescence decay traces of MACD fraction #2; middle panel: (C) 3D EEM and (D) fluorescence decay traces of MACD fraction #10; lower panel: (E) 3D EEM and (F) fluorescence decay traces of MACD fraction #14.

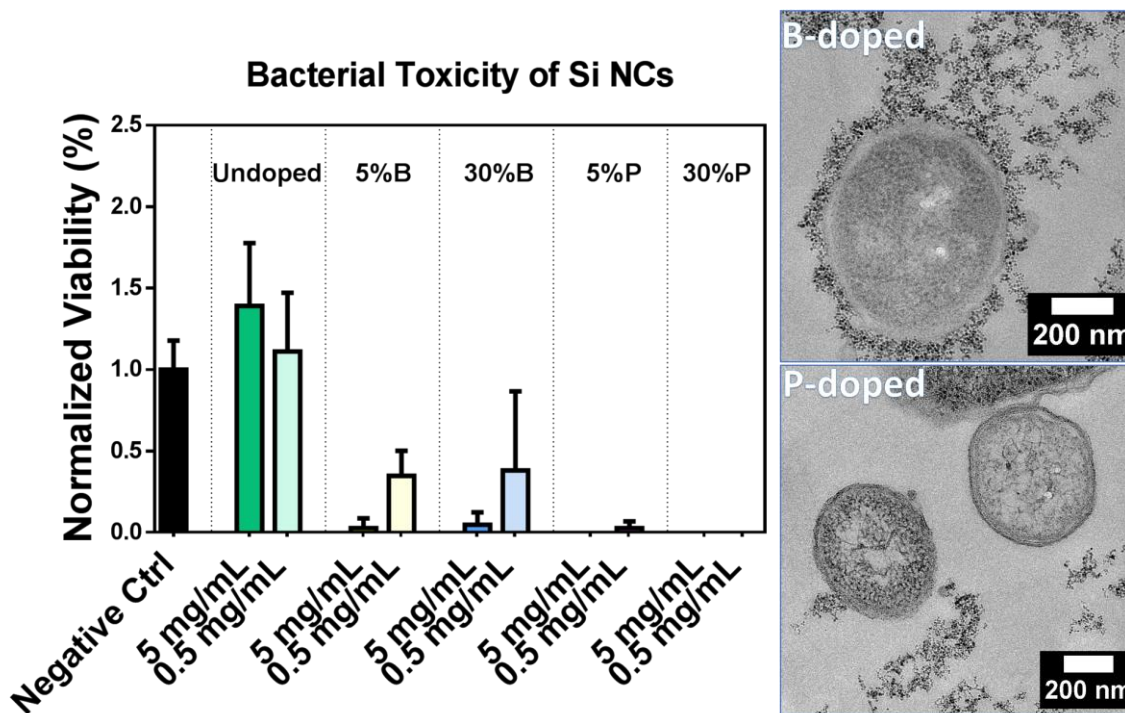
### 3.5 Conclusions

In summary, the as-synthesized MACDs are found to be actively photoswitchable, characterized by low duty cycle and excellent photostability. Furthermore, MACDs exhibited satisfying signal-to-noise ratios in different imaging buffer solutions. Due to these unique and superior photoblinking properties, MACDs are shown to exhibit enhanced spatial resolution in super-resolution localization imaging experiments. To investigate the fluorescent components within as-synthesized MACDs, we developed an efficient separation method using C<sub>18</sub> reversed phase silica gel column chromatography. This approach enables us to achieve a high product output, as can be achieved with traditional silica gel column chromatography, on a time scale commensurate with HPLC. The MACD fractions showed distinct PSDs, determined by both TEM and DLS, despite having indistinguishable chemical composition. Interestingly, the optical band gap energies of MACD fractions were found to decrease with the increasing PSD, and the fluorescence of fractions are not excitation dependent but PSD related, red-shifting from blue to cyan to yellowish green as the PSDs increase from  $6.2 \pm 2.0$  nm to  $9.2 \pm 1.7$  nm to  $15.6 \pm 6.0$  nm.

## Chapter 4

Toxicity evaluation of boron- and phosphorous- doped silicon nanocrystals towards

*Shewanella oneidensis* MR-1



Reprinted from: Zhi, B.; Mishra, S.; Hudson-Smith, N. V.; Kortshagen, U. R.; Haynes, C. L., Toxicity Evaluation of Boron- and Phosphorus- Doped Silicon Nanocrystals s towards *Shewanella oneidensis* MR-1. *ACS Applied Nano Materials* 2018, 1, 4884-4893. Copyright 2018, with permission from the American Chemical Society.

Bo Zhi is responsible for the design of this research as well as the materials characterization work and the drafting of manuscript.

## 4.1 Overview

Si NCs, also known as Si quantum dots, are regarded as green alternatives to traditional quantum dots composed of heavy metal elements. While it is well-known that the semiconductor properties of these materials can be tuned by doping with *p*-/*n*- type dopants (*i.e.*, boron and phosphorous), there is lack of systematic understanding of their potential environmental impact if released into the ecosystem. Here, we demonstrate that introduction of dopants, especially phosphorus, cause doped Si NCs to produce ROS, resulting in significant toxicity to a model microorganism, *S. oneidensis* MR-1. In addition, the interaction between bacteria cells and Si NCs was investigated using dark field microscopy and bio-TEM. Interestingly, boron-doped Si NCs tended to attach to the cell surface while this phenomenon was not observed for undoped or phosphorous-doped Si NCs.

## 4.2 Introduction

First discovered in the 1980s, semiconductor nanocrystal QDs, exhibit unique tunable luminescent properties due to quantum confinement effects.<sup>1,2</sup> Other features, such as a broad absorption range, high molar extinction coefficients, high QY, and satisfying photostability, render colloidal QDs competitive alternatives to organic dyes in applications ranging from electronic displays to biomedical research.<sup>3-8</sup> However, the rapid growth of consumer products that make use of QDs, especially group II-VI QDs like CdSe- or PbS-based QDs, has aroused safety concerns regarding their environmental

impact as well as their adverse effects on human health, due to the release of potentially toxic degradation products such as heavy metal ions (e.g.  $\text{Cd}^{2+}$  and  $\text{Pb}^{2+}$ ).<sup>9, 10</sup> To achieve maximal technological impact, QD synthesis should use green and cost-effective syntheses; however, QD precursors, such as cadmium acetylacetonate and bis(trimethylsilyl) sulfide, are known to be toxic or/and expensive, limiting their mass production and, as such, broad use in our daily life.<sup>11, 12</sup> In this context, it is desirable to find new materials that exhibit comparable luminescent performance but are suitable for large-scale synthesis in a sustainable manner.

In recent decades, group IV element (carbon, silicon, and germanium) based fluorescent materials have drawn great attention as they are conventionally considered non-toxic elements with minimal environmental impact.<sup>13-18</sup> Among this family, luminescent Si NCs, also known as Si QDs, are emerging as novel and eco-friendly semiconductor nanomaterials due to their promising optoelectronic properties, including size-tunable emission and acceptable QY, comparable to their metal based counterparts (e.g. CdSe, InAs, and PbS) that are regarded as potentially hazardous.<sup>19-26</sup> Especially, in recent years, the QY of Si NCs has been greatly improved, and in some cases, it can be as high as 90%.<sup>23, 27, 28</sup> There are a number of methods to prepare Si NCs, including, thermal annealing,<sup>29</sup> electrochemical etching,<sup>30</sup> laser ablation,<sup>31</sup> solution-phase reduction,<sup>32</sup> and thermolysis of silane.<sup>33</sup> Compared to products generated by other methods, Si NCs prepared by non-thermal plasma methods are characterized by solvent/ligand-free , narrow particle size distribution, and efficient inclusion of dopants into the NC structure.<sup>34,</sup>  
<sup>35</sup> By fine tuning the p/n-type doping level, the free carrier concentration of Si NCs is

controllable, facilitating adjustment of their LSPR performance, realizing a wide range of applications, including solar cells,<sup>36</sup> electronic devices,<sup>37, 38</sup> and light-emitting devices.<sup>39, 40</sup> Meanwhile, another consequence of p/n-type doping is the drop/rise of the Fermi level of doped Si NCs by introduction of free holes ( $h^+$ )/electrons ( $e^-$ ),<sup>35, 41</sup> which may lead to production of ROS either by oxidation of water ( $OH^- + h^+ \rightarrow \cdot OH$ )<sup>42</sup> or reduction of molecular oxygen ( $O_2 + e^- \rightarrow O_2^{\cdot -}$ )<sup>43, 44</sup>. The ROS accumulation is notoriously harmful to cell metabolism;<sup>45, 46</sup> as such, the release of doped Si NCs into the ecosystem may induce potential environmental contamination. Therefore, understanding the environmental fate of doped Si NCs can provide critical insights into the optimal use of these nanomaterials with minimized burden on the ecosystem and, perhaps, give some insight on appropriate doping schemes and levels during NC synthesis.

Herein, we report our investigation of the interaction of boron (p-type) and phosphorous (n-type) doped Si NCs with an environmentally beneficial bacterium, *S. oneidensis* MR-1.<sup>47</sup> Microorganisms, located at the bottom of the food web, serve as the foundation of the entire ecosystem.<sup>48</sup> As Gram-negative bacteria, *S. oneidensis* MR-1 are ubiquitous, able to survive in various environments, and capable of reducing metals in geochemical nutrient cycling.<sup>49</sup> Thereby, they represent excellent model microorganisms for environmental studies.<sup>16, 50, 51</sup> Our data demonstrate that doping boron or phosphorous into the Si NC structure did not induce discernible influence on particle size distribution and crystallinity but led to remarkable ROS generation, especially for P-doped Si NCs. In correlated behavior, P-doped Si NCs exhibited significant toxicity towards *S. oneidensis* MR-1 while B-doped Si NCs only exhibited toxic effects during long-term (more than 2

hour) exposure, and undoped Si NCs exhibited no impact on bacterial growth. In addition, we utilized microscopy techniques (*i.e.*, dark-field microscopy and bio-TEM) to visualize the association between Si NCs (both undoped and doped) and *S. oneidensis* MR-1. Interestingly, B-doped Si NCs tended to attach to the bacteria cell closely while undoped Si NCs and P-doped Si NCs showed no such tendency.

### 4.3 Experimental

#### 4.3.1 Si NC synthesis

A non-thermal plasma process to produce undoped silicon, boron(B)-doped silicon, and phosphorus(P)-doped silicon nanocrystals has been described in previous work.<sup>33, 52, 53</sup> Specifically, silane (SiH<sub>4</sub>), was used to produce undoped Si NCs while diborane (B<sub>2</sub>H<sub>6</sub>) and phosphine (PH<sub>3</sub>), which are diluted in H<sub>2</sub> for safety reasons, are used with SiH<sub>4</sub> for production of doped Si NCs. The formed nanocrystals were deposited on a glass substrate directly as a powdered pile by impaction.<sup>54</sup> This is a gas phase production and required no post processing of NCs. The nanocrystals are dominantly hydrogen terminated due to the nature of the precursor, revealed by FTIR and previous studies.<sup>55, 56</sup> The precursor gas rates were adjusted to achieve nominal doping concentrations from lightly (~5%) to heavily (~30%) doped as defined by  $X_B = \{2[B_2H_6]/([SiH_4]+2[B_2H_6])\} \times 100\%$  and  $X_P = \{[PH_3]/([SiH_4]+[PH_3])\} \times 100\%$  where [SiH<sub>4</sub>], [B<sub>2</sub>H<sub>6</sub>] and [PH<sub>3</sub>] represents flow rates for SiH<sub>4</sub>, B<sub>2</sub>H<sub>6</sub> and PH<sub>3</sub> precursors. It is worthwhile to note that the doping levels quoted are the nominal values calculated from gas flow rates into the synthesis reactor. The actual incorporation of dopants into the Si NCs is lower, as is the actual activation of dopants.<sup>53,</sup>

<sup>55</sup> However, both boron-doped and phosphorous-doped Si NCs exhibit localized surface

plasmon resonances in the mid-infrared, indicating that free carrier concentrations are on the order of  $10^{20}$ - $10^{21}$   $\text{cm}^{-3}$ .<sup>35</sup>

#### 4.3.2 TEM analysis

TEM sample preparation was performed by dispersing Si NCs into ultrapure water via 15 min sonication. A small droplet of suspension ( $\sim 5$   $\mu\text{L}$ ) was dropcast onto a 300-mesh gold grid coated with an ultra-thin lacey carbonfilm (Ted Pella Inc.) held with reverse-grip tweezers. The grid was air-dried for 1h. TEM images were acquired using a FEI Tecnai G<sup>2</sup> F30 TEM with an operating voltage of 300 kV.

Bacteria cell samples exposed to Si NCs were prepared for TEM imaging through a typical process of fixation, dehydration, and resin embedding. Briefly, *S. oneidensis* MR-1 was suspended in HEPES at an optical density of 0.8 and exposed to 500 ppm of each SiNC for two hours. Bacterial cells were pelleted, washed with 0.1 M sodium cacodylate buffer three times, and then fixed with a 2.5% glutaraldehyde in 0.1 M cacodylate buffer for 50 minutes. The pellet was flipped halfway through the fixation time to assure fixation throughout the pellet. Samples were washed again with sodium cacodylate and dehydrated with a series of aqueous ethanol solutions (30%, 50%, 70%, 80%, 95%, and 100%). After three washes with propylene oxide, samples were incubated with a 2:1 propylene oxide: resin mixture for two hours, 1:1 propylene oxide: resin overnight, fresh propylene oxide: resin for four hours, and then in pure resin overnight. The resin was replaced with fresh resin and cured in a 40°C oven for 24 hours, followed by a 60°C oven for 48 hours. Slices of  $\sim 70$  nm thickness were cut with a Leica EM UC6 Ultramicrotome and placed on 200

mesh copper grids with carbon and formvar supports for imaging on a FEI Tecnai G<sup>2</sup> F30 TEM at 100 kV, in either bright field or dark field mode.

#### 4.3.3 Powder XRD

Sample powder was ground in an agate mortar manually before loading onto an XRD sample holder. Powder XRD patterns were collected using a powder X'pert Pro X-ray diffraction system with a cobalt K $\alpha$  X-ray source (wavelength 1.79 Å).

#### 4.3.4 Bacterial culture and Si NC exposure

*S. oneidensis* MR-1 stock was a generous gift from the Gralnick Lab at the University of Minnesota. *S. oneidensis* MR-1 were stored at -80 °C before being inoculated onto LB agar plates. The plates were incubated at 30 °C until discernible colonies were obtained. About six colonies were transferred into 10 mL LB broth to prepare a bacterial suspension, which was incubated in an orbital shaker for 3 to 4 hours. Bacteria cells were harvested before entering stationary phase, as determined by the OD<sub>600</sub>. The optical density was measured using by Spectronic 20D. Bacteria cells were then pelleted by centrifugation at 750 × g for 10 minutes, re-dispersed in Dulbecco's phosphate-buffered saline (DPBS) buffer and suspended into HEPES buffer (2 mM HEPES and 25 mM NaCl, at pH = 7.4). The bacterial suspension was then diluted to ~0.05 OD<sub>600</sub> so that the cell density was ~10<sup>7</sup> cells/mL. The concentration of the Si NC working solution was 5 and 50 mg/mL. The subsequent nanoparticle exposure was performed by mixing the bacterial suspension with Si NC working solution (with a volume ratio of 9:1, thus, the exposure concentration was 0.5 and 5 mg/mL, respectively), and incubated for 30 minutes or 2 hours.

#### 4.3.5 Colony counting assays

To assess the potential toxic effects of Si NCs, an adapted colony counting assay (drop plate method) was used for the bacterium *S. oneidensis* MR-1.<sup>16, 51</sup> Bacterial suspensions of *c.a.*  $10^7$  cells/mL ( $\sim 0.05$  OD<sub>600</sub>) was exposed to 0.5 and 5 mg/mL of Si NCs, respectively, with a subsequent 10-fold serial dilution to dilute the bacterial suspension to a proper cell density. Aliquots of 5  $\mu$ L from three DFs of the exposed bacterial suspension (that is,  $10^{-3}$ ,  $10^{-4}$  and  $10^{-5}$ ) were dropped onto the surface of LB agar plates (1.5 wt.% agar), and the agar plates were incubated at 30 °C overnight until observable colonies formed. As the colonies formed at the DF of  $10^{-4}$  were countable, data from this DF was used for further analysis. The bacterial viability for each treatment was expressed as a ratio of colony counts to the negative control samples. The experiments were accomplished using five different types of Si NCs and repeated over four biological replicates for each type.

#### 4.3.6 CytoViva analysis

The interaction between *S. oneidensis* MR-1 and Si NCs were visualized via imaging the bacterial exposure solution using CytoViva hyperspectral microscopy (CytoViva Inc., Auburn, AL). The CytoViva system consists of an Olympus BX-41 microscope equipped with a motorized stage, a visible-near infrared hyperspectral camera system (CytoViva Hyperspectral Imaging System 1.4), and a 150 W halogen light source. Bacteria exposed solutions were drop-cast ( $\sim 5$   $\mu$ L) onto a glass slide, which was then sealed with a cover slip and clear nail polish. Slides were examined at 100X magnification with an oil immersion lens. Hyperspectral images were acquired using ENVI 4.8 software.

Hyperspectral scanning was performed using 65% light source intensity and 0.1 s acquisition time per line. Each pixel of the hyperspectral image (datacube) contains its light reflectance spectrum ranging from 400 to 1000 nm. Analysis of hyperspectral data (mapping) were performed using a spectral classification algorithm, SAM, which compared and matched pixels on the hyperspectral data of bacteria exposure solution to the reference libraries obtained by analyzing bacteria and Si NCs separately in HEPES buffer. Pixels in the images that match the hyperspectral signature were highlighted in yellow (*S. oneidensis* MR-1) or red (Si NCs).

#### 4.3.7 Detection of total ROS generation

Total ROS level was determined using the DCFDA assay under abiotic conditions.<sup>44</sup> Specifically, DCFDA in DMSO stock solution (20 mM) was diluted 100 folds in HEPES buffer. Then, 50  $\mu$ L of DCFDA working solution was mixed with 200  $\mu$ L of Si NC (*i.e.*, undoped Si NCs, 5% and 30% B doped Si NCs, and 5% or 30% P doped Si NCs) working solution of 0.5 or 5 mg/mL, respectively. In addition, negative control experiments were performed in HEPES buffer while positive control experiments were using 1 M hydrogen peroxide solution. Each condition was repeated three times in 96-well optical bottom plates (Costa, Corning, NY). The fluorescence counts were recorded by a Synergy 2 Multi-Mode microplate reader (BioTek, Winooski, VT) at Ex/Em: 485/525 nm. The counting process lasted for 2.5 hours, and data were analyzed using GraphPad Prism 6 (GraphPad-Prism Software Inc., San Diego, CA).

## 4.4 Results and discussion

#### 4.4.1 Characterization of Si NCs

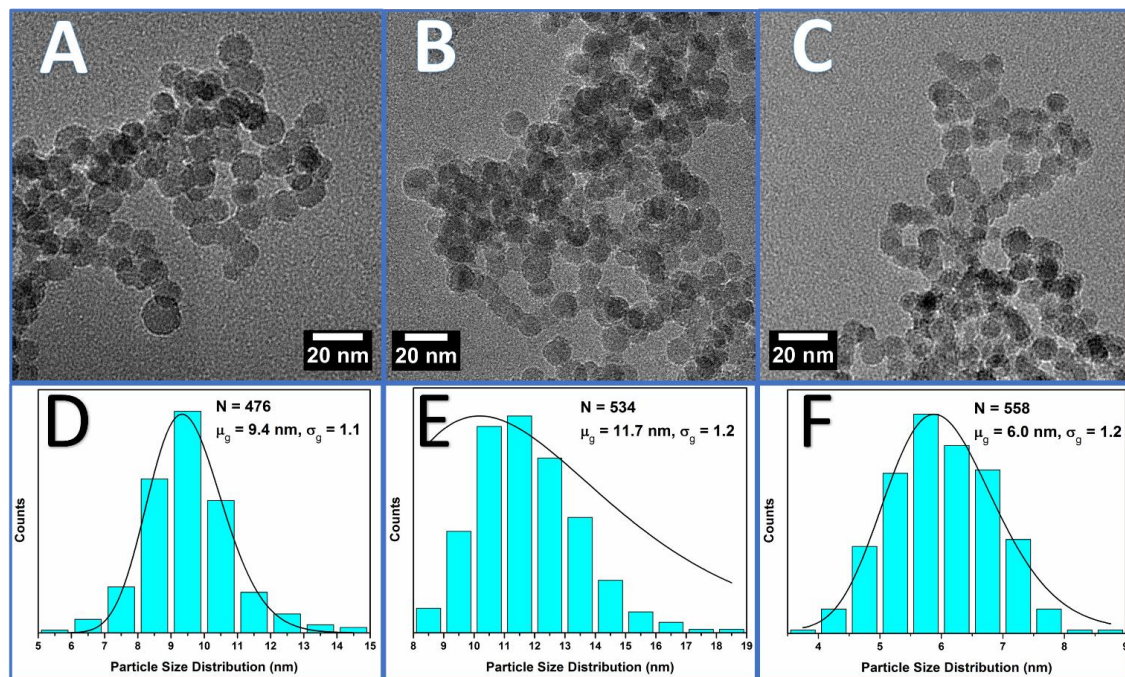


**Figure 4.1.** Morphology and size analysis of Si NCs. TEM images of (a) undoped Si NCs, (b) 5% B-doped Si NCs, and (c) 5% P-doped Si NCs. Corresponding particle size distribution of (d) undoped Si NCs, (e) 5% B-doped Si NCs, and (f) 5% P-doped Si NCs (c.a. 500 counts based on TEM data).

The fundamental properties of Si NCs were carefully examined by various characterization methods. As shown in Figure 1, the particle size and morphology of Si NCs without and with doping were investigated by TEM. All these NCs exhibit similar primary nanoparticle diameters around 10 nm (Table 1) and spherical morphology with moderate agglomeration upon suspension. Accordingly, the hydrodynamic diameters ( $>100$  nm) measured by DLS (Brookhaven ZetaPALS) are larger than TEM PSDs. In addition, PDI values  $> 0.2$  suggest moderately polydisperse distributions of Si NCs in aqueous solution.<sup>57</sup> The  $\zeta$ -potential of Si NCs fall in the range of  $-25$  to  $-50$  mV, indicative of a suitable surface charge for colloidal stability. Furthermore, the transfer of Si NCs

from water to HEPES buffer didn't induce significant change in  $\zeta$ -potential, and as such, it is clear that the media used for subsequent bacterial exposure had minimal influence on Si NC surface charge.

**Table 4.1.** Size and surface chemistry characteristics of Si NCs

Si NCs	Undoped	5% B	30% B	5% P	30% P
TEM diameter <sup>a</sup> (nm)	9.4 ( $\sigma_g = 1.15$ )	11.7 ( $\sigma_g = 1.15$ )	10.1 ( $\sigma_g = 1.16$ )	6.0 ( $\sigma_g = 1.15$ )	9.0 ( $\sigma_g = 1.16$ )
DLS diameter (nm) (in H <sub>2</sub> O)	161 ± 4	105 ± 1	104	97 ± 1	337 ± 4
PDI	0.30 ± 0.01	0.24 ± 0.01	0.22 ± 0.01	0.20 ± 0.02	0.27 ± 0.01
$\zeta$ -potential (mV) (in H <sub>2</sub> O)	-34.5 ± 1.0	-37.8 ± 0.9	-38.2 ± 0.7	-34.5 ± 0.8	-24.1 ± 1.4
$\zeta$ -potential (mV) (in HEPES)	-34.8 ± 1.0	-35.0 ± 0.4	-37.3 ± 1.5	-31.5 ± 1.1	-24.4 ± 0.8

<sup>a</sup>PSDs were calculated based on TEM data (c.a. 500 particles counted). It was assumed that the Si NC sizes are described by a log-normal distribution function that was used to fit the size histograms to determine the average particle sizes (geometric means) ( $\sigma_g$  stands for geometric standard deviation)

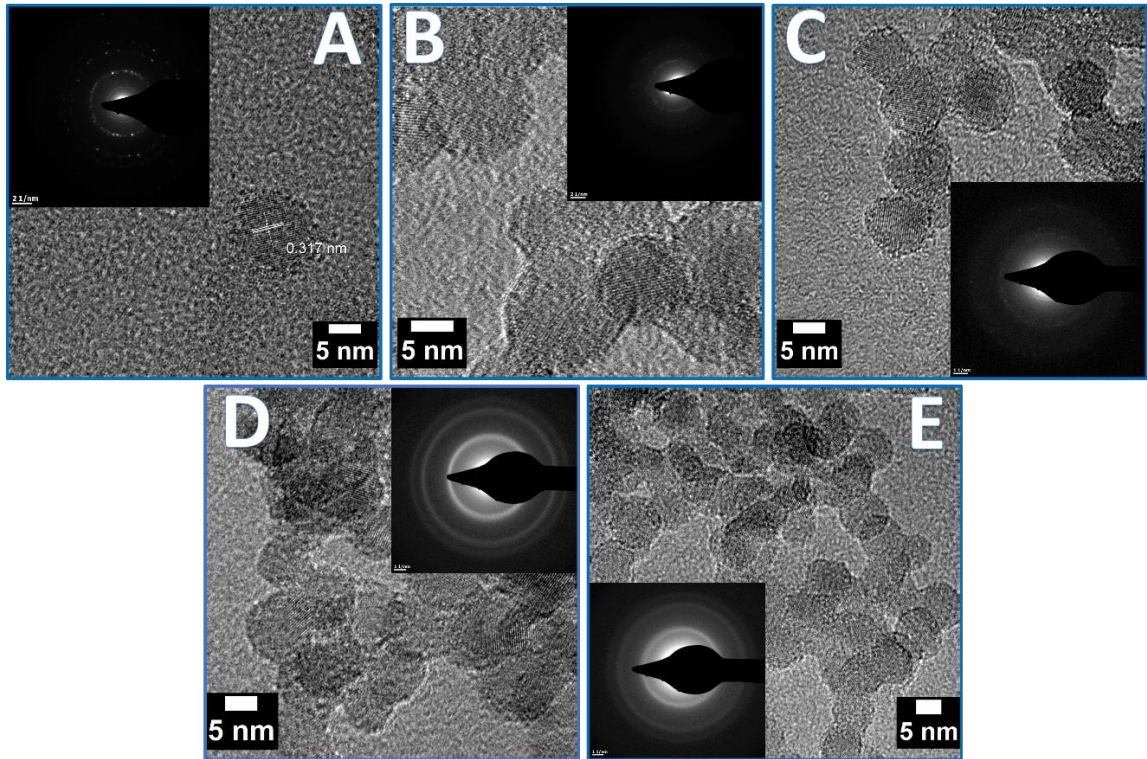


**Figure 4.2.** HRTEM images and SAED patterns (inset) of Si NCs: (a) undoped Si NCs, (b) 5% B-doped Si NCs, (c) 30% B-doped Si NCs, (d) 5% P-doped Si NCs, and (e) 30% P-doped Si NCs.

Using HRTEM, we were able to take a closer look at the structure of the Si NCs. As shown in Figure 4.2, electron diffraction patterns and crystal lattices are clearly visible for all the Si NCs. Particularly, the lattice constant of the undoped Si NCs was calculated by employing SAED data (Figure 4.2a inset). Except for the TEM artifact ring around the bright center, there are three diffraction rings, and the radius of each one can be measured directly by ImageJ (US National Institutes of Health, Bethesda MD USA). The corresponding  $d$ -spacing is the inverse of the ring radius, which can be assigned to three planes ((111), (220), and (311)) of diamond cubic Si NCs ( $Fd-3m$ ).<sup>33, 35</sup> Accordingly, the (111)  $d$ -spacing value of 0.315 nm very well matched the lattice fringe distance (0.317 nm observed in HRTEM image, Figure 4.2a). The lattice constant was calculated for the

doped Si NCs as well, and it is clear that the crystalline structure parameters of doped Si NCs are almost the identical to the undoped ones (data not shown). As TEM only reveals localized areas, we also applied powder XRD to examine the crystallinity of Si NCs. As shown in Figure 4.3, all the Si NCs exhibited the same diffraction patterns (PDF#: 27-1402, silicon, *Fd-3m*, cubic diamond), confirming that the boron- or phosphorus-doping does not change the original crystalline structure of Si NCs, in agreement with previous reports.<sup>53</sup> Moreover, the crystalline grain size of Si NCs was calculated using the Scherrer formula (Table 4.2). The grain sizes are around 7 nm, smaller than TEM diameters of ~10 nm (Table 4.1), which can be attributed to XRD instrument broadening and background fitting parameters. Based on our previous studies, phosphorous or boron atoms can either be condensed/segregated close to the Si NC surface or incorporated into the Si NC cores: For P-doped Si NCs, phosphorous atoms are largely incorporated near the surface as indicated by precedent works.<sup>53, 55, 58</sup> For B-doped Si NCs, boron atoms are also located at the surface.<sup>35</sup> However, even if a great amount of B<sub>2</sub>H<sub>6</sub> is used for synthesis, it was not observable that amorphous boron shells formed over 30% B-doped Si NCs .

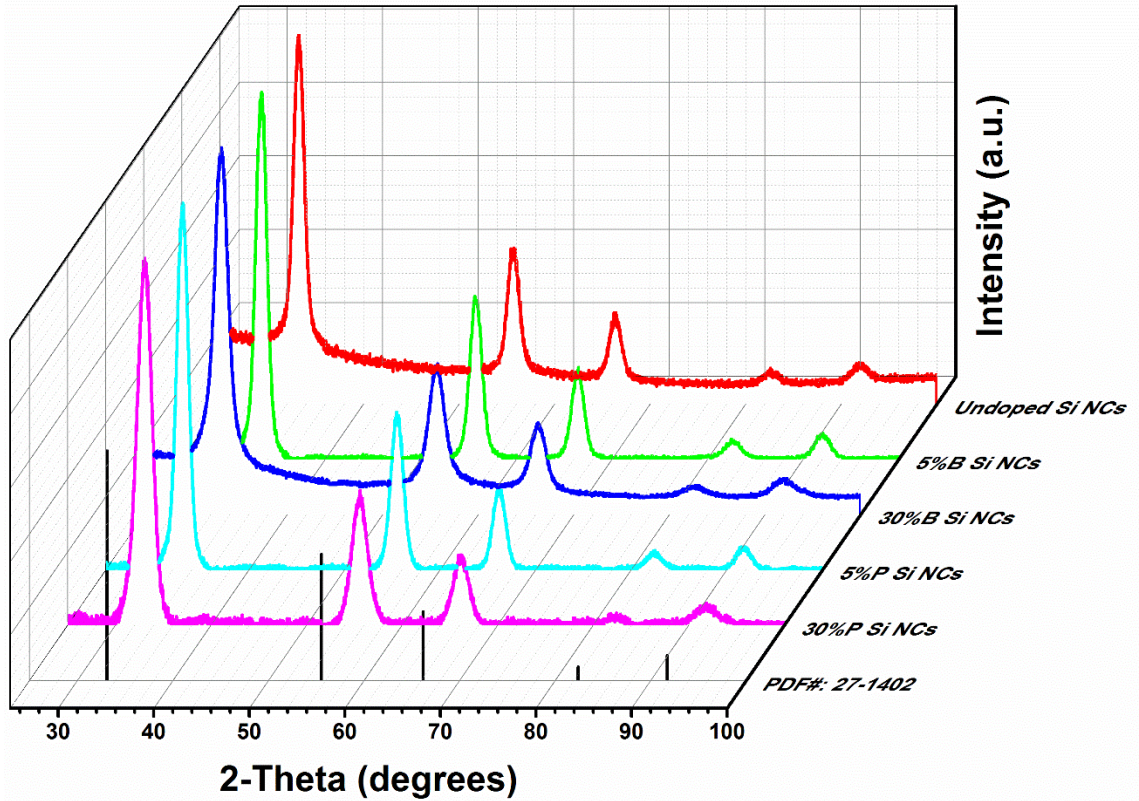


**Figure 4.3.** XRD patterns of Si NCs.

**Table 4.2.** Grain sizes of Si NCs calculated based on the Scherrer equation.

Si NCs	Grain size (nm)
Undoped	7.5
5%B	7.1
30%B	6.2
5%P	7.0
30%P	5.5

It is worthwhile to note that Si NCs with diameters  $< 5$  nm (either undoped or doped) show strong PL, revealed by previously published work.<sup>55, 59</sup> In this work, Si NCs are too large to be in the quantum confined regime and exhibit no PL. Furthermore, Si NC doping has also been observed to quench PL.<sup>55</sup> However, the Si NCs studied here show tunable mid-infrared plasmonic response, which makes them of great interest for applications such

as infrared sensors and imaging.<sup>35</sup> As such, it is interesting to study whether doping induces any environmental burden alongside the LSPR performance improvement.

#### 4.4.2 Abiotic assessment of total ROS generation

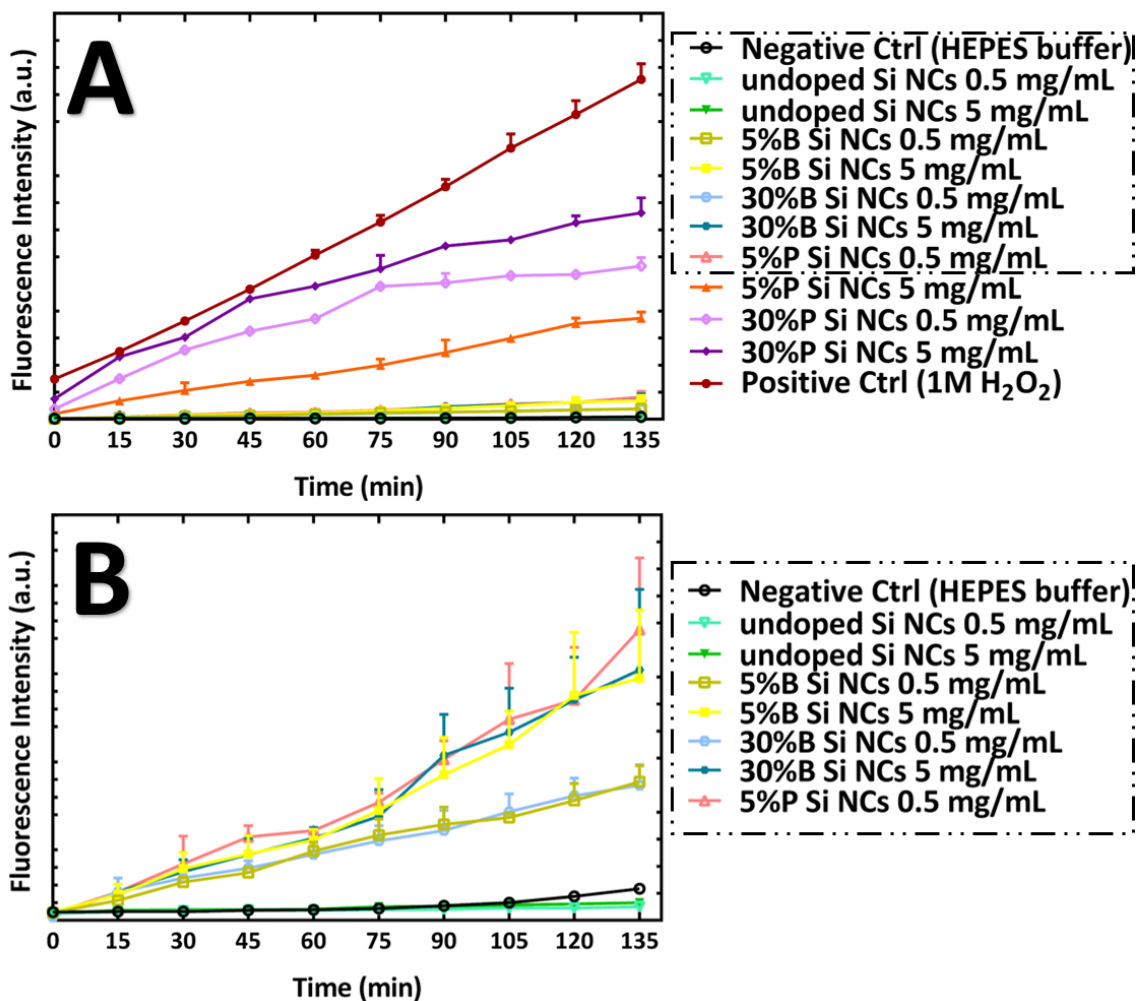


**Figure 4.4.** (a) Abiotic induction of ROS by Si NCs determined by the DCFDA assay (incubation time: 2.5 hours, n = 3), (b) enlarged view for low intensity data.

Boron, a dopant with 3 valence electrons, acts as an acceptor in Si NCs, producing a hole ( $h^+$ ) in the valence band and lowering the Fermi level. Conversely, the phosphorus acts as a donor in Si NCs, would introducing additional free electrons ( $e^-$ ) in the conduction band

and raising the Fermi level.<sup>35, 60, 61</sup> The doping-induced free carriers can result in ROS generation, as  $h^+$  can react with  $H_2O$  to form hydroxyl radical ( $\cdot OH$ ) and  $e^-$  can react with  $O_2$  to form superoxide radical ( $O_2^{\cdot -}$ ).<sup>43, 44</sup> The originally non-fluorescent reagent DCFDA can be oxidized to a fluorescent form (DCF) upon reacting with ROS; for this reason, it has been broadly used for ROS detection and quantification.<sup>62</sup> In our work, ROS generation by doped Si NCs was assessed using the DCFDA assay, and the resulting data are shown in Figure 4.4. These data reveal an overall progressive increase in fluorescence during incubation with doped Si NCs. As the colors are obscured by other data (Figure 4.4a), we plotted low-response data in a separate graph for a more clear view (Figure 4.4b). Specifically, for P-doped NCs (Figure 4.4a), a discernible high ROS level was detected from heavily doped NCs (30%) at the higher working concentration (5 mg/mL); for the B-doped counterparts (Figure 4.4b) there was a steady increase in ROS over the incubation time, though not as high as the P-doped Si NCs. Undoped Si NCs did not induce a DCFDA-based fluorescence signal (Figure 4.4b, overlapped with negative control trace). As shown in Figure 4.4a, after 30 minutes, high ROS levels were observed for the 5 mg/mL 5% P Si NCs and both 0.5 and 5 mg/mL 30% P Si NCs, while negligible for the rest, confirming that only doped P-doped Si NCs generate significant ROS. Since excessive ROS can negatively impact bacterial cells by compromising the metalloenzyme activity and DNA integrity,<sup>63</sup> it is necessary to investigate the impact of doped Si NCs by assessing their influence on bacterial viability. Based on the abiotic ROS data alone, it is straightforward to hypothesize that the P-doped Si NCs will have a larger negative impact on bacteria than B-doped or undoped Si NCs.

#### 4.4.3 Bacterial toxicity evaluation of doped Si NCs

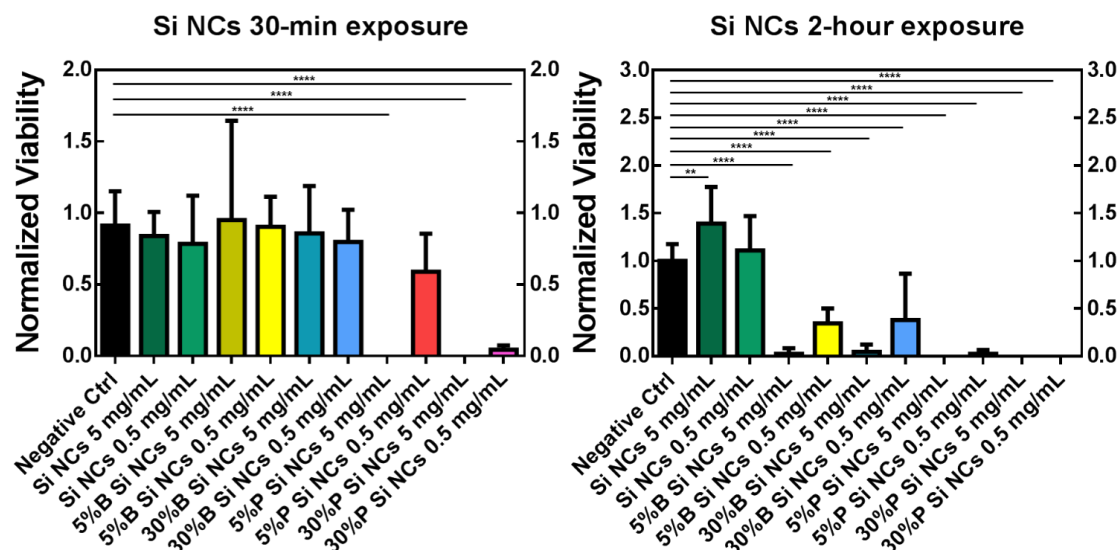


**Figure 4.5.** Bacterial viability of *S. oneidensis* MR-1 evaluated by colony counting assay (drop plate method). The asterisk indicates significance level: \* $p < 0.05$ , \*\* $p < 0.01$ , \*\*\* $p < 0.001$ , \*\*\*\* $p < 0.0001$  (examined by one-way ANOVA, followed by Dunnett's multiple comparisons test,  $n = 4$  or  $5$ ).

The colony counting assay is regarded as a gold standard method to determine the number of bacterial colony forming units in a given volume/sample for microbiological studies, and has been widely used to quantify bacterial viability in a variety of exposure conditions.<sup>51, 64, 65</sup> To probe the nanoparticle concentration and doping level-dependent response of *S. oneidensis* MR-1 to doped Si NCs, the drop plate colony counting method was employed. Briefly, aqueous suspensions of bacterial cells were exposed to doped Si NCs of various concentration/doping level and subsequently dropcast onto LB agar plates. Discernible colonies were formed over 16-hour incubation. Colony reduction compared to negative control experiments were used to quantitatively gauge any bacterial toxicity of Si NCs. Figure 4.5 demonstrates the toxicity of undoped and doped Si NCs over short exposure (30 minutes, left panel) and long exposure (2 hours, right panel), respectively.

At the 30-minute time point, remarkable ROS levels were observed for 5 mg/mL 5 %P Si NCs and both doses of 30% P Si NCs, as shown in Figure 4.4. Correspondingly, during 30-minute exposure (Figure 4.5, left panel), neither undoped Si NCs nor B-doped Si NCs exhibited toxic effects to *S. oneidensis* MR-1. A minor reduction in the viability was observed if bacteria cells were exposed to lightly P-doped Si NCs (5% P) at concentration as low as 0.5 mg/mL while at high concentration as 5 mg/mL, a significant toxic effect was detected (analyzed by one-way ANOVA, followed by Dunette's multiple comparisons tests), eradicating almost the whole bacteria population. At the 2-hour time point, , all the doped Si NCs showed a steady increase of ROS production, especially the P-doped ones. Consequently, as shown in the right panel of Figure 4.5, only undoped Si NCs did not compromise bacteria viability, and even B-doped Si NCs exhibited significant toxicity during 2-hour exposure, though ~30% *S. oneidensis* MR-1 survived the lower concentration (0.5 mg/mL). For P-doped Si NCs, likely due to the considerably high ROS level, almost no viable colonies formed, indicative of extremely high bacterial toxicity.

Compared to Gram-negative bacteria (such as *S. oneidensis* MR-1) whose cell walls are dominated by LPS, Gram-positive bacteria (such as *Bacillus subtilis*) construct their outward facing cell walls with a thick peptidoglycan layer, so the two bacterial surfaces are quite different.<sup>51</sup> Due to the lack of an outer cell membrane presenting LPS chains, Gram-positive bacteria can be more susceptible to toxicity induced by nanoparticles than Gram-negative bacteria.<sup>51, 66</sup> As such, it would be worthwhile to investigate the interaction between Si NCs and Gram-positive bacteria species as well, and this will be the subject of future work.

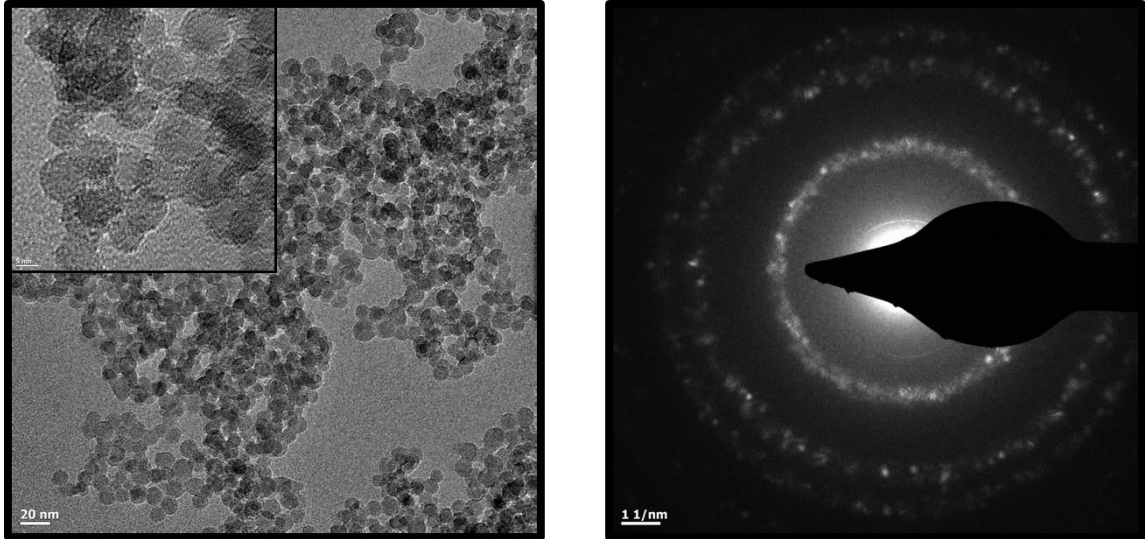


**Figure 4.6.** TEM image (left) and SAED pattern (right) of 30% B-doped Si NCs after 2-hr bacteria exposure. Bacteria exposure has no influence on particle morphology, size, and crystallinity (scale bar: 20nm, inset: 5 nm).

We also examined the transformation of doped Si NCs after exposure to bacteria cells. By applying TEM and HRTEM, we probed the morphology and crystallinity of doped Si NCs. Due to the similarity of TEM images across the Si NC variations, we representatively present the data from the 30% B-doped Si NCs after 2-hr bacteria exposure (Figure 4.6). Clearly, the particle size, shape, and diffraction pattern are almost the same as before (Figure 4.1 and 4.2). Thus, we confirmed that Si NCs remain intact with minimal transformation of crystalline structure.

#### 4.4.4 Si NC association with *S. oneidensis* MR-1 cells

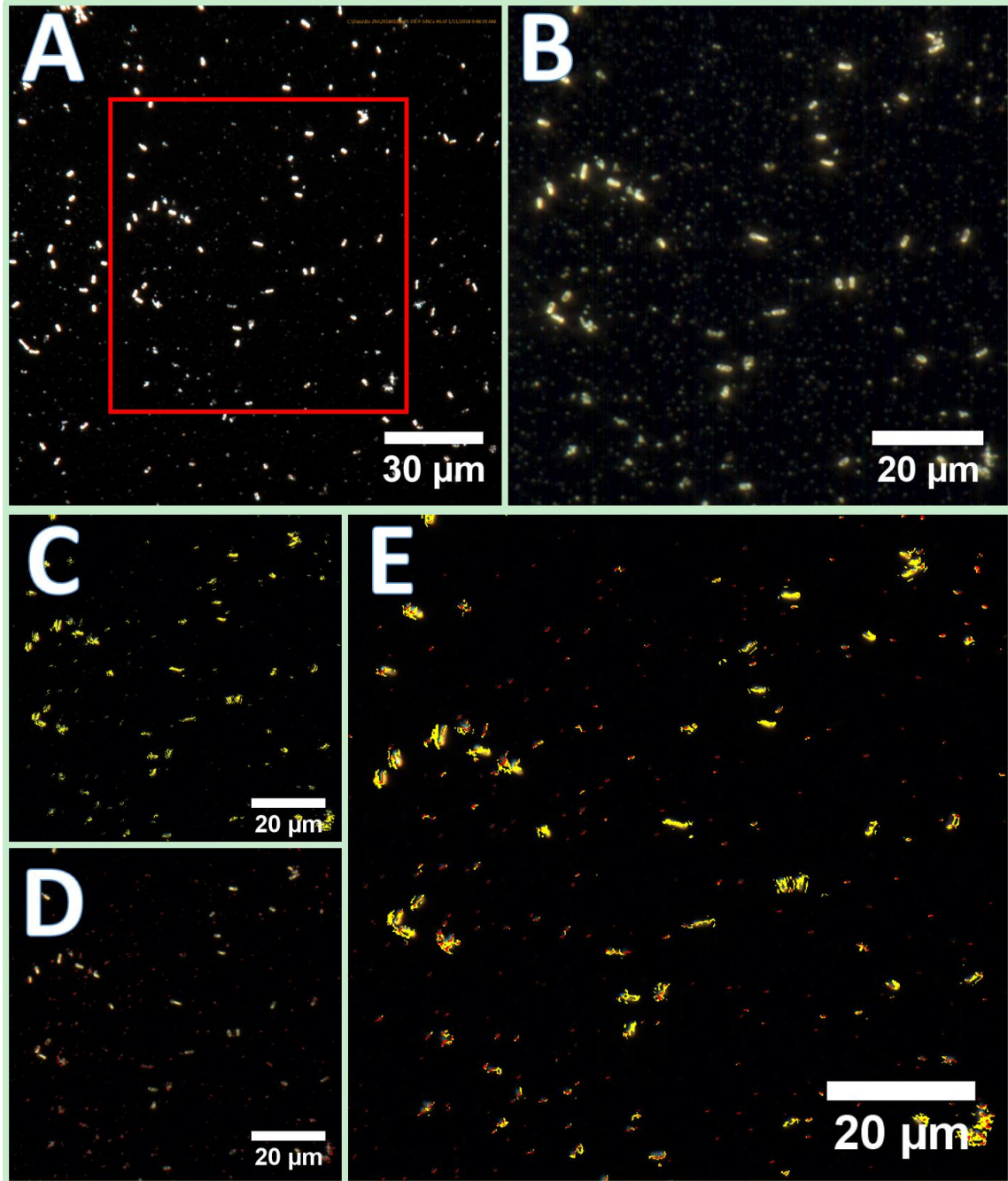


**Figure 4.7.** CytoViva-enhanced dark-field analysis of the interaction between 5% P-doped Si NCs with *S. oneidensis* MR-1. (a) dark-field image of bacteria exposure solution, (b) hyperspectral image of boxed area in A. Mapping (c) bacteria cells alone and (d) 5% P-doped Si NCs alone in the hyperspectral data. (e) Merged mapping results of (c) and (d) where bacteria cells are false-colored yellow while 5% P-doped Si NCs with red.

While the colony counting assay provided a quantitative way to analyze general bacterial response exposed to Si NCs, these data do not indicate if and how Si NCs interact with *S. oneidensis* MR-1 cells. To directly visualize the interaction between Si NCs and bacteria cells, CytoViva microscope analysis was performed to complement the viability data.

Equipped with a hyperspectral imaging system, CytoViva enhanced darkfield microscopy serves as a novel optical approach with great potential in biological research as it allows visualization and identification of specific components in bio-related milieu.<sup>67</sup> The hyperspectral data acquisition (hyperspectral “pushbroom” scanning) generates a 3D data cube composed of two spatial (x,y) and one spectral (z) dimensions.<sup>68</sup> In other words, a hyperspectral image can be considered a dark field image with corresponding spectral information associated with each pixel of the image.<sup>69</sup> In our study, CytoViva hyperspectral microscopy was utilized to probe the presence of Si NCs associated with *S. oneidensis* MR-1 cells. The workflow includes dark field imaging, hyperspectral data acquisition, construction of spectral library, spectral library filtering, and finally, mapping of bacteria cells and Si NCs in exposure solutions. Representative data are shown for the interaction of 5% P-doped Si NCs with *S. oneidensis* MR-1 cells (Figure 4.7); the analysis results for reference samples (*i.e.*, *S. oneidensis* MR-1 cells, undoped, and doped Si NCs) are shown in Figure 4.8 through 4.13, including dark field images, hyperspectral images, and spectral libraries; for interaction between *S. oneidensis* MR-1 cells and other Si NCs, namely, undoped, 5% B-, 30% B-, and 30% P- doped Si NCs, results are shown in Figure 4.14 through 4.17. The spectral library filter function was used to validate that there was

no spectral overlap between the bacteria libraries and all Si NC libraries. As such, we are confident applying these library data for subsequent mapping experiments.

Figure 4.7a exhibits the original dark field image of *S. oneidensis* exposed to 5% P-doped Si NCs; after hyperspectral scanning, the centered area highlighted with red box was magnified and is shown in the resulting hyperspectral image (Figure 4.7b). Clearly, visible rod-shaped cells are surrounded with well-dispersed particles. To further distinguish Si NCs from *S. oneidensis* MR-1 cells, spectral libraries for bacteria cells and 5% P-doped Si NCs were loaded into the SAM function to map the location of Si NCs and cells in the hyperspectral image. The SAM function is a convenient and automated mapping method, wherein the algorithm differentiates the spectral libraries and provides information about the location of endmember pixels in an input image.<sup>69, 70</sup> The mapping results for cells alone and Si NCs alone are displayed in Figure 4.7c and 4.7d. The pixels representing bacteria cells are false-colored with yellow while Si NCs are false-colored with red. The merge of the two provides a direct view as to the co-localization of *S. oneidensis* MR-1 with 5% P-doped Si NCs, as shown in Figure 4.7e. The proximity between the spectral signatures for bacterial cells and Si NCs suggest potential physical contact between the micron-scale bacteria and the nanoscale Si NCs. However, CytoViva is not a super-resolution technique, and it is still limited by the diffraction limit. So, to further probe the association between bacteria cells and Si NCs, TEM micrographs of resin-embedded cells were acquired to complement CytoViva data.

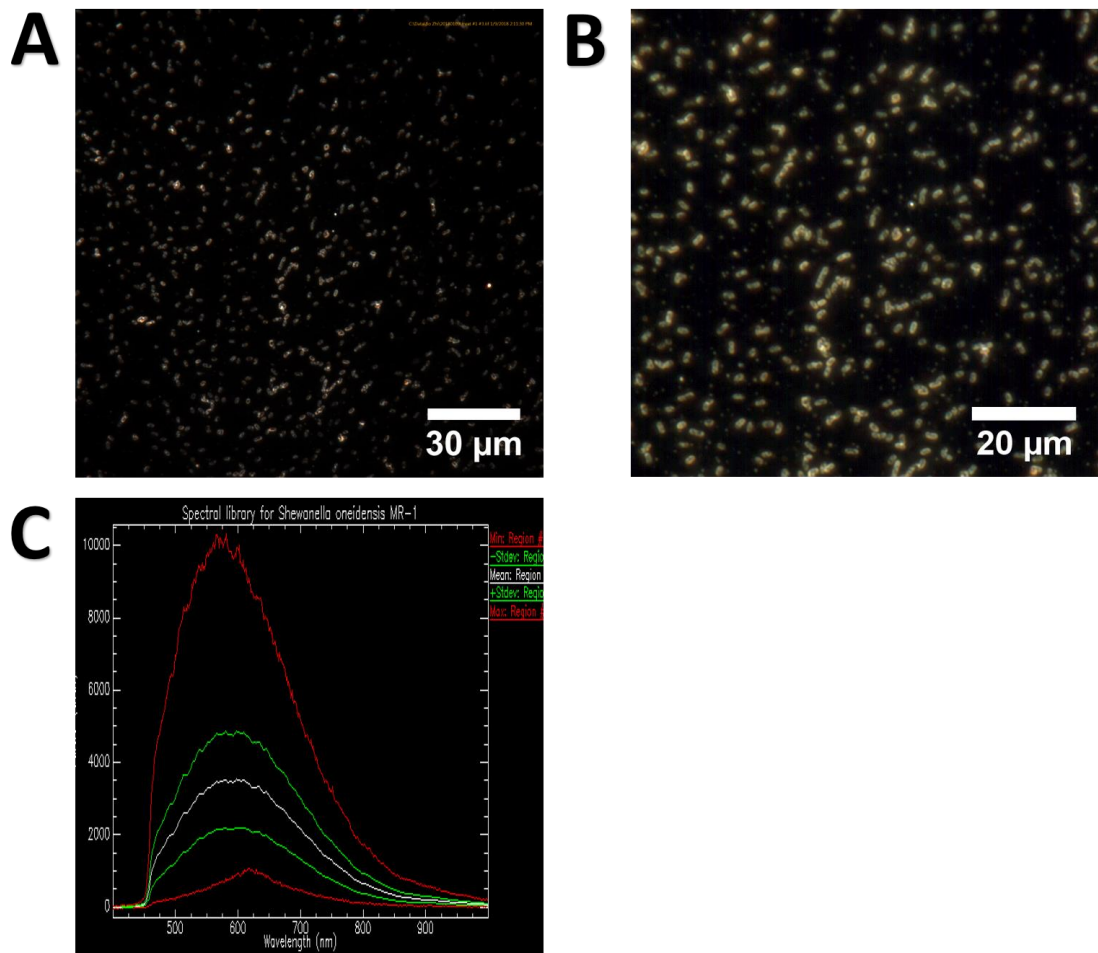


**Figure 4.8.** CytoViva analysis of *S. oneidensis* MR-1 cells: (a) dark field image, (b) hyperspectral image, and (c) spectral library of *S. oneidensis* MR-1 cells, generated by ROI tool.

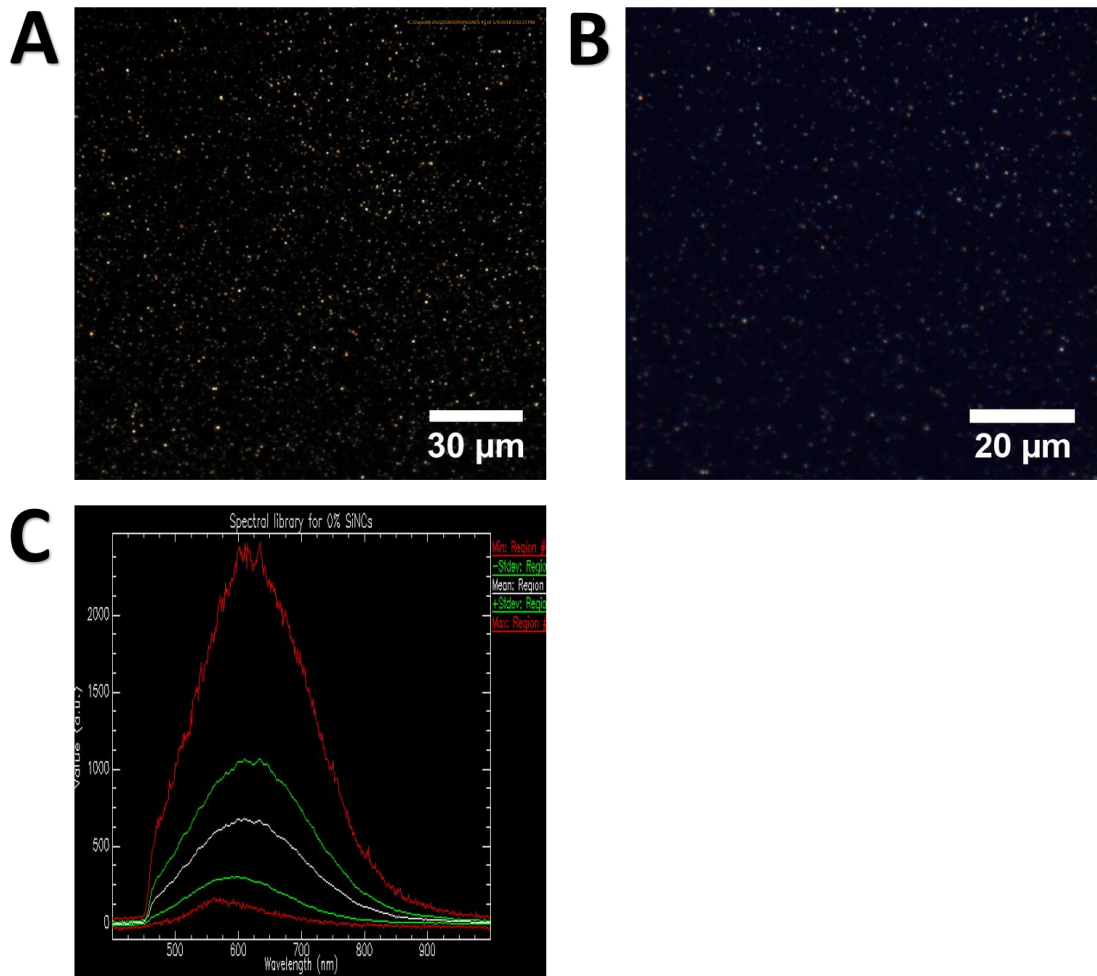


**Figure 4.9.** CytoViva analysis of undoped Si NCs: (a) dark field image, (b) hyperspectral image, and (c) spectral library of undoped Si NCs, generated by ROI tool.

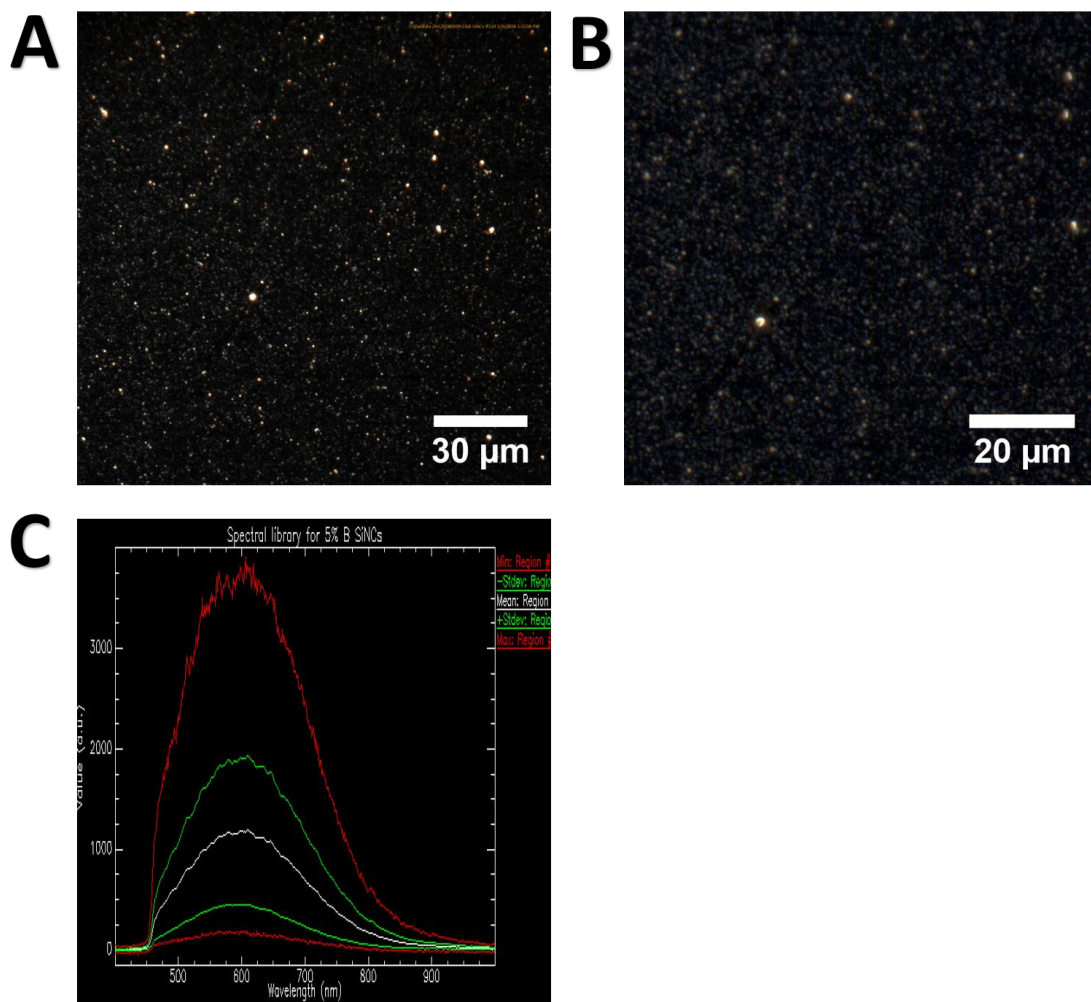


**Figure 4.10.** CytoViva analysis of 5% B-doped Si NCs: (a) dark field image, (b) hyperspectral image, and (c) spectral library of 5% B-doped Si NCs, generated by ROI tool.

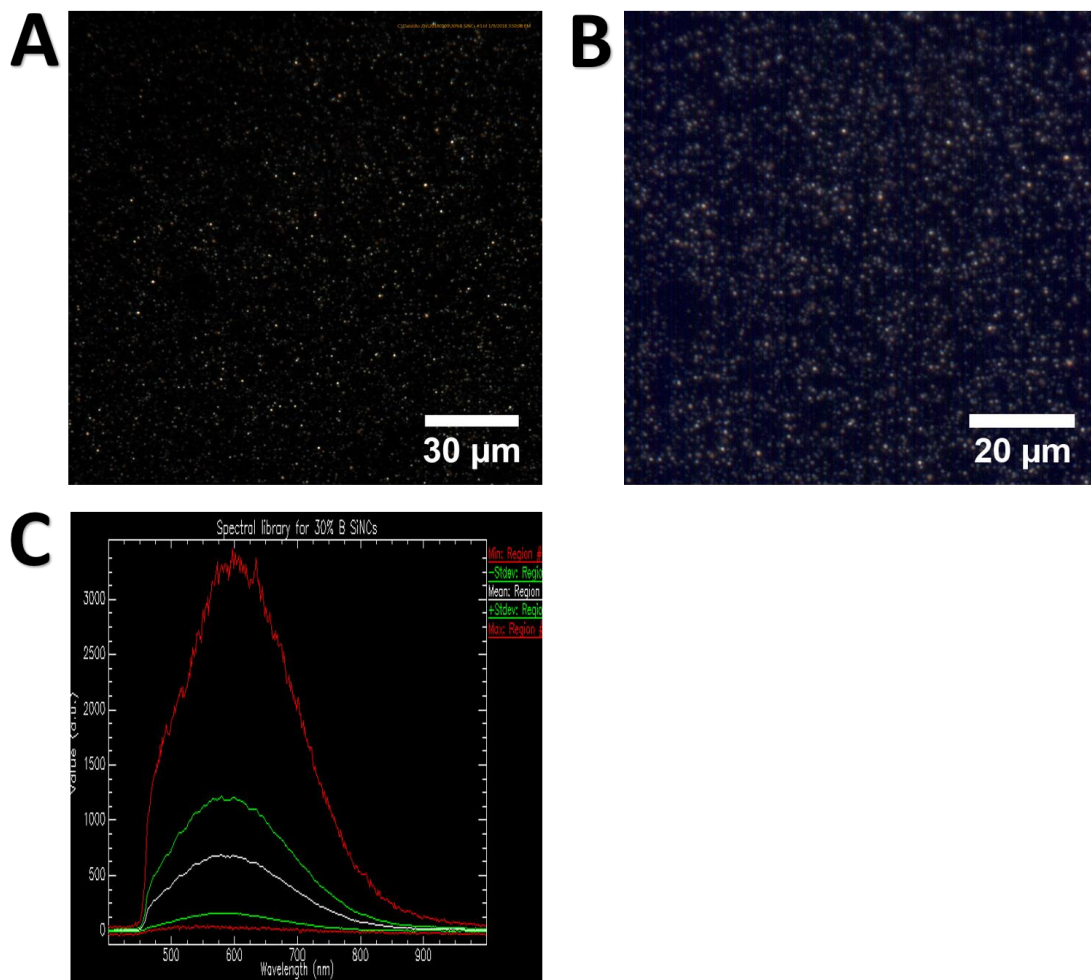


**Figure 4.11.** CytoViva analysis of 30% B-doped Si NCs: (a) dark field image, (b) hyperspectral image, and (c) spectral library of 30% B-doped Si NCs, generated by ROI tool.

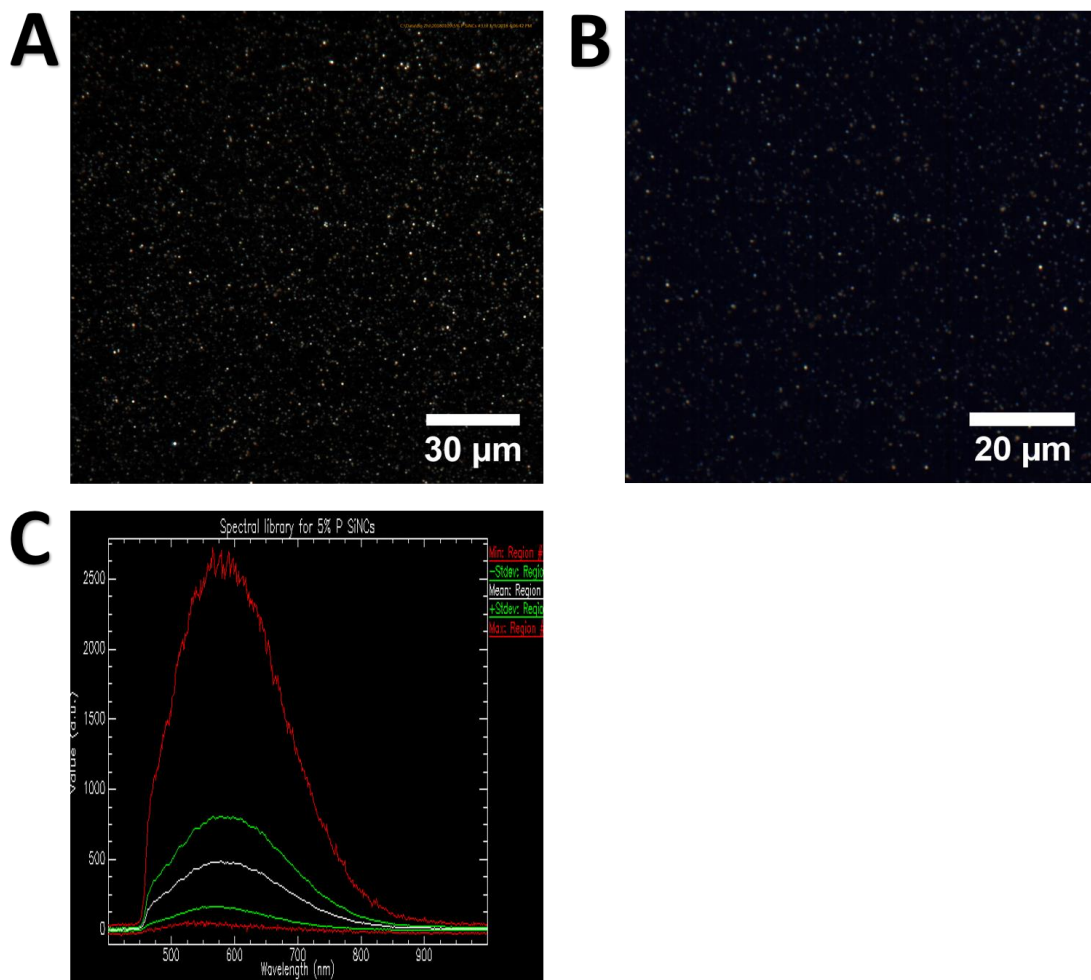


**Figure 4.12.** CytoViva analysis of 5% P-doped Si NCs: (a) dark field image, (b) hyperspectral image, and (c) spectral library of 5% P-doped Si NCs, generated by ROI tool.

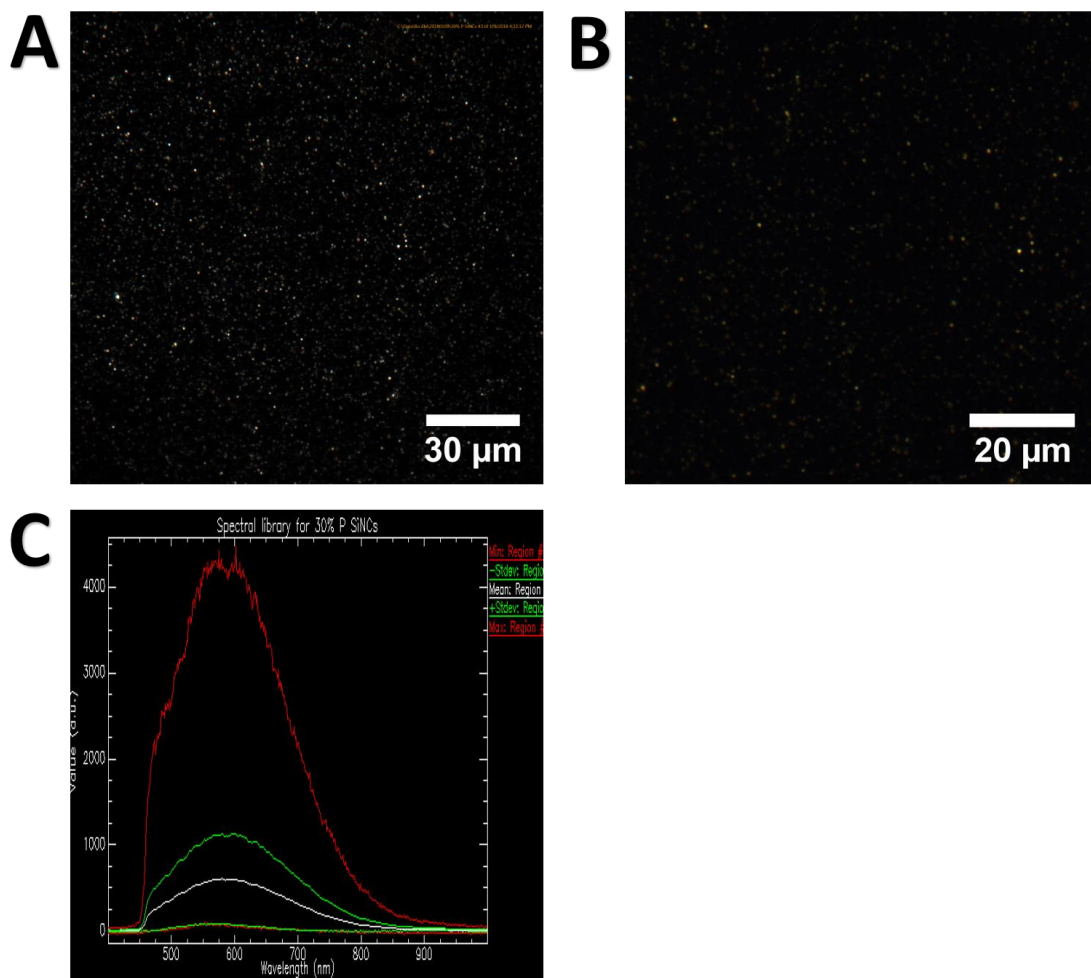


**Figure 4.13.** CytoViva analysis of 30% P-doped Si NCs: (a) dark field image, (b) hyperspectral image, and (c) spectral library of 30% P-doped Si NCs, generated by ROI tool.

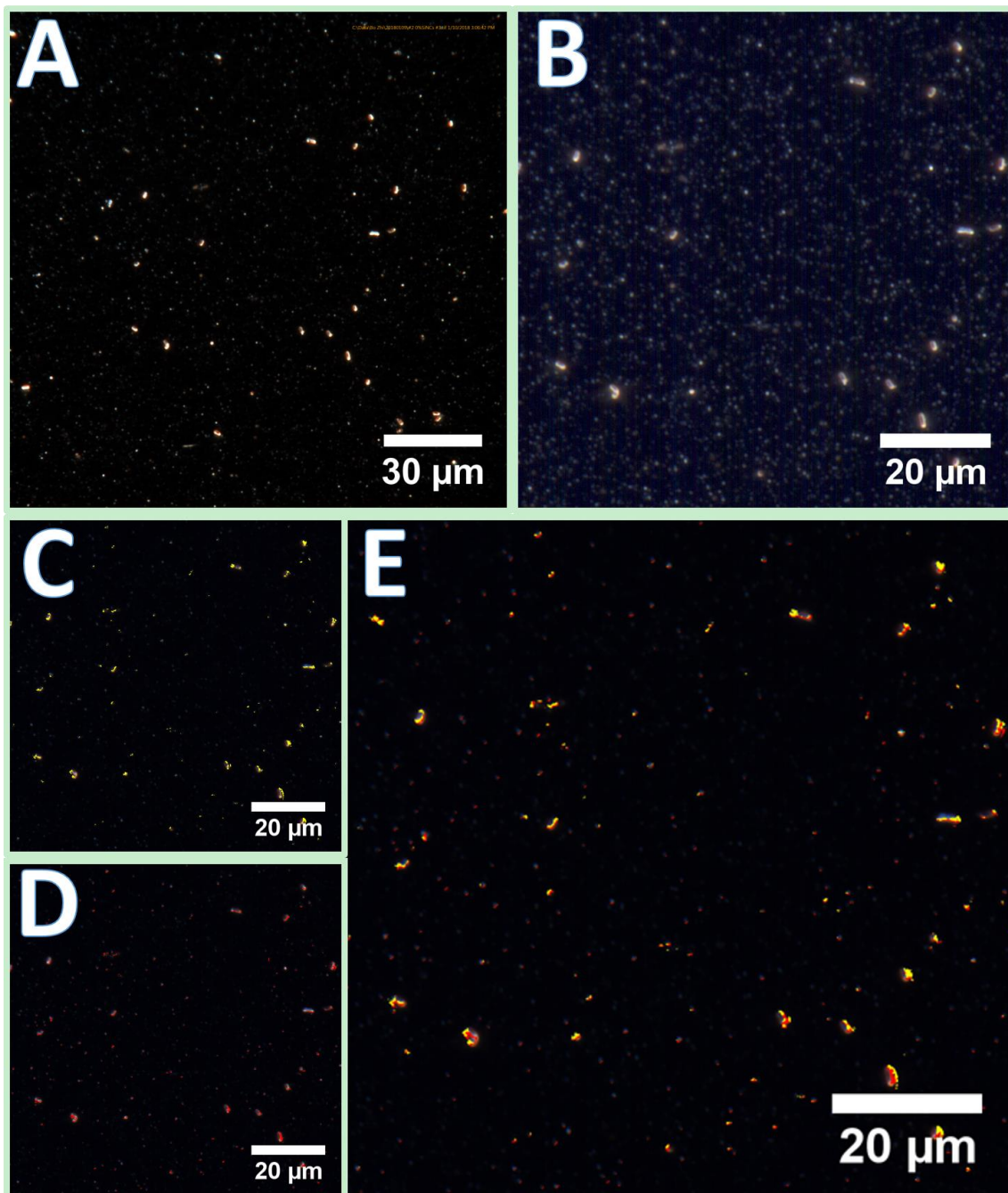


**Figure 4.14.** CytoViva enhanced darkfield analysis of the interaction between undoped Si NCs with *S. oneidensis* MR-1. (a) darkfield image of bacteria exposure solution, (b) hyperspectral image of bacteria exposure solution. Mapping (c) bacteria cells alone and (d) undoped Si NCs alone in the hyperspectral data. (e) The merge of mapping results (c) and (d) (bacteria cells are false colored with yellow while undoped Si NCs with red).

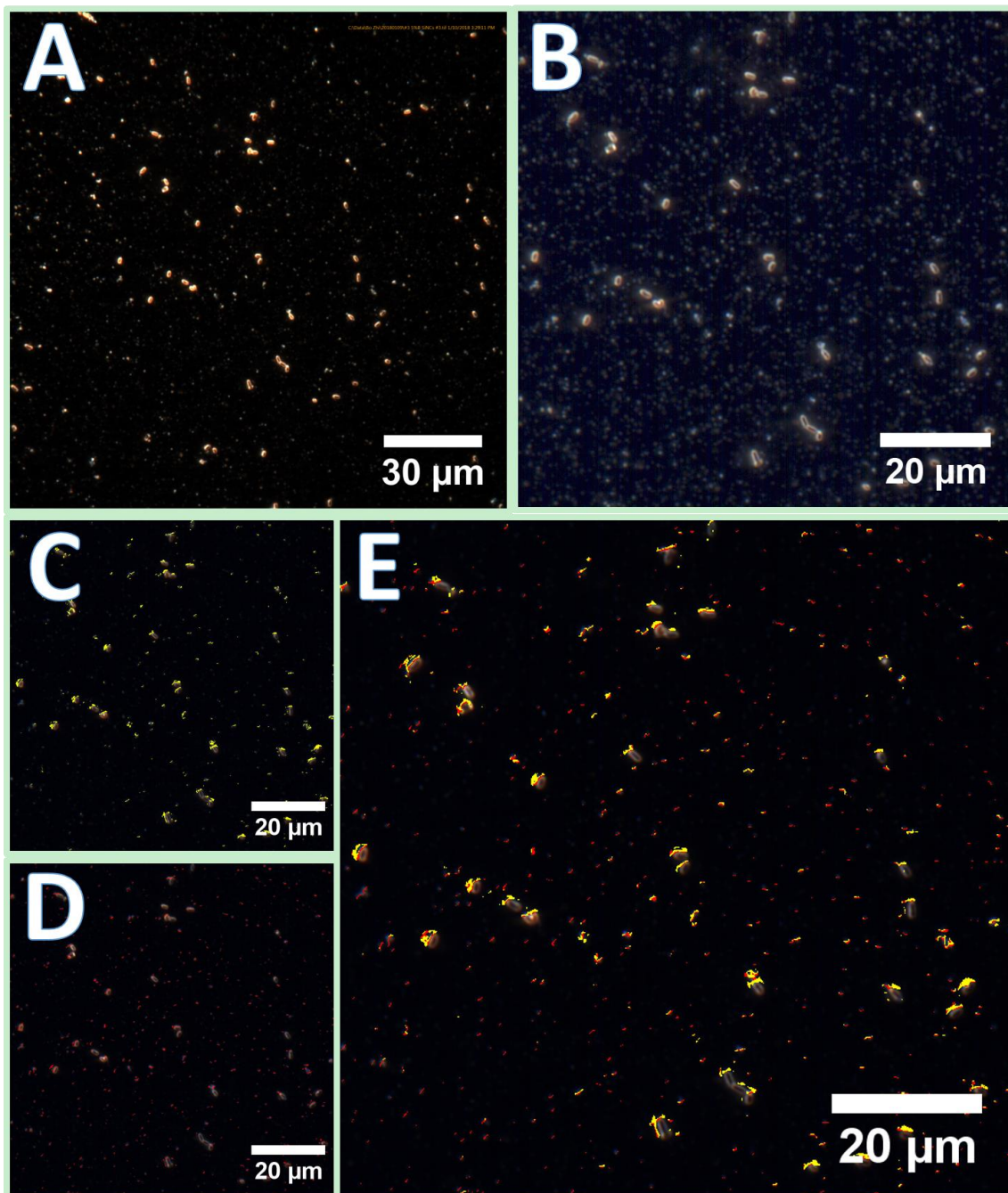


**Figure 4.15.** CytoViva enhanced darkfield analysis of the interaction between 5% B-doped Si NCs with *S. oneidensis* MR-1. (a) darkfield image of bacteria exposure solution, (b) hyperspectral image of bacteria exposure solution. Mapping (c) bacteria cells alone and (d) 5%B doped Si NCs alone in the hyperspectral data. (e) The merge of mapping results (c) and (d) (bacteria cells are false colored with yellow while 5% B-doped Si NCs with red).

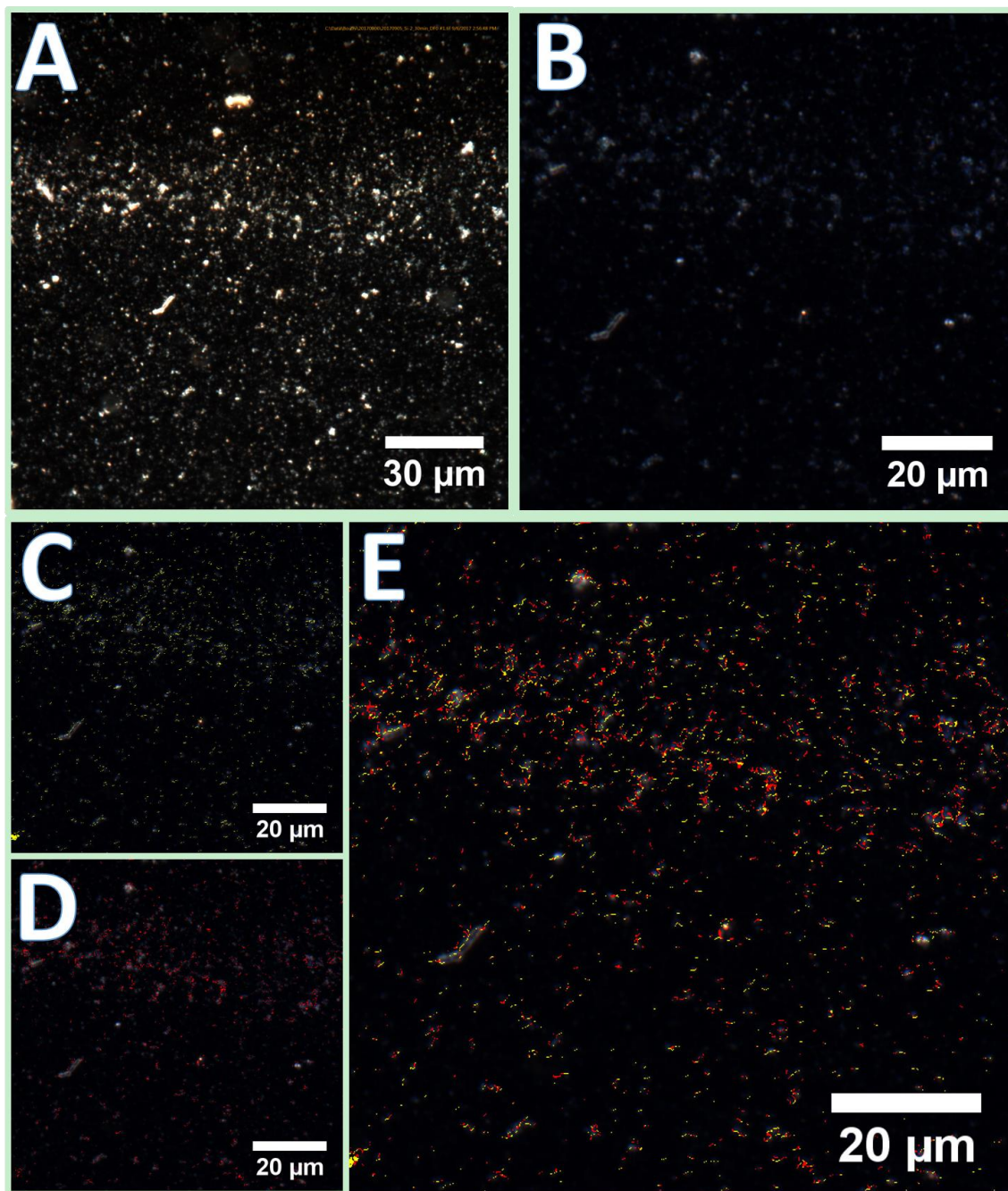


**Figure 4.16.** CytoViva enhanced darkfield analysis of the interaction between 30% B-doped Si NCs with *S. oneidensis* MR-1. (a) darkfield image of bacteria exposure solution, (b) hyperspectral image of bacteria exposure solution. Mapping (c) bacteria cells alone and (d) 30%B doped Si NCs alone in the hyperspectral data. (e) The merge of mapping results (c) and (d) (bacteria cells are false colored with yellow while 30% B-doped Si NCs with red).

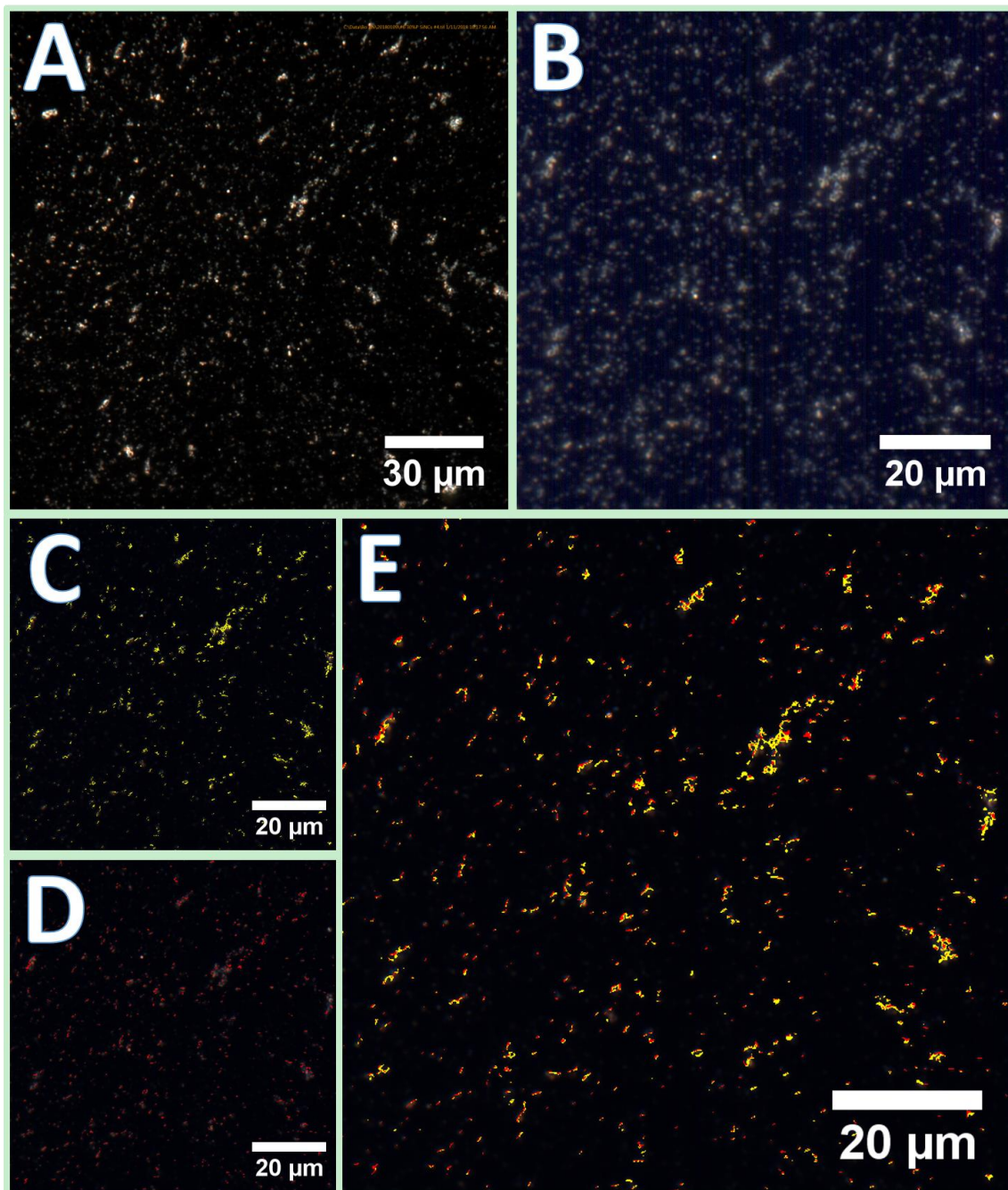


**Figure 4.17.** CytoViva enhanced darkfield analysis of the interaction between 30% P-doped Si NCs with *S. oneidensis* MR-1. (a) darkfield image of bacteria exposure solution, (b) hyperspectral image of bacteria exposure solution. Mapping (c) bacteria cells alone and (d) 30%P doped Si NCs alone in the hyperspectral data. (e) The merge of mapping results (c) and (d) (bacteria cells are false colored with yellow while 30% P-doped Si NCs with red).

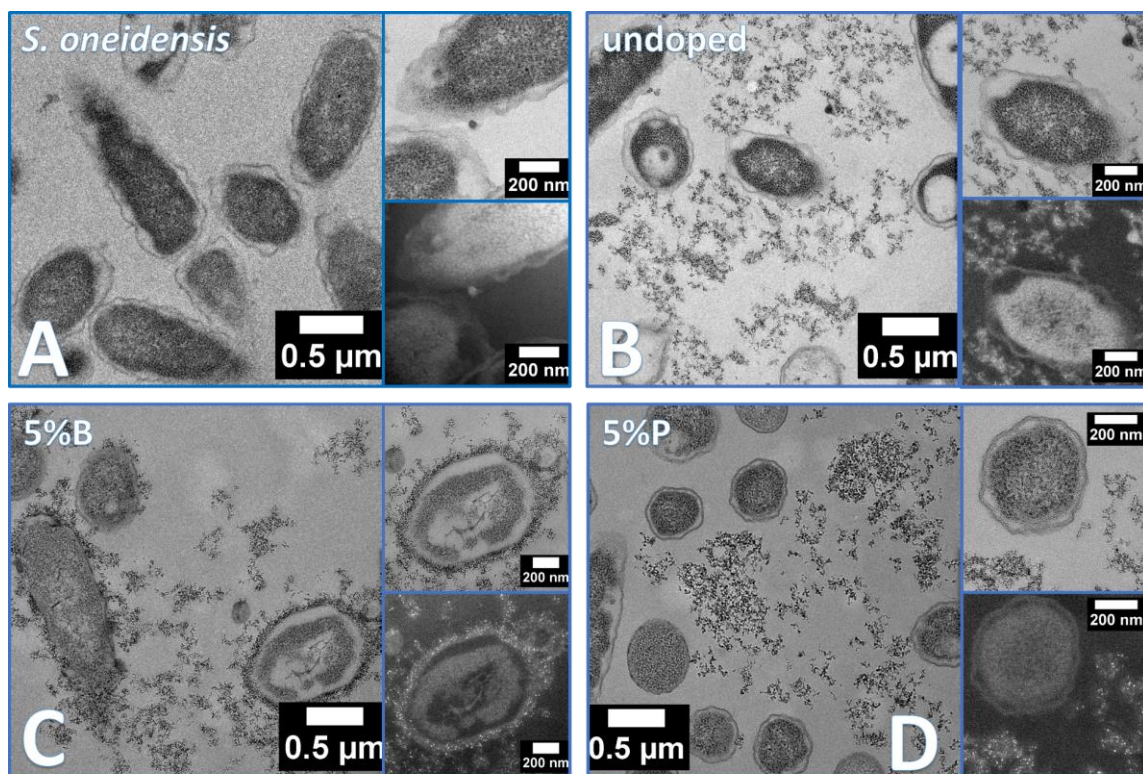


**Figure 4.18.** Bio-TEM images of *S. oneidensis* MR-1 cells alone (a), and *S. oneidensis* MR-1 cells exposed to undoped Si NCs (b), 5% B-doped Si NCs (c), and 5% P-doped Si NCs (d). The right column in each section displays corresponding magnified view in both bright field mode (upper panel) and dark field mode (lower panel). The dark field TEM diffraction angle was set to reveal the crystalline Si NCs.

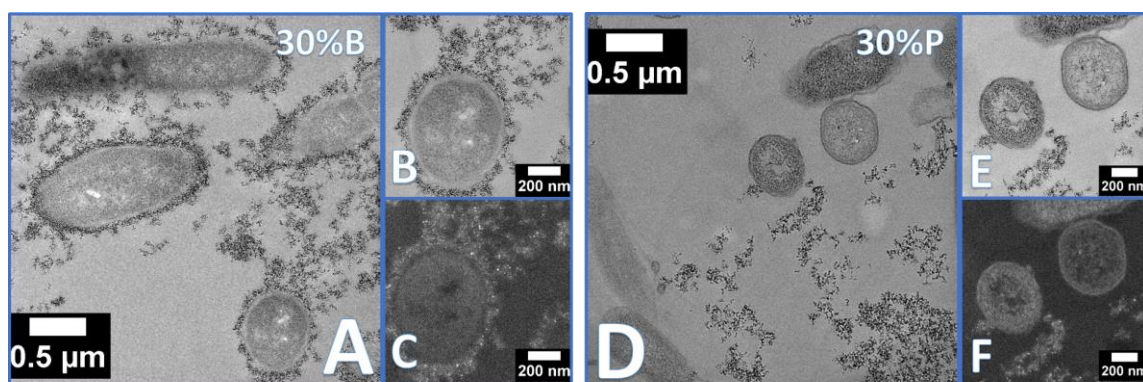


**Figure 4.19.** TEM images of *S. oneidensis* MR-1 exposed to 30% B-doped Si NCs: (a) bright field image, (b) zoom-in view of (a), and (c) corresponding dark field image. TEM images of *S. oneidensis* MR-1 exposed to 30% P-doped Si NCs: (d) bright field image, (e) zoom-in view of (d), and (f) corresponding dark field image.

Figure 4.18 exhibits a series of TEM images of *S. oneidensis* MR-1 cells in the presence of a variety of 5 mg/mL Si NCs after 2-hour exposure (please refer to Figure 4.19 for the data of 30% B/P-doped Si NCs). By taking advantage of electron microscopy, we were able to obtain snapshots of localized interaction at high magnification. As shown in Figure 4.18(a), *S. oneidensis* MR-1 cells appear as rod-shaped, matching previous CytoViva data, and moreover, like other Gram-negative bacteria species, outer membrane vesicles form outside the cell membrane.<sup>71</sup> Such features enable us to distinguish bacteria cells from Si NCs. Figure 4.18(b) through 4.18(d) (and Figure 4.19) shows the interaction between *S. oneidensis* and non-/doped Si NCs. Overall, *S. oneidensis* MR-1 cells remained intact and there was no observable internalization of Si NCs into the bacterial cells. In the case of undoped Si NCs (Figure 4.18(b)), both nanoparticles and cells are well-dispersed in the field of view, but no attachment was observed. Furthermore, dark field TEM was also employed to locate and identify the highly crystalline Si NCs distributed in exposure samples.<sup>72</sup> Clearly, in dark field mode, undoped Si NCs appeared as white bright dots due to their strong electron diffraction at the chosen angle, and so, it is easy to discern them outside individual cells. Interestingly, B-doped Si NCs demonstrated a distinctive interaction pattern. As revealed by both Figure 4.18(c) and Figure 4.19(a), there was significant attachments of B-doped Si NCs to the cell surface of *S. oneidensis* MR-1. Such association was more obvious in the dark field image (lower panel of the right column in Figure 4.18(c)). However, such tight association was not observed for P-doped Si NCs, even when the doping level was as high as 30% (Figure 4.18(d) and Figure 4.19(b)). On the other hand, it suggests that close proximity with Si NCs does not automatically have

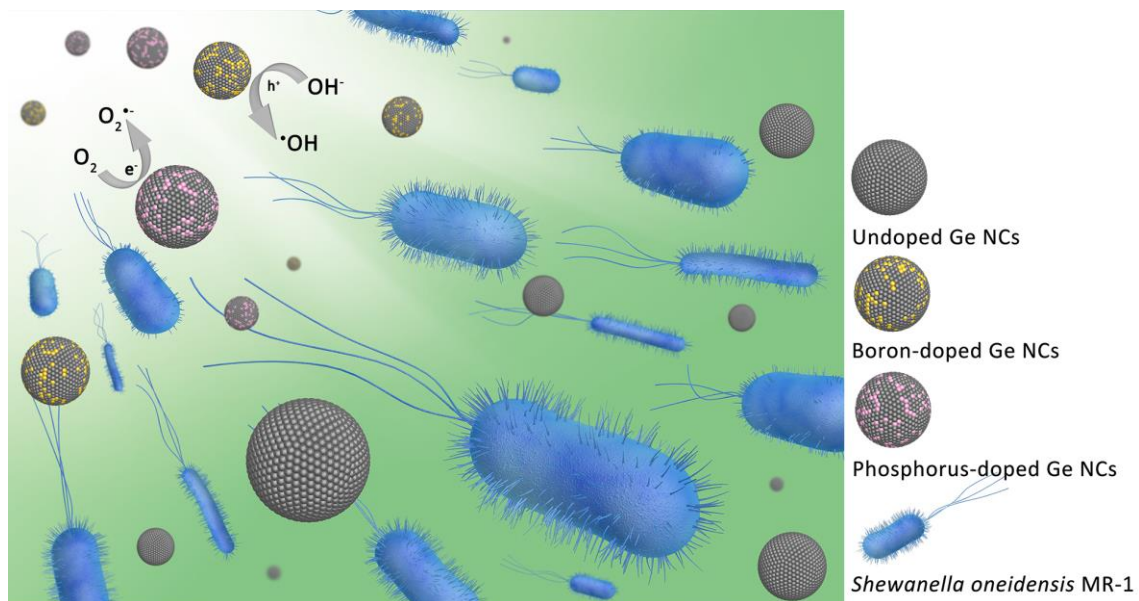
a toxic effect on bacteria, but that high ROS levels caused by P-doped Si NCs in biological matrices indirectly inhibited bacterial colony formation.

#### **4.5 Conclusions**

Our results indicate that the dopant type (boron and phosphorous) and nominal doping level (up to 30%) have little influence on the morphology, particle size distribution, and crystalline structure of Si NCs. However, doping with boron or phosphorus does alter the ROS generation capability of doped Si NCs, dependent on the doping level. P-doped Si NCs have exhibited significant ROS levels in HEPES buffer. Accordingly, P-doped Si NCs had significant toxic effects to *S. oneidensis* MR-1 while undoped Si NCs were non-toxic and B-doped Si NCs only exhibited toxicity during long exposures (at least 2 hours). The interaction patterns of Si NCs with bacteria cells were also thoroughly examined by a combination of CytoViva enhanced dark-field microscopy and bio-TEM. Interestingly, compared to undoped and P-doped Si NCs, B-doped Si NCs showed significant attachment to the bacterial cell surface, but this interaction does not necessarily induce toxicity.

## Chapter 5

### Bacterial toxicity of germanium nanocrystals induced by doping with boron and phosphorous



Reproduced from: Zhi, B.; Yang, Y.; Hudson-Smith, N. V.; Kortshagen, U. R.; Haynes, C. L., Bacterial Toxicity of Germanium Nanocrystals Induced by Doping with Boron and Phosphorous. *ACS Applied Nano Materials*, DOI: 10.1021/acsanm.9b00525. Copyright 2019, with permission from the American Chemical Society.

Bo Zhi is responsible for the design of this research as well as the TEM analysis, XPS tests, EDS tests, bacterial toxicity evaluation, bio-TEM imaging, hyperspectral imaging and the drafting of manuscript.

## 5.1 Overview

Though characterized by excellent optical and electronical performance, traditional Cd or Pb based semiconductor NCs, namely QDs, are arousing environmental concerns due to the toxic heavy metal contents. In this context, germanium nanocrystals have sparked research interests in recent years as Ge is conventionally regarded as an environmentally benign element. While it is well-known that doping with *p/n*-type impurities (such as boron/phosphorus) can tune the original performance of semiconductor materials, few efforts have been devoted to investigating how doped germanium nanocrystals may influence the environment if released into the ecosystem. In this study, we demonstrate that the addition of dopants induces the production of ROS, leading to significant toxic effects towards a model organism, *S. oneidensis* MR-1.

## 5.2 Introduction

Almost thirty years have passed since the first report on semiconductor NCs in 1981,<sup>1</sup> and for more than two decades, myriad of research efforts on colloidal semiconductor NCs (*i.e.*, QDs) have formed a significant branch of nanoscience, due to their notable luminescent performance controlled through the tuning of particle size or shape (via the quantum confinement effect).<sup>2</sup> Typically, an individual QD is comprised of hundreds to thousands of atoms of binary or tertiary semiconductors such as CdSe, ZnTe, InAs, PbSe, or CuInS<sub>2</sub>.<sup>2-5</sup> Various QDs have been extensively explored as harvesters and emitters of light energy and as such, they are relevant for application in photovoltaic devices, photocatalysis, display technology, photoelectrodes, and *in vitro/in vivo* bioimaging.<sup>6-11</sup> However, due to the heavy metal content, such as Cd and Pb, the potential toxic effects of

QDs have aroused serious discussion and debates regarding their environmental impacts as well as potential adverse effects on human health;<sup>2, 12-14</sup> as such, it is necessary to suppress the release of toxic components or replace Cd/Pb with environmentally benign alternatives before QD-inclusive products can be commercialized without safety concerns. Currently, two approaches are proposed to address these concerns: the first focuses on the use of eco-friendly and long-lasting coatings to prevent the breakdown of QDs while the second aims to synthesize Cd/Pb-free QDs with comparable or even improved performance; the latter option is more promising, but requires advances in materials science and nanochemistry.<sup>3, 15</sup>

Recently, fluorescent materials that are made of group IV elements (*e.g.*, C, Si, and Ge) are gaining interest as they are conventionally regarded as inert and non-toxic elements presenting minimal environmental burden and negligible influence on human health.<sup>16-20</sup> Among this group, Ge NCs are attracting attention due to their favorable features. Specifically, like traditional Cd/Pb-based QDs, the optical properties of Ge NCs are tunable; however, due to the relatively large Bohr exciton radius (~24 nm), Ge NCs are more sensitive to quantum confinement effects and thus are expected to exhibit quantum confinement at even larger particle sizes than Cd- or Pb-based QDs.<sup>21, 22</sup> In addition, compared to Si NCs, the narrower bandgap of Ge NCs grant them the capability to absorb in the visible range of the electromagnetic spectrum;<sup>23</sup> after appropriate surface passivation and size control, the emission of Ge NCs (>1600 nm) can reach the far end of the NIR II biological transparency window (1000-1700 nm), while most Si NCs emit in

NIR I region (700-950 nm).<sup>22, 24, 25</sup> This optical range makes Ge NCs excellent candidates for bioimaging applications.<sup>26-28</sup>

Over the last two decades, a wide array of methods has been developed to fabricate Ge NCs, including laser ablation,<sup>29</sup> solution phase synthesis,<sup>28, 30</sup> reductive thermal processing,<sup>31</sup> and electrochemical etching.<sup>32</sup> Compared to those approaches, nonthermal plasma methods are exemplified by high purity products, narrow particle size distributions, and efficient incorporation of dopants.<sup>22</sup> Generally, the introduction of dopants refers to the addition of a small percentage of the non-primary element into the inherent crystalline structure of an intrinsic semiconductor material. Typically, *p*-type semiconductor nanocrystals are synthesized by doping intrinsic materials with trivalent impurities (such as boron, aluminum, or gallium) during fabrication while *n*-type semiconductor nanocrystals are created via the incorporation of pentavalent dopants (such as phosphorus, arsenic, or antimony). For semiconductor nanocrystals, the intentional doping plays a critical role in enhancing the materials' original electrical,<sup>33</sup> optical,<sup>34, 35</sup> and magnetic<sup>36</sup> properties, leading to a wide range of applications for transistors,<sup>23, 37</sup> photovoltaics,<sup>38</sup> thermoelectric devices,<sup>39</sup> and light emitting devices.<sup>40</sup>

However, alongside the incorporation of *p*-/*n*- type dopants, redundant holes ( $h^+$ ) or electrons ( $e^-$ ) are introduced into the nanoscale network as well,<sup>41</sup> making it possible to generate ROS via two potential pathways: oxidation of water at the surface of nanocrystals ( $OH^- + h^+ \rightarrow \cdot OH$ )<sup>42</sup> or reduction of molecular oxygen ( $O_2 + e^- \rightarrow O_2^{\cdot -}$ ).<sup>43, 44</sup> Endogenous ROS accumulation can induce harmful oxidative stress and consequently, damage cellular compartments and disrupt cell function.<sup>45</sup> By this route, the release of doped Ge NCs may

bring about adverse effects to organisms within the environment. In this context, it is necessary to carefully examine the environmental fate of doped Ge NCs and understand their potential influence on the ecosystem before maximal technological impact of Ge NCs can be achieved.

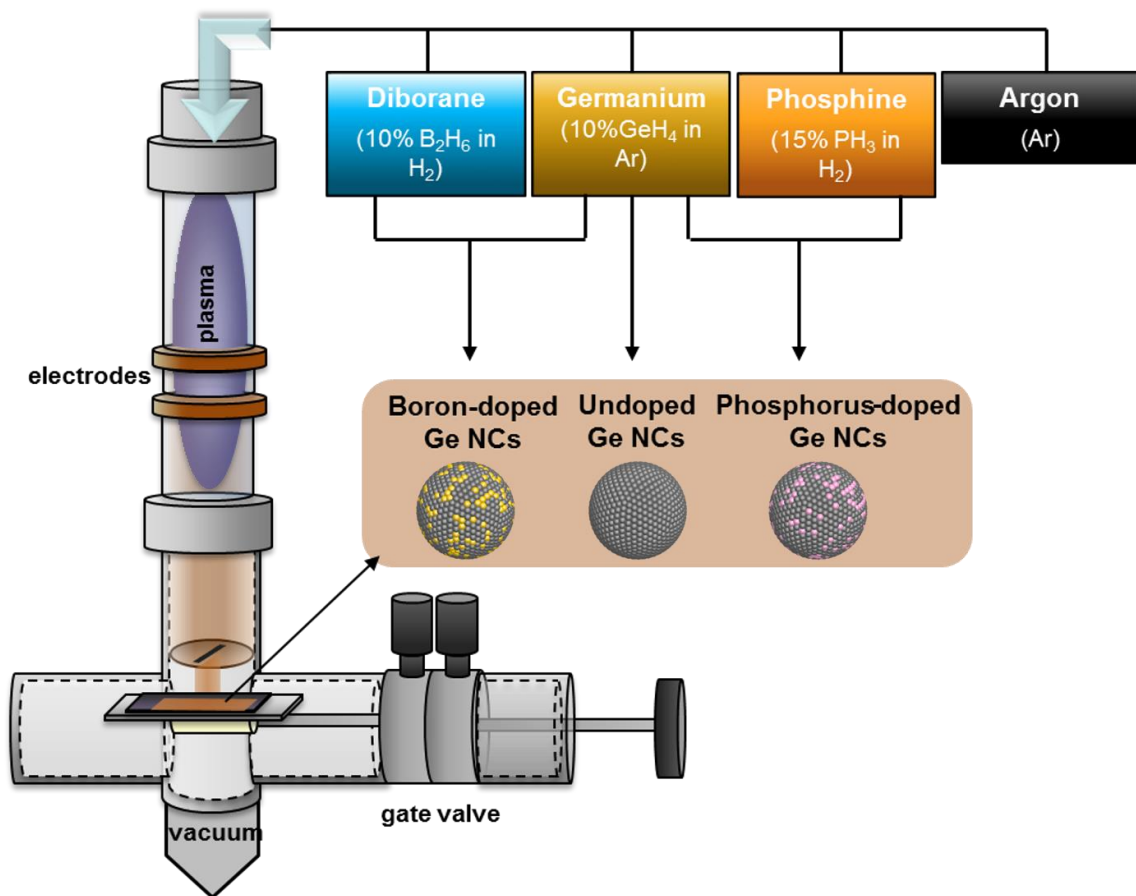
In this work, we report our investigation of the interaction of boron- and phosphorus-doped Ge NCs with *S. oneidensis* MR-1, an environmentally relevant bacterium, which is often used as a model microorganism for bioremediation studies due to its unique capability to reduce metal ions and oxides.<sup>46</sup> Our results demonstrate that the incorporation of boron and phosphorus into the Ge NC structure did not induce remarkable variation in terms of original NC size distributions and material crystallinities but led to ROS generation, especially for 30% P-doped Ge NCs. Thus, while undoped Ge NCs showed negligible influence on bacterial viability during both short-term (15 minutes) and long-term (1 hour) exposures, after 1-hour exposure, 30% P-doped Ge NCs exhibited significant dose-dependent bacterial toxicity while the other tested NCs only showed moderate toxic effects.

## **5.3 Experimental**

### **5.3.1 Ge NC synthesis**

In previous work, germanium tetrachloride ( $\text{GeCl}_4$ ) vapor and hydrogen gas ( $\text{H}_2$ ) were used as precursors to produce undoped Ge NCs using a nonthermal plasma approach.<sup>47</sup> In this study, as shown in Scheme 1, Ar was used as buffer gas and germane ( $\text{GeH}_4$ ) was used to produce undoped Ge NCs without chlorine on the surface, while diborane ( $\text{B}_2\text{H}_6$ )

or phosphine (PH<sub>3</sub>), which were diluted into hydrogen (H<sub>2</sub>) were mixed with GeH<sub>4</sub> to produce boron-doped (B-doped) or phosphorus-doped (P-doped) Ge NCs. The nonthermal plasma reactor set-up is describe in our previous work.<sup>24</sup> The precursor gas rates were adjusted to obtain lightly (~10%) and heavily (~30%) doped Ge NCs as defined by  $X_B = \{2[B_2H_6]/([GeH_4] + 2[B_2H_6])\} \times 100\%$  and  $X_P = \{[PH_3]/([GeH_4] + [PH_3])\} \times 100\%$  where [GeH<sub>4</sub>], [B<sub>2</sub>H<sub>6</sub>], and [PH<sub>3</sub>] represent the gas flow rates. The final incorporation of dopants in the Ge NCs was lower than these calculated nominal values based on gas flow rates.



**Scheme 5.1.** Illustration of the plasma synthesis set-up for undoped and doped Ge NCs.

### 5.3.2 TEM imaging

The preparation of TEM samples was conducted by dispersing Ge NCs into ultrapure water via 10 min sonication. ~2  $\mu\text{L}$  of suspension was dropcast onto ultra-thin lacey carbon films (Ted Pella Inc.). The grid was dried under ambient conditions. Ge NC images were obtained using a FEI Tecnai G<sup>2</sup> F30 transmission electron microscope with an accelerating voltage of 300 kV.

For bio-TEM imaging, bacteria cells treated with various Ge NCs were prepared through a typical process of fixation, dehydration, and resin embedding. In brief, *S. oneidensis* MR-1 was suspended in HEPES at an OD<sub>600</sub> of 0.8 and exposed to 1000 mg/L of each undoped and doped Ge NC for one hour. Bacterial cells were pelleted, washed with 0.1 M sodium cacodylate buffer three times, and then fixed with a 2.5% glutaraldehyde in 0.1 M cacodylate buffer for 50 minutes. The pellet was flipped halfway through the fixation time to assure fixation throughout the pellet. Samples were washed again with sodium cacodylate and dehydrated with a series of aqueous ethanol solutions (30%, 50%, 70%, 80%, 95%, and 100%). After three washes with propylene oxide, samples were incubated with a 2:1 propylene oxide: resin mixture for two hours, 1:1 propylene oxide: resin overnight, fresh propylene oxide: resin for four hours, and then in pure resin overnight. The resin was replaced with fresh resin and cured in a 40°C oven for 24 hours, followed by a 60°C oven for 48 hours. Slices of ~70 nm thickness were cut with a Leica EM UC6 Ultramicrotome and placed on 200 mesh copper grids with carbon and formvar supports for TEM imaging with a FEI Tecnai G<sup>2</sup> F30 at 100 kV (cells) or 300 kV (NPs), in either bright field or dark field mode.

### 5.3.3 Powder XRD

Sample powder was deposited on the glass substrate. Powder XRD patterns were collected using a powder Bruker D8 Discover 2D X-ray diffraction system with a copper  $K\alpha$  X-ray source (wavelength 1.54 Å).

### 5.3.4 FTIR and XPS analyses

Undoped and doped Ge NCs were deposited onto an aluminum-coated silicon wafer substrate from the nonthermal plasma. Spectra were obtained using a Bruker Alpha FTIR spectrometer in a nitrogen-purged glovebox.

XPS measurements were conducted using PHI 5000 VersaProbe III equipped with Al  $K\alpha$  source (1486.6 eV). X-ray source type is Focused X-ray Source (FXS) and X-ray setting is 100 $\mu$ 25W15KV (X-ray beam size: 100  $\mu$ m, power: 25 W, and e-beam energy: 15 kV). High-resolution scans of Ge (Ge2p&3d), C (1s), and O (1s) atoms were performed with a pass energy of 55 eV. It is important to note that the quantitative doping levels with boron and phosphorus could not be detected by XPS because Ge peaks (Ge3s 180.1 eV and Ge3p ~120-125 eV) overlapped with those of B (B1s 188 eV) and P (P2s 189 eV and P2p ~135 eV).

### 5.3.5 Bacterial culture and Ge NC exposure

*S. oneidensis* stock was stored at -80 °C before being inoculated onto LB agar plates. The plates were incubated at 30 °C until discernible colonies formed. About five colonies were transferred into LB broth to prepare a bacterial suspension, which was incubated in an orbital shaker for 3 to 4 hours. Bacteria cells were collected before entering stationary

phase, as determined by the OD<sub>600</sub>. Bacteria cells were then pelleted by centrifugation at 750 × g for 10 minutes, washed with DPBS buffer and re-dispersed into HEPES buffer (pH = 7.4). The bacterial suspension was then diluted to ~0.2 OD<sub>600</sub> so that the cell density was ~2×10<sup>8</sup> CFUs/mL. The concentrations of Ge NC working solutions were 100, 1000, and 10000 mg/L. Subsequently, the bacterial suspension was treated with Ge NC solutions (with a volume ratio of 9:1, thus, the exposure concentrations were 10, 100, and 1000 mg/L, respectively), and incubated for 15 minutes or 1 hour at 30 °C.

### 5.3.6 Colony counting assays

To gauge the potential acute toxic effects of Ge NCs, an adapted colony counting assay (drop plate method) was applied for the bacterium *S. oneidensis* MR-1.<sup>17, 18</sup> Bacterial suspensions of *c.a.* 2×10<sup>8</sup> CFUs/mL (~0.2 OD<sub>600</sub>) were treated with Ge NCs at various concentrations (*i.e.*, 10, 100, and 1000 mg/L, respectively). A subsequent 10-fold serial dilution was performed to dilute the exposure suspensions to a proper cell density (DF was 10<sup>-4</sup>). Six 8 µL droplets of diluted bacteria exposure suspensions, as well as untreated negative controls, were dropped onto LB agar plates, which were dried under air flow in a biohood and then incubated at 30 °C for 18 hours until discernible colonies formed. The bacterial viability for each treatment was expressed as a ratio of colony counts to the negative control samples. The experiments were accomplished using five different types of Ge NCs (that is, undoped and doped ones) and repeated over four biological replicates for each NC type.

In addition, colony counting assays were applied to determine the toxicity of the supernatants of doped Ge NCs. Specifically, doped Ge NCs were dispersed into HEPES

buffer via a rigorous vortexing and sonication to prepare 10,000 mg/L suspensions. Afterwards, these suspensions were centrifuged down to a pellet at  $15000 \times g$  and supernatants were collected. 180  $\mu\text{L}$  of bacteria suspension was exposed to 20  $\mu\text{L}$  of each supernatant to simulate 1000 mg/L exposure, followed by toxicity assessments at 15-minute and 1-hour time intervals.

### 5.3.7 Curcumin method and ascorbic acid method

These colorimetric techniques were performed to reveal the presence of any released boron or phosphorus compounds, respectively.<sup>48, 49</sup>

Specifically, for the curcumin method, 0, 2.5, 5.0, 10.0, 15.0, and 20.0 mg/L boric acid solutions were prepared as boron standards. 200  $\mu\text{L}$  of each standard and unknown samples (supernatants of 1000 mg/L boron doped Ge NCs) were transferred to microcentrifuge tubes and acidified using 100  $\mu\text{L}$  of 0.1 M HCl. Afterwards, 70  $\mu\text{L}$  of extraction solution (2-ethyl-1,3-hexanediol 10% (v/v) in chloroform) was added to each tube and mixed by vortexing. The mixtures were centrifuged at  $15,000 \times g$  for 5 min to separate the organic phase. 50  $\mu\text{L}$  of the organic-depleted solution were transferred into a new tube including 200  $\mu\text{L}$  of acid mix (sulfuric acid (conc.) and acetic acid (conc.) in 1:1 (v/v) ratio) and underwent a vigorous vortexing. Then, 250  $\mu\text{L}$  of curcumin solution (1 mg/ml, dissolved in methyl-isobutyl-ketone) was added to each tube, and the mixtures were agitated until they formed a homogenous dark red color, after which the tubes were centrifuged at  $15,000 \times g$  for 1 min and the reaction mixtures were incubated at room temperature. After 1 h, the reactions were terminated by adding 500  $\mu\text{L}$  of water, and the tubes were centrifuged again to form well-defined phase separation. The upper organic

phase was transferred into a 96-well UV microplate, and the absorbance was recorded at 540 nm. The absorbance values for the boron standards were plotted against boron quantities to construct a calibration curve, which was used to quantify the amount of released boron. In parallel, for the ascorbic acid method, 0, 1.0, 2.5, 5.0, 10, and 25 mg/L  $\text{KH}_2\text{PO}_4$  solutions were used as phosphorus standards while the supernatants collected from 1000 mg/L P-doped Ge NCs were completely digested into orthophosphate using ammonium persulfate, which was further gently boiled for around 30 minutes. In addition, a combined reagent was prepared by mixing 5 mL of 2.5 M  $\text{H}_2\text{SO}_4$ , 0.5 mL of 2.8 mg/mL antimony potassium tartrate solution, 1.5 mL of 40 mg/mL ammonium molybdate solution, and 3 mL of 0.05 M ascorbic acid solution. Afterwards, 200  $\mu\text{L}$  of the combined reagent was mixed with 200  $\mu\text{L}$  of each of the phosphorus standards and supernatants in 1.5 mL tubes, and the mixtures were incubated for 5-10 minutes in the ambient environment, after which 200  $\mu\text{L}$  of each mixture were transferred into a 96-well UV microplate for the measurement of absorbance at 670 nm. A standard curve was prepared based on the assay results and used to determine the concentration of phosphorus in the supernatants.

### 5.3.8 Measurement of total ROS generation

Total ROS production was assessed using the DCFDA assays under abiotic conditions (*i.e.*, bacteria cells not included).<sup>43</sup> Specifically, 50  $\mu\text{L}$  of DCFDA working solution (0.2 mM) was mixed with 200  $\mu\text{L}$  of Ge NC suspensions at various concentrations (10, 100, and 1000 mg/L, respectively). In addition, negative control experiments were performed in HEPES buffer, while positive control experiments in 0.1 M hydrogen peroxide solution. Each condition was repeated three times in 96-well optical bottom plates (Costa, Corning,

NY), which were transferred to a Synergy 2 Multi-Mode microplate reader (BioTek, Winooski, VT). The fluorescence counting was performed at Ex/Em: 485/525 nm over the course of 1.25 hours.

In addition, HPF assays and DHE assays were conducted to probe ROS speciation, namely hydroxyl radical ( $\cdot\text{OH}$ ) and superoxide radical ( $\text{O}_2^{\cdot-}$ ), respectively.<sup>50, 51</sup> To enhance the measurable fluorescence signals in both assays, Ge NC suspensions as high as 10000 mg/L were used to react with the HPF and DHE dyes. To be more specific, for HPF assays, the negative control reference was HEPES buffer while the positive control reference was the mixture of 10  $\mu\text{M}$  iron(II) perchlorate and 0.1 mM of  $\text{H}_2\text{O}_2$ ; for the DHE assays, the negative control reference was 300 mM N-acetyl cysteine solution while the positive control reference was 150  $\mu\text{M}$  antimycin A solution. To initiate the reactions, 10  $\mu\text{M}$  HPF or DHE solutions were mixed with the negative control, the positive control, and Ge NC suspensions, respectively. At 15-minute and 1-hour intervals, mixtures were centrifuged down to pellets at a speed of  $16,000 \times g$ . To minimize the influence from the color of the Ge NC suspensions, colorless supernatants were collected and transferred into a microplate reader for emission measurement. The filter set was excitation/emission of 490/515 nm for HPF assays while it was 518/606 nm for DHE assays.

### 5.3.9 Hyperspectral imaging analysis

The association between *S. oneidensis* MR-1 and varied Ge NCs were visualized using CytoViva enhanced darkfield microscopy and hyperspectral microscopy (CytoViva Inc., Auburn, AL). The entire system is composed of an upright optical microscope (Olympus

BX43), a microscope digital camera (AmScope MU1000), a visible-near infrared hyperspectral imaging system, and a 150W quartz halogen light source (Fiber-Lite® DC-950). Reference samples are bacteria culture solution (OD = 0.5) and Ge NC suspensions (100 mg/L), which were used for spectral library construction; samples used for hyperspectral mapping were bacteria exposure solution with different Ge NCs (exposure time: 1 hour, OD: 0.5, Ge NC concentration: 100 mg/L). Regarding sample mounting, typically, bacteria exposure solutions were dropcast (~3  $\mu$ L) onto a 3"x1" glass slide and then sealed with an 18x18mm coverglass. Slides were examined under 100x magnification in darkfield mode and then subsequent hyperspectral scans were conducted using ENVI 4.8 software. "Pushbroom hyperspectral scanning" was performed using 60-80% light source intensity (depending on the intensity of sample reflectance) and 0.25s exposure time per line (696 lines in total for a typical full scan). Each pixel of the hyperspectral image (*i.e.*, hyperspectral 3D datacube) contains its spatial information (x and y) and corresponding reflectance spectral data (z). Analysis of hyperspectral data (mapping) was performed using SAM classification, which automatically compared and matched pixels on the hyperspectral data of bacteria exposure solution to the reference libraries obtained by analyzing bacteria and Ge NCs separately in HEPES buffer. Pixels in the images that match the hyperspectral signature were highlighted in red (*S. oneidensis* MR-1) or green (Ge NCs). As the SAM method is based on only the direction of pixel vectors but not recorded light intensity, the classification is insensitive to the illumination of the sample in the recording.

#### **5.4 Results and discussion**

### 5.4.1 Materials characterization of Ge NCs

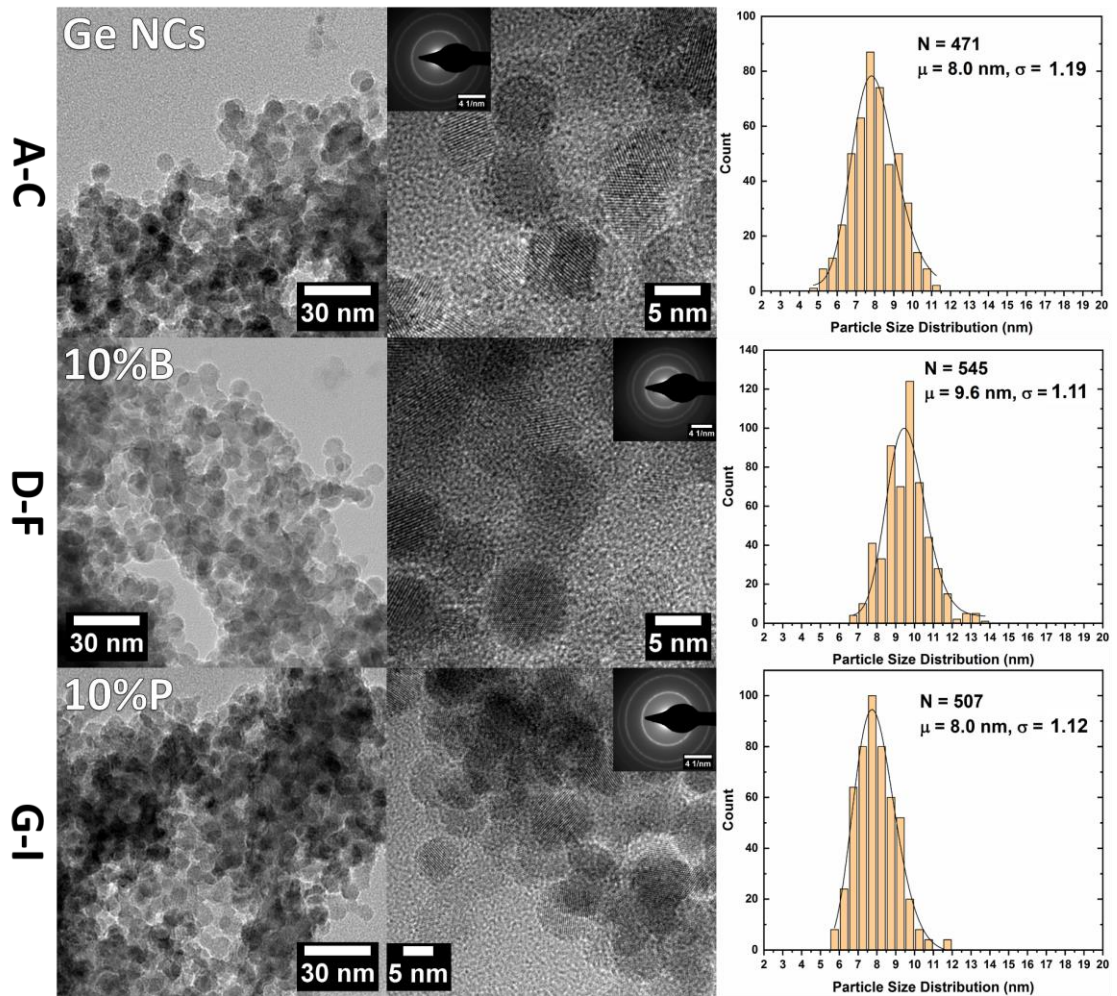


**Figure 5.1.** TEM, high-resolution TEM (inset: SAED patterns), and PSDs of (a-c) undoped Ge NCs, (d-f) 10% B-doped Ge NCs, and (g-i) 10% P-doped Ge NCs. The PSDs are fit to log-normal distributions with geometric mean  $\mu$  and geometric standard deviation  $\sigma$ ; the number of counts (N) is approximately 500.

A wide range of characterization techniques were applied to perform a careful examination on Ge NCs fundamental properties. As shown in both Figure 1, particle sizes and morphologies are revealed by TEM. Generally, all five Ge NC types show similar round shapes with moderate agglomeration and similar PSDs, within the range of 7-10 nm. Furthermore, by comparing the SAED patterns and HRTEM images, it is confirmed

that all Ge NCs also exhibit similar crystalline structures. Based on this similarity, we chose the SAED data from the undoped Ge NCs (Figure 5.1b) as representative to calculate  $d$ -spacing values (Table 5.1). Specifically, there are at least three visible diffraction rings, and the  $d$ -spacing is the reciprocal of each ring radius, which corresponds to the (111), (220), and (311) planes of the diamond cubic structure (Ge, PDF#04-0545,  $Fd-3m$ ).<sup>47</sup> As such,  $d_{111}$  (0.331 nm) is in agreement with the lattice fringe distance (0.325 nm) calculated using the HRTEM image (exposed (111) plane) and consistent with previous publications (0.327 nm).<sup>52</sup> Tables 5.2-5.5 reveal the  $d$ -spacing values for doped Ge NCs.

**Table 5.1.**  $d$ -spacing values of undoped Ge NCs (calculated using the SAED pattern).

Ring radius (nm <sup>-1</sup> )	$d$ -spacing (nm)	( $hkl$ )
<b>3.021</b>	0.331	(111)
<b>5.124</b>	0.195	(220)
<b>5.989</b>	0.167	(311)

**Table 5.2.**  $d$ -spacing values of 10% B-doped Ge NCs (calculated using the SAED pattern).

Ring radius (nm <sup>-1</sup> )	$d$ -spacing (nm)	( $hkl$ )
<b>3.135</b>	0.319	(111)
<b>5.291</b>	0.189	(220)
<b>6.211</b>	0.161	(311)

**Table 5.3.**  $d$ -spacing values of 30% B-doped Ge NCs (calculated using the SAED pattern).

Ring radius (nm <sup>-1</sup> )	$d$ -spacing (nm)	( $hkl$ )
<b>3.031</b>	0.330	(111)
<b>5.076</b>	0.197	(220)
<b>5.780</b>	0.173	(311)

**Table 5.4.** *d*-spacing values of 10% P-doped Ge NCs (calculated using the SAED pattern).

Ring radius (nm <sup>-1</sup> )	<i>d</i> -spacing (nm)	( <i>hkl</i> )
3.049	0.328	(111)
4.926	0.203	(220)
5.747	0.174	(311)

**Table 5.5.** *d*-spacing values of 30% P-doped Ge NCs (calculated using the SAED pattern).

Ring radius (nm <sup>-1</sup> )	<i>d</i> -spacing (nm)	( <i>hkl</i> )
3.077	0.325	(111)
5.464	0.183	(220)
5.883	0.170	(311)

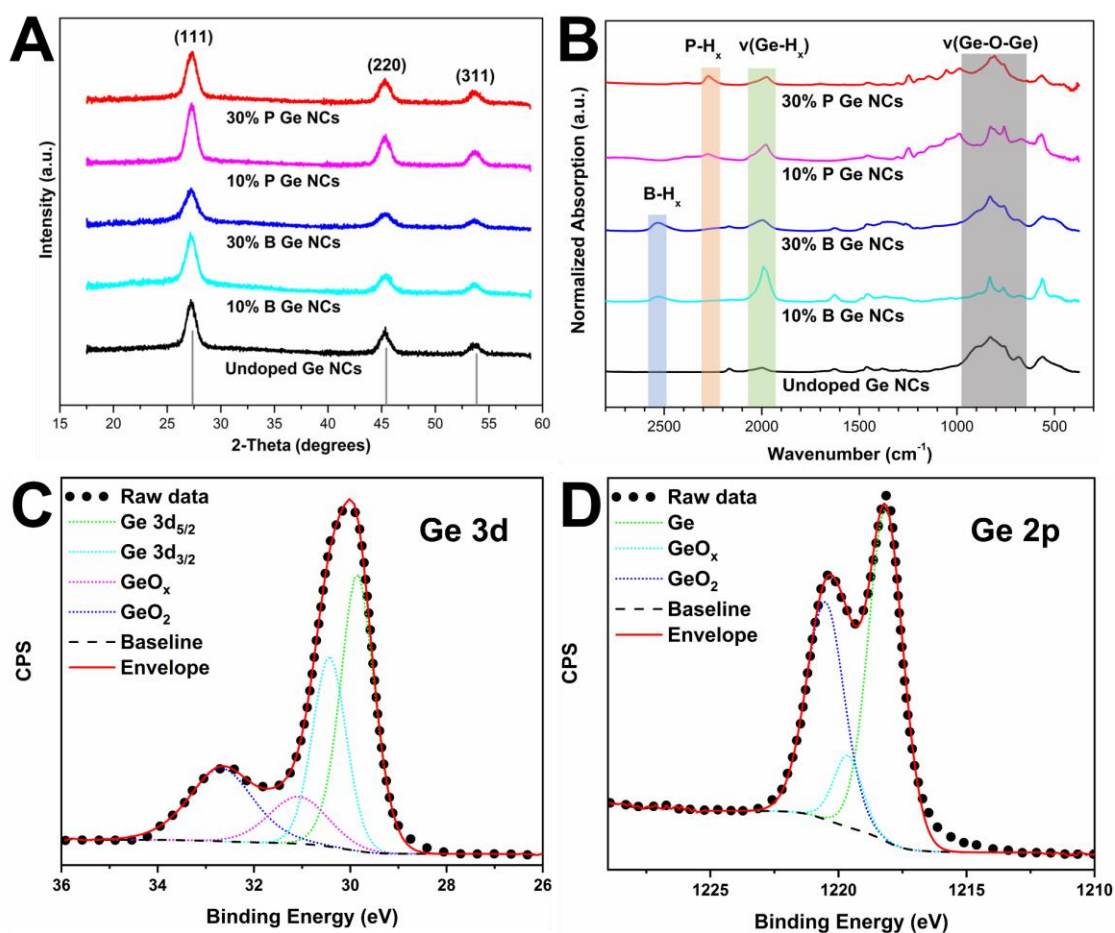


**Figure 5.2.** (a) XRD and (b) FTIR spectra for Ge NCs; high-resolution (c) Ge 3d and (d) Ge 2p XPS spectra for undoped Ge NCs.

As TEM imaging samples only a small percentage of the total sample, we also applied powder XRD to probe the overall crystallinity of Ge NCs, as shown in Figure 5.2a. The XRD spectra exhibit several characteristic diffraction peaks that can be assigned to the (111), (220), and (311) planes of diamond cubic Ge NCs (PDF#: 04-0545, Ge, *Fd-3m*). More importantly, the diffraction patterns are almost identical regardless of doping state, confirming that neither boron nor phosphorus dopants induce variation to the original crystal structures of Ge NCs, in line with the SAED and HRTEM results. This is similar to characteristics observed in our previous work on silicon nanocrystals (Si NCs).<sup>18</sup> In addition, the grain sizes of all Ge NCs are calculated to be 6-8 nm by the Scherrer equation. As TEM images depict the outline of an entire particle while XRD probes the crystalline domain, the difference between TEM size range (7-10 nm) and XRD size range (6-8 nm) indicates that there may be a variation from the periphery to the center, motivating us to investigate the surface properties of Ge NCs via FTIR.

Figure 5.2b shows the FTIR results for the Ge NCs synthesized via nonthermal plasma. Ge-H<sub>x</sub> stretching modes are present at around 2000 cm<sup>-1</sup> for all Ge NC samples, which means that NCs are largely hydrogen terminated.<sup>53</sup> For B-doped Ge NCs, the boron-hydride stretch modes are visible at ~2500 cm<sup>-1</sup>; for P-doped Ge NCs, the phosphorus-hydride stretches can be seen at ~2300 cm<sup>-1</sup>.<sup>54</sup> These stretching modes are more prominent for heavily (30%) doped samples than lightly (10%) doped samples while neither of them is observable for undoped Ge NCs. In addition, as Ge is subject to oxidation under ambient conditions,<sup>55</sup> all Ge NCs exhibit broad shoulders at ~800 cm<sup>-1</sup> that can be ascribed to the

Ge-O-Ge stretching;<sup>56</sup> however, these features are not present for freshly synthesized samples (Figure 5.3).

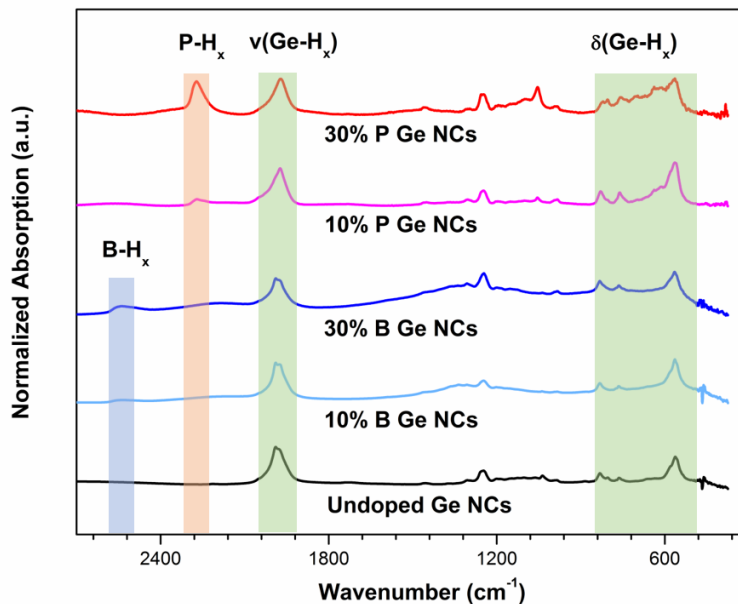


**Figure 5.3.** FTIR spectra for freshly synthesized Ge NCs.

As the surface chemistry of colloidal particles influences how they interact with bacteria cells, it is necessary to understand the surface oxidation status of air stable Ge NCs. Hence, we employed high-resolution XPS to probe the Ge 3d and 2p energy levels. As the spectra appear almost identical for all Ge NCs, data for undoped Ge NCs are chosen as representative for further discussion, as depicted in Figure 5.2c and 5.2d, respectively. The split spin-orbit components (3d<sub>3/2</sub> and 3d<sub>5/2</sub>) for the element Ge in the 3d spectra (Figure 5.2c) peak around 29.8-30.5 eV, while sub-oxides (GeO<sub>x</sub>, x<2) and oxides (GeO<sub>2</sub>) are located in a higher binding energy range between 31.0-32.7 eV.<sup>55</sup> The presence of zero-valent Ge and oxide-related Ge are visible in the 2p spectra (Figure 5.2d) as well. Interestingly, the XPS peak area for oxidized Ge (namely, GeO<sub>x</sub> and GeO<sub>2</sub>) in the 3d

region is relatively smaller than that in the 2p region: for a qualitative comparison, the peak area ratio for oxidized Ge/ non-oxidized Ge is roughly 30/70 in the 3d spectra while it is around 50/50 in the 2p spectra. It is well-known that the inelastic mean free path ( $\lambda_{\text{IMFP}}$ ) of an ejected electron is a function of its kinetic energy (KE), and the XPS sampling depth (where 95.7% photoelectrons emanate) is defined as  $3 * \lambda_{\text{IMFP}}$ .<sup>57</sup> The  $\lambda_{\text{IMFP}}$  of Ge 3d (KE = 1480.3 eV) and Ge 2p (KE = 270.4 eV) are 28.7 Å and 8.58 Å, respectively.<sup>58</sup> As such, corresponding sampling depths are 8.61 nm and 2.57 nm for photoelectron recoil from 3d and 2p energy levels, respectively. In other words, Ge 3d signals originate from deeper layers than Ge 2p signals. Therefore, these data reveal that for air stable Ge NCs, the oxidation degree of the outer NC region (~50%) is more severe than that for NC inner regions (~30%).

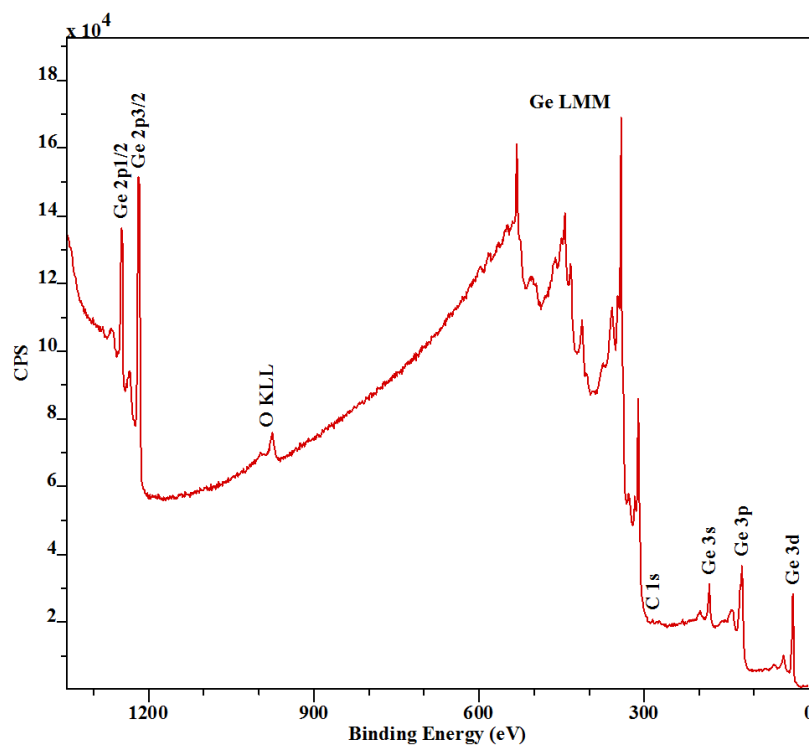


**Figure 5.4.** XPS survey spectrum for undoped Ge NCs.

As the nominal doping percentage (*i.e.*, 10% or 30%) indicates the precursor gas flow rate during syntheses but not actual dopant incorporation level, we attempted to investigate the actual doping levels for boron and phosphorus by XPS survey scan. Unfortunately, due to peaks overlapping with one another, it is difficult to distinguish oxygen, boron, and phosphorus. As shown in Figure 5.4, the Ge LMM peak groups (300-600 eV) overlap with O 1s (531 eV), and for boron and phosphorus, Ge 3s (180 eV) overlaps with B 1s (188 eV) and P 2s (189 eV) while Ge 3p (120-125 eV) overlaps with P 2p (135-136 eV). Therefore, we chose EDS (integrated with TEM) to assess B and P doping levels. The summary of atomic percentages is available in Figure 5.5 and Table 5.6. Overall, air stable Ge NCs exhibit approximate 70% germanium and 20% oxygen. Specifically, the nominally 10% B-doped Ge NCs contain  $3.8 \pm 0.7\%$  incorporated boron, while the boron doping increases to  $14.1 \pm 1.9\%$  for the nominally 30% B-doped nanocrystals. For P-doped Ge NCs, the phosphorus % are  $1.5 \pm 0.1\%$  and  $5.5 \pm 0.2\%$  for the nominally 10% and 30% P-doped NCs, respectively; these actual doping percentages are similar to the values for doped Si NCs described in our previous work.<sup>18</sup>

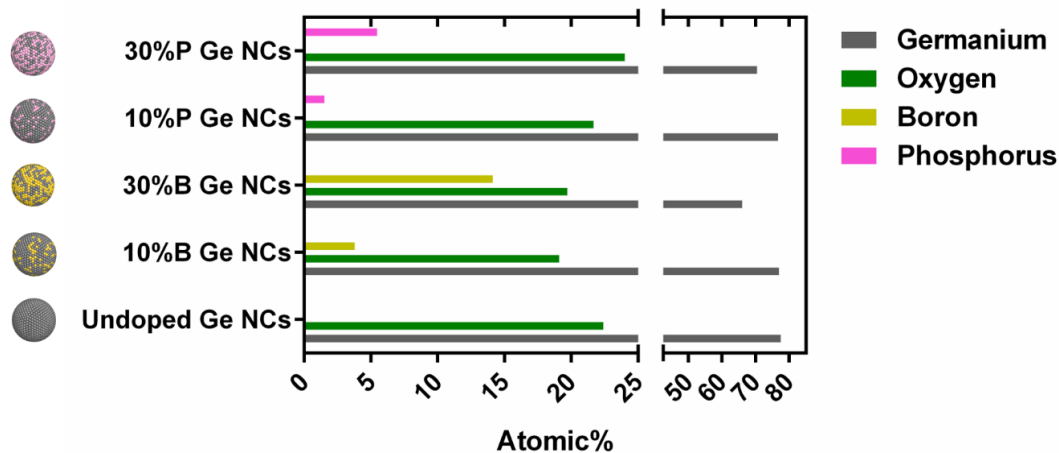


**Figure 5.5.** Comparison of doping levels of Ge NCs.

**Table 5.6.** Atomic percentage summary of Ge NCs.

Atomic% (N = 4 or 5)	Germanium	Oxygen	Boron	Phosphorus
Undoped Ge NCs	77.6 ± 1.1	22.4 ± 1.1	N/A	N/A
10%B Ge NCs	77.1 ± 3.9	19.1 ± 3.7	3.8 ± 0.7	N/A
30%B Ge NCs	66.1 ± 1.8	19.7 ± 1.8	14.1 ± 1.9	N/A
10%P Ge NCs	76.8 ± 0.7	21.7 ± 0.6	N/A	1.5 ± 0.1
30%P Ge NCs	70.5 ± 0.3	24.0 ± 0.5	N/A	5.5 ± 0.2

**Table 5.7.** PSD and  $\zeta$ -potential summary for undoped and doped Ge NCs.

Ge NCs	Undoped	10% B	30% B	10% P	30% P
<b>TEM diameter<sup>a</sup> (nm)</b>	8.0 ( $\sigma = 1.2$ )	9.6 ( $\sigma = 1.1$ )	8.7 ( $\sigma = 1.1$ )	8.0 ( $\sigma = 1.1$ )	7.7 ( $\sigma = 1.1$ )
<b>XRD grain size (nm)</b>	7.7	7.0	6.1	7.7	7.4
<b>DLS diameter (nm) in water</b>	40 ± 3	32 ± 1	42 ± 1	48 ± 1	28 ± 1
<b>PDI in water</b>	0.25 ± 0.04	0.24 ± 0.05	0.22 ± 0.05	0.26 ± 0.06	0.30 ± 0.03
<b>DLS diameter (nm) in HEPES</b>	36 ± 3	34 ± 2	40 ± 1	49 ± 1	27 ± 2
<b>PDI in HEPES</b>	0.25 ± 0.03	0.20 ± 0.04	0.16 ± 0.04	0.21 ± 0.02	0.36 ± 0.07
<b><math>\zeta</math>-potential (mV) in water</b>	-30.6 ± 1.1	-21.3 ± 1.9	-29.3 ± 2.1	-22.8 ± 1.3	-28.2 ± 2.3
<b><math>\zeta</math>-potential (mV) in HEPES</b>	-25.4 ± 1.0	-39.2 ± 0.8	-37.2 ± 1.2	-19.5 ± 2.7	-24.9 ± 1.8

<sup>a</sup>Particle size distributions (PSDs) were analyzed using TEM particle counting data (*c.a.* 500 particles counted). As Ge NCs were prepared via plasma method (an aerosol-related chemical process), the log-normal function was applied to fit the size histograms to determine the average particle sizes (geometric mean diameter, with  $\sigma$  representing geometric standard deviation).<sup>59</sup>

To optimize subsequent bacterial exposure experiments, the stability of Ge NCs was characterized by DLS in both ultrapure water and HEPES buffer. Ge NC suspensions were sonicated for 15-20 minutes prior to measurements. Table 5.7 summarizes the PSD and surface charge status of Ge NCs considered herein alongside previous PSD results

calculated using TEM and XRD. As revealed in TEM images, moderate agglomeration of Ge NCs is visible for all types of Ge NCs and as such, the hydrodynamic diameters detected by DLS are much larger (~30-50 nm) than those measured via TEM and XRD results (<10 nm). Accordingly, the PDI in either water or HEPES buffer were measured to be greater than 0.2, indicative of moderately polydisperse distributions.<sup>60</sup> In addition,  $\zeta$ -potential values fall in the range of -20 to 40 mV, demonstrating an acceptable colloidal stability.<sup>61</sup> It is also worth noting that the transfer from water to HEPES buffer did not induce a dramatic change to the  $\zeta$ -potentials, proving that the buffer media used for following bacterial exposures has negligible influence on Ge NC surface charge.

#### 5.4.2 Bacterial toxicity assessment of Ge NCs

The colony counting assay, or CFU count method, serves as a gold standard for bacterial cell assessment and has been applied to evaluate the bacterial toxic effects of a variety of nanomaterials.<sup>12, 18</sup> In this work, the colony counting assay (drop plate method) was used to investigate the doping level and material concentration-dependent responses of *S. oneidensis* MR-1 exposed to five different types of Ge NCs, namely, undoped, 10%/30% B-doped, and 10%/30% P-doped Ge NCs, with Ge NC concentrations ranging from 10 to 1000 mg/L. Based on our previous work, such a concentration range is optimized to reveal the toxic effects of semiconductor nanocrystals at low, medium, and high doses.<sup>12, 18</sup> In brief, *S. oneidensis* MR-1 cell suspensions were exposed to Ge NCs in HEPES media and subsequently dropcast onto agar plates. After an incubation of 16 to 18 hours, observable colonies form and then counting was performed. Thus, a decrease in the number of

colonies compared to the negative control can be used to quantify the toxic effects of Ge NCs. Figure 5.6 depicts the toxicity evaluation results for undoped and doped Ge NCs both for a short exposure (15 minutes, upper panel) and a long exposure (1-hour, lower panel).

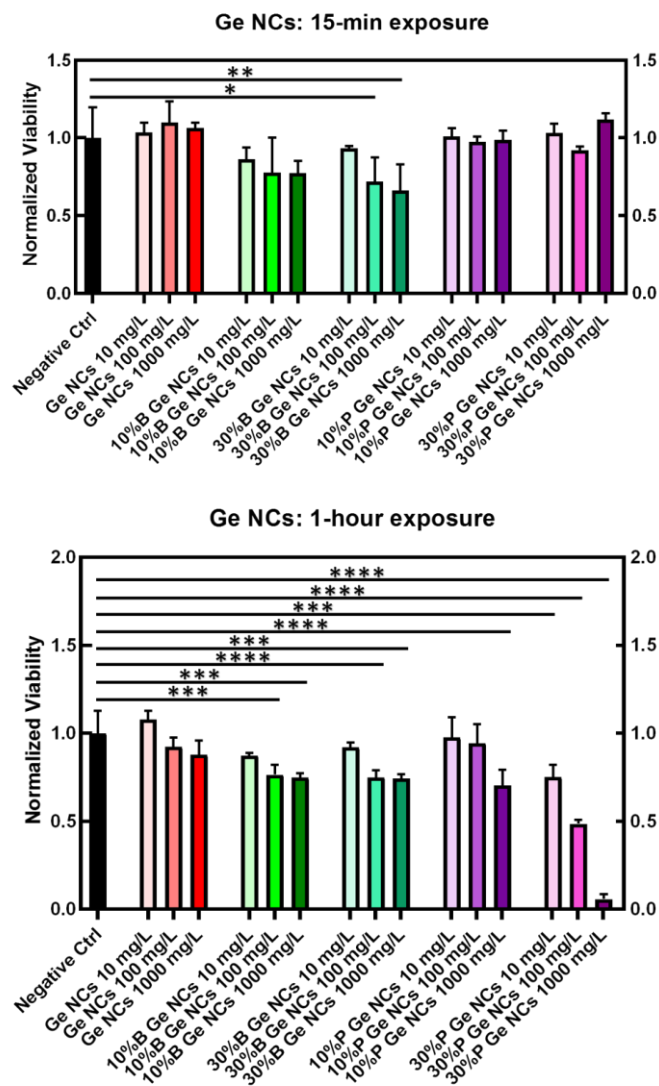


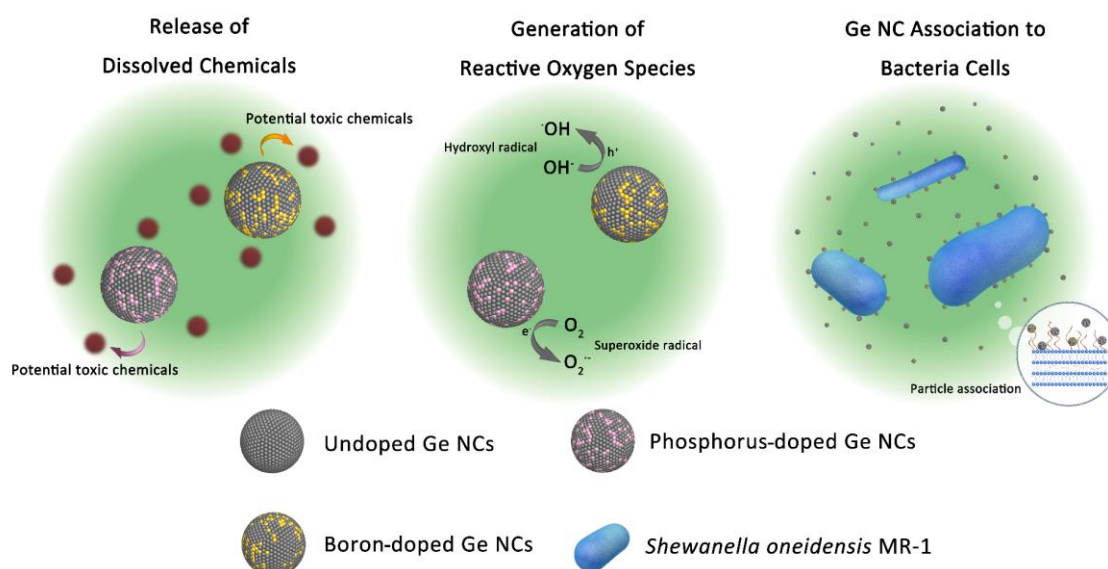
**Figure 5.6.** Bacterial viability of *S. oneidensis* exposed to Ge NCs, evaluated by the colony counting assay (drop plate method). The asterisks indicate statistical significance level: \* $p < 0.05$ , \*\* $p < 0.01$ , \*\*\* $p < 0.001$ , \*\*\*\* $p < 0.0001$  (examined by one-way ANOVA, followed by Dunnett's multiple comparison tests,  $n = 4$  or 5 biological replicates).

For the 15-min exposure, it is noticeable that only high doses (100 and 1000 mg/L) of 30% B-doped Ge NCs show significant toxicities, while the rest exhibit overall low or negligible toxic effects. Though a minor reduction in viability is observed for 5% B-doped, this is not a statistically significant toxicity to the bacteria cells. However, after 1-hour exposure, the story unfolds differently: undoped Ge NCs remain non-toxic and the overall viabilities show a steady decrease for bacteria exposed to the Ge-doped NCs of higher concentrations, indicative of a concentration dependency of the general toxicity. Specifically, 30% P-doped Ge NCs, especially at dose as high as 1000 mg/L, prove to be extremely toxic in the long-term exposure, eliminating nearly the entire bacteria population. Similarly, 10% P-doped NCs exhibit moderate toxic effects at 1000 mg/L, though ~70% of the colonies survive. For B-doped Ge NCs, the toxicity of either 10% or 30% is mild at 100 and 1000 mg/L while negligible at 10 mg/L. Overall, undoped Ge NCs are determined to be not toxic (based on colony-forming ability) through all measurements, but doped ones significantly compromise colony viability over a longer exposure time and especially at high concentrations, similar to our previous findings on doped Si NCs.<sup>18</sup> In addition, the toxicity of P-doped Ge NCs also correlates to their phosphorus doping levels while such correlation is not observed for B-doped Ge NCs.

#### 5.4.3 Investigation of the microbial toxicity mechanism(s) of Ge NCs

To gain a better understanding as to the nature of the bacterial toxicity triggered by doping Ge NCs with boron/phosphorus, we worked to elucidate how doped Ge NCs interact with *S. oneidensis* MR-1 cells. We investigated three hypothetical pathways, as illustrated in Scheme 5.2: A) doped Ge NCs may release boron/phosphorus-related compounds via

dissolution, especially during a long-term exposure, and these chemical species may be harmful to bacteria cells;<sup>62</sup> B) doping with boron/phosphorus atoms introduces free holes ( $h^+$ ) or electrons ( $e^-$ ) into the original Ge NC structures, leading to the production of lethal ROS via either the oxidation of water or the reduction of molecular oxygen;<sup>43</sup> and C) if doped Ge NCs are physically associated with the bacterial cells, they may penetrate or disrupt the outer membrane of *S. oneidensis* MR-1, damaging the cell integrity.<sup>63</sup> In this context, additional experimental efforts were invested to test each of aforementioned hypotheses.



**Scheme 5.2.** Illustration of potential interaction pathways between doped Ge NCs and bacteria cells.

#### 5.4.4 Potential toxic chemicals released during transformation of doped Ge NCs

Colorimetric curcumin and ascorbic acid methods were applied to investigate the potential dissolution of boron and phosphorus dopants, respectively.<sup>48, 49</sup> As curcumin reacts with borates to form red colored rosocyanine that absorbs at 540 nm, it is a classical method to detect trace amounts of boron. When the supernatants of B-doped Ge NCs were tested

against curcumin assays, the occurrence of color reactions (from yellow to dark red) indicated the existence of released boron compounds and moreover, based on the calibration curve derived from curcumin assays (Figure 5.7a), we interpolated that for 10% B-doped Ge NCs (1000 mg/L), the concentration of released boron was  $1.5 \pm 0.2$  mg/L while for 30% B-doped Ge NCs (1000 mg/L), it was  $3.4 \pm 0.1$  mg/L. Similarly, ascorbic acid assays serve as a sensitive method to detect trace amounts of phosphorus in aqueous samples. In this method, antimony potassium tartrate and ammonium molybdate react with orthophosphate to form an antimony-phospho-molybdate complex in acidic medium, which can be reduced to a blue-colored complex by ascorbic acid. The color variation is proportional to the concentration of orthophosphate and can be reflected by the absorbance at 650 nm or 880 nm. In our tests, a calibration curve was prepared based on the ascorbic acid method (Figure 5.7b) and as such, it was determined that the concentration of released phosphorus was  $1.8 \pm 0.1$  mg/L for 10% P-doped Ge NCs (1000 mg/L) while it was  $2.3 \pm 0.1$  mg/L for 30% P-doped Ge NCs (1000 mg/L).

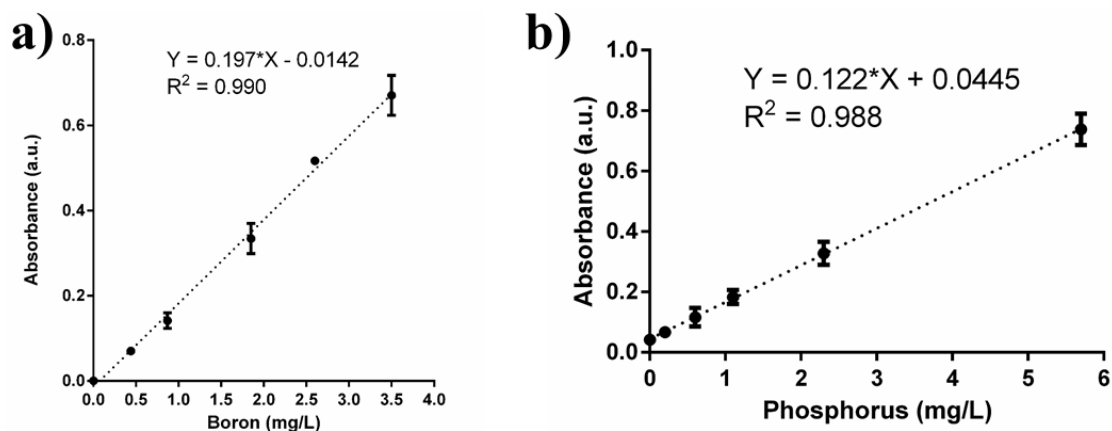
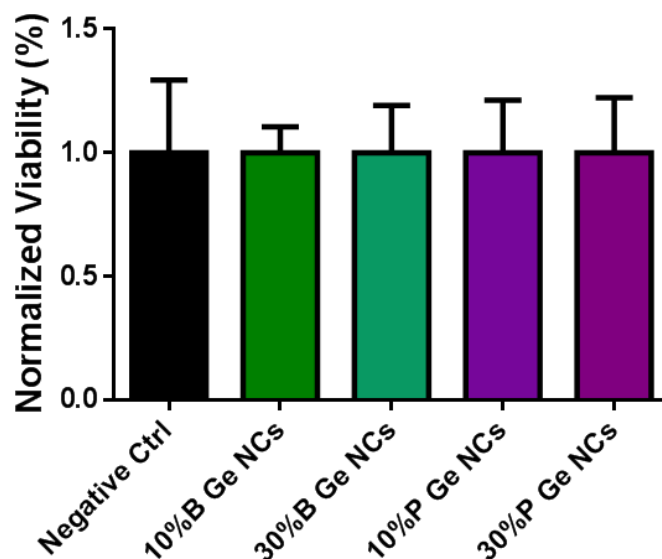


**Figure 5.7.** (a) Calibration curve to determine the concentration of boron. (n = 3) (b) Calibration curve to determine the concentration of phosphorus. (n = 3)

### Supernatants of doped Ge NCs: 1000 mg/L, 15-minute exposure



### Supernatants of doped Ge NCs: 1000 mg/L, 1-hour exposure

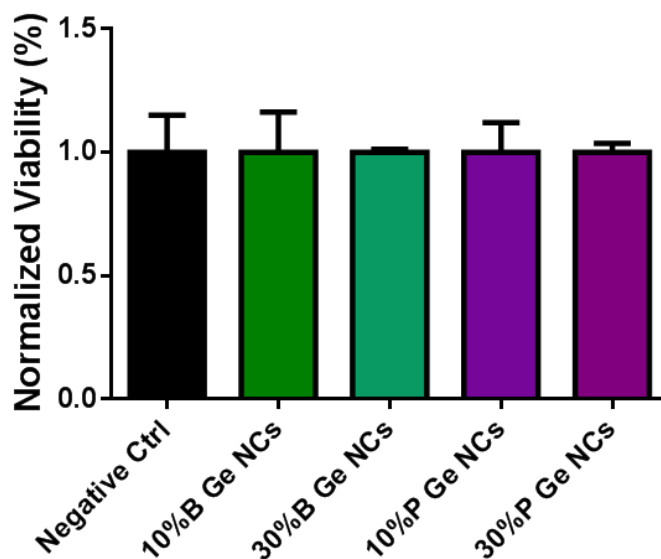


**Figure 5.8.** Colony counting experiments using the supernatants of Ge NCs. There are no significant differences among the different experimental conditions.

In addition, to further investigate the influence of the dissolved boron/phosphorus-containing chemicals, we tested the toxicity of the supernatants of doped Ge NCs via colony counting assay as well. As shown in Figure 5.8, compared to the negative control

exposure, all the supernatants exhibit no significant toxic effects over either 15-minute or 1-hour exposure. Therefore, it can be concluded that although dissolved boron/phosphorus-related chemicals were released from doped Ge NCs during the exposure, they did not induce significant toxicity towards bacterial cells.

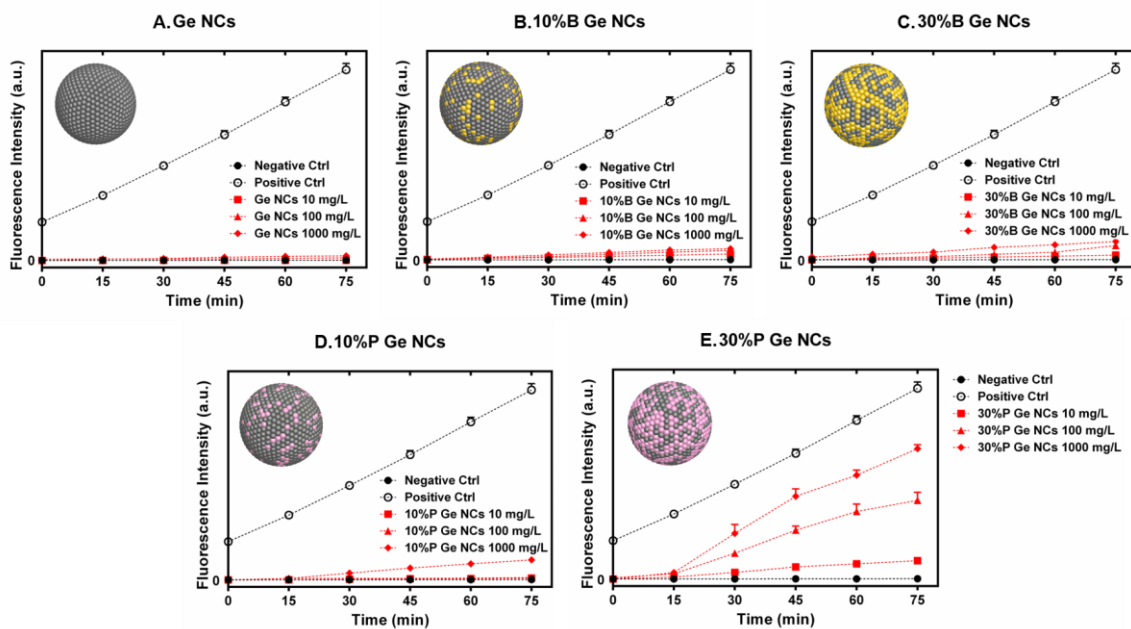


**Figure 5.9.** Abiotic assessment of ROS generation by DCFDA assay (incubation time = 75 minutes, n = 3): (A) undoped Ge NCs, (B) 10%B Ge NCs, (C) 30%B Ge NCs, (D) 10%P Ge NCs, and (E) 30%P Ge NCs.

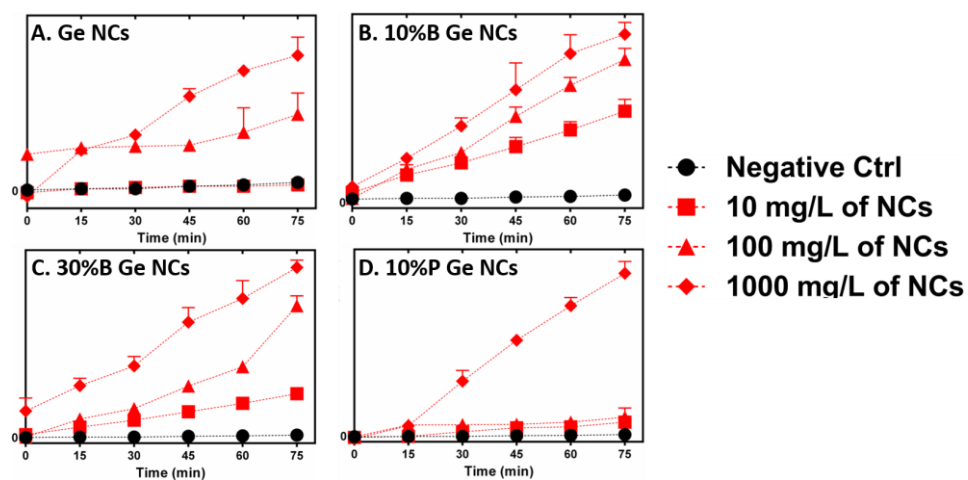


**Figure 5.10.** Enlarged views for the abiotic ROS generation of varied Ge NCs.

#### 5.4.5 Abiotic measurement of total ROS production

It is well-known that the addition of trivalent impurities such as boron atoms into Ge creates deficiencies of valence electrons, named “holes ( $h^+$ )”, while the addition of pentavalent impurities such as phosphorus contributes free electrons ( $e^-$ ), greatly increasing the conductivity of the intrinsic semiconductor.<sup>22</sup> However, as a side effect, these doping-induced free charge carriers can result in the generation of ROS free radicals. For instance, holes ( $h^+$ ) may interact with water ( $H_2O$ ) to form hydroxyl radicals ( $\cdot OH$ ) while electrons ( $e^-$ ) may reduce molecular oxygen ( $O_2$ ) and produce superoxide radicals ( $O_2^{\cdot -}$ ).<sup>18, 43</sup> The DCFDA assay is widely used for the detection of total ROS generation as the nonfluorescent DCFDA is “turned-on” to be fluorescent DCF via oxidation by ROS radicals.<sup>64</sup> In this work, ROS generation by doped Ge NCs was evaluated using the DCFDA assay, and the results are shown in Figure 5.9. These data demonstrate an overall steady rise in fluorescence response during incubation with Ge NCs. As low-intensity data obscure one another in the full-scale graphs, these regions are magnified for a clearer view, except for 30% P-doped Ge NCs (Figure 5.10). To be more specific, Ge NCs without doping induce negligible ROS, even at a working concentration as high as 1000 mg/L. For B-doped Ge NCs, a progressive but modest ROS generation is visible for both lightly and heavily doped NCs; on the other hand, P-doped Ge NCs, especially heavily doped ones, generated significantly high ROS responses after 30 minutes, which also depends on the concentration of P-doped Ge NCs. In biological systems, excess ROS is known to inhibit the activity of metalloenzymes and the integrity of DNA;<sup>65</sup> from these data, one can

extrapolate that ROS generation induced by doping likely plays a role in the decreased number of bacterial colonies described in Figure 5.6.

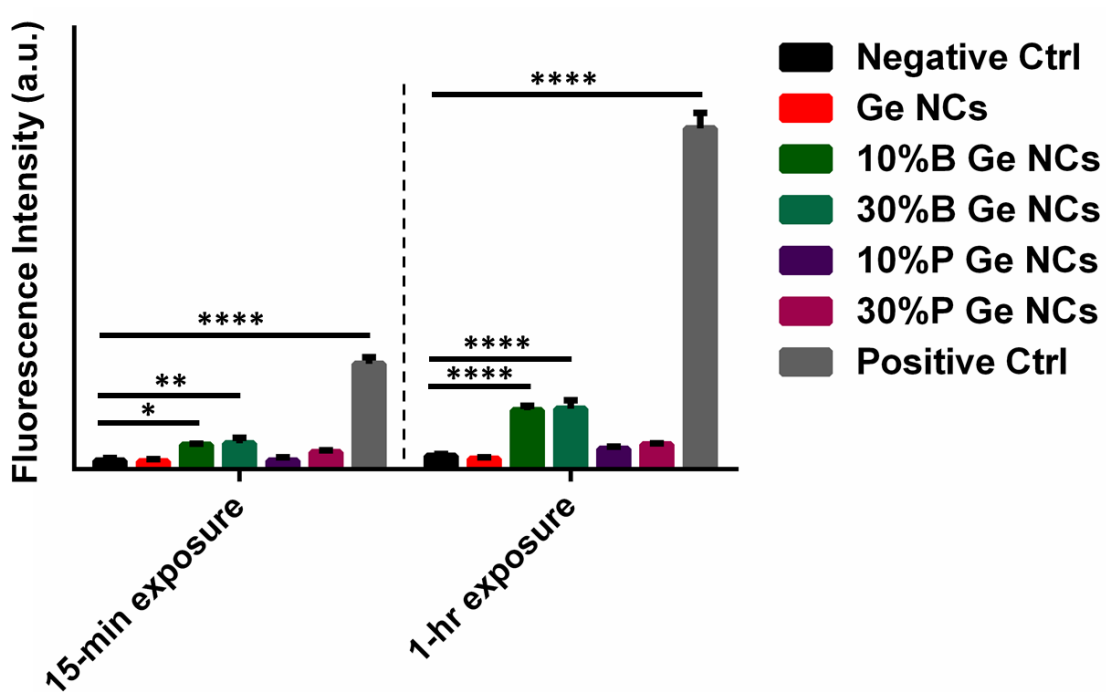


**Figure 5.11.** Hydroxyl radical generation at 15-minute and 1-hour time intervals, as measured by cell-free HPF assays. The asterisks indicate statistical significance level: \* $p < 0.05$ , \*\* $p < 0.01$ , \*\*\* $p < 0.001$ , \*\*\*\* $p < 0.0001$  (examined by two-way ANOVA, followed by Sidak's multiple comparison tests,  $n = 3$ ).

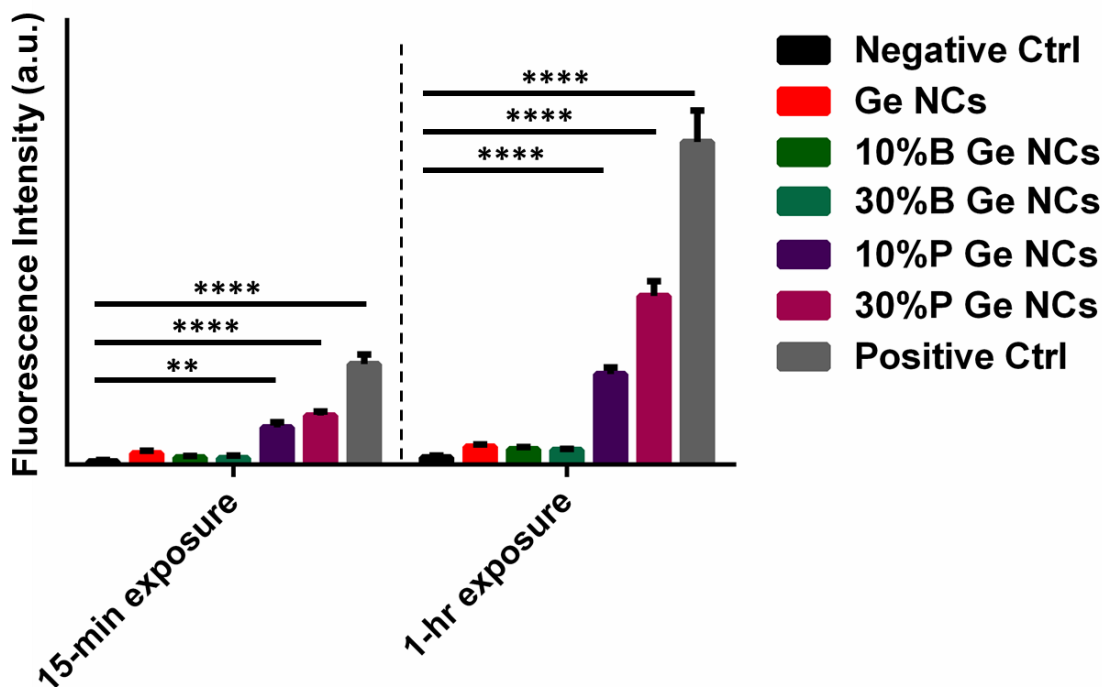


**Figure 5.12.** Superoxide radical generation at 15-minute and 1-hour time intervals, as measured by DHE assays. The asterisks indicate statistical significance level: \* $p < 0.05$ , \*\* $p < 0.01$ , \*\*\* $p < 0.001$ , \*\*\*\* $p < 0.0001$  (examined by two-way ANOVA, followed by Sidak's multiple comparison tests,  $n = 3$ ).

Furthermore, HPF and DHE assays were performed to distinguish specific ROS species, that is, hydroxyl radical ( $\cdot\text{OH}$ ) and superoxide radical ( $\text{O}_2^{\cdot-}$ ), respectively.<sup>50, 51</sup> As shown in Figure 5.11, after a 15-minute exposure, it is observable that the fluorescence signals from B-doped Ge NCs and the positive control were significantly different from that of the negative control while undoped and P-doped Ge NCs did not generate distinguishable hydroxyl radical signals from the negative control. Such a discrepancy was more discernible after 1-hour exposure. Therefore, it can be concluded that the generation of hydroxyl radical at measurable levels is exclusive to B-doped Ge NCs. On the other hand, the formation of superoxide radical is depicted in Figure 5.12. After either 15-minute or 1-hour exposure, significant amounts of superoxide ROS were detected for P-doped Ge

NCs and as exposure proceeded, it is noticeable that the generation of superoxide kept increasing as well, especially for 30% P-doped Ge NCs. However, such a phenomenon was not significantly observable for undoped and B-doped Ge NCs and so, the doping of phosphorus should be responsible for the generation of superoxide radicals. Based on these observations, future work will quantitatively investigate how doping with boron or phosphorus influences the distribution of charge carriers and consequently, induces the generation of difference types of ROS species.

#### 5.4.6 Ge NC association with *S. oneidensis* MR-1 cells

Although the colony counting assay and the free radical assays can quantify the overall bacterial response, it is important to investigate if and how the Ge NCs interact directly with the bacterial cells. Therefore, hyperspectral imaging was employed to directly visualize these interactions.

The hyperspectral imaging system, integrated with enhanced dark-field microscopy, provides a label-free approach to visualize and identify nanoparticles within a biological matrix.<sup>66</sup> Generally, the work flow includes acquisition of dark-field images to locate appropriate ROI, hyperspectral line-by-line scans to generate a 3D datacube composed of sample lateral information ( $x$ ,  $y$ ) and associated hyperspectral data ( $z$ ), construction of spectral libraries for reference samples, and then identification of specific components in exposure samples via SAM classification method.<sup>67</sup> The result of the SAM classification is an image showing the best match to a known spectrum (*i.e.*, a reference library) for each pixel when the angle formed between reference spectrum and image spectrum is smaller

than the spectral threshold.<sup>68</sup> As the vector angle is used in lieu of vector length, SAM is notable for its insensitivity to changes in brightness.

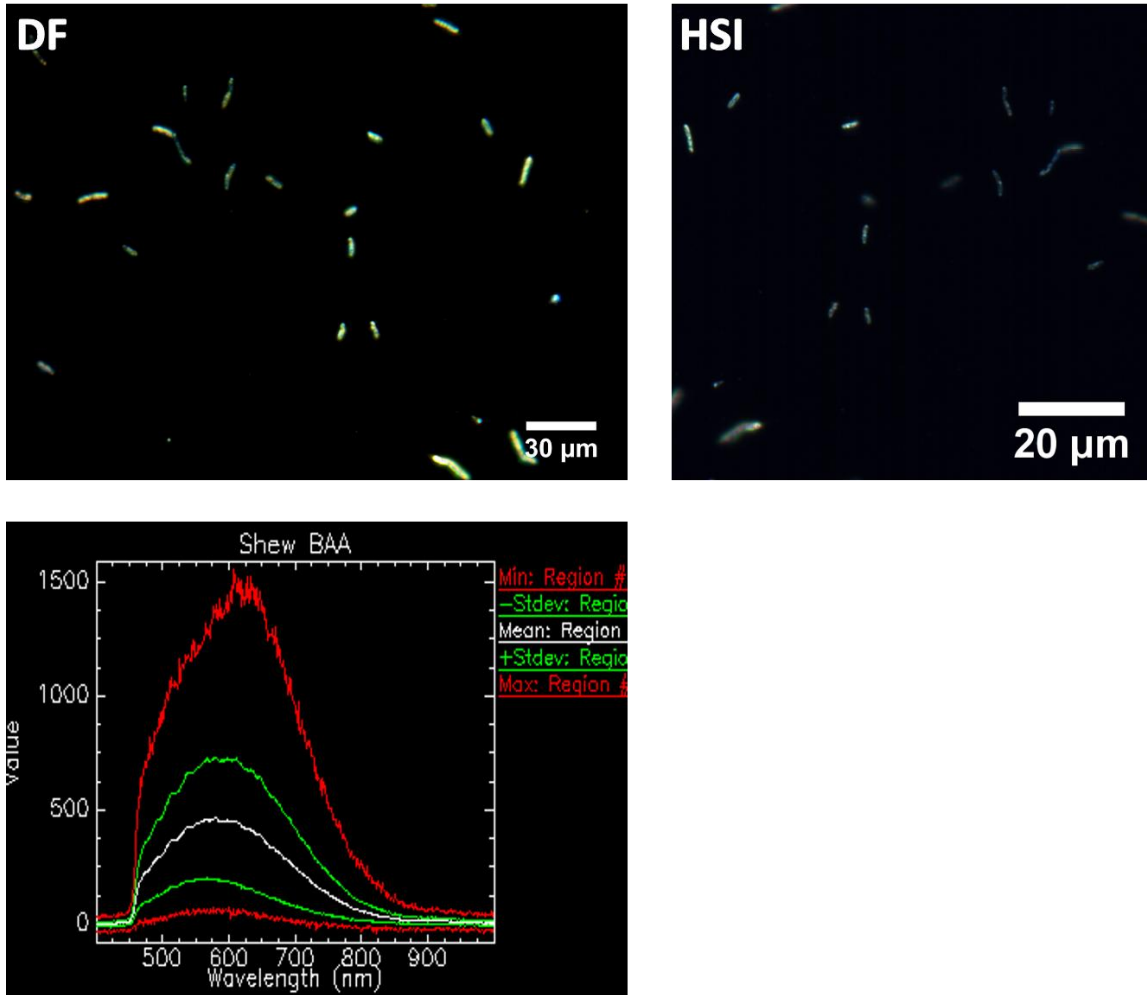


**Figure 5.13.** CytoViva analysis of *S. oneidensis* cells: DF image, HSI image, and spectral library for *S. oneidensis* MR-1 cells, generated using the ROI tool.

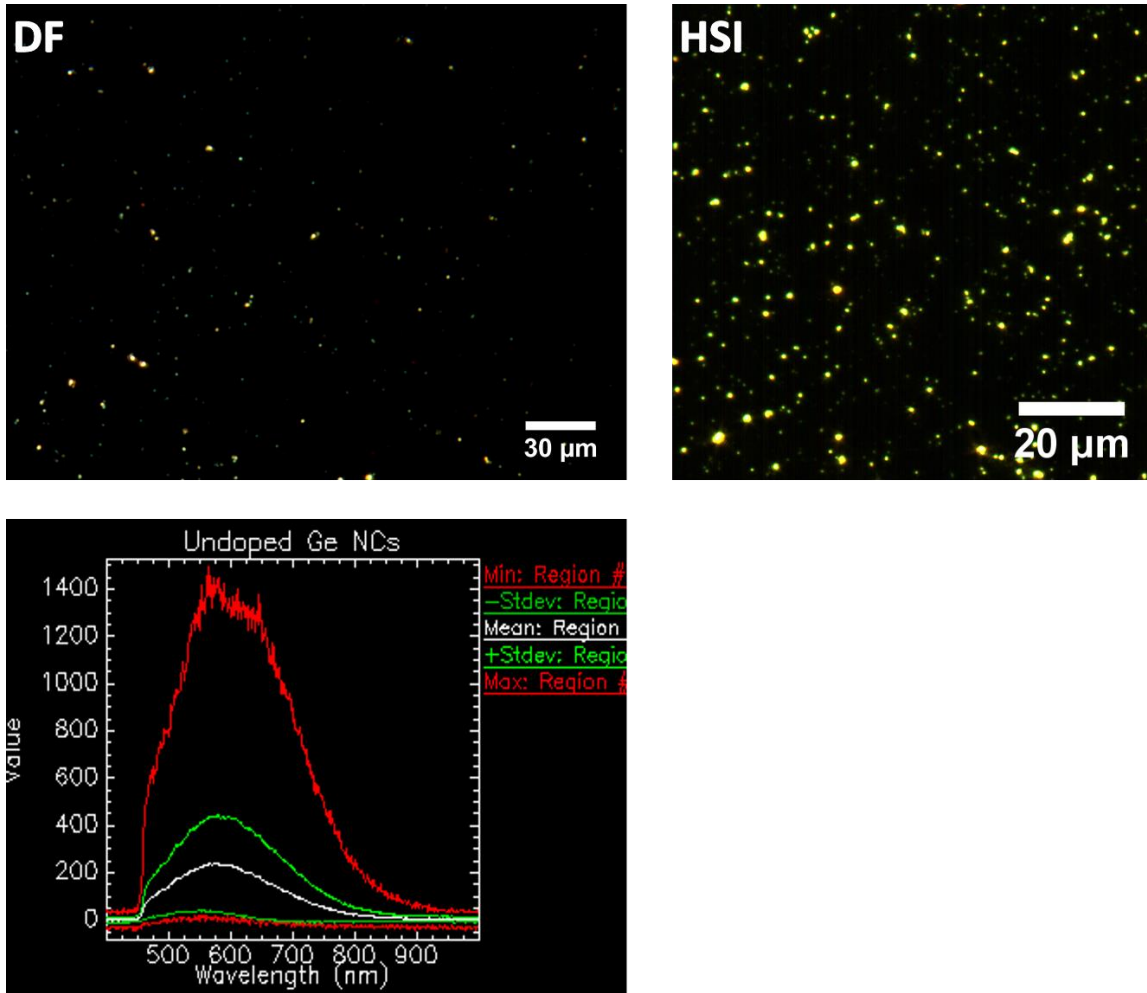


**Figure 5.14.** CytoViva analysis of undoped Ge NCs: DF image, HSI image, and spectral library for undoped Ge NCs, generated using the ROI tool.

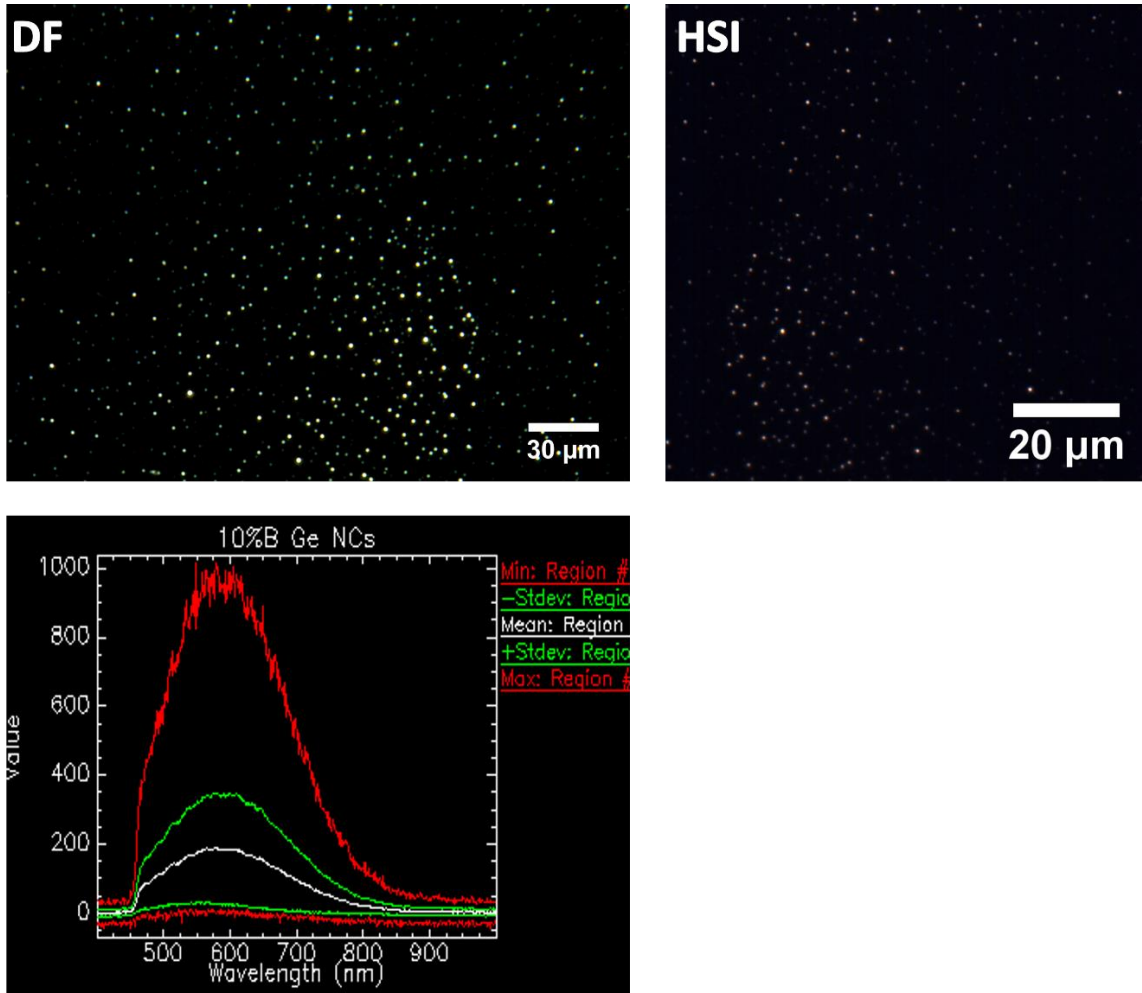


**Figure 5.15.** CytoViva analysis of 10% B-doped Ge NCs: DF image, HSI image, and spectral library for 10% B-doped Ge NCs, generated using the ROI tool.

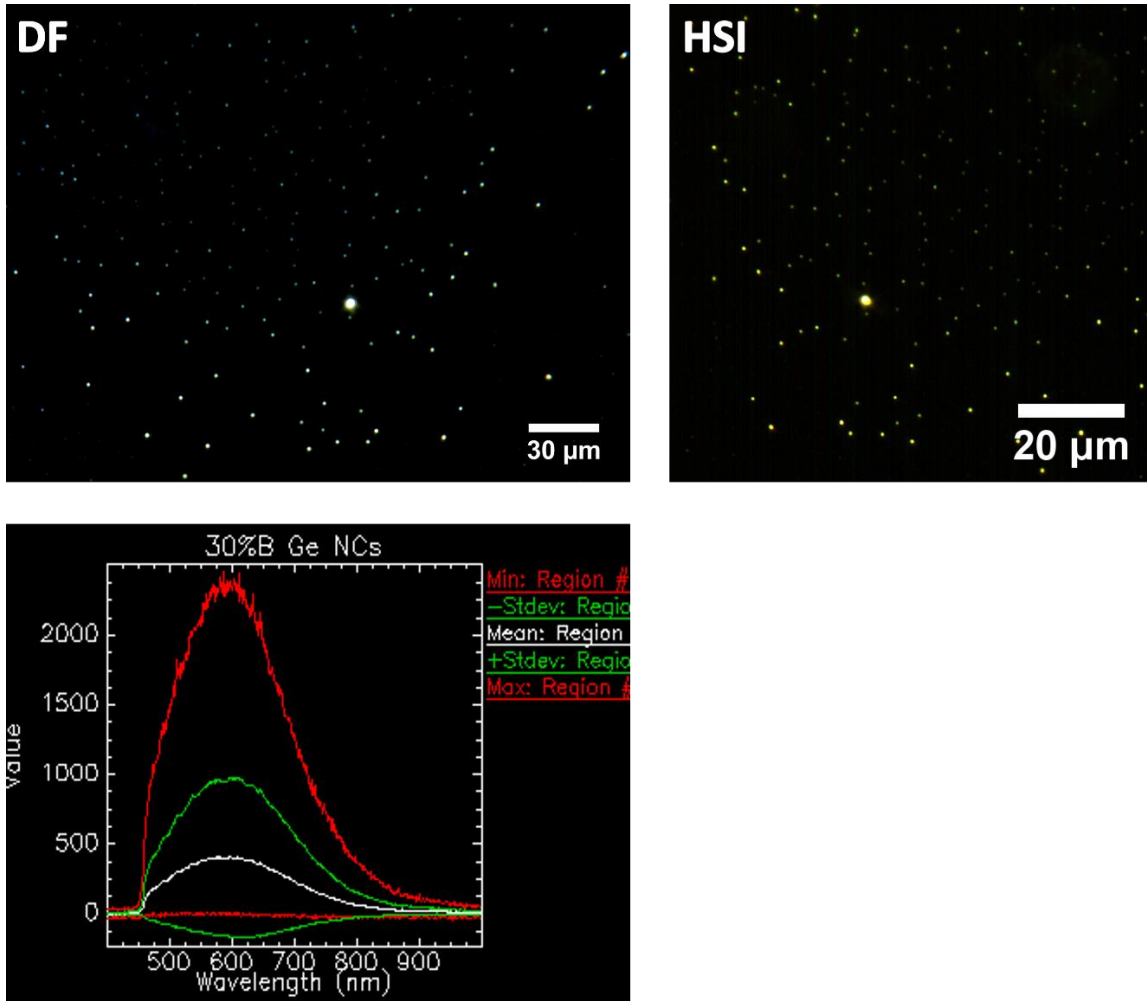


**Figure 5.16.** CytoViva analysis of 30% B-doped Ge NCs: DF image, HSI image, and spectral library for 30% B-doped Ge NCs, generated using the ROI tool.

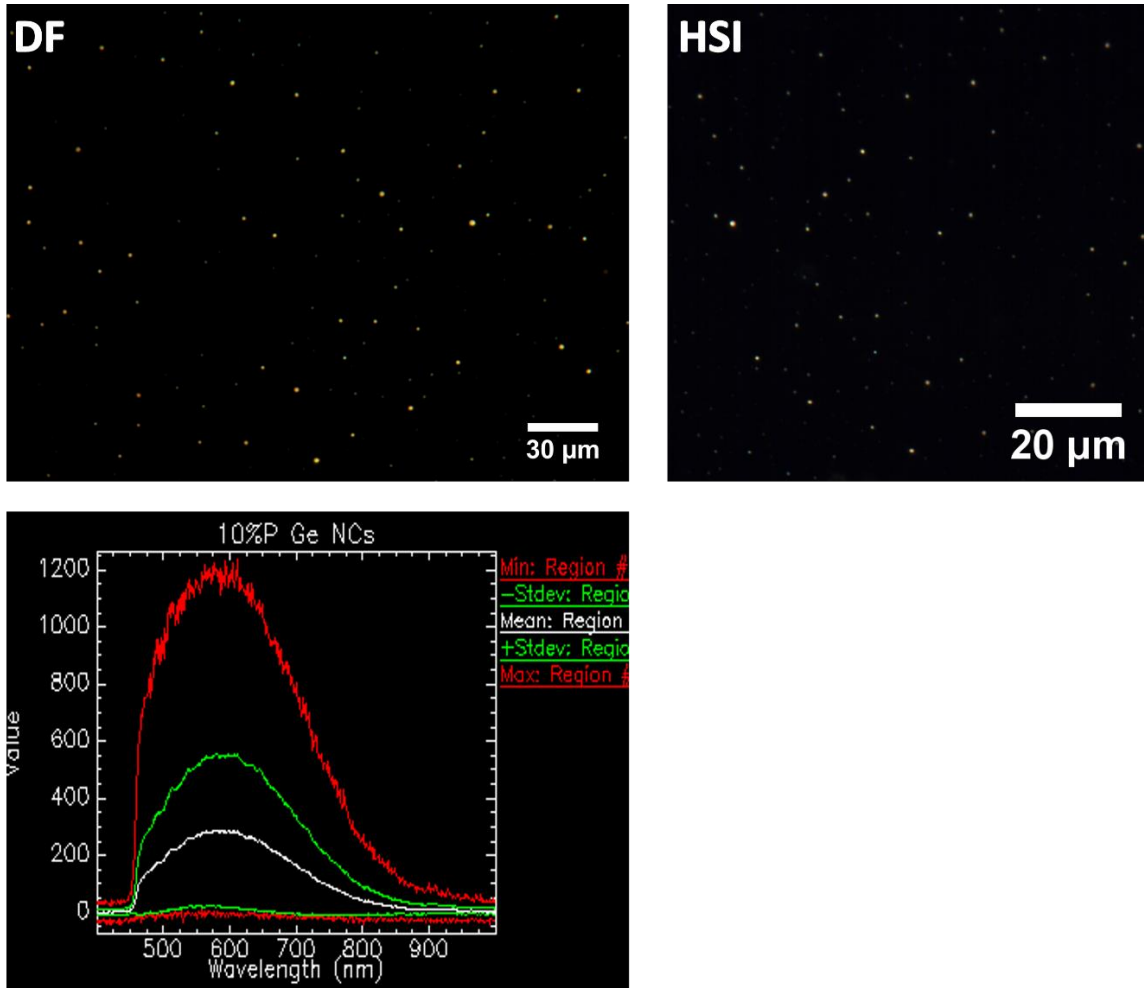


**Figure 5.17.** CytoViva analysis of 10% P-doped Ge NCs: DF image, HSI image, and spectral library for 10% P-doped Ge NCs, generated using the ROI tool.

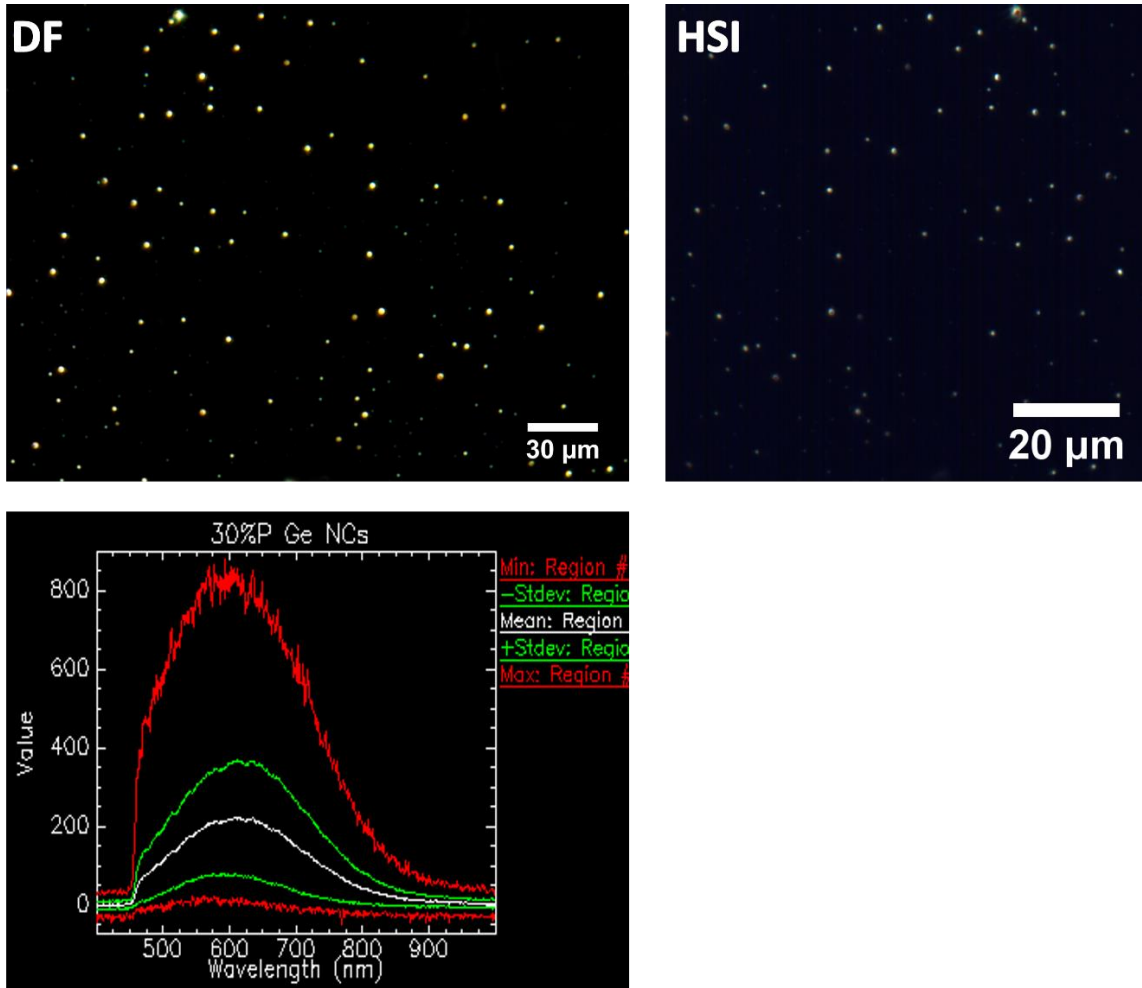


**Figure 5.18.** CytoViva analysis of 30% P-doped Ge NCs: DF image, HSI image, and spectral library for 30% P-doped Ge NCs, generated using the ROI tool.

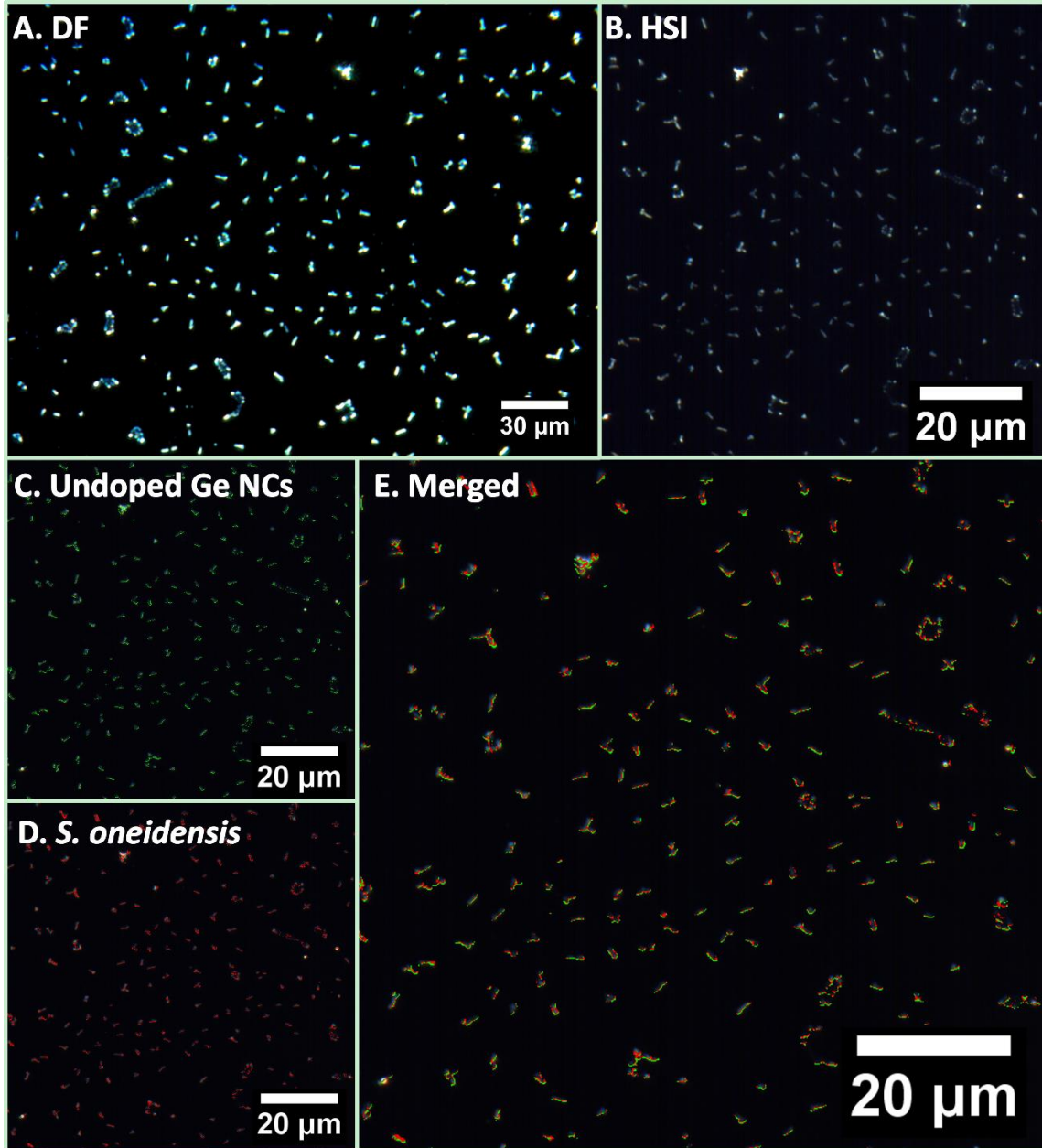


**Figure 5.19.** Enhanced DF analysis of the association between *S. oneidensis* MR-1 cells with undoped Ge NCs: (a) DF image of bacteria exposure solution, (b) HSI image of ROI in a. Mapping (c) undoped Ge NCs alone and (d) *S. oneidensis* MR-1 cells alone in the HSI data. (e) Merged mapping results of (c) and (d) where bacteria cells are false-colored red while undoped Ge NCs with green.

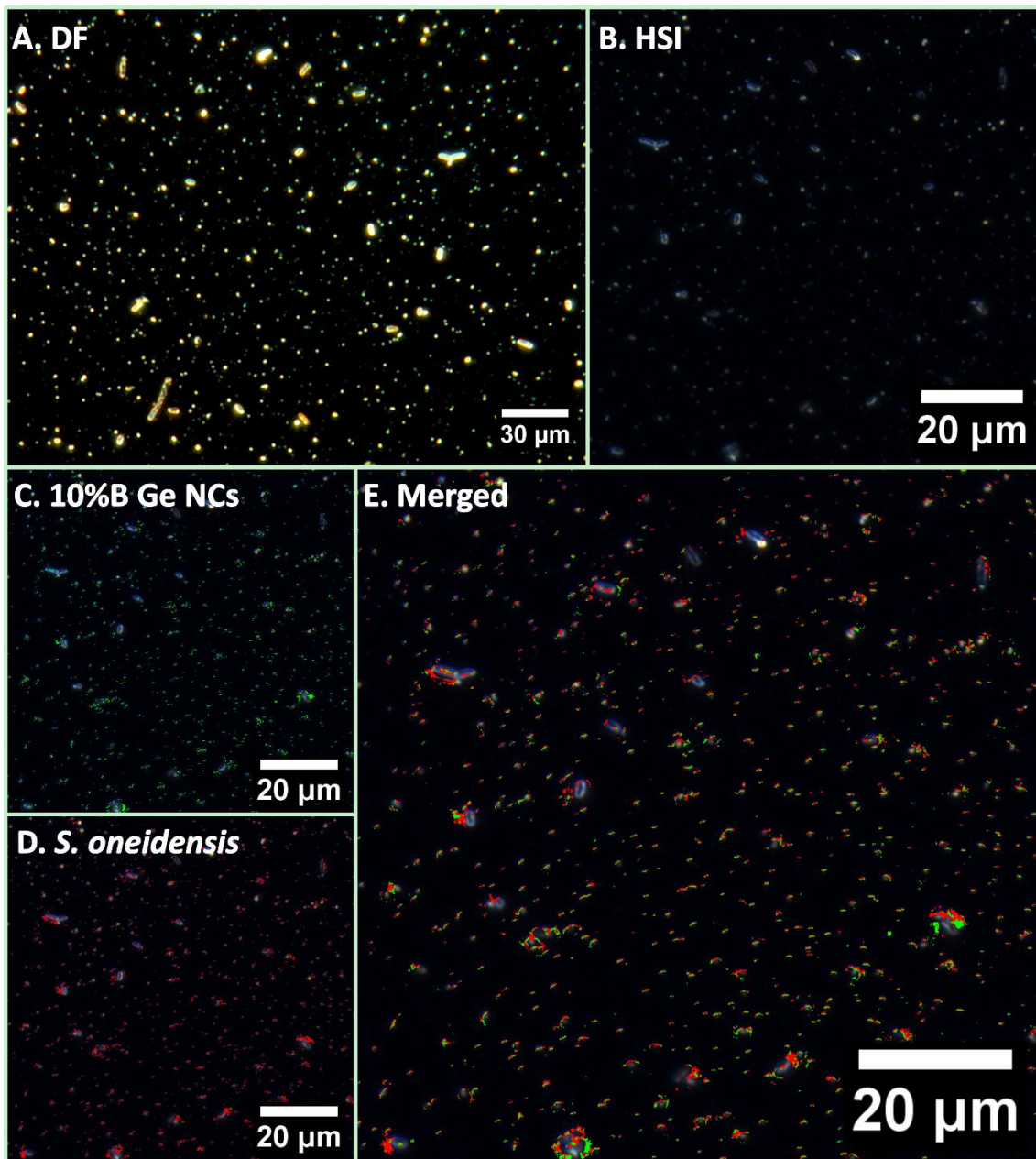


**Figure 5.20.** Enhanced DF analysis of the association between *S. oneidensis* MR-1 cells with 10% B-doped Ge NCs: (a) DF image of bacteria exposure solution, (b) HSI image of ROI in a. Mapping (c) 10% B-doped Ge NCs alone and (d) *S. oneidensis* MR-1 cells alone in the HSI data. (e) Merged mapping results of (c) and (d) where bacteria cells are false-colored red while 10% B-doped Ge NCs with green.

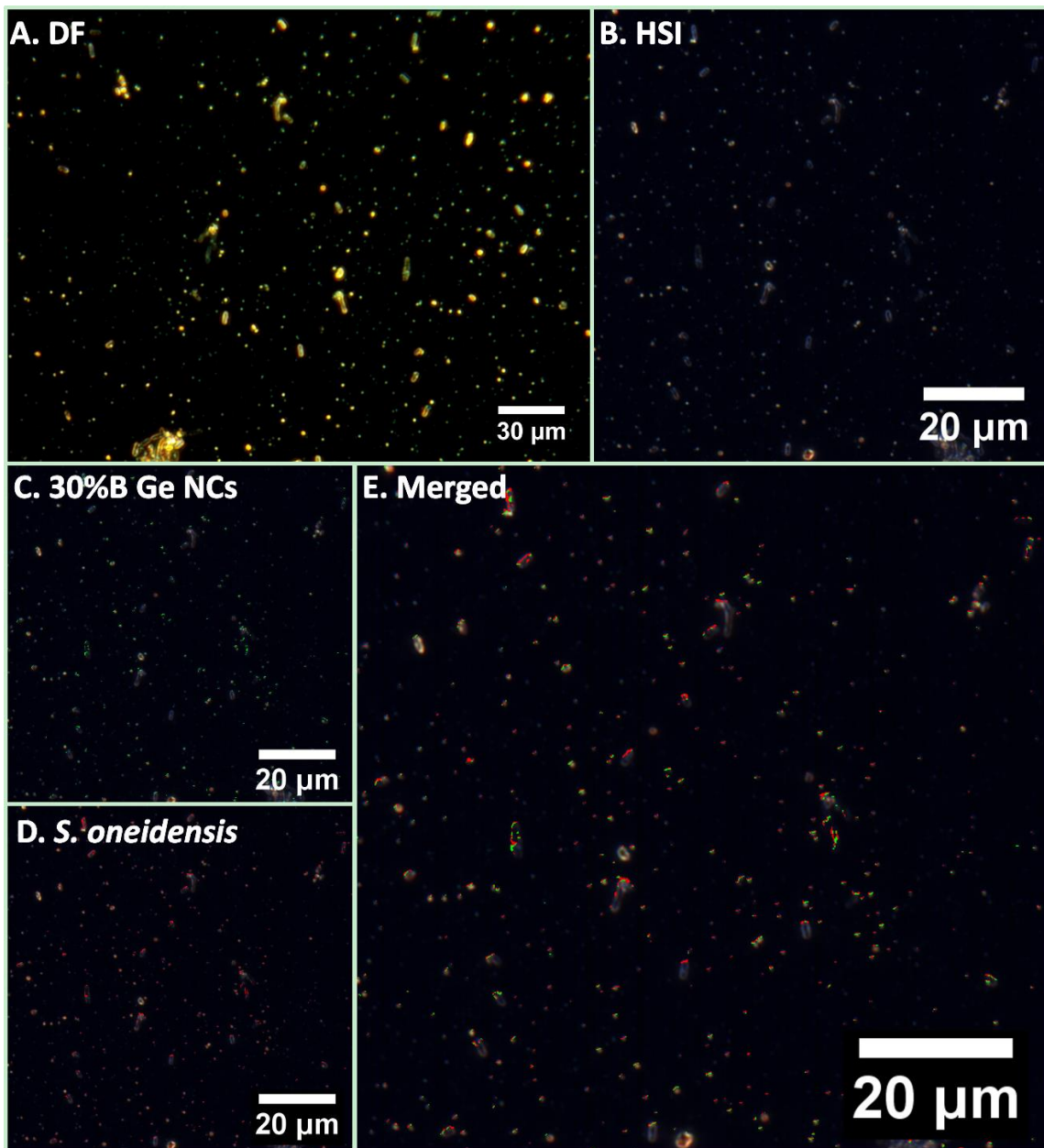


**Figure 5.21.** Enhanced DF analysis of the association between *S. oneidensis* MR-1 cells with 30% B-doped Ge NCs: (a) DF image of bacteria exposure solution, (b) HSI image of ROI in a. Mapping (c) 30% B-doped Ge NCs alone and (d) *S. oneidensis* MR-1 cells alone in the HSI data. (e) Merged mapping results of (c) and (d) where bacteria cells are false-colored red while 30% B-doped Ge NCs with green.

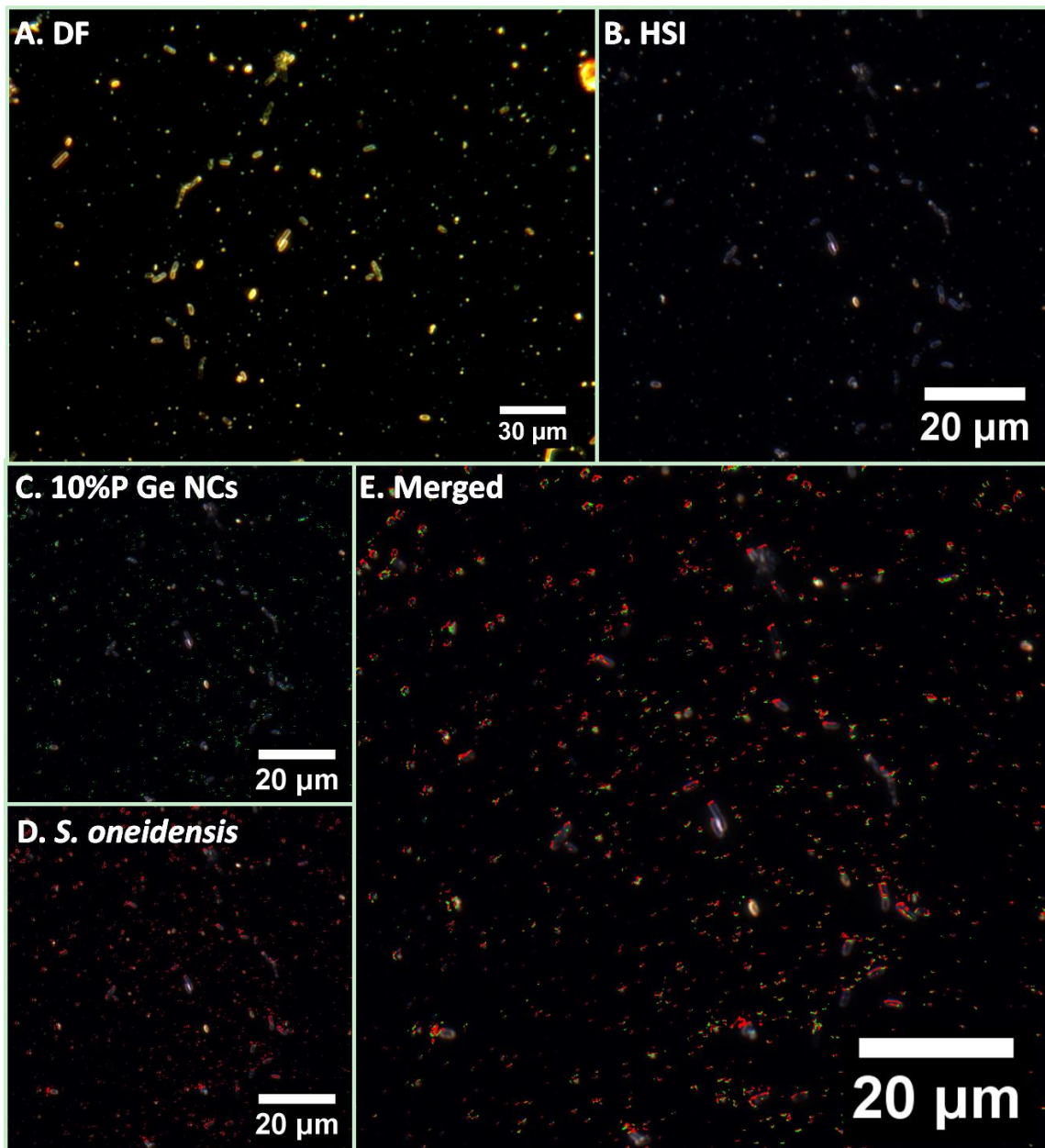


**Figure 5.22.** Enhanced DF analysis of the association between *S. oneidensis* MR-1 cells with 10% P-doped Ge NCs: (a) DF image of bacteria exposure solution, (b) HSI image of ROI in a. Mapping (c) 10% P-doped Ge NCs alone and (d) *S. oneidensis* MR-1 cells alone in the HSI data. (e) Merged mapping results of (c) and (d) where bacteria cells are false-colored red while 10% P-doped Ge NCs with green.

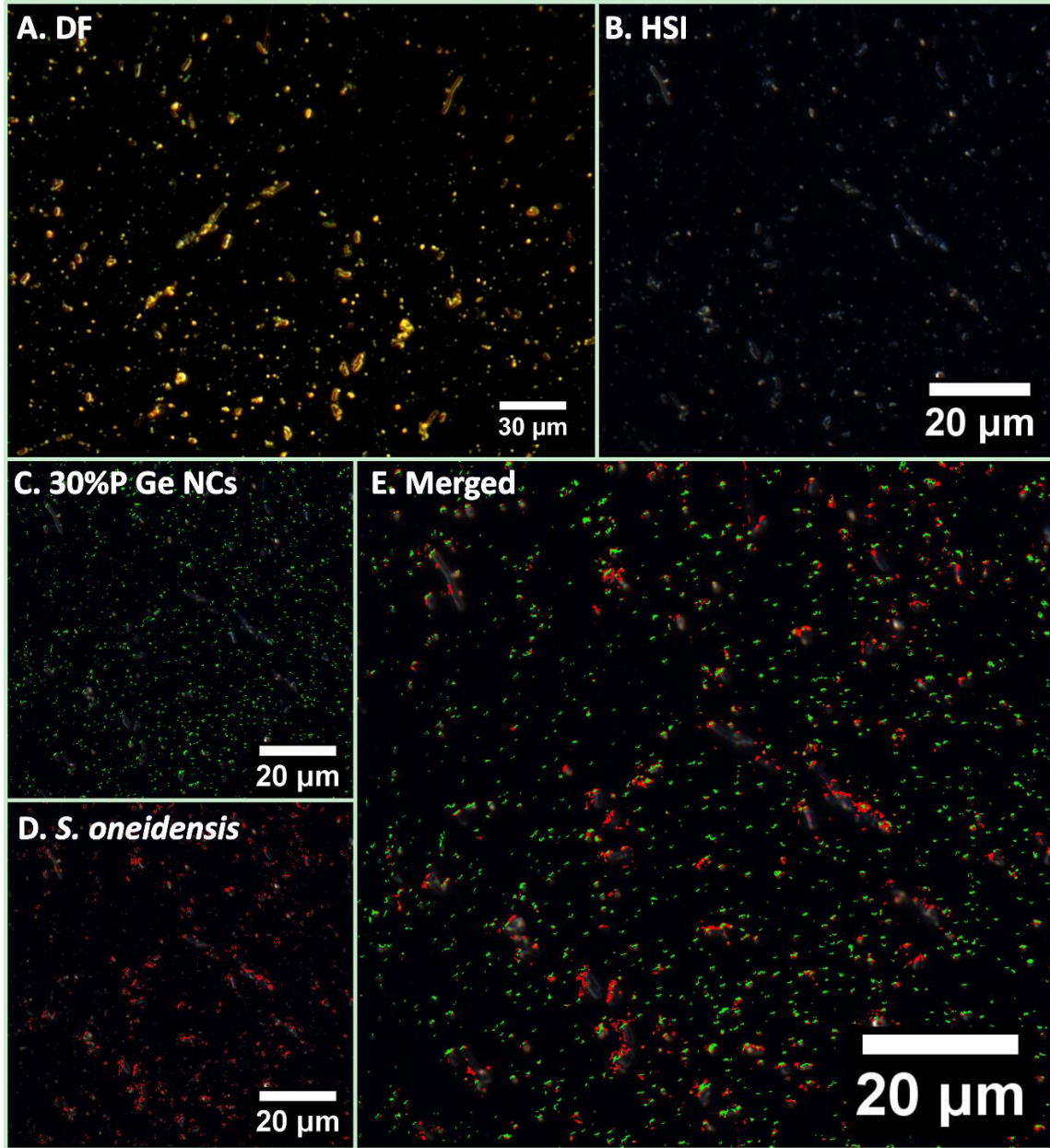


**Figure 5.23.** Enhanced DF analysis of the association between *S. oneidensis* MR-1 cells with 30% P-doped Ge NCs: (a) DF image of bacteria exposure solution, (b) HSI image of ROI in a. Mapping (c) 30% P-doped Ge NCs alone and (d) *S. oneidensis* MR-1 cells alone in the HSI data. (e) Merged mapping results of (c) and (d) where bacteria cells are false-colored red while 30% P-doped Ge NCs with green.

Reference libraries for *S. oneidensis* MR-1 cells and Ge NCs are shown in Figure 5.13 through 5.18 while analyses for the association between Ge NCs and *S. oneidensis* MR-1 cells Figure 5.19 through 5.23. Figure 5.19a shows the original dark-field image of *S. oneidensis* MR-1 exposed to undoped Ge NCs and after a “pushbroom” scan, the centered area was magnified, and the result is shown in the hyperspectral image (Figure 5.19b). It is clear that rod-like assemblies of bacteria are spread across the entire view in both dark-field and hyperspectral images. To further classify undoped Ge NCs and bacteria cells, respective reference libraries were imported into the SAM classification function to identify their locations in the hyperspectral image. The classification results for Ge NCs alone and cells alone are exhibited in Figure 5.19c and d. Pixels depicting Ge NCs are pseudo-colored with green while *S. oneidensis* MR-1 cells are pseudo-colored with red. The merge of the two (Figure 5.19e) provides a straightforward observation pertaining to the colocalization of undoped Ge NCs and bacteria cells. The adjacency between NC pixels and cell pixels indicates a potential physical contact between nanoscale Ge NCs and micron-scale *S. oneidensis* MR-1 cells. With that being said, hyperspectral imaging is not a super-resolution technique and is still restricted by the diffraction limit. Under such circumstances, to further investigate the association behavior between Ge NCs and bacteria cells, resin-embedded samples were prepared for TEM analysis to complement hyperspectral imaging data.

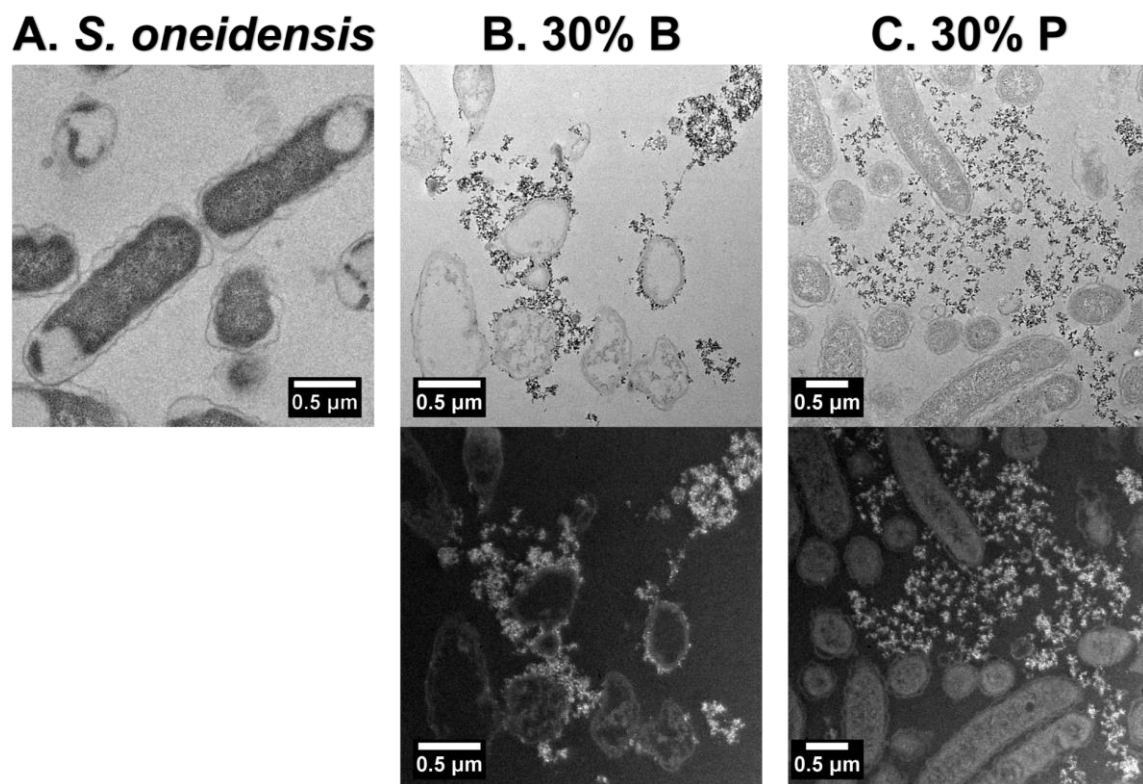


**Figure 5.24.** (upper level) BF TEM images for (a) *S. oneidensis* MR-1 cells and bacteria cells exposed to (b) 30% B-doped Ge NCs and (c) 30% P-doped Ge NCs; (lower level) DF TEM images for bacteria cells exposed to (b) 30% B-doped Ge NCs and (c) 30% P-doped Ge NCs.

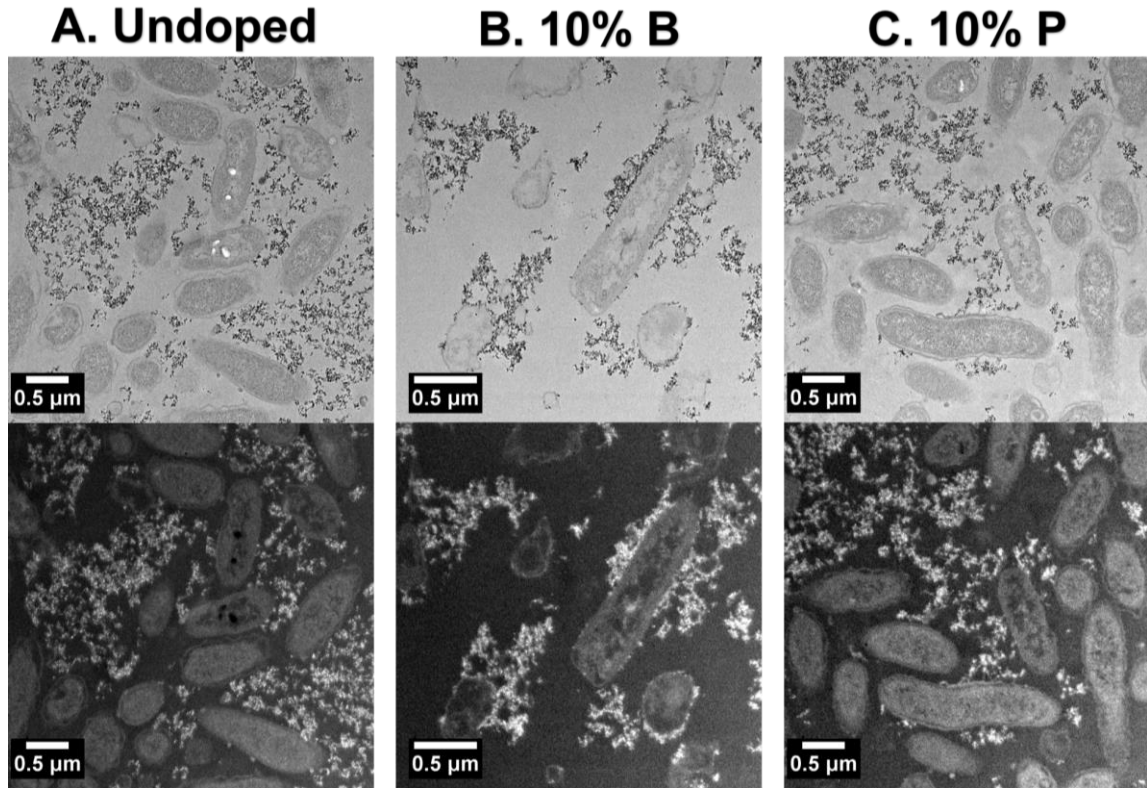


**Figure 5.25.** BF (upper) and DF (lower) bio-TEM images of *S. oneidensis* MR-1 cells exposed to (a) undoped, (b) 10% B-doped, and (c) 10% P-doped Ge NCs. For the DF images, Ge NC diffraction angles were chosen so that Ge NCs would appear bright compared to other features.

Electron microscopy grants the capability to acquire highly magnified images that illustrate the localized interaction between Ge NCs and bacteria cells. As revealed in Figure 5.24a, *S. oneidensis* MR-1 cells show a rod-like morphology, in line with previous hyperspectral imaging results; in addition, like other Gram-negative bacterial species, outer membrane vesicles are present outside the membranes, which helps to distinguish bacteria cells from Ge NCs. Figure 5.25a through 5.25c show the interaction between bacteria cells and Ge NCs (undoped, 10% B- and 10% P- doped) while imaging results for 30% B- and 30% P- doped Ge NCs can be found in Figure 5.24b and 5.24c. Generally, bacteria cells remain intact in each exposure condition, and there is no discernible

penetration of Ge NCs into cellular structures. In the cases of undoped and P-doped Ge NCs, both bacteria cells and Ge NCs are well-distributed across the field of view without remarkable attachment, but for B-doped Ge NCs, the proximity between NCs and cells is noticeable for both lightly and heavily doped NCs, demonstrating a distinct interaction pattern compared to the other Ge NCs. Due to the intense electron diffraction from highly crystalline Ge NCs, these particles appear as bright white dots at a set angle in the dark-field mode while bacteria cells appear dimmed. In other words, it is convenient to differentiate bacteria cells and Ge NCs by taking advantage of the DF TEM imaging. In Figure 5.24b and Figure 5.25b (lower), it can be confirmed that there is a significant attachment of B-doped Ge NCs to the surface of bacteria cells. Such phenomenon was observed for B-doped Si NCs as well in our previous study.<sup>18</sup> As doped boron prefers to reside at the NC surface,<sup>69</sup> boron in this state could serve as a Lewis acidic surface site that would interact with electron-donating groups such as carbonyls from cell membranes, forming donor-acceptor complexes.<sup>70</sup> However, such tight binding is not observed for undoped and toxic P-doped Ge NCs, even if NCs are heavily doped with phosphorus and as such, it implies that the physical association between Ge NCs and bacteria cells does not directly impact the bacterial viability but that high ROS levels induced by doping, despite a longer physical distance between the NCs and the bacterial cells, has suppressed the formation of bacterial colonies.

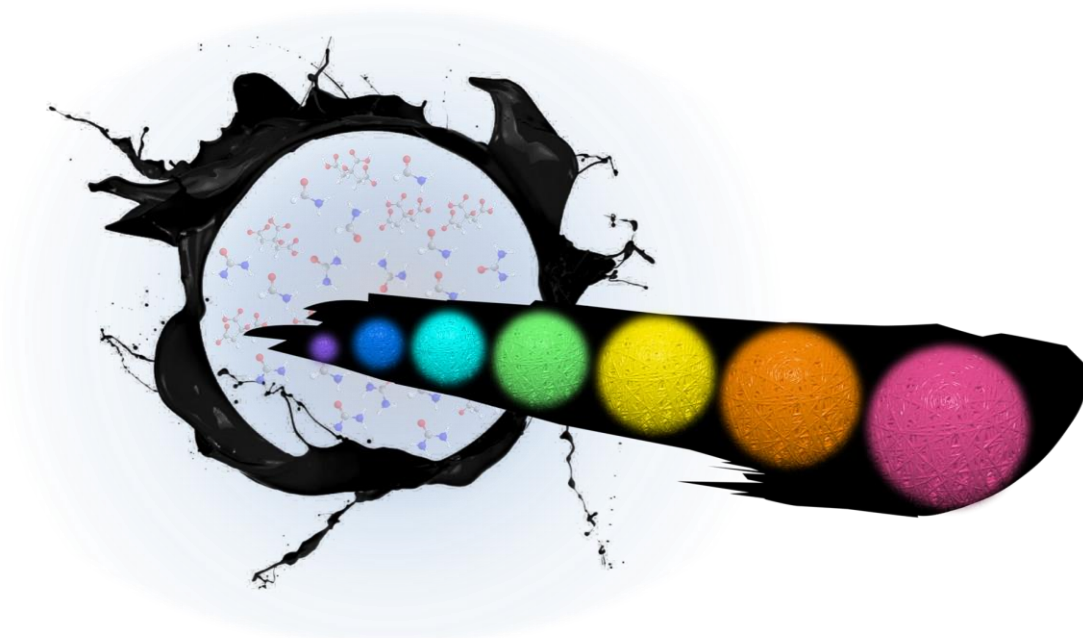
## 5.5 Conclusions

Herein, our results demonstrate that the type of dopants (boron and phosphorus) and the actual doping level (up to c.a. 15%) have negligible impact on the morphology, NC size

distribution, and crystallinity of Ge NCs. However, the introduction of boron or phosphorus induces the aqueous production of ROS, dependent on the dopant type, doping level, and NC concentration. P-doped Ge NCs, especially 30% doped ones, exhibit significantly high levels of ROS in HEPES buffer. Accordingly, over a long-time exposure (one hour), 30% P-doped Ge NCs at a concentration as 1000 mg/L show a significant toxicity towards *S. oneidensis* MR-1, while undoped Ge NCs are non-toxic and the rest of the other doped Ge NCs exhibit moderate toxic effects. The interaction between Ge NCs and bacteria cells was carefully examined by a combination of hyperspectral imaging and bio-TEM. Interestingly, compared to undoped and P-doped Ge NCs, the B-doped NCs are tightly associated with the surface of bacteria cells, probably due to the Lewis acid-base attraction. That being said, such attachment does not automatically result in toxicity to the bacteria.

## Chapter 6

The preparation of multicolor carbon dots via an automatic reversed-phase separation



Bo Zhi is responsible for the design of this research as well as new citric acid carbon dot synthesis, TEM analysis, optical property measurements and the drafting of manuscript.

## 6.1 Overview

An automated chromatographic separation technique was applied to purify as-made CDs whose emission shifted upon excitation of varied wavelengths, leading to acquisition of CD fractions exhibiting discrete varied colors. In addition, as revealed by TEM and DLS measurements, the particle sizes of CD fractions tend to increase alongside the redshift of emissions; however, the size differences were not significantly different from one another. Blue and red emitting fractions were chosen as representatives for subsequent cell imaging experiments, and interestingly, the smaller particles (blue fractions) localized in a broader range of organelles (mainly mitochondria and lysosomes) while larger particles (red fractions) were primarily trapped in lysosomes.

## 6.2 Introduction

The accidental discovery of luminescent carbon fragments in 2004 during the purification of CNTs triggered studies on carbon-based fluorescent NPs, i.e., CDs.<sup>1</sup> Typically, CDs are carbon nanostructures whose sizes are around 10 nm, as revealed by microscopic techniques, such as TEM and AFM.<sup>2-4</sup> In recent decades, a significant deal of research efforts have forged the field of CDs as a fast-growing topic and continues to attract an increasing number of researchers to improve synthetic strategies, fine tune the luminescence performance, and design CD-based applications.<sup>5-7</sup>

However, there are two main barriers that are hampering the development of the field of CDs: one lacks of clarity regarding the luminescence mechanism for the CD and the other is the preparation of multicolor CDs that can cover the entire visible range.<sup>8,9</sup> Fortunately,

in most recent years, both barriers have witnessed breakthroughs. For mechanistic studies, researchers are weighing three dominating hypotheses, namely, size effect,<sup>10</sup> molecular fluorophore,<sup>11</sup> and surface state-induced emission<sup>12</sup>; on the other hand, an increasing number of successful syntheses of colorful CDs have been reported.<sup>13-15</sup> Among these successful cases, a chromatographic post-treatment of as-made CDs plays a critical role to obtain colorful components, such as anion-exchange column chromatography,<sup>16</sup> normal phase silica chromatography,<sup>17</sup> and reversed phase silica chromatography.<sup>18</sup> However, the CD components are highly similar to one another in terms of physiochemical properties and so, it takes careful operation to separate different colored fractions. As such, though it seems to be an effective method to separate CDs via column chromatography, the process can be quite labor intensive and time-consuming, which can be as long as several hours.<sup>17</sup> It is desirable to develop a more efficient method for CD separation.

Under such context, in this work, an automated chromatographic apparatus was applied to separate as-made CD mixtures that were obtained by reacting citric acid and urea in formamide. An individual separation process took no longer than 20 minutes and obtained CD fractions exhibiting discrete rainbow-like emissions upon 365 nm UV illumination. Interestingly, as revealed by TEM and DLS tests, longer wavelength emitting CD fractions tend to possess larger particle sizes; however, statistical examination did not indicate there was significant difference from one another. Ongoing simulation experiment indicates that the condensed polyamide networks within the CD structures may be responsible for the varied emissions. Moreover, two representative CD fractions, that is, blue and red fractions, were chosen for subsequent cell imaging experiments. The localization patterns

for CD fractions were varied: blue fractions were observed in a wide range of organelles while red fractions were primarily enclosed in lysosomes.

## **6.3 Experimental**

### **6.3.1 Synthesis and separation of as-made CDs**

All the used chemicals, solvents, and consumables were purchased via Fisher Scientific without further purification. The as-made CDs that contain multicolor components were synthesized by fine tuning the reactants ratio, reaction temperature, and reaction duration in a CEM Discover SP microwave reactor. The as-made CDs used for separation were obtained by reacting 7 mmol citric acid with 10 mmol urea in 15 ml of formamide under 200 °C for 1 hour. The crudes were further filtered to remove bulk carbon residue before column chromatographic separation was performed.

To achieve an efficient separation, a CombiFlash automated chromatography instrument was utilized in combination with a reversed-phase silica column, RediSep Rf C18 Aq (size: 50 g). Specifically, after a default column equilibration, 1 ml of as-made CD solution was injected into the column, and the separation program started automatically. At the beginning of the separation, pure water (solvent A) was used as the mobile phase and as the separation proceeded, the volume% of acetone (solvent B) keeps increasing from 0% to 40% in 14 minutes when all colored components were collected. After the separation, the column was washed with pure acetone and pure water, respectively, to completely remove non-fluorescent residues. It is optional to perform the separation on collected CD fractions once or twice more to further purify the components.

### 6.3.2 Material characterization of CDs

The PSD of carbon dots was determined by TEM (FEI Tecnai G<sup>2</sup> F30 TEM at 300 kV) and DLS (Microtrac NANO-flex<sup>®</sup> 180° DLS System). UV-vis extinction spectra were obtained using a Mikropack DH-2000 UV-Vis-NIR spectrometer. Fluorescence spectra and EEMs were measured with a PTI QuantaMaster<sup>™</sup> 400. ATR-FTIR were obtained using a Thermo Scientific Nicolet iS5 Fourier Transform Infrared Spectrometer with an iD5 Attenuated Total Reflectance attachment.

### 6.3.3 Cell Imaging and Cell Viability Analysis

*Oncorhynchus mykiss* (rainbow trout) epithelial gill cells (ATCC, CRL-2523) were cultured with Leibovitz's L-15 media supplemented with 10% fetal bovine serum and 1% antibiotics (complete media). Cells were grown at 19°C in ambient atmosphere; subcultures from passage 5-10 were used for all imaging experiments. After reaching 75% confluence, cells were incubated with 5 µg/mL CACDs (unseparated or separated) in pheno-red free medium for 2 h (Thermo Fisher Scientific, A14291DJ). For co-localization analyses, the following staining reagents were used: LysoTracker Blue (Invitrogen L7525), LysoTracker Red (Invitrogen L7528), MitoTracker Deep Red (Invitrogen M22426). The staining process followed the manufacturer's protocols. Images were taken with a Zeiss LSM710 confocal microscope and a 60× (NA 1.4) oil immersion objective. 1-5 mW laser power was used for live-cell imaging.

The cell viability of the different fractions of CDs was determined using the MTS proliferation assay (Promega, G3580). Trout gill epithelial cells were seeded in 96 well

plates at 50,000 cells per well in 200  $\mu$ L of complete media. Cells reached 100% confluency overnight. A stock solution of each type of carbon dot was prepared by bath sonicating the carbon dots for 30 min in 18 M $\Omega$ •cm water (Advantage A10, Millipore)). CDs were diluted in complete media and cells were exposed to a range of concentrations of carbon dots for either 1 or 24 h. Control cells were exposed to media diluted with nanopure water equivalent to the amount used for exposure to carbon dots. For negative controls, lysis solution (Promega) was added 45 min before the end of the carbon dot exposure period. Following the exposure period, cells were rinsed 3x with 100  $\mu$ L of media without FBS or phenol red, which were found to interfere with the absorbance measurements, to remove any unbound carbon dots. Cells were incubated with 20  $\mu$ L of MTS solution in 100  $\mu$ L of media (without FBS or phenol red) for 4 h at 19°C in ambient atmosphere and then the absorbance at 485 nm was determined using a Beckman Coulter DTX 880 Multimode Detector.

## **6.4 Results and discussion**

### 6.4.1 Screening of synthesis conditions for as-made CDs

As-made CDs were prepared by reacting citric acid with urea in formamide with a controlled molar ratio in the range of 0.1 – 0.9, incremented by 0.2 (that is, five different molar ratios) to control the extent of carbonization, the reaction temperature was adjusted from 120 °C to 200 °C, incremented by 20 °C (that is, five different temperatures); in addition, for each molar ratio-temperature pair, the reaction was performed at five different durations: 10 minutes, 30 minutes, 1 hour, 2 hour, and 4 hour, respectively. As such, the total screening process involved 125 reactions. After each reaction, the UV-vis

extinction was measured and it revealed that there were three prominent peaks around 350, 450, and 550 nm for the most of the entire 125 syntheses (Figure 6.1 (left)) while the rest exhibited no discernible peaks. Upon excitation at these wavelengths, the as-made CDs would emit around 440 (blue), 530 (green), and 600 nm (red), as depicted in the FL spectra (Figure 6.1 (right)), indicating that the as-made CDs were consisted of varied colored components. Afterwards, to estimate the percentages of these colored components, the emission peak areas of blue, green, and red were calculated and compared with one another. As longer-wavelength emitting CDs should provide an improved tissue penetration depth for subsequent imaging experiments, red-emitting CD components were preferred and therefore, the red peak ratio (that is, the peak area of red emission/the sum of peak areas of blue, green, and red emissions) was used to evaluated each CD reactions, that is, the as-made CDs containing the most red-emitting components were chosen for next separation. As described in Figure 6.1, the CD products obtained after one-hour reaction exhibited the highest red peak ratio and so, they were selected for further separation by an automated chromatographic instrument. Please note that the peak area calculation was performed once and so, one-way ANOVA was not conducted to compare red peak area ratios.

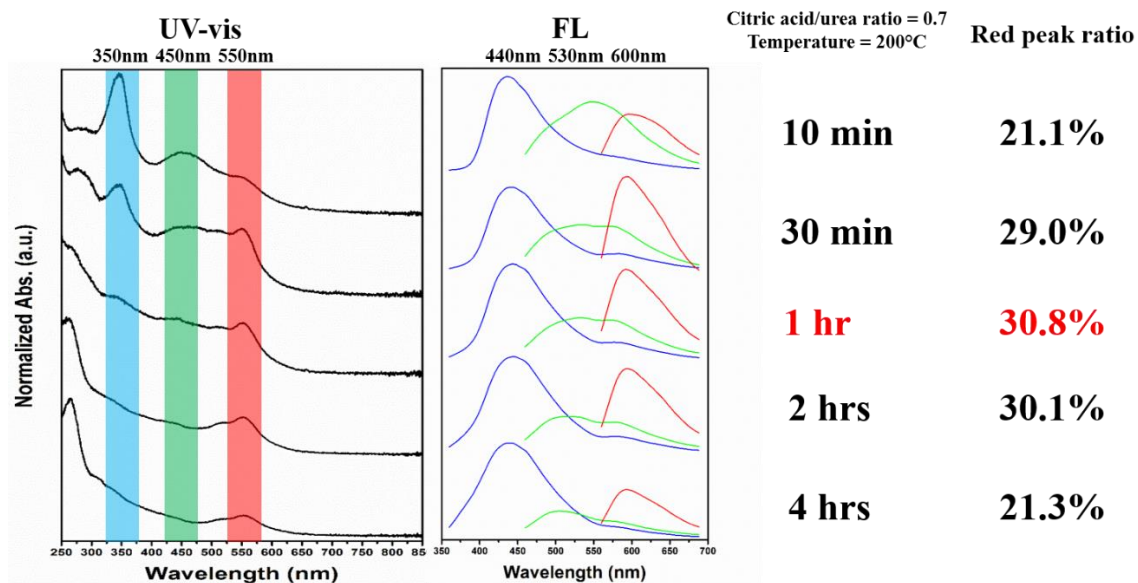


**Figure 6.1.** Representative UV-vis (left) and FL (right) spectra of as-made CD reactions. Citric acid to urea molar ratio was kept at 0.7 and the reaction temperature was 200 °C.

#### 6.4.2 Separation for as-made CDs and characterization of CD fractions

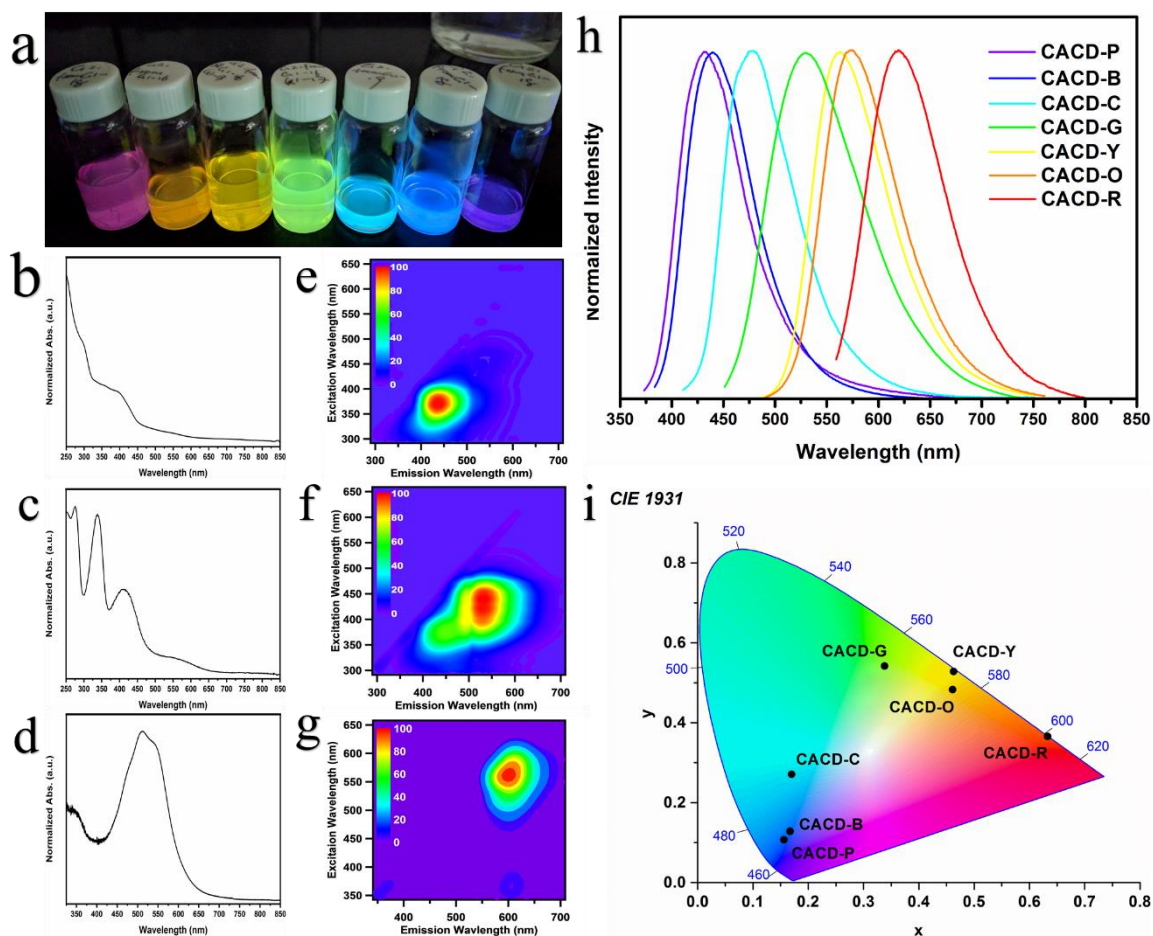


**Figure 6.2.** (a) Photographic image of obtained CD fractions, (b)-(d) UV-vis extinction spectra and (e)-(g) 2D EEM of representative blue, green, and red fractions, (h) the normalized FL spectra and (i) the chromaticity diagram of CD fractions.

After three rounds of separation, the obtained CD fractions exhibited seven discrete colors upon 365 nm UV illumination, covering the entire visible spectrum, as shown in Figure 6.2a. The UV-vis spectra for blue, green, and red fractions (CACD-B, G, and R) are depicted in Figure 6.2(b)-(d). Basically, a typical  $\pi-\pi^*$  transition appears in the region 200 – 250 nm while a  $n-\pi^*$  transition shows up around 350 nm.<sup>19, 20</sup> Particularly, for CACD-G and R, low energy bands are observable in the region of 400 – 450 nm and 500 – 550 nm, which are typically related to the narrowing of electronic band gaps for longer

wavelength CDs.<sup>21, 22</sup> In addition, EEM tests were performed to investigate the emission behavior of CD fractions: Figure 6.2(e)-(g) represent the global emission peaks for CACD-B, G, and R, and it can be deduced that for CACD-B, G, and R, the excitation/emission maxima can be achieved at (370 nm, 440 nm), (440 nm, 530 nm), and (560 nm, 600 nm). In such way, we also acquired the excitation/emission maxima for the rest of CD fractions, as summarized in Table 6.1. These CD fractions emitted differently upon optimized excitation, representing a red shift in 1D FL spectra (Figure 6.2h). Moreover, based on the emission data, the chromaticity of CD fractions can be determined by CIE 1931 diagram (Figure 6.2i), which quantitatively defines the color of their emission wavelengths, that is, purple, blue, cyan, green, yellow, orange, and red. It is worthwhile to mention that even with the aid of an automated chromatographic instrument, it is extremely challenging to completely separate as-made CDs because the physicochemical properties of components are highly similar to one another. Therefore, it is noticeable that the peak width for each CD fraction is quite broad (Table 6.1) (i.e., larger than 70 nm).

**Table 6.1.** Fluorescence properties of obtained CD fractions.

	<b>Ex/Em (nm, nm)</b>	<b>FWHM (nm)</b>	<b>CIE 1931 coordinates (x, y)</b>	<b>QY (%)</b>
<b>CACD-P</b>	372, 443	77	0.167, 0.128	60.1
<b>CACD-B</b>	370, 440	77	0.156, 0.107	49.7
<b>CACD-C</b>	400, 480	81	0.170, 0.271	4.5
<b>CACD-G</b>	440, 530	109	0.338, 0.542	15.1
<b>CACD-Y</b>	470, 560	86	0.463, 0.528	13.1
<b>CACD-O</b>	468, 564	87	0.461, 0.483	12.3
<b>CACD-R</b>	560, 600	92	0.633, 0.366	9.8

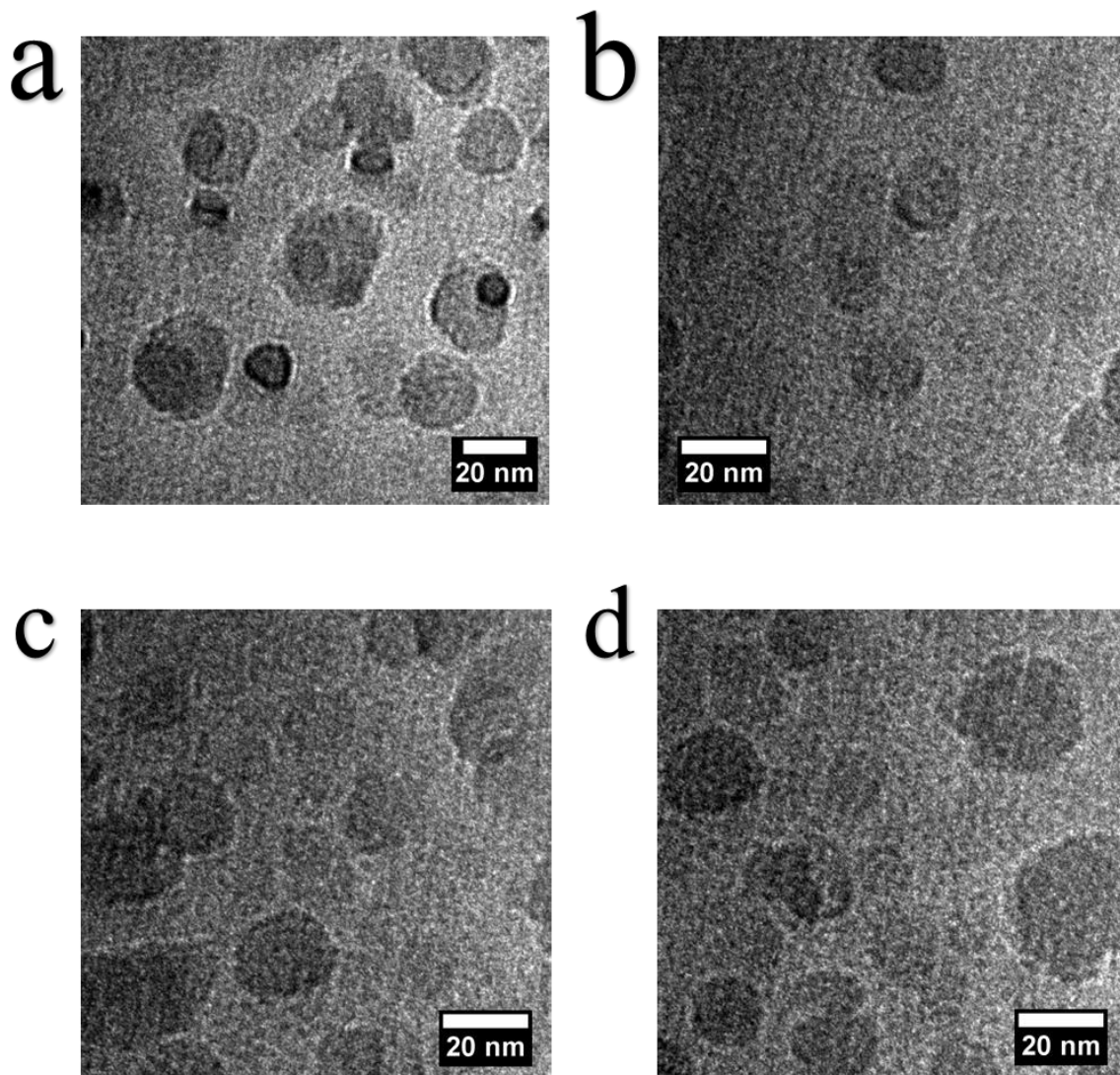


**Figure 6.3.** TEM images of (a) as-made CDs, (b) CACD-B, (c) CACD-G, and (d) CACD-R fractions.

TEM experiments were conducted to investigate the morphology and sizes of CD fractions, as shown in Figure 6.3. In general, as-made CDs as well as CD fractions exhibit a round 2D shape and there is no discernible crystal lattice fringe, indicative of the nature of amorphous carbon. Additionally, the average sizes for as-made CDs, CACD-B, G, and R fractions are  $19.2 \pm 7.6$  nm,  $15.7 \pm 1.5$  nm,  $17.4 \pm 3.9$  nm, and  $20.1 \pm 5.8$  nm, respectively. As revealed by subsequent one-way ANOVA tests, there is no significant difference

among these particle sizes. DLS was also applied to probe the sizes of CD products, as shown in Figure 6.4. The DLS sizes for as-made CDs, CACD-B, G, and R fractions are  $21 \pm 4$  nm,  $11 \pm 2$  nm,  $15 \pm 4$  nm, and  $27 \pm 4$  nm, respectively. With that being said, these CDs tended to form aggregates and sonication as long as two hours is preferred before running DLS measurements. As the fractions were dissolved in different solvents, such as water and acetone,  $\zeta$ -potential was not measured.

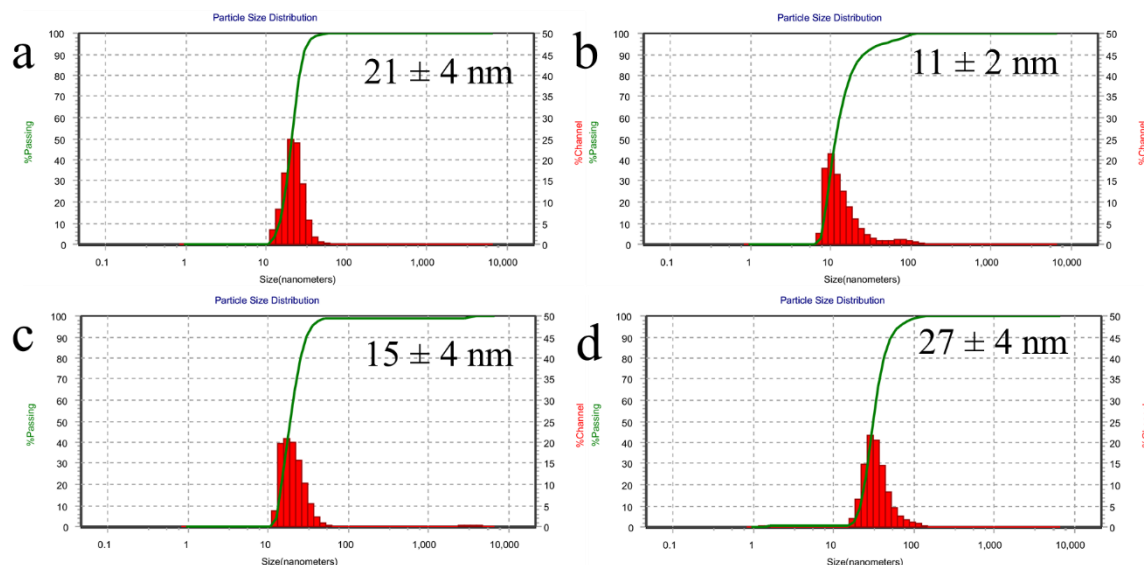


**Figure 6.4.** DLS measurements for (a) as-made CDs, (b) CACD-B, (c) CACD-G, and (d) CACD-R fractions.

The chemical bonding within the different colored carbon dots was assessed using ATR-FTIR. The IR spectra for each dot as well as the parent mixture is shown in Figure 6.5. Broadly speaking, the carbon dot fractions, and as-made CDs exhibit similar ATR-FTIR spectra. The broad feature between  $\approx 3500$ - $2800$   $\text{cm}^{-1}$  contains contributions from N-H, O-H, and C-H stretching modes.<sup>23</sup> The sharper feature between  $1600$   $\text{cm}^{-1}$  –  $1450$   $\text{cm}^{-1}$  contains peaks associated with C=O stretching ( $1642$   $\text{cm}^{-1}$ ) and N-H bending ( $1549$   $\text{cm}^{-1}$ )

that are typically observed for carbon dots.<sup>24</sup> At lower wavenumber, the peaks at 1455  $\text{cm}^{-1}$  and 1090  $\text{cm}^{-1}$  can be attributed to C-N stretching<sup>23</sup> and O-C-O bending modes. Although the ATR-FTIR data are generally similar, slight changes are observed between the different fractions and between the fractions and the as-made CDs. For example, the as-made CDs feature a resolvable C-H stretching mode centered at 2965  $\text{cm}^{-1}$  which becomes progressively less intense in CACD-B, G, and R fractions. In CACD-B, the peak at 1590  $\text{cm}^{-1}$ , which is tentatively assigned as being an N-H bending mode, is noticeably more intense.<sup>24, 25</sup> CACD-B also displays a pronounced peak at 1340  $\text{cm}^{-1}$ , in a region characteristic of C-N stretching.<sup>24</sup> Despite these relatively subtle differences, an analysis of Figure 6.5 supports the idea that both the nature and concentration of chemical bonds present in each of the CD fractions are similar. On a separate note, ongoing theoretical experiment indicates that small fluorophores may contribute to the short-wavelength emission as well as greenish luminescence after forming hydrogen bonding interaction. In addition, it is also revealed that the polyamide complex formed by reacting citric acid and urea may contribute to the red emission.

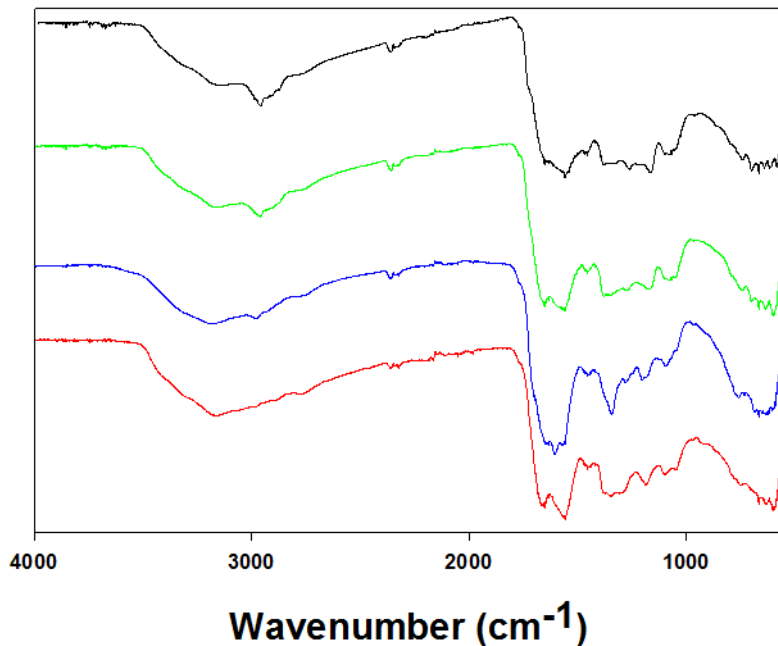


**Figure 6.5.** ATR-IR spectra of CACD-B (blue), G (green), and R (red) compared to the as-made CDs (black).

#### 6.4.3 Cellular toxicity experiments and bio-imaging experiments

In our previous study, CDs were found to be internalized rapidly by living cells and exhibited unique distribution patterns in cells<sup>26</sup>. Here, the uptake and distribution of multi-color CACDs were evaluated in rainbow gill trout epithelial cells. First, 5  $\mu\text{g}/\text{mL}$  as-made CDs was incubated with gill cells for 2 h and subjected to live-cell imaging. This concentration was chosen as concentrations below 100  $\mu\text{g}/\text{mL}$  had no impact on the cell viability of the trout gill cells (Figure 6.6 and 6.7). As shown in Figure 6.8, abundant as-made CDs were noted inside cells. Interestingly, when excited with different laser wavelengths, the emitted fluorescence signals localized to distinct intracellular positions, which indicates that as-made CDs of different excitation/emission properties might transport to different locations upon uptake. As-made CDs excited with shorter wavelengths (blue color in Figure 6.8) appeared to be more diffuse than CDs excited with

longer wavelengths (red color in Figure 6.8) inside cells. In light of this finding, we further used CD fractions to investigate their distribution patterns. Two groups of CD fractions with separate spectra were selected, namely CACD-B (excited by 405 nm laser) and CACD-R (excited by 561 nm laser). In addition, we also introduced a variety of organelle-specific stains to probe possible co-localization with CDs. As shown in Figure 6.9, the red dots mainly co-localized with lysosomes. In comparison, part of the CACD-B co-localized with lysosomes (Figure 6.10) while part of them co-localized with mitochondria (Figure 6.11). Moreover, upon exposure to CACD-B, enlarged lysosomes were formed in cells (Figure 6.10), suggesting impaired lysosomal fusion-fission balance and higher toxicity induced by smaller CDs<sup>27</sup>. CACD-B, albeit at higher concentrations than used for imaging (100 µg/mL), were the only fraction of carbon dots to induce a significant decrease in cell viability (Figure 6.6 and 6.7). We reported before that MACDs were found predominantly in mitochondria after cell internalization (Figure 6.12)<sup>26</sup>. Taken together, we conclude that CACDs of different sizes could localize in distinct subcellular regions where some particles tend to penetrate into more organelles (*e.g.*, lysosomes and mitochondria) and the rest are primarily trapped in lysosomes. By comparing CACDs and MACDs, we also conclude that CDs made of different materials could impact their intracellular distributions.

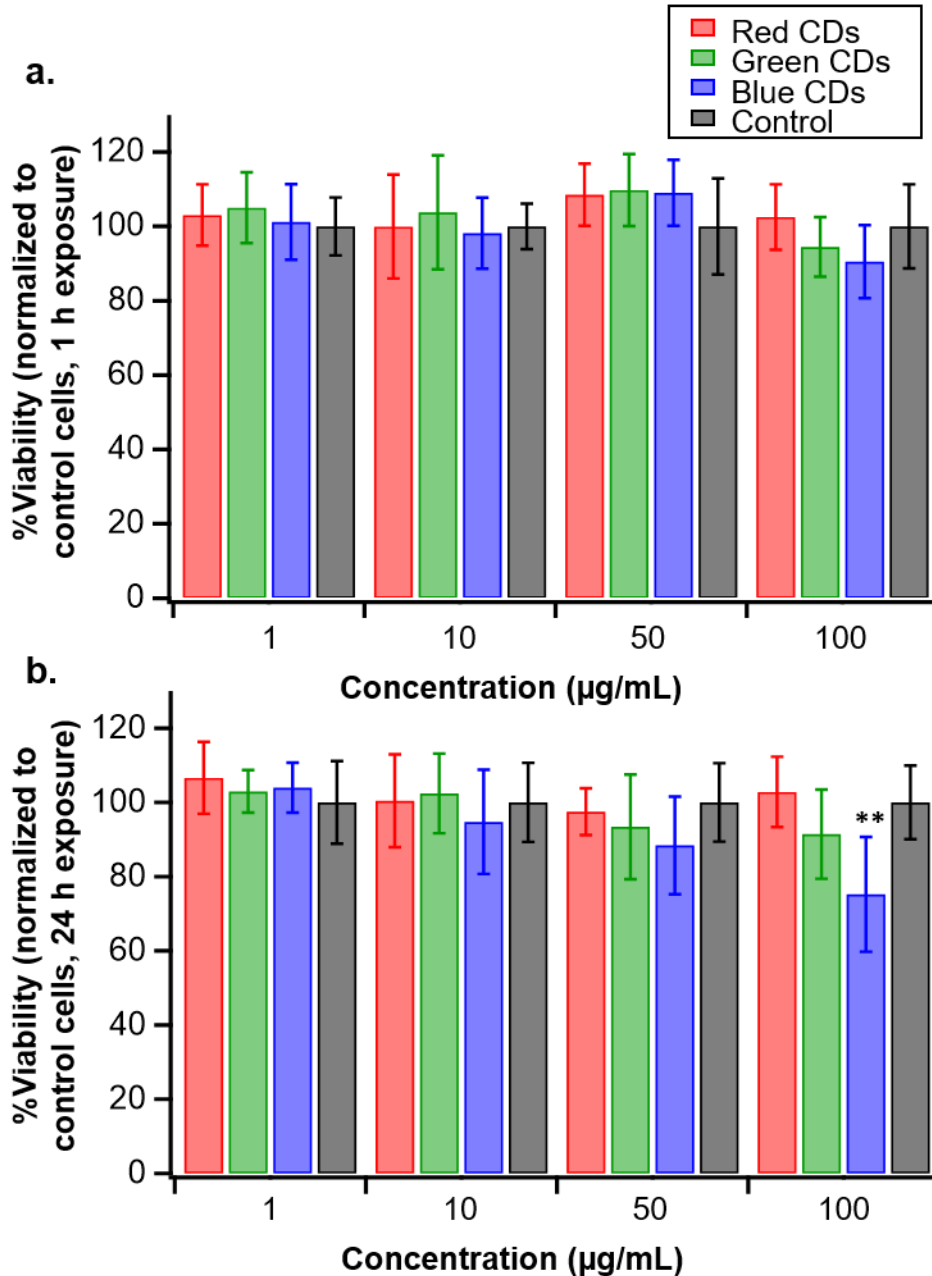


**Figure 6.6.** Impact of fractionated carbon dots on cell viability. (a) Red, blue and green carbon dots caused no significant decrease in trout gill epithelial cell viability following 1 h exposure to 1, 10, 50, or 100 µg/mL of carbon dots. (b) Red and green carbon dots caused no significant decrease in cell viability following exposure for 24 h at all concentrations studied. Blue carbon dots did cause a significant decrease in cell viability following exposure to 100 µg/mL. \*\*,  $p < 0.01$ .

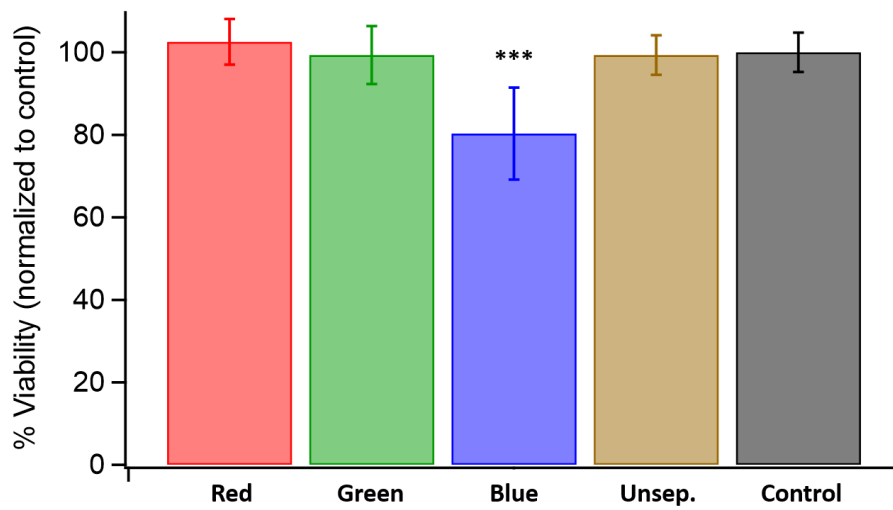


**Figure 6.7.** Comparison of fractionated and unfractionated carbon dots on cell viability following 2 h exposure to 100  $\mu\text{g}/\text{mL}$  of carbon dots. The blue carbon dots caused a significant decrease in viability compared to control cells. \*\*\*,  $p < 0.001$ .

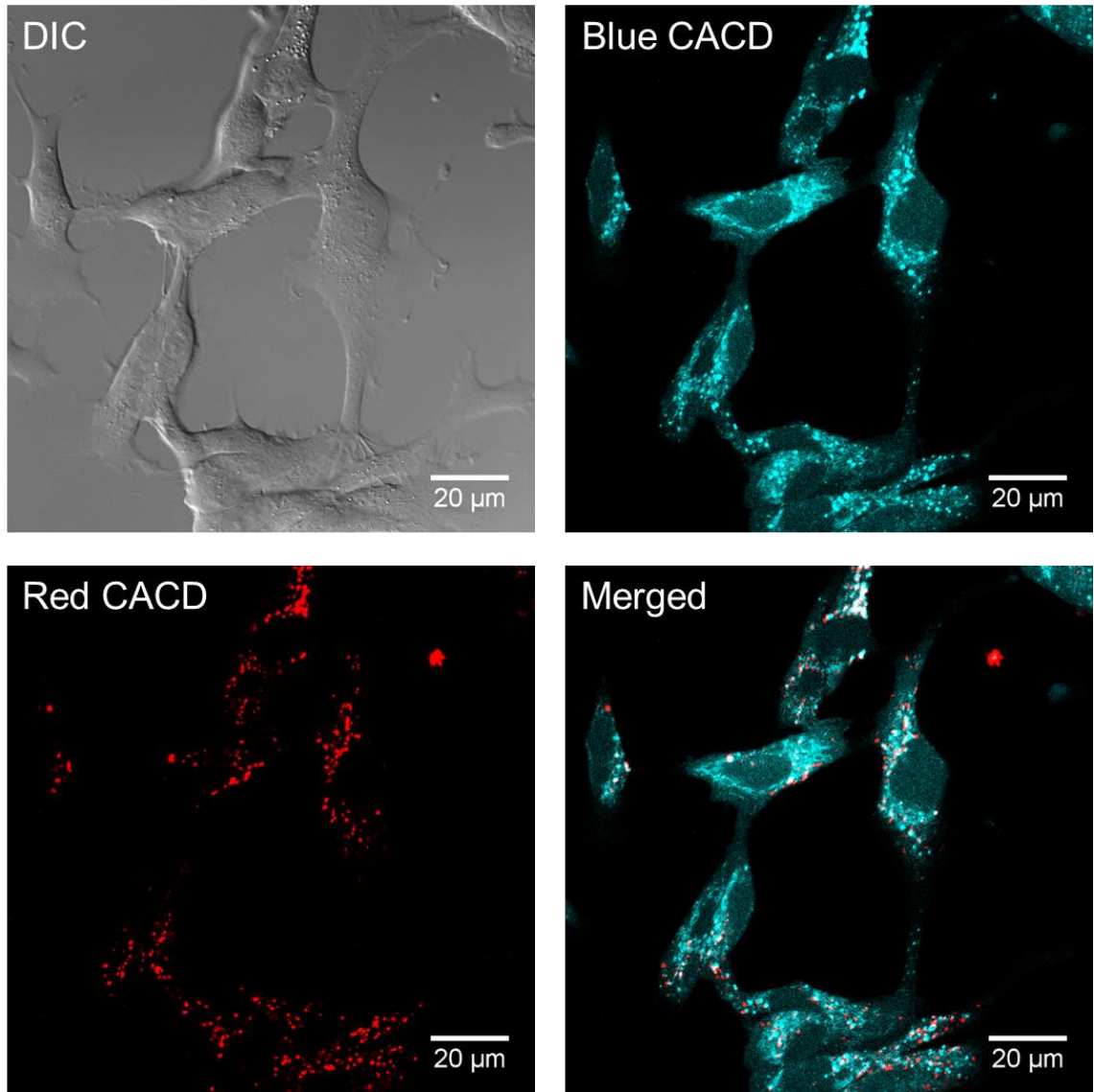


**Figure 6.8.** Distribution of unseparated CACDs in living gill cells.

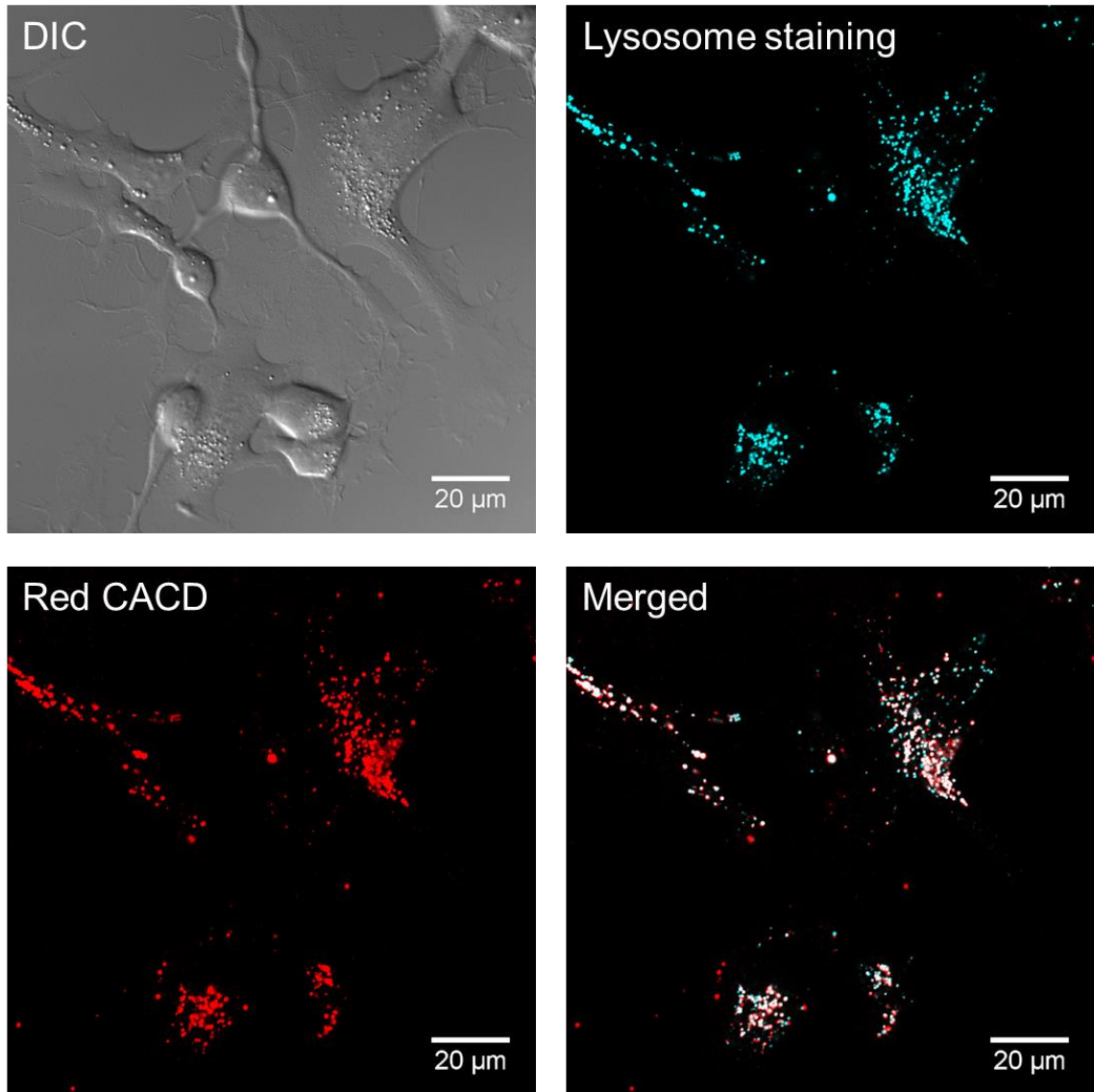


**Figure 6.9.** Red CACDs mainly localizes in lysosomes upon uptake.

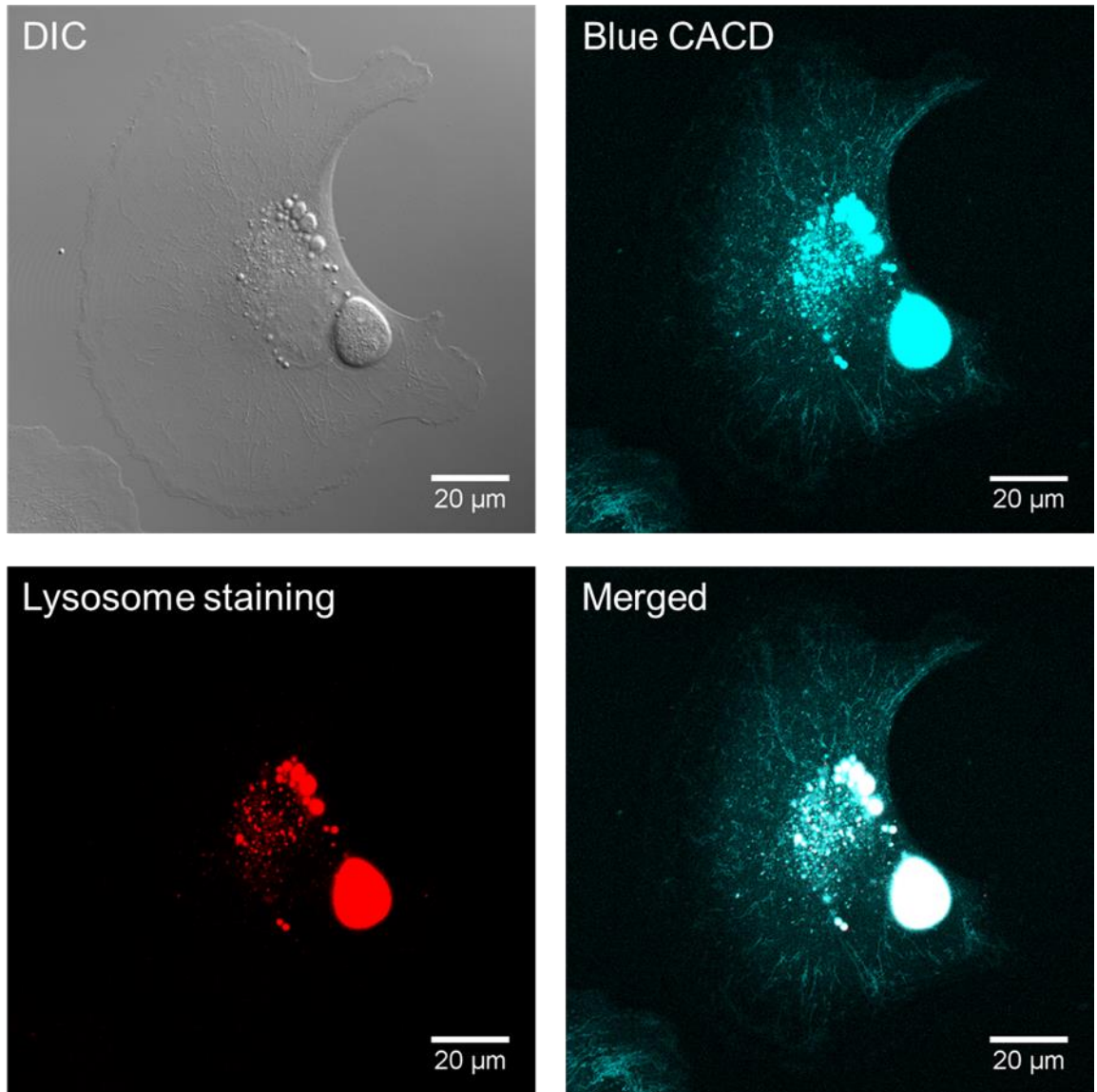


**Figure 6.10.** Some blue CACDs could localize in lysosomes upon uptake.

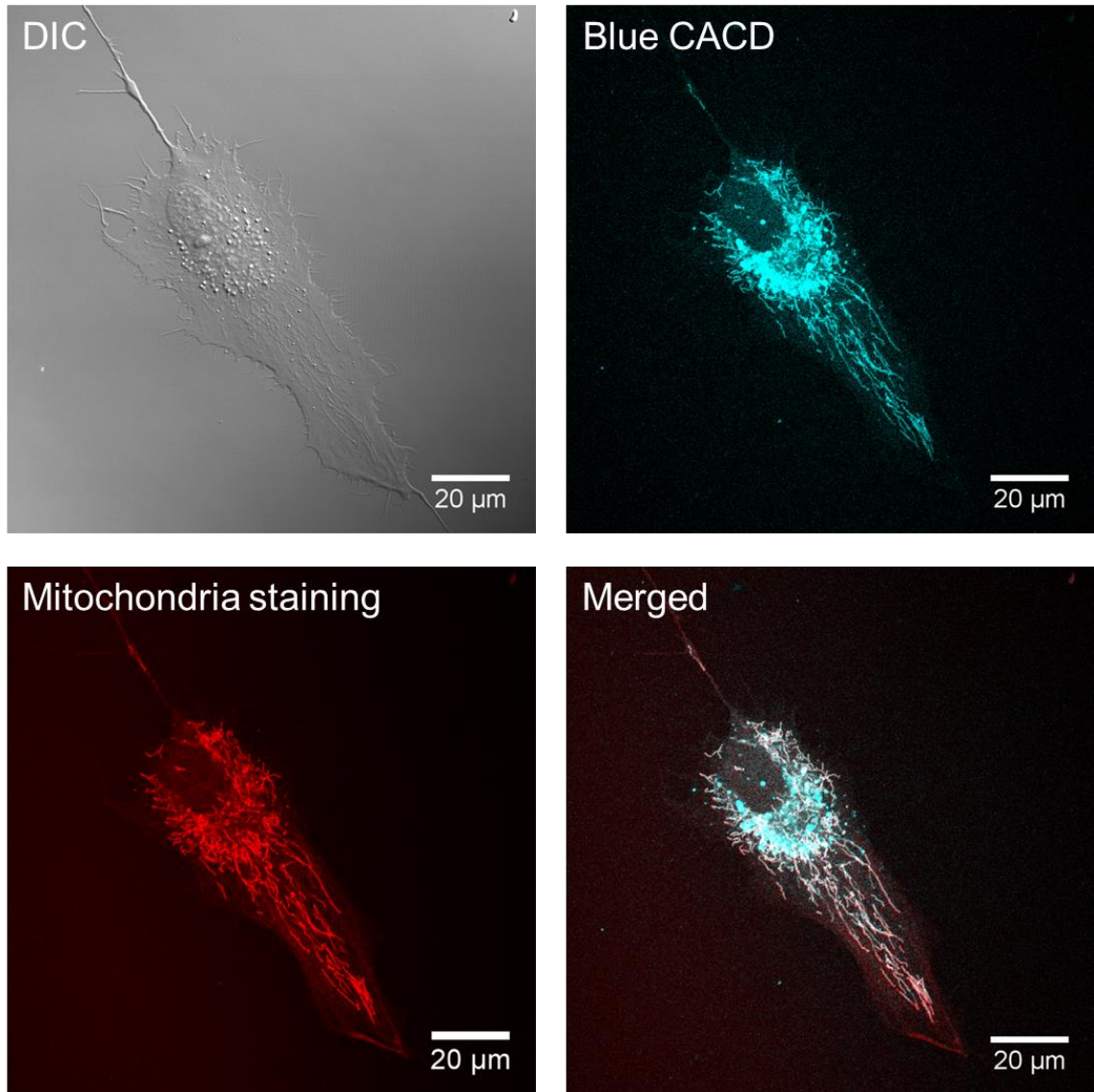


**Figure 6.11.** Some blue CACDs could localize in mitochondria upon uptake.

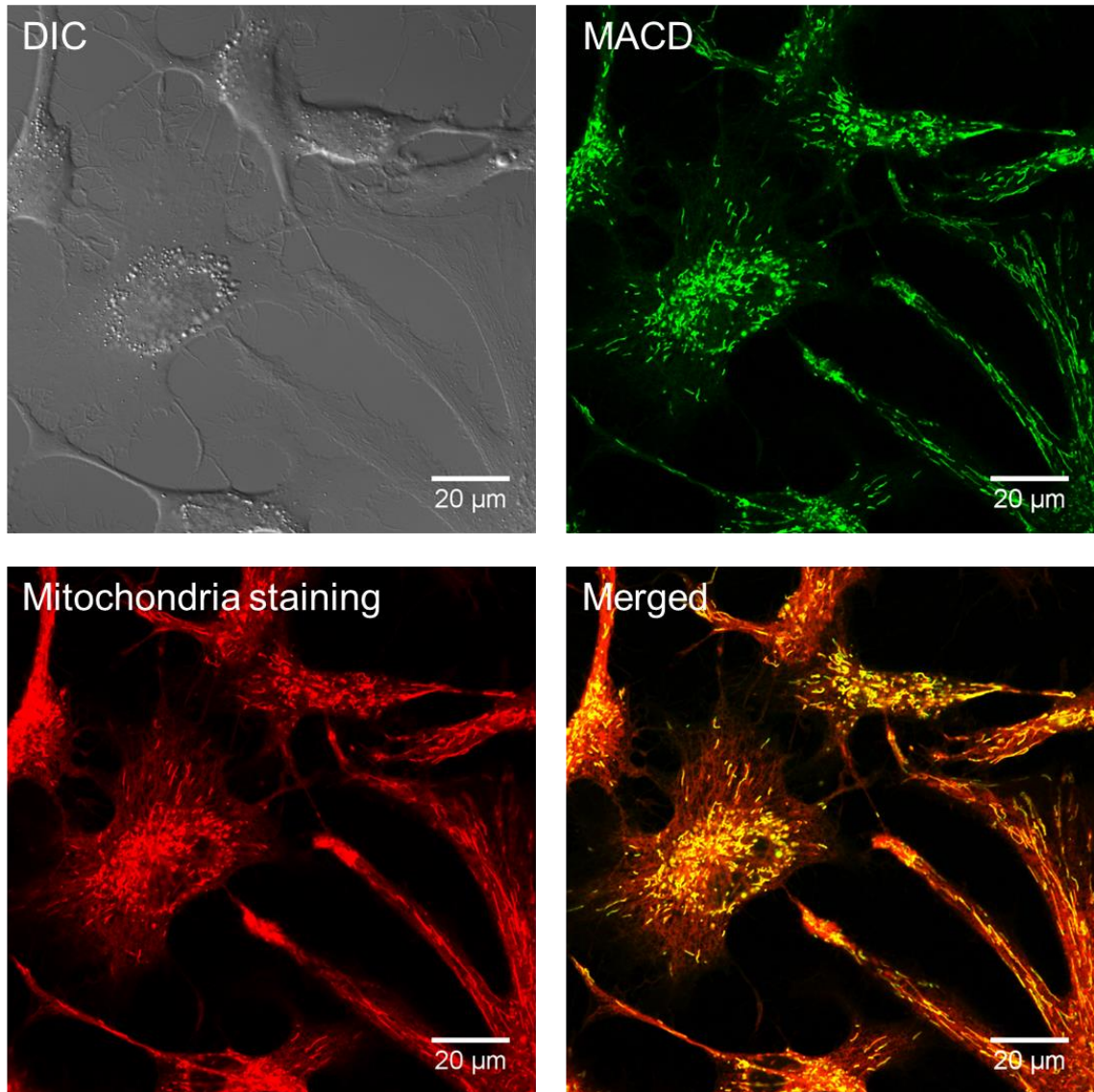


**Figure 6.12.** MACDs mainly localize in mitochondria upon uptake.

## 6.5 Conclusions

In summary, the as-made CDs can be separated efficiently via an automated chromatographic instrument and consequently, obtained CD fractions exhibit discrete colors, covering the entire visible spectrum. Though longer wavelength emitting CD fractions tend to show a larger particle size, statistical analyses reveal that there is no

significant difference. In addition, as evinced by subsequent imaging experiments, some CD fractions, such as CACD-B, tend to reside in organelles (*e.g.*, lysosomes and mitochondria) while other CD fractions, such as CACD-R, are primarily trapped in lysosomes.

## Concluding remarks

In the most recent decade, a significant number of CDs of varying size and physiochemical properties have been successfully synthesized. The versatility of their surface chemistry grants extensive turnabilities in applications such as bio-imaging, sensing, photocatalysts, LED devices, cancer treatment, drug delivery, and self-healing materials. Though CDs are under extensive research recently, significant challenges remain on the path to a complete understanding, such as the elucidation of the structures of varied CDs and the controllable synthesis of longer wavelength-emitting CDs as well as the development of analytical methods to quantify the carbonization that contributes to the formation of CDs.

On the other hand, it has been serving as a traditional method to intentionally dope impurities into intrinsic structures to fine tune the original bandgap and the density of free carriers, and as such, to control the properties of bulk semiconductor materials as well as semiconductor nanocrystals. Such a “charge engineering” strategy is promising to achieve breakthroughs in many optoelectronic, photonic, and spin-based nanotechnologies. However, with the prospering growth of the market of semiconductor products, an increasing amount of doped semiconductor materials, namely, E-wastes, have been released into the environment and their footprints are spread across the ecosystem. From a sustainability perspective, it is necessary to understand the environmental fate of these doped semiconductors to foster a green and efficient semiconductor manufacturing industry.

## Bibliography

### Chapter One

1. X. Xu, R. Ray, Y. Gu, H. J. Ploehn, L. Gearheart, K. Raker and W. A. Scrivens, *J. Am. Chem. Soc.*, 2004, **126**, 12736-12737.
2. B. Yao, H. Huang, Y. Liu and Z. Kang, *Trends Chem.*, 2019, **1**, 235-246.
3. L. Xiao and H. Sun, *Nanoscale Horiz.*, 2018, **3**, 565-597.
4. M. Shamsipur, A. Barati and S. Karami, *Carbon*, 2017, **124**, 429-472.
5. J. Li, B. Wang, H. Zhang and J. Yu, *Small*, 2019, **0**, 1805504.
6. Y. Yan, J. Chen, N. Li, J. Tian, K. Li, J. Jiang, J. Liu, Q. Tian and P. Chen, *ACS Nano*, 2018, **12**, 3523-3532.
7. N. Li, A. Than, X. Wang, S. Xu, L. Sun, H. Duan, C. Xu and P. Chen, *ACS Nano*, 2016, **10**, 3622-3629.
8. B. Zhi, M. J. Gallagher, B. P. Frank, T. Y. Lyons, T. A. Qiu, J. Da, A. C. Mensch, R. J. Hamers, Z. Rosenzweig, D. H. Fairbrother and C. L. Haynes, *Carbon*, 2018, **129**, 438-449.
9. J. Li, X. Li, L. Zeng, S. Fan, M. Zhang, W. Sun, X. Chen, M. O. Tadé and S. Liu, *Nanoscale*, 2019, **11**, 3877-3887.
10. Y. Choi, Y. Choi, O.-H. Kwon and B.-S. Kim, *Chem. Asian J.*, 2018, **13**, 586-598.
11. Y. Zhang, A. A. Tamijani, M. E. Taylor, B. Zhi, C. L. Haynes, S. E. Mason and R. J. Hamers, *J. Am. Chem. Soc.*, 2019.
12. M. Pirsaeheb, S. Mohammadi, A. Salimi and M. Payandeh, *Microchim. Acta*, 2019, **186**, 231.
13. S. Pramanik, S. K. E. Hill, B. Zhi, N. V. Hudson-Smith, J. J. Wu, J. N. White, E. A. McIntire, V. S. S. K. Kondeti, A. L. Lee, P. J. Bruggeman, U. R. Kortshagen and C. L. Haynes, *Environ. Sci.: Nano*, 2018, **5**, 1890-1901.
14. M. J. Gallagher, J. T. Buchman, T. A. Qiu, B. Zhi, T. Y. Lyons, K. M. Landy, Z. Rosenzweig, C. L. Haynes and D. H. Fairbrother, *Environ. Sci.: Nano*, 2018, **5**, 1694-1710.
15. Z. Zhang, D. Zhang, C. Shi, W. Liu, L. Chen, Y. Miao, J. Diwu, J. Li and S. Wang, *Environ. Sci.: Nano*, 2019.
16. Y. Han, L. Shi, X. Luo, X. Chen, W. Yang, W. Tang, J. Wang, T. Yue and Z. Li, *Carbon*, 2019, **149**, 355-363.

17. R. Su, D. Wang, M. Liu, J. Yan, J.-X. Wang, Q. Zhan, Y. Pu, N. R. Foster and J.-F. Chen, *ACS Omega*, 2018, **3**, 13211-13218.
18. S. D. Pritzl, F. Pschunder, F. Ehrat, S. Bhattacharyya, T. Lohmüller, M. A. Huergo and J. Feldmann, *Nano Lett.*, 2019, DOI: 10.1021/acs.nanolett.9b01071.
19. C. H. Li, R. S. Li, C. M. Li, C. Z. Huang and S. J. Zhen, *Chem. Commun.*, 2019, **55**, 6437-6440.
20. B. Zhi, Y. Cui, S. Wang, B. P. Frank, D. N. Williams, R. P. Brown, E. S. Melby, R. J. Hamers, Z. Rosenzweig, D. H. Fairbrother, G. Orr and C. L. Haynes, *ACS Nano*, 2018, **12**, 5741-5752.
21. H. Liu, Y. Sun, Z. Li, J. Yang, A. Aryee, L. Qu, D. Du and Y. Lin, *Nanoscale*, 2019, DOI: 10.1039/C9NR01678C.
22. J. Wang, X. Hu, H. Ding, X. Huang, M. Xu, Z. Li, D. Wang, X. Yan, Y. Lu, Y. Xu, Y. Chen, P. C. Morais, Y. Tian, R. Q. Zhang and H. Bi, *ACS Appl. Mater. Interfaces*, 2019, **11**, 18203-18212.
23. L. Xiao, H. Guo, S. Wang, J. Li, Y. Wang and B. Xing, *Environ. Sci.: Nano*, 2019, **6**, 1493-1506.
24. A. Pyne, S. Layek, A. Patra and N. Sarkar, *J. Mater. Chem. C*, 2019, **7**, 6414-6425.
25. Y. Fanglong, W. Zhibin, L. Xiaohong, L. Yunchao, T. Zhan'ao, F. Louzhen and Y. Shihe, *Adv. Mater.*, 2017, **29**, 1604436.
26. T. Hu, Z. Wen, C. Wang, T. Thomas, C. Wang, Q. Song and M. Yang, *Nanoscale Adv.*, 2019, **1**, 1413-1420.
27. E. Liu, D. Li, X. Zhou, G. Zhou, H. Xiao, D. Zhou, P. Tian, R. Guo and S. Qu, *ACS Sustain. Chem. Eng*, 2019, **7**, 9301-9308.
28. X. Feng, K. Jiang, H. Zeng and H. Lin, *Nanomaterials*, 2019, **9**, 725.
29. L. Vallan, R. Canton-Vitoria, H. B. Gobeze, Y. Jang, R. Arenal, A. M. Benito, W. K. Maser, F. D'Souza and N. Tagmatarchis, *J. Am. Chem. Soc.*, 2018, **140**, 13488-13496.
30. D. Kong, Y. Wang, S. Huang, Y. V. Lim, J. Zhang, L. Sun, B. Liu, T. Chen, P. Valdivia y Alvarado and H. Y. Yang, *J. Mater. Chem. A*, 2019, **7**, 12751-12762.
31. J. B. Essner and G. A. Baker, *Environ. Sci.: Nano*, 2017, **4**, 1216-1263.
32. J. T. Margraf, F. Lodermeier, V. Strauss, P. Haines, J. Walter, W. Peukert, R. D. Costa, T. Clark and D. M. Guldi, *Nanoscale Horiz.*, 2016, **1**, 220-226.
33. G. A. M. Hutton, B. C. M. Martindale and E. Reisner, *Chem. Soc. Rev.*, 2017, **46**, 6111-6123.
34. C. Hu, M. Li, J. Qiu and Y.-P. Sun, *Chem. Soc. Rev.*, 2019, **48**, 2315-2337.

35. D. Chen, H. Gao, X. Chen, G. Fang, S. Yuan and Y. Yuan, *ACS Photonics*, 2017, **4**, 2352-2358.
36. J. Schneider, C. J. Reckmeier, Y. Xiong, M. von Seckendorff, A. S. Susa, P. Kasák and A. L. Rogach, *J. Phys. Chem. C*, 2017, **121**, 2014-2022.
37. Z. L. Wu, Z. X. Liu and Y. H. Yuan, *J. Mater. Chem. B*, 2017, **5**, 3794-3809.
38. Z. Sun, X. Li, Y. Wu, C. Wei and H. Zeng, *New J. Chem.*, 2018, **42**, 4603-4611.
39. L. Vallan, E. P. Urriolabeitia, F. Ruipérez, J. M. Matxain, R. Canton-Vitoria, N. Tagmatarchis, A. M. Benito and W. K. Maser, *J. Am. Chem. Soc.*, 2018, **140**, 12862-12869.
40. O. Kozák, M. Sudolská, G. Pramanik, P. Cígler, M. Otyepka and R. Zbořil, *Chem. Mater.*, 2016, **28**, 4085-4128.
41. K. Jiang, S. Sun, L. Zhang, Y. Lu, A. Wu, C. Cai and H. Lin, *Angew. Chem. Int. Ed.*, 2015, **54**, 5360-5363.
42. F. Yuan, T. Yuan, L. Sui, Z. Wang, Z. Xi, Y. Li, X. Li, L. Fan, Z. a. Tan, A. Chen, M. Jin and S. Yang, *Nat. Commun.*, 2018, **9**, 2249.
43. L. Bao, C. Liu, Z.-L. Zhang and D.-W. Pang, *Adv. Mater.*, 2015, **27**, 1663-1667.
44. X. Tan, Y. Li, X. Li, S. Zhou, L. Fan and S. Yang, *Chem. Commun.*, 2015, **51**, 2544-2546.
45. J. Zhu, X. Bai, X. Chen, H. Shao, Y. Zhai, G. Pan, H. Zhang, E. V. Ushakova, Y. Zhang, H. Song and A. L. Rogach, *Adv. Opt. Mater.*, 2019, **7**, 1801599.
46. K. Jiang, X. Feng, X. Gao, Y. Wang, C. Cai, Z. Li and H. Lin, *Nanomaterials*, 2019, **9**, 529.
47. S. Hu, A. Trinchi, P. Atkin and I. Cole, *Angew. Chem. Int. Ed.*, 2015, **54**, 2970-2974.
48. S. Y. Lim, W. Shen and Z. Q. Gao, *Chem. Soc. Rev.*, 2015, **44**, 362-381.
49. S. Hu, *Chem. Rec.*, 2016, **16**, 219-230.
50. X. Sun and Y. Lei, *Trends Anal. Chem.*, 2017, **89**, 163-180.
51. P. M. Gharat, J. M. Chethodil, A. P. Srivastava, P. P. K, H. Pal and S. Dutta Choudhury, *Photochem. Photobiol. Sci.*, 2019, **18**, 110-119.
52. D. Shen, Y. Long, J. Wang, Y. Yu, J. Pi, L. Yang and H. Zheng, *Nanoscale*, 2019, **11**, 5998-6003.
53. H. Ding, S. B. Yu, J. S. Wei and H. M. Xiong, *ACS Nano*, 2016, **10**, 484-491.
54. Y. Song, S. Zhu, S. Zhang, Y. Fu, L. Wang, X. Zhao and B. Yang, *J. Mater. Chem. C*, 2015, **3**, 5976-5984.

55. Y. Xiong, J. Schneider, E. V. Ushakova and A. L. Rogach, *Nano Today*, 2018, **23**, 124-139.
56. S. Kalytchuk, K. Poláková, Y. Wang, J. P. Froning, K. Cepe, A. L. Rogach and R. Zbořil, *ACS Nano*, 2017, **11**, 1432-1442.
57. J. B. Essner, J. A. Kist, L. Polo-Parada and G. A. Baker, *Chem. Mater.*, 2018, **30**, 1878-1887.
58. K. Mishra, S. Koley and S. Ghosh, *J. Phys. Chem. Lett.*, 2019, **10**, 335-345.
59. M. Shamsipur, A. Barati, A. A. Taherpour and M. Jamshidi, *J. Phys. Chem. Lett.*, 2018, **9**, 4189-4198.
60. J. Du, N. Xu, J. Fan, W. Sun and X. Peng, *Small*, 2019, 1805087.
61. Y. Wang, Q. Su and X. Yang, *Chem. Commun.*, 2018, **54**, 11312-11315.
62. V. Mishra, A. Patil, S. Thakur and P. Kesharwani, *Drug Discov. Today*, 2018, **23**, 1219-1232.
63. T. Zhang, J. Zhu, Y. Zhai, H. Wang, X. Bai, B. Dong, H. Wang and H. Song, *Nanoscale*, 2017, **9**, 13042-13051.
64. B. Yuan, X. Sun, J. Yan, Z. Xie, P. Chen and S. Zhou, *Phys. Chem. Chem. Phys.*, 2016, **18**, 25002-25009.
65. J. Zhang and S.-H. Yu, *Mater. Today*, 2016, **19**, 382-393.
66. V. Sharma, P. Tiwari and S. M. Mobin, *J. Mater. Chem. B*, 2017, **5**, 8904-8924.
67. M. Tuerhong, Y. Xu and X.-B. Yin, *Chin. J. Anal. Chem.*, 2017, **45**, 139-150.
68. J. V. Frangioni, *Curr. Opin. Chem. Biol.*, 2003, **7**, 626-634.
69. J. Peng, W. Gao, B. K. Gupta, Z. Liu, R. Romero-Aburto, L. Ge, L. Song, L. B. Alemany, X. Zhan, G. Gao, S. A. Vithayathil, B. A. Kaiparettu, A. A. Marti, T. Hayashi, J.-J. Zhu and P. M. Ajayan, *Nano Lett.*, 2012, **12**, 844-849.
70. Y. Dong, H. Pang, S. Ren, C. Chen, Y. Chi and T. Yu, *Carbon*, 2013, **64**, 245-251.
71. W. Chen, F. Li, C. Wu and T. Guo, *Appl. Phys. Lett.*, 2014, **104**, 063109.
72. M. M. F. Chang, I. R. Ginjom, M. Ngu-Schwemlein and S. M. Ng, *Microchim. Acta*, 2016, **183**, 1899-1907.
73. T. Yuan, T. Meng, P. He, Y. Shi, Y. Li, X. Li, L. Fan and S. Yang, *J. Mater. Chem. C*, 2019, DOI: 10.1039/C9TC01730E.
74. X. Gong, W. Lu, Y. Liu, Z. Li, S. Shuang, C. Dong and M. M. F. Choi, *J. Mater. Chem. B*, 2015, **3**, 6813-6819.

75. B.-P. Jiang, B. Zhou, X.-C. Shen, Y.-X. Yu, S.-C. Ji, C.-C. Wen and H. Liang, *Chem.: Eur. J.*, 2015, **21**, 18993-18999.
76. C. Liu, R. Wang, B. Wang, Z. Deng, Y. Jin, Y. Kang and J. Chen, *Microchim. Acta*, 2018, **185**, 539.
77. L. Guo, J. Ge, W. Liu, G. Niu, Q. Jia, H. Wang and P. Wang, *Nanoscale*, 2016, **8**, 729-734.
78. N. Dhenadhayalan, K.-C. Lin, R. Suresh and P. Ramamurthy, *J. Phys. Chem. C*, 2016, **120**, 1252-1261.
79. F. Gao, S. Ma, J. Li, K. Dai, X. Xiao, D. Zhao and W. Gong, *Carbon*, 2017, **112**, 131-141.
80. Q. Fang, Y. Dong, Y. Chen, C.-H. Lu, Y. Chi, H.-H. Yang and T. Yu, *Carbon*, 2017, **118**, 319-326.
81. K. Holá, M. Sudolská, S. Kalytchuk, D. Nachtigallová, A. L. Rogach, M. Otyepka and R. Zbořil, *ACS Nano*, 2017, **11**, 12402-12410.
82. B. Wang, Y. Wang, H. Wu, X. Song, X. Guo, D. Zhang, X. Ma and M. Tan, *RSC Adv.*, 2014, **4**, 49960-49963.
83. D. Qu, M. Zheng, P. Du, Y. Zhou, L. Zhang, D. Li, H. Tan, Z. Zhao, Z. Xie and Z. Sun, *Nanoscale*, 2013, **5**, 12272-12277.
84. S. Sun, L. Zhang, K. Jiang, A. Wu and H. Lin, *Chem. Mater.*, 2016, **28**, 8659-8668.
85. L. Song, Y. Cui, C. Zhang, Z. Hu and X. Liu, *RSC Adv.*, 2016, **6**, 17704-17712.
86. Y. Ding, J. Zheng, J. Wang, Y. Yang and X. Liu, *J. Mater. Chem. C*, 2019, **7**, 1502-1509.
87. C. Reckmeier, J. Schneider, A. Sussha and A. Rogach, *Opt. Express*, 2016, **24**, A312-A340.
88. Y. Wang, Q. Su and X. Yang, *Chem. Commun.*, 2018, **54**, 11312-11315.
89. Z. Wang, F. Yuan, X. Li, Y. Li, H. Zhong, L. Fan and S. Yang, *Adv. Mater.*, 2017, **29**, 1702910.
90. W. Zhu, X. Meng, H. Li, F. He, L. Wang, H. Xu, Y. Huang, W. Zhang, X. Fang and T. Ding, *Opt. Mater.*, 2019, **88**, 412-416.
91. Q. Wang, S. Zhang, Y. Zhong, X.-F. Yang, Z. Li and H. Li, *Anal. Chem.*, 2017, **89**, 1734-1741.
92. Q. Liu, D. Li, Z. Zhu, S. Yu, Y. Zhang, D. Yu and Y. Jiang, *RSC Adv.*, 2018, **8**, 4850-4856.

93. F. Yuan, T. Yuan, L. Sui, Z. Wang, Z. Xi, Y. Li, X. Li, L. Fan, A. Chen and M. Jin, *Nat. Commun.*, 2018, **9**, 2249.
94. Z. Liu, A. Nahhas, L. Liu, E. Ada, X. Zhang and S. K. Manohar, *J. Nanomater.*, 2018, **2018**, 7.
95. J. Ge, M. Lan, B. Zhou, W. Liu, L. Guo, H. Wang, Q. Jia, G. Niu, X. Huang, H. Zhou, X. Meng, P. Wang, C.-S. Lee, W. Zhang and X. Han, *Nat. Commun.*, 2014, **5**, 4596-4596.
96. L. Meng, M. Lan, L. Guo, L. Xie, W. Hui, J. Ge, W. Liu, Y. Wang and P. Wang, *RSC Adv.*, 2015, **5**, 26886-26890.
97. J. Ge, Q. Jia, W. Liu, L. Guo, Q. Liu, M. Lan, H. Zhang, X. Meng and P. Wang, *Adv. Mater.*, 2015, **27**, 4169-4177.
98. F. Jenkins, J. Robinson, J. Gellatly and G. Salmond, *Food Cosmet Toxicol.*, 1972, **10**, 671-679.
99. J. Bus and J. Popp, *Food Chem. Toxicol.*, 1987, **25**, 619-626.
100. T. Tišler and J. Zagorc-Končan, *Water Air Soil Pollut.*, 1997, **97**, 315-322.
101. G. Pedersen, J. Brynskov and T. Saermark, *Scand. J. Gastroenterol.*, 2002, **37**, 74-79.
102. Z. D. Zujovic, L. Zhang, G. A. Bowmaker, P. A. Kilmartin and J. Travas-Sejdic, *Macromolecules*, 2008, **41**, 3125-3135.
103. J. Zazo, J. Casas, A. Mohedano, M. Gilarranz and J. Rodriguez, *Environ. Sci. Technol.*, 2005, **39**, 9295-9302.
104. J. Zhan, B. J. Geng, K. Wu, G. Xu, L. Wang, R. Y. Guo, B. Lei, F. F. Zheng, D. Y. Pan and M. H. Wu, *Carbon*, 2018, **130**, 153-163.
105. H. Ding, J.-S. Wei, P. Zhang, Z.-Y. Zhou, Q.-Y. Gao and H.-M. Xiong, *Small*, 2018, **14**, 1800612.
106. J. Zhu, X. Bai, J. Bai, G. Pan, Y. Zhu, Y. Zhai, H. Shao, X. Chen, B. Dong, H. Zhang and H. Song, *Nanotechnology*, 2018, **29**, 085705.
107. M. Zheng, Y. Li, Y. Zhang and Z. Xie, *RSC Adv.*, 2016, **6**, 83501-83504.
108. C. J. Reckmeier, Y. Wang, R. Zboril and A. L. Rogach, *J. Phys. Chem. C*, 2016, **120**, 10591-10604.
109. M. Wu, J. Zhan, B. Geng, P. He, K. Wu, L. Wang, G. Xu, Z. Li, L. Yin and D. Pan, *Nanoscale*, 2017, **9**, 13195-13202.
110. H. Wang, C. Sun, X. Chen, Y. Zhang, V. L. Colvin, Q. Rice, J. Seo, S. Feng, S. Wang and W. W. Yu, *Nanoscale*, 2017, **9**, 1909-1915.

111. A. Sciortino, E. Marino, B. v. Dam, P. Schall, M. Cannas and F. Messina, *J. Phys. Chem. Lett.*, 2016, **7**, 3419-3423.
112. P. Jing, D. Han, D. Li, D. Zhou, D. Shen, G. Xiao, B. Zou and S. Qu, *Nanoscale Horiz.*, 2018, **4**, 175-181.
113. J. C. Vinci, I. M. Ferrer, S. J. Seedhouse, A. K. Bourdon, J. M. Reynard, B. A. Foster, F. V. Bright and L. A. Colón, *J. Phys. Chem. Lett.*, 2012, **4**, 239-243.
114. F. Arcudi, L. Đorđević and M. Prato, *Angew. Chem. Int. Ed.*, 2016, **55**, 2107-2112.
115. N. Fuyuno, D. Kozawa, Y. Miyauchi, S. Mouri, R. Kitaura, H. Shinohara, T. Yasuda, N. Komatsu and K. Matsuda, *Adv. Opt. Mater.*, 2014, **2**, 983-989.
116. Y. Zhou, P. Y. Liyanage, D. L. Geleroff, Z. Peng, K. J. Mintz, S. D. Hettiarachchi, R. R. Pandey, C. C. Chusuei, P. L. Blackwelder and R. M. Leblanc, *ChemPhysChem*, 2018, **19**, 2589-2597.
117. Y. Jiao, X. Gong, H. Han, Y. Gao, W. Lu, Y. Liu, M. Xian, S. Shuang and C. Dong, *Anal. Chim. Acta*, 2018, **1042**, 125-132.
118. P. Lesani, S. M. Ardekani, A. Dehghani, M. Hassan and V. G. Gomes, *Sens. Actuators B Chem.*, 2019, **285**, 145-155.
119. A. A. Kokorina, E. S. Prikhozhdenko, N. V. Tarakina, A. V. Sapelkin, G. B. Sukhorukov and I. Y. Goryacheva, *Carbon*, 2018, **127**, 541-547.
120. P. Zhao, X. Li, G. Baryshnikov, B. Wu, H. Ågren, J. Zhang and L. Zhu, *Chem. Sci.*, 2018, **9**, 1323-1329.
121. K. J. Mintz, Y. Zhou and R. M. Leblanc, *Nanoscale*, 2019, **11**, 4634-4652.
122. L. Liu and Z. Xu, *Anal. Methods*, 2019, **11**, 760-766.
123. C.-Y. Chen, Y.-H. Tsai and C.-W. Chang, *New J. Chem.*, 2019, **43**, 6153-6159.
124. A. Koutsioukis, A. Akouros, R. Zboril and V. Georgakilas, *Nanoscale*, 2018, **10**, 11293-11296.
125. A. Blumer, A. Ehrenfeucht, D. Haussler and M. K. Warmuth, *Inf. Process. Lett.*, 1987, **24**, 377-380.
126. P. Domingos, *Data Min. Knowl. Discov.*, 1999, **3**, 409-425.
127. M. Xiang, Q. Dan, Y. Dongxue, N. Bing, Z. Yikang, F. Hongyou and S. Zaicheng, *Adv. Mater.*, 2018, **30**, 1704740.
128. L. Pan, S. Sun, A. Zhang, K. Jiang, L. Zhang, C. Dong, Q. Huang, A. Wu and H. Lin, *Adv. Mater.*, 2015, **27**, 7782-7787.
129. H. Nie, M. Li, Q. Li, S. Liang, Y. Tan, L. Sheng, W. Shi and S. X.-A. Zhang, *Chem. Mater.*, 2014, **26**, 3104-3112.

130. J. Shangguan, D. He, X. He, K. Wang, F. Xu, J. Liu, J. Tang, X. Yang and J. Huang, *Anal. Chem.*, 2016, **88**, 7837-7843.
131. Y. Wang, L. Lu, H. Peng, J. Xu, F. Wang, R. Qi, Z. Xu and W. Zhang, *Chem. Commun.*, 2016, **52**, 9247-9250.
132. C. Wang, Z. Xu, H. Cheng, H. Lin, M. G. Humphrey and C. Zhang, *Carbon*, 2015, **82**, 87-95.
133. W. Liu, S. Xu, Z. Li, R. Liang, M. Wei, D. G. Evans and X. Duan, *Chem. Mater.*, 2016, **28**, 5426-5431.
134. K. Jiang, S. Sun, L. Zhang, Y. Wang, C. Cai and H. Lin, *ACS Appl. Mater. Interfaces*, 2015, **7**, 23231-23238.
135. J. Chen, Y. Li, K. Lv, W. Zhong, H. Wang, Z. Wu, P. Yi and J. Jiang, *Sens. Actuators B Chem.*, 2016, **224**, 298-306.
136. J. He, H. Zhang, J. Zou, Y. Liu, J. Zhuang, Y. Xiao and B. Lei, *Biosens. Bioelectron.*, 2016, **79**, 531-535.
137. N. Wang, Y. Wang, T. Guo, T. Yang, M. Chen and J. Wang, *Biosens. Bioelectron.*, 2016, **85**, 68-75.
138. P. Shen and Y. Xia, *Anal. Chem.*, 2014, **86**, 5323-5329.
139. L. Zhang, Y. Han, J. Zhu, Y. Zhai and S. Dong, *Anal. Chem.*, 2015, **87**, 2033-2036.
140. J. F. Y. Fong, S. F. Chin and S. M. Ng, *Biosens. Bioelectron.*, 2016, **85**, 844-852.
141. G. Li, H. Fu, X. Chen, P. Gong, G. Chen, L. Xia, H. Wang, J. You and Y. Wu, *Anal. Chem.*, 2016, **88**, 2720-2726.
142. H. Li, C. Sun, R. Vijayaraghavan, F. Zhou, X. Zhang and D. R. MacFarlane, *Carbon*, 2016, **104**, 33-39.
143. X. Yan, Y. Song, C. Zhu, H. Li, D. Du, X. Su and Y. Lin, *Anal. Chem.*, 2018, **90**, 2618-2624.
144. X. Cui, Y. Wang, J. Liu, Q. Yang, B. Zhang, Y. Gao, Y. Wang and G. Lu, *Sens. Actuators B Chem.*, 2017, **242**, 1272-1280.
145. W.-S. Zou, Q.-C. Zhao, J. Zhang, X.-M. Chen, X.-F. Wang, L. Zhao, S.-H. Chen and Y.-Q. Wang, *Anal. Chim. Acta*, 2017, **970**, 64-72.
146. A. Kumar, A. R. Chowdhuri, D. Laha, T. K. Mahto, P. Karmakar and S. K. Sahu, *Sens. Actuators B Chem.*, 2017, **242**, 679-686.
147. X. Li, Y. Zheng, Y. Tang, Q. Chen, J. Gao, Q. Luo and Q. Wang, *Spectrochim. Acta A*, 2019, **206**, 240-245.
148. L. Li, D. Liu, A. Shi and T. You, *Sens. Actuators B Chem.*, 2018, **255**, 1762-1770.

149. M. Yang, W. Kong, H. Li, J. Liu, H. Huang, Y. Liu and Z. Kang, *Microchim. Acta*, 2015, **182**, 2443-2450.
150. S. Sun, K. Jiang, S. Qian, Y. Wang and H. Lin, *Anal. Chem.*, 2017, **89**, 5542-5548.
151. X. Miao, X. Yan, D. Qu, D. Li, F. F. Tao and Z. Sun, *ACS Appl. Mater. Interfaces*, 2017, **9**, 18549-18556.
152. W. Gao, H. Song, X. Wang, X. Liu, X. Pang, Y. Zhou, B. Gao and X. Peng, *ACS Appl. Mater. Interfaces*, 2018, **10**, 1147-1154.
153. C. Liu, D. Ning, C. Zhang, Z. Liu, R. Zhang, J. Zhao, T. Zhao, B. Liu and Z. Zhang, *ACS Appl. Mater. Interfaces*, 2017, **9**, 18897-18903.
154. L. Cao, X. Wang, M. J. Mezziani, F. Lu, H. Wang, P. G. Luo, Y. Lin, B. A. Harruff, L. M. Veca, D. Murray, S. Y. Xie and Y. P. Sun, *J. Am. Chem. Soc.*, 2007, **129**, 11318-11319.
155. S. T. Yang, J. H. Liu, P. Wang, S. N. Yang, L. Ge, S. J. Yan and Y. P. P. Sun, *Chemistryselect*, 2018, **3**, 6374-6381.
156. S. Kim, Y. Choi, G. Park, C. Won, Y. J. Park, Y. Lee, B. S. Kim and D. H. Min, *Nano Res.*, 2017, **10**, 503-519.
157. S. Y. Lim, W. Shen and Z. Gao, *Chem. Soc. Rev.*, 2015, **44**, 362-381.
158. J. Zhang and S. H. Yu, *Mater. Today*, 2016, **19**, 382-393.
159. B. S. B. Kasibabu, S. L. D'souza, S. Jha, R. K. Singhal, H. Basu and S. K. Kailasa, *Anal. Methods*, 2015, **7**, 2373-2378.
160. Z. Y. Wang, H. Liao, H. Wu, B. B. Wang, H. D. Zhao and M. Q. Tan, *Anal. Methods*, 2015, **7**, 8911-8917.
161. W. Li, Y. Zheng, H. Zhang, Z. Liu, W. Su, S. Chen, Y. Liu, J. Zhuang and B. Lei, *ACS Appl. Mater. Interfaces*, 2016, **8**, 19939-19945.
162. P. Das, M. Bose, S. Ganguly, S. Mondal, A. K. Das, S. Banerjee and N. C. Das, *Nanotechnology*, 2017, **28**, 195501.
163. X. Zhai, P. Zhang, C. Liu, T. Bai, W. Li, L. Dai and W. Liu, *Chem. Commun.*, 2012, **48**, 7955-7957.
164. A. M. Chizhik, S. Stein, M. O. Dekaliuk, C. Battle, W. Li, A. Huss, M. Platen, I. A. Schaap, I. Gregor, A. P. Demchenko, C. F. Schmidt, J. Enderlein and A. I. Chizhik, *Nano Lett.*, 2016, **16**, 237-242.
165. B. Kong, A. Zhu, C. Ding, X. Zhao, B. Li and Y. Tian, *Adv. Mater.*, 2012, **24**, 5844-5848.

166. Y. Cheng, C. Li, R. Mu, Y. Li, T. Xing, B. Chen and C. Huang, *Anal. Chem.*, 2018, **90**, 11358-11365.
167. Y. C. Song, W. Shi, W. Chen, X. H. Li and H. M. Ma, *J. Mater. Chem.*, 2012, **22**, 12568-12573.
168. C. H. Lee, R. Rajendran, M. S. Jeong, H. Y. Ko, J. Y. Joo, S. Cho, Y. W. Chang and S. Kim, *Chem. Commun.*, 2013, **49**, 6543-6545.
169. S. Ruan, J. Qian, S. Shen, J. Chen, J. Zhu, X. Jiang, Q. He, W. Yang and H. Gao, *Bioconjug. Chem.*, 2014, **25**, 2252-2259.
170. X. W. Zhao, J. L. Zhang, L. H. Shi, M. Xian, C. Dong and S. M. Shuang, *RSC Adv.*, 2017, **7**, 42159-42167.
171. N. Puvvada, B. N. Kumar, S. Konar, H. Kalita, M. Mandal and A. Pathak, *Sci. Technol. Adv. Mater.*, 2012, **13**, 045008.
172. W. J. Lu, X. J. Gong, Z. H. Yang, Y. X. Zhang, Q. Hu, S. M. Shuang, C. Dong and M. M. F. Choi, *RSC Adv.*, 2015, **5**, 16972-16979.
173. T. Pal, S. Mohiyuddin and G. Packirisamy, *ACS Omega*, 2018, **3**, 831-843.
174. Y. Cui and J. Irudayaraj, *Wiley Interdiscip. Rev. Nanomed. Nanobiotechnol.*, 2015, **7**, 387-407.
175. G. Lemenager, E. De Luca, Y. P. Sun and P. P. Pompa, *Nanoscale*, 2014, **6**, 8617-8623.
176. S. K. Das, Y. Liu, S. Yeom, D. Y. Kim and C. I. Richards, *Nano Lett.*, 2014, **14**, 620-625.
177. S. Khan, N. C. Verma, A. Gupta and C. K. Nandi, *Sci. Rep.*, 2015, **5**, 11423.
178. N. C. Verma, S. Khan and C. K. Nandi, *Methods Appl. Fluoresc.*, 2016, **4**, 044006.
179. H. Wang, Q. Ma, Y. Wang, C. Wang, D. Qin, D. Shan, J. Chen and X. Lu, *Anal. Chim. Acta*, 2017, **973**, 34-42.
180. S. T. Yang, L. Cao, P. G. Luo, F. Lu, X. Wang, H. Wang, M. J. Mezziani, Y. Liu, G. Qi and Y. P. Sun, *J. Am. Chem. Soc.*, 2009, **131**, 11308-11309.
181. H. Tao, K. Yang, Z. Ma, J. Wan, Y. Zhang, Z. Kang and Z. Liu, *Small*, 2012, **8**, 281-290.
182. X. Huang, F. Zhang, L. Zhu, K. Y. Choi, N. Guo, J. Guo, K. Tackett, P. Anilkumar, G. Liu, Q. Quan, H. S. Choi, G. Niu, Y. P. Sun, S. Lee and X. Chen, *ACS Nano*, 2013, **7**, 5684-5693.
183. H. Y. Ko, Y. W. Chang, G. Paramasivam, M. S. Jeong, S. Cho and S. Kim, *Chem. Commun.*, 2013, **49**, 10290-10292.

184. T. Feng, X. Ai, G. An, P. Yang and Y. Zhao, *ACS Nano*, 2016, **10**, 4410-4420.
185. J. Tang, B. Kong, H. Wu, M. Xu, Y. Wang, Y. Wang, D. Zhao and G. Zheng, *Adv. Mater.*, 2013, **25**, 6569-6574.
186. P. Huang, J. Lin, X. Wang, Z. Wang, C. Zhang, M. He, K. Wang, F. Chen, Z. Li, G. Shen, D. Cui and X. Chen, *Adv. Mater.*, 2012, **24**, 5104-5110.
187. A. Kleinauskas, S. Rocha, S. Sahu, Y. P. Sun and P. Juzenas, *Nanotechnology*, 2013, **24**, 325103.
188. S. Khan, N. C. Verma, Chethana and C. K. Nandi, *ACS Appl. Nano Mater.*, 2018, **1**, 483-487.

## Chapter Two

1. Xu, X.; Ray, R.; Gu, Y.; Ploehn, H. J.; Gearheart, L.; Raker, K.; Scrivens, W. A., Electrophoretic Analysis and Purification of Fluorescent Single-Walled Carbon Nanotube Fragments. *Journal of the American Chemical Society* **2004**, 126, 12736-12737.
2. Georgakilas, V.; Perman, J. A.; Tucek, J.; Zboril, R., Broad Family of Carbon Nanoallotropes: Classification, Chemistry, and Applications of Fullerenes, Carbon Dots, Nanotubes, Graphene, Nanodiamonds, and Combined Superstructures. *Chem. Rev.* **2015**, 115, 4744-822.
3. Hong, G.; Diao, S.; Antaris, A. L.; Dai, H., Carbon Nanomaterials for Biological Imaging and Nanomedicinal Therapy. *Chemical Reviews* **2015**, 115, 10816-10906.
4. Lim, S. Y.; Shen, W.; Gao, Z., Carbon Quantum Dots and Their Applications. *Chem. Soc. Rev.* **2015**, 44, 362-81.
5. Hsiao, W. W.; Hui, Y. Y.; Tsai, P. C.; Chang, H. C., Fluorescent Nanodiamond: A Versatile Tool for Long-Term Cell Tracking, Super-Resolution Imaging, and Nanoscale Temperature Sensing. *Acc. Chem. Res.* **2016**, 49, 400-7.
6. Zhu, S.; Meng, Q.; Wang, L.; Zhang, J.; Song, Y.; Jin, H.; Zhang, K.; Sun, H.; Wang, H.; Yang, B., Highly Photoluminescent Carbon Dots for Multicolor Patterning, Sensors, and Bioimaging. *Angew. Chem., Int. Ed.* **2013**, 52, 3953-7.
7. Luo, Z.; Qi, G.; Chen, K.; Zou, M.; Yuwen, L.; Zhang, X.; Huang, W.; Wang, L., Microwave-Assisted Preparation of White Fluorescent Graphene Quantum Dots as a Novel Phosphor for Enhanced White-Light-Emitting Diodes. *Advanced Functional Materials* **2016**, 26, 2739-2744.
8. Zhai, X.; Zhang, P.; Liu, C.; Bai, T.; Li, W.; Dai, L.; Liu, W., Highly Luminescent Carbon Nanodots by Microwave-Assisted Pyrolysis. *Chem. Commun. (Camb)* **2012**, 48, 7955-7.

9. Li, Y.; Luo, C.; Jiang, C.; Huang, R.; Wang, Y.; Peng, H.; Travas-Sejdic, J., Luminescent Carbon Nanoparticles as a Donor for the FRET-Based Detection of Oligonucleotide Hybridization. *RSC Advances* **2014**, 4, 25201-25204.
10. Weng, C.-I.; Chang, H.-T.; Lin, C.-H.; Shen, Y.-W.; Unnikrishnan, B.; Li, Y.-J.; Huang, C.-C., One-Step Synthesis of Biofunctional Carbon Quantum Dots for Bacterial Labeling. *Biosensors and Bioelectronics* **2015**, 68, 1-6.
11. Chandra, S.; Laha, D.; Pramanik, A.; Ray Chowdhuri, A.; Karmakar, P.; Sahu, S. K., Synthesis of Highly Fluorescent Nitrogen and Phosphorus Doped Carbon Dots for the Detection of Fe<sup>3+</sup> Ions in Cancer Cells. *Luminescence* **2016**, 31, 81-87.
12. Gong, Y.; Yu, B.; Yang, W.; Zhang, X., Phosphorus, and Nitrogen Co-Doped Carbon Dots as a Fluorescent Probe for Real-Time Measurement of Reactive Oxygen and Nitrogen Species inside Macrophages. *Biosensors and Bioelectronics* **2016**, 79, 822-828.
13. Pang, S.; Zhang, Y.; Wu, C.; Feng, S., Fluorescent Carbon Dots Sensor for Highly Sensitive Detection of Guanine. *Sensors and Actuators B: Chemical* **2016**, 222, 857-863.
14. Shi, B.; Su, Y.; Zhang, L.; Huang, M.; Liu, R.; Zhao, S., Nitrogen and Phosphorus Co-Doped Carbon Nanodots as a Novel Fluorescent Probe for Highly Sensitive Detection of Fe<sup>3+</sup> in Human Serum and Living Cells. *ACS Applied Materials & Interfaces* **2016**, 8, 10717-10725.
15. Wang, W.; Li, Y.; Cheng, L.; Cao, Z.; Liu, W., Water-Soluble and Phosphorus-Containing Carbon Dots with Strong Green Fluorescence for Cell Labeling. *Journal of Materials Chemistry B* **2014**, 2, 46-48.
16. Feng, T.; Ai, X.; An, G.; Yang, P.; Zhao, Y., Charge-Convertible Carbon Dots for Imaging-Guided Drug Delivery with Enhanced in Vivo Cancer Therapeutic Efficiency. *ACS Nano* **2016**, 10, 4410-20.
17. Gong, X.; Zhang, Q.; Gao, Y.; Shuang, S.; Choi, M. M. F.; Dong, C., Phosphorus and Nitrogen Dual-Doped Hollow Carbon Dot as a Nanocarrier for Doxorubicin Delivery and Biological Imaging. *ACS Applied Materials & Interfaces* **2016**, 8, 11288-11297.
18. Zhang, F.; Wang, Y.; Miao, Y.; He, Y.; Yang, Y.; Liu, X., Optimal Nitrogen and Phosphorus Codoping Carbon Dots Towards White Light-Emitting Device. *Applied Physics Letters* **2016**, 109, 083103.
19. Li, H.; He, X.; Kang, Z.; Huang, H.; Liu, Y.; Liu, J.; Lian, S.; Tsang, C. H. A.; Yang, X.; Lee, S.-T., Water-Soluble Fluorescent Carbon Quantum Dots and Photocatalyst Design. *Angewandte Chemie International Edition* **2010**, 49, 4430-4434.
20. Ming, H.; Ma, Z.; Liu, Y.; Pan, K.; Yu, H.; Wang, F.; Kang, Z., Large Scale Electrochemical Synthesis of High Quality Carbon Nanodots and Their Photocatalytic Property. *Dalton Transactions* **2012**, 41, 9526-9531.

21. Yu, B. Y.; Kwak, S.-Y., Carbon Quantum Dots Embedded with Mesoporous Hematite Nanospheres as Efficient Visible Light-Active Photocatalysts. *Journal of Materials Chemistry* **2012**, *22*, 8345-8353.
22. Zhu, S. J.; Song, Y. B.; Zhao, X. H.; Shao, J. R.; Zhang, J. H.; Yang, B., The Photoluminescence Mechanism in Carbon Dots (Graphene Quantum Dots, Carbon Nanodots, and Polymer Dots): Current State and Future Perspective. *Nano Research* **2015**, *8*, 355-381.
23. Sun, Y.-P.; Zhou, B.; Lin, Y.; Wang, W.; Fernando, K. A. S.; Pathak, P.; Meziani, M. J.; Harruff, B. A.; Wang, X.; Wang, H.; Luo, P. G.; Yang, H.; Kose, M. E.; Chen, B.; Veca, L. M.; Xie, S.-Y., Quantum-Sized Carbon Dots for Bright and Colorful Photoluminescence. *Journal of the American Chemical Society* **2006**, *128*, 7756-7757.
24. Bao, L.; Zhang, Z.-L.; Tian, Z.-Q.; Zhang, L.; Liu, C.; Lin, Y.; Qi, B.; Pang, D.-W., Electrochemical Tuning of Luminescent Carbon Nanodots: From Preparation to Luminescence Mechanism. *Advanced Materials* **2011**, *23*, 5801-5806.
25. Peng, J.; Gao, W.; Gupta, B. K.; Liu, Z.; Romero-Aburto, R.; Ge, L.; Song, L.; Alemany, L. B.; Zhan, X.; Gao, G.; Vithayathil, S. A.; Kaiparettu, B. A.; Marti, A. A.; Hayashi, T.; Zhu, J.-J.; Ajayan, P. M., Graphene Quantum Dots Derived from Carbon Fibers. *Nano Letters* **2012**, *12*, 844-849.
26. Shinde, D. B.; Pillai, V. K., Electrochemical Preparation of Luminescent Graphene Quantum Dots from Multiwalled Carbon Nanotubes. *Chemistry – A European Journal* **2012**, *18*, 12522-12528.
27. Zhao, A.; Chen, Z.; Zhao, C.; Gao, N.; Ren, J.; Qu, X., Recent Advances in Bioapplications of C-Dots. *Carbon* **2015**, *85*, 309-327.
28. Wang, Y. F.; Hu, A. G., Carbon Quantum Dots: Synthesis, Properties and Applications. *J. Mater. Chem. C* **2014**, *2*, 6921-6939.
29. Li, X.; Lau, S. P.; Tang, L.; Ji, R.; Yang, P., Sulphur Doping: A Facile Approach to Tune the Electronic Structure and Optical Properties of Graphene Quantum Dots. *Nanoscale* **2014**, *6*, 5323-5328.
30. Sarkar, S.; Das, K.; Ghosh, M.; Das, P. K., Amino Acid Functionalized Blue and Phosphorous-Doped Green Fluorescent Carbon Dots as Bioimaging Probe. *RSC Advances* **2015**, *5*, 65913-65921.
31. Wang, H.-X.; Yang, Z.; Liu, Z.-G.; Wan, J.-Y.; Xiao, J.; Zhang, H.-L., Facile Preparation of Bright-Fluorescent Soft Materials from Small Organic Molecules. *Chemistry – A European Journal* **2016**, n/a-n/a.
32. Schwenke, A. M.; Hoeppeener, S.; Schubert, U. S., Synthesis and Modification of Carbon Nanomaterials Utilizing Microwave Heating. *Adv. Mater.* **2015**, *27*, 4113-41.

33. Gawande, M. B.; Shelke, S. N.; Zboril, R.; Varma, R. S., Microwave-Assisted Chemistry: Synthetic Applications for Rapid Assembly of Nanomaterials and Organics. *Accounts of Chemical Research* **2014**, 47, 1338-1348.
34. Kappe, C. O.; Dallinger, D.; Murphree, S. S., Experimental Protocols. In *Practical Microwave Synthesis for Organic Chemists*, Wiley-VCH Verlag GmbH & Co. KGaA: 2009; pp 203-290.
35. Tang, L.; Ji, R.; Cao, X.; Lin, J.; Jiang, H.; Li, X.; Teng, K. S.; Luk, C. M.; Zeng, S.; Hao, J.; Lau, S. P., Deep Ultraviolet Photoluminescence of Water-Soluble Self-Passivated Graphene Quantum Dots. *ACS Nano* **2012**, 6, 5102-5110.
36. Wang, Q.; Zheng, H.; Long, Y.; Zhang, L.; Gao, M.; Bai, W., Microwave-Hydrothermal Synthesis of Fluorescent Carbon Dots from Graphite Oxide. *Carbon* **2011**, 49, 3134-3140.
37. Zhang, P.; Li, W.; Zhai, X.; Liu, C.; Dai, L.; Liu, W., A Facile and Versatile Approach to Biocompatible "Fluorescent Polymers" from Polymerizable Carbon Nanodots. *Chemical Communications* **2012**, 48, 10431-10433.
38. Song, Y.; Shi, W.; Chen, W.; Li, X.; Ma, H., Fluorescent Carbon Nanodots Conjugated with Folic Acid for Distinguishing Folate-Receptor-Positive Cancer Cells from Normal Cells. *Journal of Materials Chemistry* **2012**, 22, 12568-12573.
39. Chandra, S.; Das, P.; Bag, S.; Laha, D.; Pramanik, P., Synthesis, Functionalization and Bioimaging Applications of Highly Fluorescent Carbon Nanoparticles. *Nanoscale* **2011**, 3, 1533-1540.
40. Lin, Y.-C.; Lin, C.-Y.; Chiu, P.-W., Controllable Graphene N-Doping with Ammonia Plasma. *Applied physics letters* **2010**, 96, 133110.
41. Ma, L.; Hu, H.; Zhu, L.; Wang, J., Boron and Nitrogen Doping Induced Half-Metallicity in Zigzag Triwing Graphene Nanoribbons. *The Journal of Physical Chemistry C* **2011**, 115, 6195-6199.
42. Liu, H.; Liu, Y.; Zhu, D., Chemical Doping of Graphene. *Journal of Materials Chemistry* **2011**, 21, 3335-3345.
43. Dong, X.; Su, Y.; Geng, H.; Li, Z.; Yang, C.; Li, X.; Zhang, Y., Fast One-Step Synthesis of N-Doped Carbon Dots by Pyrolyzing Ethanolamine. *Journal of Materials Chemistry C* **2014**, 2, 7477-7481.
44. Lu, W.; Gong, X.; Nan, M.; Liu, Y.; Shuang, S.; Dong, C., Comparative Study for N and S Doped Carbon Dots: Synthesis, Characterization and Applications for Fe<sup>3+</sup> Probe and Cellular Imaging. *Analytica Chimica Acta* **2015**, 898, 116-127.
45. Arcudi, F.; Đorđević, L.; Prato, M., Synthesis, Separation, and Characterization of Small and Highly Fluorescent Nitrogen-Doped Carbon Nanodots. *Angewandte Chemie International Edition* **2016**, 55, 2107-2112.

46. Dong, Y.; Pang, H.; Yang, H. B.; Guo, C.; Shao, J.; Chi, Y.; Li, C. M.; Yu, T., Carbon-Based Dots Co-Doped with Nitrogen and Sulfur for High QY and Excitation-Independent Emission. *Angewandte Chemie International Edition* **2013**, *52*, 7800-7804.
47. Shan, X.; Chai, L.; Ma, J.; Qian, Z.; Chen, J.; Feng, H., B-Doped Carbon Quantum Dots as a Sensitive Fluorescence Probe for Hydrogen Peroxide and Glucose Detection. *Analyst* **2014**, *139*, 2322-2325.
48. Jahan, S.; Mansoor, F.; Naz, S.; Lei, J.; Kanwal, S., Oxidative Synthesis of Highly Fluorescent Boron/Nitrogen Co-Doped Carbon Nanodots Enabling Detection of Photosensitizer and Carcinogenic Dye. *Analytical Chemistry* **2013**, *85*, 10232-10239.
49. Barman, M. K.; Jana, B.; Bhattacharyya, S.; Patra, A., Photophysical Properties of Doped Carbon Dots (N, P, and B) and Their Influence on Electron/Hole Transfer in Carbon Dots–Nickel (II) Phthalocyanine Conjugates. *The Journal of Physical Chemistry C* **2014**, *118*, 20034-20041.
50. Li, H.; Shao, F.-Q.; Zou, S.-Y.; Yang, Q.-J.; Huang, H.; Feng, J.-J.; Wang, A.-J., Microwave-Assisted Synthesis of N,P-Doped Carbon Dots for Fluorescent Cell Imaging. *Microchimica Acta* **2016**, *183*, 821-826.
51. Sun, X.; Bruckner, C.; Lei, Y., One-Pot and Ultrafast Synthesis of Nitrogen and Phosphorus Co-Doped Carbon Dots Possessing Bright Dual Wavelength Fluorescence Emission. *Nanoscale* **2015**, *7*, 17278-17282.
52. Wu, W.; Zhan, L.; Fan, W.; Song, J.; Li, X.; Li, Z.; Wang, R.; Zhang, J.; Zheng, J.; Wu, M.; Zeng, H., Cu–N Dopants Boost Electron Transfer and Photooxidation Reactions of Carbon Dots. *Angewandte Chemie International Edition* **2015**, *54*, 6540-6544.
53. Li, F.; Liu, C.; Yang, J.; Wang, Z.; Liu, W.; Tian, F., Mg/N Double Doping Strategy to Fabricate Extremely High Luminescent Carbon Dots for Bioimaging. *RSC Advances* **2014**, *4*, 3201-3205.
54. Ren, X. Y.; Yuan, X. X.; Wang, Y. P.; Liu, C. L.; Qin, Y.; Guo, L. P.; Liu, L. H., Facile Preparation of Gd<sup>3+</sup> Doped Carbon Quantum Dots: Photoluminescence Materials with Magnetic Resonance Response as Magnetic Resonance/Fluorescence Bimodal Probes. *Optical Materials* **2016**, *57*, 56-62.
55. Sun, D.; Ban, R.; Zhang, P.-H.; Wu, G.-H.; Zhang, J.-R.; Zhu, J.-J., Hair Fiber as a Precursor for Synthesizing of Sulfur- and Nitrogen-Co-Doped Carbon Dots with Tunable Luminescence Properties. *Carbon* **2013**, *64*, 424-434.
56. Zhang, L.; Xia, Z., Mechanisms of Oxygen Reduction Reaction on Nitrogen-Doped Graphene for Fuel Cells. *The Journal of Physical Chemistry C* **2011**, *115*, 11170-11176.

57. Wang, H.; Sun, P.; Cong, S.; Wu, J.; Gao, L.; Wang, Y.; Dai, X.; Yi, Q.; Zou, G., Nitrogen-Doped Carbon Dots for "Green" Quantum Dot Solar Cells. *Nanoscale Research Letters* **2016**, 11, 27-27.
58. Guo, Y.; Wang, Z.; Shao, H.; Jiang, X., Hydrothermal Synthesis of Highly Fluorescent Carbon Nanoparticles from Sodium Citrate and Their Use for the Detection of Mercury Ions. *Carbon* **2013**, 52, 583-589.
59. Baker, S. N.; Baker, G. A., Luminescent Carbon Nanodots: Emergent Nanolights. *Angewandte Chemie International Edition* **2010**, 49, 6726-6744.
60. Xiao, A.; Wang, C.; Chen, J.; Guo, R.; Yan, Z.; Chen, J., Carbon and Metal Quantum Dots Toxicity on the Microalgae *Chlorella Pyrenoidosa*. *Ecotoxicology and Environmental Safety* **2016**, 133, 211-217.
61. Liu, W.; Yao, J.; Jin, J.; Ma, J.; Masakorala, K., Microbial Toxicity of a Type of Carbon Dots to *Escherichia Coli*. *Archives of Environmental Contamination and Toxicology* **2015**, 69, 506-514.
62. Raven, P. H.; Mason, K. A.; Johnson, G. B.; Losos, J. B.; Singer, S. R., *Biology*. New York, NY: McGraw-Hill: 2011.
63. Shi, L.; Rosso, K. M.; Clarke, T. A.; Richardson, D. J.; Zachara, J. M.; Fredrickson, J. K., Molecular Underpinnings of Fe(III) Oxide Reduction by *Shewanella Oneidensis* Mr-1. *Front. Microbiol.* **2012**, 3, 50.
64. Janda, J. M.; Abbott, S. L., The Genus *Shewanella*: From the Briny Depths Below to Human Pathogen. *Critical Reviews in Microbiology* **2014**, 40, 293-312.
65. Gunsolus, I. L.; Mousavi, M. P.; Hussein, K.; Bühlmann, P.; Haynes, C. L., Effects of Humic and Fulvic Acids on Silver Nanoparticle Stability, Dissolution, and Toxicity. *Environmental Science & Technology* **2015**, 49, 8078-8086.
66. Feng, Z. V.; Gunsolus, I. L.; Qiu, T. A.; Hurley, K. R.; Nyberg, L. H.; Frew, H.; Johnson, K. P.; Vartanian, A. M.; Jacob, L. M.; Lohse, S. E.; Torelli, M. D.; Hamers, R. J.; Murphy, C. J.; Haynes, C. L., Impacts of Gold Nanoparticle Charge and Ligand Type on Surface Binding and Toxicity to Gram-Negative and Gram-Positive Bacteria. *Chem. Sci.* **2015**, 6, 5186-5196.
67. Hang, M. N.; Gunsolus, I. L.; Wayland, H.; Melby, E. S.; Mensch, A. C.; Hurley, K. R.; Pedersen, J. A.; Haynes, C. L.; Hamers, R. J., Impact of Nanoscale Lithium Nickel Manganese Cobalt Oxide (Nmc) on the Bacterium *Shewanella Oneidensis* Mr-1. *Chem. Mater.* **2016**, 28, 1092-1100.
68. Sahu, S.; Behera, B.; Maiti, T. K.; Mohapatra, S., Simple One-Step Synthesis of Highly Luminescent Carbon Dots from Orange Juice: Application as Excellent Bio-Imaging Agents. *Chemical Communications* **2012**, 48, 8835-8837.

69. Lakowicz, J. R., *Principles of Fluorescence Spectroscopy*. Springer Science & Business Media: 2013.
70. Qiu, T. A.; Torelli, M. D.; Vartanian, A. M.; Rackstraw, N. B.; Buchman, J. T.; Jacob, L. M.; Murphy, C. J.; Hamers, R. J.; Haynes, C. L., Quantification of Free Polyelectrolytes Present in Colloidal Suspension, Revealing a Source of Toxic Responses for Polyelectrolyte-Wrapped Gold Nanoparticles. *Analytical Chemistry* **2017**, 89, 1823-1830.
71. Sk, M. P.; Jaiswal, A.; Paul, A.; Ghosh, S. S.; Chattopadhyay, A., Presence of Amorphous Carbon Nanoparticles in Food Caramels. *Scientific Reports* **2012**, 2, 383.
72. Himaja, A. L.; Karthik, P. S.; Singh, S. P., Carbon Dots: The Newest Member of the Carbon Nanomaterials Family. *The Chemical Record* **2015**, 15, 595-615.
73. Merkus, H. G., *Particle Size Measurements: Fundamentals, Practice, Quality*. Springer Science & Business Media: 2009; Vol. 17.
74. Pavia, D.; Lampman, G.; Kriz, G.; Vyvyan, J., *Introduction to Spectroscopy*. Cengage Learning: 2008.
75. Jiang, K.; Sun, S.; Zhang, L.; Lu, Y.; Wu, A.; Cai, C.; Lin, H., Red, Green, and Blue Luminescence by Carbon Dots: Full-Color Emission Tuning and Multicolor Cellular Imaging. *Angewandte Chemie International Edition* **2015**, 54, 5360-5363.
76. Li, W.; Zhang, Z.; Kong, B.; Feng, S.; Wang, J.; Wang, L.; Yang, J.; Zhang, F.; Wu, P.; Zhao, D., Simple and Green Synthesis of Nitrogen-Doped Photoluminescent Carbonaceous Nanospheres for Bioimaging. *Angewandte Chemie International Edition* **2013**, 52, 8151-8155.
77. Zhang, Y.; Liu, X.; Fan, Y.; Guo, X.; Zhou, L.; Lv, Y.; Lin, J., One-Step Microwave Synthesis of N-Doped Hydroxyl-Functionalized Carbon Dots with Ultra-High Fluorescence QYs. *Nanoscale* **2016**, 8, 15281-15287.
78. Pavia, D. L.; Lampman, G. M.; Kriz, G. S., *Introduction to Spectroscopy: A Guide for Students of Organic Chemistry*. Harcourt College Publishers: 2001.
79. Silverstein, R. M.; Webster, F. X.; Kiemle, D. J.; Bryce, D. L., *Spectrometric Identification of Organic Compounds*. John Wiley & Sons: 2014.
80. Dang, H.; Huang, L.-K.; Zhang, Y.; Wang, C.-F.; Chen, S., Large-Scale Ultrasonic Fabrication of White Fluorescent Carbon Dots. *Industrial & Engineering Chemistry Research* **2016**, 55, 5335-5341.
81. Zhang, Y.; Wang, Y.; Guan, Y.; Feng, L., Uncovering the Pka Dependent Fluorescence Quenching of Carbon Dots Induced by Chlorophenols. *Nanoscale* **2015**, 7, 6348-55.
82. Algarra, M.; Perez-Martin, M.; Cifuentes-Rueda, M.; Jimenez-Jimenez, J.; Esteves da Silva, J. C. G.; Badosz, T. J.; Rodriguez-Castellon, E.; Lopez Navarrete, J. T.;

Casado, J., Carbon Dots Obtained Using Hydrothermal Treatment of Formaldehyde. Cell Imaging in Vitro. *Nanoscale* **2014**, 6, 9071-9077.

83. Liu, J.; Ge, X.; Sun, L.; Wei, R.; Liu, J.; Shi, L., Light Modulation (Vis-Nir Region) Based on Lanthanide Complex-Functionalized Carbon Dots. *RSC Advances* **2016**, 6, 47427-47433.

84. Permatasari, F. A.; Aimon, A. H.; Iskandar, F.; Ogi, T.; Okuyama, K., Role of C–N Configurations in the Photoluminescence of Graphene Quantum Dots Synthesized by a Hydrothermal Route. *Sci. Rep.* **2016**, 6, 21042.

85. Hu, Q.; Paa, M. C.; Zhang, Y.; Gong, X.; Zhang, L.; Lu, D.; Liu, Y.; Liu, Q.; Yao, J.; Choi, M. M. F., Green Synthesis of Fluorescent Nitrogen/Sulfur-Doped Carbon Dots and Investigation of Their Properties by Hplc Coupled with Mass Spectrometry. *RSC Advances* **2014**, 4, 18065-18073.

86. Zhang, Y.; Wang, y.; Guan, Y.; Feng, L., Uncovering the P<sub>k</sub>a Dependent Fluorescence Quenching of Carbon Dots Induced by Chlorophenols. *Nanoscale* **2015**, 7, 6348-6355.

87. Permatasari, F. A.; Aimon, A. H.; Iskandar, F.; Ogi, T.; Okuyama, K., Role of C–N Configurations in the Photoluminescence of Graphene Quantum Dots Synthesized by a Hydrothermal Route. *Scientific Reports* **2016**, 6, 21042.

88. Lu, W.; Gong, X.; Nan, M.; Liu, Y.; Shuang, S.; Dong, C., Comparative Study for N and S Doped Carbon Dots: Synthesis, Characterization and Applications for Fe<sup>3+</sup> Probe and Cellular Imaging. *Analytica Chimica Acta* **2015**, 898, 116-127.

89. Artyushkova, K.; Kiefer, B.; Halevi, B.; Knop-Gericke, A.; Schlogl, R.; Atanassov, P., Density Functional Theory Calculations of Xps Binding Energy Shift for Nitrogen-Containing Graphene-Like Structures. *Chemical Communications* **2013**, 49, 2539-2541.

90. Pan, D.; Zhang, J.; Li, Z.; Wu, M., Hydrothermal Route for Cutting Graphene Sheets into Blue-Luminescent Graphene Quantum Dots. *Advanced Materials* **2010**, 22, 734-738.

91. Peng, H.; Trivas-Sejdic, J., Simple Aquous Solution Route to Luminescent Carbogenic Dots from Carbohydrates. *Chem. Mater.* **2009**, 21, 5563-5565.

92. Wang, W.; Damm, C.; Waiter, J.; Nacken, T. J.; Peukert, W., Photobleaching and Stabilization of Carbon Nanodots Produced by Solvothermal Synthesis. *Phys. Chem. Chem. Phys.* **2016**, 18, 466-475.

93. Zhang, X.; Wang, H.; Wang, H.; Zhang, Q.; Xie, J.; Tian, Y.; Wang, J.; Xie, Y., Single-Layered Graphitic-C<sub>3</sub>N<sub>4</sub> Quantum Dots Fo Two-Photon Fluorescence Imaging of Cellular Nucleus. *Adv. Mater.* **2014**, 26, 4438-4443.

94. Zhao, Q.-L.; Zhang, Z.-L.; Huang, B.-H.; Pens, J.; Zhang, M.; Pang, D.-W., Facile Preparation of Low Cytotoxicity Fluorescent Carbon NCs by Electrooxidation of Graphite. *Chem. Commun.* **2008**, 5116-5118.
95. Zhu, S.; Meng, Q.; Wang, L.; Zhang, J.; Song, Y.; Jin, H.; Zhang, K.; Sun, H.; Wang, H.; Yang, B., Highly Photoluminescent Carbon Dots for Multicolor Patterning, Sensors, and Bioimaging. *Angew. Chem.* **2013**, 125, 4045-4049.
96. Janda, J. M., The Prokaryotes: Volume 6: Proteobacteria: Gamma Subclass. **2006**.
97. Serres, M. H.; Riley, M., Genomic Analysis of Carbon Source Metabolism of *Shewanella Oneidensis* Mr-1: Predictions Versus Experiments. *Journal of bacteriology* **2006**, 188, 4601-4609.

### Chapter Three

1. Huang, B.; Bates, M.; Zhuang, X., Super-Resolution Fluorescence Microscopy. *Annu. Rev. Biochem.* **2009**, 78, 993-1016.
2. Sauer, M.; Heilemann, M., Single-Molecule Localization Microscopy in Eukaryotes. *Chem. Rev.* **2017**, 117, 7478-7509.
3. Gahlmann, A.; Moerner, W. E., Exploring Bacterial Cell Biology with Single-Molecule Tracking and Super-Resolution Imaging. *Nat. Rev. Microbiol.* **2014**, 12, 9-22.
4. Cui, Y.; Irudayaraj, J., Inside Single Cells: Quantitative Analysis with Advanced Optics and Nanomaterials. *Wiley Interdiscip. Rev. Nanomed. Nanobiotechnol.* **2015**, 7, 387-407.
5. Abbe, E., Ueber Einen Neuen Beleuchtungsapparat Am Mikroskop. *Archiv für Mikroskopische Anatomie* **1873**, 9, 469-480.
6. Huang, B.; Babcock, H.; Zhuang, X., Breaking the Diffraction Barrier: Super-Resolution Imaging of Cells. *Cell* **2010**, 143, 1047-58.
7. Rust, M. J.; Bates, M.; Zhuang, X., Sub-Diffraction-Limit Imaging by Stochastic Optical Reconstruction Microscopy (Storm). *Nat. Methods* **2006**, 3, 793-5.
8. Betzig, E.; Patterson, G. H.; Sougrat, R.; Lindwasser, O. W.; Olenych, S.; Bonifacino, J. S.; Davidson, M. W.; Lippincott-Schwartz, J.; Hess, H. F., Imaging Intracellular Fluorescent Proteins at Nanometer Resolution. *Science* **2006**, 313, 1642-1645.
9. Dempsey, G. T.; Vaughan, J. C.; Chen, K. H.; Bates, M.; Zhuang, X., Evaluation of Fluorophores for Optimal Performance in Localization-Based Super-Resolution Imaging. *Nat. Methods* **2011**, 8, 1027-36.

10. Vogelsang, J.; Cordes, T.; Forthmann, C.; Steinhauer, C.; Tinnefeld, P., Controlling the Fluorescence of Ordinary Oxazine Dyes for Single-Molecule Switching and Superresolution Microscopy. *Proc. Natl. Acad. Sci. U. S. A.* **2009**, 106, 8107-12.
11. Heilemann, M.; van de Linde, S.; Mukherjee, A.; Sauer, M., Super - Resolution Imaging with Small Organic Fluorophores. *Angew. Chem., Int. Ed.* **2009**, 48, 6903-6908.
12. Georgakilas, V.; Perman, J. A.; Tucek, J.; Zboril, R., Broad Family of Carbon Nanoallotropes: Classification, Chemistry, and Applications of Fullerenes, Carbon Dots, Nanotubes, Graphene, Nanodiamonds, and Combined Superstructures. *Chem. Rev.* **2015**, 115, 4744-822.
13. Lim, S. Y.; Shen, W.; Gao, Z., Carbon Quantum Dots and Their Applications. *Chem. Soc. Rev.* **2015**, 44, 362-81.
14. Liu, W. J.; Li, C.; Ren, Y. J.; Sun, X. B.; Pan, W.; Li, Y. H.; Wang, J. P.; Wang, W. J., Carbon Dots: Surface Engineering and Applications. *J. Mater. Chem. B* **2016**, 4, 5772-5788.
15. Zhu, S.; Song, Y.; Shao, J.; Zhao, X.; Yang, B., Non-Conjugated Polymer Dots with Crosslink-Enhanced Emission in the Absence of Fluorophore Units. *Angew. Chem., Int. Ed.* **2015**, 54, 14626-37.
16. Peng, Z. L.; Han, X.; Li, S. H.; Al-Youbi, A. O.; Bashammakh, A. S.; El-Shahawi, M. S.; Leblanc, R. M., Carbon Dots: Biomacromolecule Interaction, Bioimaging and Nanomedicine. *Coordin. Chem. Rev.* **2017**, 343, 256-277.
17. Hsiao, W. W.; Hui, Y. Y.; Tsai, P. C.; Chang, H. C., Fluorescent Nanodiamond: A Versatile Tool for Long-Term Cell Tracking, Super-Resolution Imaging, and Nanoscale Temperature Sensing. *Acc. Chem. Res.* **2016**, 49, 400-7.
18. Wang, Y. F.; Hu, A. G., Carbon Quantum Dots: Synthesis, Properties and Applications. *J. Mater. Chem. C* **2014**, 2, 6921-6939.
19. Shamsipur, M.; Barati, A.; Karami, S., Long-Wavelength, Multicolor, and White-Light Emitting Carbon-Based Dots: Achievements Made, Challenges Remaining, and Applications. *Carbon* **2017**, 124, 429-472.
20. Wang, Y.; Kalytchuk, S.; Wang, L.; Zhovtiuk, O.; Cepe, K.; Zboril, R.; Rogach, A. L., Carbon Dot Hybrids with Oligomeric Silsesquioxane: Solid-State Luminophores with High Photoluminescence QY and Applicability in White Light Emitting Devices. *Chem. Commun. (Camb)* **2015**, 51, 2950-3.
21. Kalytchuk, S.; Polakova, K.; Wang, Y.; Froning, J. P.; Cepe, K.; Rogach, A. L.; Zboril, R., Carbon Dot Nanothermometry: Intracellular Photoluminescence Lifetime Thermal Sensing. *ACS Nano* **2017**, 11, 1432-1442.
22. Zhi, B.; Gallagher, M. J.; Frank, B. P.; Lyons, T. Y.; Qiu, T. A.; Da, J.; Mensch, A. C.; Hamers, R. J.; Rosenzweig, Z.; Fairbrother, D. H.; Haynes, C. L., Investigation of

Phosphorous Doping Effects on Polymeric Carbon Dots: Fluorescence, Photostability, and Environmental Impact. *Carbon* **2018**, 129, 438-449.

23. Alivisatos, A. P., Semiconductor Clusters, NCs, and Quantum Dots. *Science* **1996**, 271, 933-937.

24. Zhang, Z.; Guan, Y.; Wang, S.; Ogden, W. A.; Zhi, B.; Haynes, C. L.; Douglas, C. J., Unconventional Synthesis of Dibenzo[G,S]Rubicene Via Tandem Sonogashira Cross-Coupling and Tetra-Dehydro-Diels–Alder Cycloaddition Cascade. **2019**.

25. Ding, C.; Zhu, A.; Tian, Y., Functional Surface Engineering of C-Dots for Fluorescent Biosensing and in Vivo Bioimaging. *Acc. Chem. Res.* **2014**, 47, 20-30.

26. Feng, T.; Ai, X.; An, G.; Yang, P.; Zhao, Y., Charge-Convertible Carbon Dots for Imaging-Guided Drug Delivery with Enhanced in Vivo Cancer Therapeutic Efficiency. *ACS Nano* **2016**, 10, 4410-20.

27. Hu, S.; Tian, R.; Dong, Y.; Yang, J.; Liu, J.; Chang, Q., Modulation and Effects of Surface Groups on Photoluminescence and Photocatalytic Activity of Carbon Dots. *Nanoscale* **2013**, 5, 11665-71.

28. Zhu, S.; Meng, Q.; Wang, L.; Zhang, J.; Song, Y.; Jin, H.; Zhang, K.; Sun, H.; Wang, H.; Yang, B., Highly Photoluminescent Carbon Dots for Multicolor Patterning, Sensors, and Bioimaging. *Angew. Chem., Int. Ed.* **2013**, 52, 3953-7.

29. Choi, H.; Ko, S. J.; Choi, Y.; Joo, P.; Kim, T.; Lee, B. R.; Jung, J. W.; Choi, H. J.; Cha, M.; Jeong, J. R.; Hwang, I. W.; Song, M. H.; Kim, B. S.; Kim, J. Y., Versatile Surface Plasmon Resonance of Carbon-Dot-Supported Silver Nanoparticles in Polymer Optoelectronic Devices. *Nat. Photonics* **2013**, 7, 732-738.

30. Chizhik, A. M.; Stein, S.; Dekaliuk, M. O.; Battle, C.; Li, W.; Huss, A.; Platen, M.; Schaap, I. A.; Gregor, I.; Demchenko, A. P.; Schmidt, C. F.; Enderlein, J.; Chizhik, A. I., Super-Resolution Optical Fluctuation Bio-Imaging with Dual-Color Carbon Nanodots. *Nano Lett.* **2016**, 16, 237-42.

31. He, H.; Liu, X.; Li, S.; Wang, X.; Wang, Q.; Li, J.; Wang, J.; Ren, H.; Ge, B.; Wang, S.; Zhang, X.; Huang, F., High-Density Super-Resolution Localization Imaging with Blinking Carbon Dots. *Anal. Chem.* **2017**, 89, 11831-11838.

32. Khan, S.; Verma, N. C.; Gupta, A.; Nandi, C. K., Reversible Photoswitching of Carbon Dots. *Sci. Rep.* **2015**, 5, 11423.

33. Sun, Y. P.; Zhou, B.; Lin, Y.; Wang, W.; Fernando, K. A.; Pathak, P.; Mezziani, M. J.; Harruff, B. A.; Wang, X.; Wang, H.; Luo, P. G.; Yang, H.; Kose, M. E.; Chen, B.; Veca, L. M.; Xie, S. Y., Quantum-Sized Carbon Dots for Bright and Colorful Photoluminescence. *J. Am. Chem. Soc.* **2006**, 128, 7756-7.

34. Hutton, G. A. M.; Martindale, B. C. M.; Reisner, E., Carbon Dots as Photosensitisers for Solar-Driven Catalysis. *Chem. Soc. Rev.* **2017**, 46, 6111-6123.

35. Martindale, B. C. M.; Hutton, G. A. M.; Caputo, C. A.; Prantl, S.; Godin, R.; Durrant, J. R.; Reisner, E., Enhancing Light Absorption and Charge Transfer Efficiency in Carbon Dots through Graphitization and Core Nitrogen Doping. *Angew. Chem., Int. Ed.* **2017**, *56*, 6459-6463.
36. Cayuela, A.; Soriano, M. L.; Carrillo-Carrion, C.; Valcarcel, M., Semiconductor and Carbon-Based Fluorescent Nanodots: The Need for Consistency. *Chem. Commun. (Camb)* **2016**, *52*, 1311-26.
37. Wu, Z. L.; Liu, Z. X.; Yuan, Y. H., Carbon Dots: Materials, Synthesis, Properties and Approaches to Long-Wavelength and Multicolor Emission. *J. Mater. Chem. B* **2017**, *5*, 3794-3809.
38. Qiao, Z. A.; Wang, Y.; Gao, Y.; Li, H.; Dai, T.; Liu, Y.; Huo, Q., Commercially Activated Carbon as the Source for Producing Multicolor Photoluminescent Carbon Dots by Chemical Oxidation. *Chem. Commun. (Camb)* **2010**, *46*, 8812-4.
39. Ming, H.; Ma, Z.; Liu, Y.; Pan, K.; Yu, H.; Wang, F.; Kang, Z., Large Scale Electrochemical Synthesis of High Quality Carbon Nanodots and Their Photocatalytic Property. *Dalton Trans.* **2012**, *41*, 9526-31.
40. Yeh, T. F.; Syu, J. M.; Cheng, C.; Chang, T. H.; Teng, H. S., Graphite Oxide as a Photocatalyst for Hydrogen Production from Water. *Adv. Funct. Mater.* **2010**, *20*, 2255-2262.
41. Wang, Q.; Zheng, H.; Long, Y.; Zhang, L.; Gao, M.; Bai, W., Microwave-Hydrothermal Synthesis of Fluorescent Carbon Dots from Graphite Oxide. *Carbon* **2011**, *49*, 3134-3140.
42. Liu, H.; Ye, T.; Mao, C., Fluorescent Carbon Nanoparticles Derived from Candle Soot. *Angew. Chem., Int. Ed.* **2007**, *46*, 6473-5.
43. Tian, L.; Ghosh, D.; Chen, W.; Pradhan, S.; Chang, X. J.; Chen, S. W., Nanosized Carbon Particles from Natural Gas Soot. *Chem. Mater.* **2009**, *21*, 2803-2809.
44. Zhai, X.; Zhang, P.; Liu, C.; Bai, T.; Li, W.; Dai, L.; Liu, W., Highly Luminescent Carbon Nanodots by Microwave-Assisted Pyrolysis. *Chem. Commun. (Camb)* **2012**, *48*, 7955-7.
45. Moon, B. J.; Oh, Y.; Shin, D. H.; Kim, S. J.; Lee, S. H.; Kim, T. W.; Park, M.; Bae, S., Facile and Purification-Free Synthesis of Nitrogenated Amphiphilic Graphitic Carbon Dots. *Chem. Mater.* **2016**, *28*, 1481-1488.
46. Chowdhury, D.; Gogoi, N.; Majumdar, G., Fluorescent Carbon Dots Obtained from Chitosan Gel. *RSC Adv.* **2012**, *2*, 12156-12159.
47. Jia, X.; Li, J.; Wang, E., One-Pot Green Synthesis of Optically Ph-Sensitive Carbon Dots with Upconversion Luminescence. *Nanoscale* **2012**, *4*, 5572-5.

48. Lai, C. W.; Hsiao, Y. H.; Peng, Y. K.; Chou, P. T., Facile Synthesis of Highly Emissive Carbon Dots from Pyrolysis of Glycerol; Gram Scale Production of Carbon Dots/MSIO(2) for Cell Imaging and Drug Release. *J. Mater. Chem. C* **2012**, 22, 14403-14409.
49. Pan, D.; Zhang, J.; Li, Z.; Wu, C.; Yan, X.; Wu, M., Observation of Ph-, Solvent-, Spin-, and Excitation-Dependent Blue Photoluminescence from Carbon Nanoparticles. *Chem. Commun. (Camb)* **2010**, 46, 3681-3.
50. Wu, X.; Tian, F.; Wang, W.; Chen, J.; Wu, M.; Zhao, J. X., Fabrication of Highly Fluorescent Graphene Quantum Dots Using L-Glutamic Acid for in Vitro/in Vivo Imaging and Sensing. *J. Mater. Chem. C Mater.* **2013**, 1, 4676-4684.
51. Wu, Y.; Liu, X.; Wu, Q.; Yi, J.; Zhang, G., Carbon Nanodots-Based Fluorescent Turn-on Sensor Array for Biothiols. *Anal. Chem.* **2017**, 89, 7084-7089.
52. Ding, H.; Yu, S. B.; Wei, J. S.; Xiong, H. M., Full-Color Light-Emitting Carbon Dots with a Surface-State-Controlled Luminescence Mechanism. *ACS Nano* **2016**, 10, 484-91.
53. Wang, F.; Xie, Z.; Zhang, B.; Liu, Y.; Yang, W.; Liu, C. Y., Down- and up-Conversion Luminescent Carbon Dot Fluid: Inkjet Printing and Gel Glass Fabrication. *Nanoscale* **2014**, 6, 3818-23.
54. Bourlinos, A. B.; Stassinopoulos, A.; Anglos, D.; Zboril, R.; Karakassides, M.; Giannelis, E. P., Surface Functionalized Carbogenic Quantum Dots. *Small* **2008**, 4, 455-8.
55. Schwenke, A. M.; Hoepfner, S.; Schubert, U. S., Synthesis and Modification of Carbon Nanomaterials Utilizing Microwave Heating. *Adv. Mater.* **2015**, 27, 4113-41.
56. Horikoshi, S.; Serpone, N., *Microwaves in Nanoparticle Synthesis: Fundamentals and Applications*. John Wiley & Sons: 2013.
57. Panduric, N.; Salic, A.; Zelic, B., Fully Integrated Biotransformation of Fumaric Acid by Permeabilized Baker's Yeast Cells with in Situ Separation of L-Malic Acid Using Ultrafiltration, Acidification and Electrodialysis. *Biochem. Eng. J.* **2017**, 125, 221-229.
58. Pham, S. N.; Kuether, J. E.; Gallagher, M. J.; Hernandez, R. T.; Williams, D. N.; Zhi, B.; Mensch, A. C.; Hamers, R. J.; Rosenzweig, Z.; Fairbrother, H.; Krause, M. O. P.; Feng, Z. V.; Haynes, C. L., Carbon Dots: A Modular Activity to Teach Fluorescence and Nanotechnology at Multiple Levels. *Journal of Chemical Education* **2017**, 94, 1143-1149.
59. Gong, X.; Paau, M. C.; Hu, Q.; Shuang, S.; Dong, C.; Choi, M. M., UHPLC Combined with Mass Spectrometric Study of as-Synthesized Carbon Dots Samples. *Talanta* **2016**, 146, 340-50.

60. Vinci, J. C.; Ferrer, I. M.; Seedhouse, S. J.; Bourdon, A. K.; Reynard, J. M.; Foster, B. A.; Bright, F. V.; Colon, L. A., Hidden Properties of Carbon Dots Revealed after Hplc Fractionation. *J. Phys. Chem. Lett.* **2013**, *4*, 239-43.
61. Hola, K.; Sudolska, M.; Kalytchuk, S.; Nachtigallova, D.; Rogach, A. L.; Otyepka, M.; Zboril, R., Graphitic Nitrogen Triggers Red Fluorescence in Carbon Dots. *ACS Nano* **2017**, *11*, 12402-12410.
62. Nie, H.; Li, M. J.; Li, Q. S.; Liang, S. J.; Tan, Y. Y.; Sheng, L.; Shi, W.; Zhang, S. X. A., Carbon Dots with Continuously Tunable Full-Color Emission and Their Application in Ratiometric Ph Sensing. *Chem. Mater.* **2014**, *26*, 3104-3112.
63. Vinci, J. C.; Colon, L. A., Fractionation of Carbon-Based Nanomaterials by Anion-Exchange Hplc. *Anal. Chem.* **2012**, *84*, 1178-83.
64. Gong, X.; Hu, Q.; Paau, M. C.; Zhang, Y.; Shuang, S.; Dong, C.; Choi, M. M., Red-Green-Blue Fluorescent Hollow Carbon Nanoparticles Isolated from Chromatographic Fractions for Cellular Imaging. *Nanoscale* **2014**, *6*, 8162-70.
65. So, R. C.; Sanggo, J. E.; Jin, L.; Diaz, J. M. A.; Guerrero, R. A.; He, J., Gram-Scale Synthesis and Kinetic Study of Bright Carbon Dots from Citric Acid and Citrus Japonica Via a Microwave-Assisted Method. *ACS Omega* **2017**, *2*, 5196-5208.
66. Mitchell, H. D.; Markillie, L. M.; Chrisler, W. B.; Gaffrey, M. J.; Hu, D.; Szymanski, C. J.; Xie, Y.; Melby, E. S.; Dohnalkova, A.; Taylor, R. C.; Grate, E. K.; Cooley, S. K.; McDermott, J. E.; Heredia-Langner, A.; Orr, G., Cells Respond to Distinct Nanoparticle Properties with Multiple Strategies as Revealed by Single-Cell Rna-Seq. *ACS Nano* **2016**, *10*, 10173-10185.
67. Klein, T.; Proppert, S.; Sauer, M., Eight Years of Single-Molecule Localization Microscopy. *Histochem. Cell Biol.* **2014**, *141*, 561-75.
68. Thompson, R. E.; Larson, D. R.; Webb, W. W., Precise Nanometer Localization Analysis for Individual Fluorescent Probes. *Biophys. J.* **2002**, *82*, 2775-83.
69. Shen, J.; Zhang, J. H.; Xiao, H.; Wu, J. M.; He, K. M.; Lv, Z. Z.; Li, Z. J.; Xu, M.; Zhang, Y. Y., Mitochondria Are Transported Along Microtubules in Membrane Nanotubes to Rescue Distressed Cardiomyocytes from Apoptosis. *Cell Death Dis.* **2018**, *9*, 81.
70. Saxton, W. M.; Hollenbeck, P. J., The Axonal Transport of Mitochondria. *J. Cell. Sci.* **2012**, *125*, 2095-104.
71. Bian, J.; Li, J.; Kalytchuk, S.; Wang, Y.; Li, Q.; Lau, T. C.; Niehaus, T. A.; Rogach, A. L.; Zhang, R. Q., Efficient Emission Facilitated by Multiple Energy Level Transitions in Uniform Graphitic Carbon Nitride Films Deposited by Thermal Vapor Condensation. *Chemphyschem* **2015**, *16*, 954-9.

72. Miao, X.; Qu, D.; Yang, D.; Nie, B.; Zhao, Y.; Fan, H.; Sun, Z., Synthesis of Carbon Dots with Multiple Color Emission by Controlled Graphitization and Surface Functionalization. *Adv. Mater.* **2018**, 30, 1704740.
73. Zhang, Y.; Wang, Y.; Guan, Y.; Feng, L., Uncovering the Pka Dependent Fluorescence Quenching of Carbon Dots Induced by Chlorophenols. *Nanoscale* **2015**, 7, 6348-55.
74. Permatasari, F. A.; Aimon, A. H.; Iskandar, F.; Ogi, T.; Okuyama, K., Role of C–N Configurations in the Photoluminescence of Graphene Quantum Dots Synthesized by a Hydrothermal Route. *Sci. Rep.* **2016**, 6, 21042.
75. Yuan, F.; Wang, Z.; Li, X.; Li, Y.; Tan, Z.; Fan, L.; Yang, S., Bright Multicolor Bandgap Fluorescent Carbon Quantum Dots for Electroluminescent Light-Emitting Diodes. *Adv. Mater.* **2017**, 29, 1604436.
76. Zhan, J.; Geng, B. J.; Wu, K.; Xu, G.; Wang, L.; Guo, R. Y.; Lei, B.; Zheng, F. F.; Pan, D. Y.; Wu, M. H., A Solvent-Engineered Molecule Fusion Strategy for Rational Synthesis of Carbon Quantum Dots with Multicolor Bandgap Fluorescence. *Carbon* **2018**, 130, 153-163.
77. Lakowicz, J. R., *Principles of Fluorescence Spectroscopy*. Springer Science & Business Media: 2013.
78. Valeur, B.; Berberan-Santos, M. N., *Molecular Fluorescence: Principles and Applications*. John Wiley & Sons: 2012.
79. Berezin, M. Y.; Achilefu, S., Fluorescence Lifetime Measurements and Biological Imaging. *Chem. Rev.* **2010**, 110, 2641-84.
80. Gan, Z.; Xu, H.; Hao, Y., Mechanism for Excitation-Dependent Photoluminescence from Graphene Quantum Dots and Other Graphene Oxide Derivates: Consensus, Debates and Challenges. *Nanoscale* **2016**, 8, 7794-807.
81. Hu, D.; Zhao, B.; Xie, Y.; Orr, G.; Li, A. D., Understanding Super-Resolution Nanoscopy and Its Biological Applications in Cell Imaging. *Phys. Chem. Chem. Phys.* **2013**, 15, 14856-61.
82. Cui, Y.; Hu, D.; Markillie, L. M.; Chrisler, W. B.; Gaffrey, M. J.; Ansong, C.; Sussel, L.; Orr, G., Fluctuation Localization Imaging-Based Fluorescence in Situ Hybridization (Flifish) for Accurate Detection and Counting of Rna Copies in Single Cells. *Nucleic Acids Res.* **2018**, 46, e7.

## Chapter Four

1. Ekimov, A. I.; Onushchenko, A. A., Quantum Size Effect in Three-Dimensional Microscopic Semiconductor Crystals. *JETP Lett.* **1981**, 34, 345-349.

2. Michalet, X.; Pinaud, F. F.; Bentolila, L. A.; Tsay, J. M.; Doose, S.; Li, J. J.; Sundaresan, G.; Wu, A. M.; Gambhir, S. S.; Weiss, S., Quantum Dots for Live Cells, in Vivo Imaging, and Diagnostics. *Science* **2005**, 307, 538-44.
3. Lim, X., The Nanolight Revolution Is Coming. *Nature* **2016**, 531.
4. Wu, X.; Liu, H.; Liu, J.; Haley, K. N.; Treadway, J. A.; Larson, J. P.; Ge, N.; Peale, F.; Bruchez, M. P., Immunofluorescent Labeling of Cancer Marker Her2 and Other Cellular Targets with Semiconductor Quantum Dots. *Nat. Biotechnol.* **2003**, 21, 41-6.
5. Zhang, F.; Zhong, H.; Chen, C.; Wu, X. G.; Hu, X.; Huang, H.; Han, J.; Zou, B.; Dong, Y., Brightly Luminescent and Color-Tunable Colloidal  $\text{Ch}_3\text{nh}_3\text{pbx}_3$  (X = Br, I, Cl) Quantum Dots: Potential Alternatives for Display Technology. *ACS Nano* **2015**, 9, 4533-42.
6. Bourzac, K., Quantum Dots Go on Display: Adoption by Tv Makers Could Expand the Market for Light-Emitting Nanocrystals. *Nature* **2013**, 493, 283-284.
7. Sanderson, K., Quantum Dots Go Large. *Nature* **2009**, 459, 760-1.
8. Kamat, P. V.; Scholes, G. D., Quantum Dots Continue to Shine Brightly. *J. Phys. Chem. Lett.* **2016**, 7, 584-5.
9. Choi, H. S.; Liu, W.; Misra, P.; Tanaka, E.; Zimmer, J. P.; Itty Ipe, B.; Bawendi, M. G.; Frangioni, J. V., Renal Clearance of Quantum Dots. *Nat. Biotechnol.* **2007**, 25, 1165-70.
10. Hardman, R., A Toxicologic Review of Quantum Dots: Toxicity Depends on Physicochemical and Environmental Factors. *Environ. Health Perspect* **2006**, 114, 165-72.
11. Chen, Y.; Li, S.; Huang, L.; Pan, D., Low-Cost and Gram-Scale Synthesis of Water-Soluble Cu-in-S/Zns Core/Shell Quantum Dots in an Electric Pressure Cooker. *Nanoscale* **2014**, 6, 1295-8.
12. Huang, Z.; Zhai, G. M.; Zhang, Z. M.; Zhang, C. W.; Xia, Y.; Lian, L. Y.; Fu, X. M.; Zhang, D. L.; Zhang, J. B., Low Cost and Large Scale Synthesis of Pbs Quantum Dots with Hybrid Surface Passivation. *CrystEngComm* **2017**, 19, 946-951.
13. Park, J. H.; Gu, L.; von Maltzahn, G.; Ruoslahti, E.; Bhatia, S. N.; Sailor, M. J., Biodegradable Luminescent Porous Silicon Nanoparticles for in Vivo Applications. *Nat. Mater.* **2009**, 8, 331-6.
14. Alsharif, N. H.; Berger, C. E.; Varanasi, S. S.; Chao, Y.; Horrocks, B. R.; Datta, H. K., Alkyl-Capped Silicon Nanocrystals Lack Cytotoxicity and Have Enhanced Intracellular Accumulation in Malignant Cells Via Cholesterol-Dependent Endocytosis. *Small* **2009**, 5, 221-8.
15. Allix, M.; Chenu, S.; Veron, E.; Poumeyrol, T.; Kouadri-Boudjelthia, E. A.; Alahrache, S.; Porcher, F.; Massiot, D.; Fayon, F., C Considerable Improvement of Long-

Persistent Luminescence in Germanium and Tin Substituted ZnGa<sub>2</sub>O<sub>4</sub>. *Chem. Mater.* **2013**, 25, 1600-1606.

16. Zhi, B.; Gallagher, M. J.; Frank, B. P.; Lyons, T. Y.; Qiu, T. A.; Da, J.; Mensch, A. C.; Hamers, R. J.; Rosenzweig, Z.; Fairbrother, D. H.; Haynes, C. L., Investigation of Phosphorous Doping Effects on Polymeric Carbon Dots: Fluorescence, Photostability, and Environmental Impact. *Carbon* **2018**, 129, 438-449.

17. Zhi, B.; Cui, Y.; Wang, S.; Frank, B. P.; Williams, D. N.; Brown, R. P.; Melby, E. S.; Hamers, R. J.; Rosenzweig, Z.; Fairbrother, D. H.; Orr, G.; Haynes, C. L., Malic Acid Carbon Dots: From Super-Resolution Live-Cell Imaging to Highly Efficient Separation. *ACS Nano* **2018**, 12, 5741-5752.

18. Pham, S. N.; Kuether, J. E.; Gallagher, M. J.; Hernandez, R. T.; Williams, D. N.; Zhi, B.; Mensch, A. C.; Hamers, R. J.; Rosenzweig, Z.; Fairbrother, H.; Krause, M. O. P.; Feng, Z. V.; Haynes, C. L., Carbon Dots: A Modular Activity to Teach Fluorescence and Nanotechnology at Multiple Levels. *Journal of Chemical Education* **2017**, 94, 1143-1149.

19. Cheng, X.; Lowe, S. B.; Reece, P. J.; Gooding, J. J., Colloidal Silicon Quantum Dots: From Preparation to the Modification of Self-Assembled Monolayers (Sams) for Bio-Applications. *Chem. Soc. Rev.* **2014**, 43, 2680-700.

20. Montalti, M.; Cantelli, A.; Battistelli, G., Nanodiamonds and Silicon Quantum Dots: Ultrastable and Biocompatible Luminescent Nanoprobes for Long-Term Bioimaging. *Chem. Soc. Rev.* **2015**, 44, 4853-921.

21. Hessel, C. M.; Rasch, M. R.; Hueso, J. L.; Goodfellow, B. W.; Akhavan, V. A.; Puvanakrishnan, P.; Tunnel, J. W.; Korgel, B. A., Alkyl Passivation and Amphiphilic Polymer Coating of Silicon Nanocrystals for Diagnostic Imaging. *Small* **2010**, 6, 2026-34.

22. Ahire, J. H.; Wang, Q.; Coxon, P. R.; Malhotra, G.; Brydson, R.; Chen, R.; Chao, Y., Highly Luminescent and Nontoxic Amine-Capped Nanoparticles from Porous Silicon: Synthesis and Their Use in Biomedical Imaging. *ACS Appl. Mater. Interfaces* **2012**, 4, 3285-92.

23. Jurbergs, D.; Rogojina, E.; Mangolini, L.; Kortshagen, U., Silicon Nanocrystals with Ensemble Quantum Yields Exceeding 60%. *Appl. Phys. Lett.* **2006**, 88, 233116.

24. Li, Q.; Luo, T. Y.; Zhou, M.; Abroshan, H.; Huang, J.; Kim, H. J.; Rosi, N. L.; Shao, Z.; Jin, R., Silicon Nanoparticles with Surface Nitrogen: 90% Quantum Yield with Narrow Luminescence Bandwidth and the Ligand Structure Based Energy Law. *ACS Nano* **2016**, 10, 8385-93.

25. Godefroo, S.; Hayne, M.; Jivanescu, M.; Stesmans, A.; Zacharias, M.; Lebedev, O. I.; Van Tendeloo, G.; Moshchalkov, V. V., Classification and Control of the Origin of Photoluminescence from Si Nanocrystals. *Nat. Nanotechnol.* **2008**, 3, 174.

26. Pavesi, L.; Turan, R., *Silicon Nanocrystals: Fundamentals, Synthesis and Applications*. John Wiley & Sons: 2010.

27. Li, Q.; He, Y.; Chang, J.; Wang, L.; Chen, H.; Tan, Y.-W.; Wang, H.; Shao, Z., Surface-Modified Silicon Nanoparticles with Ultrabright Photoluminescence and Single-Exponential Decay for Nanoscale Fluorescence Lifetime Imaging of Temperature. *J. Am. Chem. Soc.* **2013**, 135, 14924-14927.
28. Li, Q.; Luo, T.-Y.; Zhou, M.; Abroshan, H.; Huang, J.; Kim, H. J.; Rosi, N. L.; Shao, Z.; Jin, R., Silicon Nanoparticles with Surface Nitrogen: 90% Quantum Yield with Narrow Luminescence Bandwidth and the Ligand Structure Based Energy Law. *ACS Nano* **2016**, 10, 8385–8393.
29. Hessel, C. M.; Henderson, E. J.; Veinot, J. G. C., Hydrogen Silsesquioxane: A Molecular Precursor for Nanocrystalline Si–SiO<sub>2</sub> Composites and Freestanding Hydride-Surface-Terminated Silicon Nanoparticles. *Chem. Mater.* **2006**, 18, 6139-6146.
30. Heinrich, J. L.; Curtis, C. L.; Credo, G. M.; Sailor, M. J.; Kavanagh, K. L., Luminescent Colloidal Silicon Suspensions from Porous Silicon. *Science* **1992**, 255, 66-8.
31. Okada, R.; Iijima, S., Oxidation Property of Silicon Small Particles. *Appl. Phys. Lett.* **1991**, 58, 1662-1663.
32. Heath, J. R., A Liquid-Solution-Phase Synthesis of Crystalline Silicon. *Science* **1992**, 258, 1131-3.
33. Mangolini, L.; Thimsen, E.; Kortshagen, U., High-Yield Plasma Synthesis of Luminescent Silicon Nanocrystals. *Nano Lett.* **2005**, 5, 655-9.
34. Kortshagen, U. R.; Sankaran, R. M.; Pereira, R. N.; Girshick, S. L.; Wu, J. J.; Aydil, E. S., Nonthermal Plasma Synthesis of Nanocrystals: Fundamental Principles, Materials, and Applications. *Chem. Rev.* **2016**, 116, 11061-127.
35. Kramer, N. J.; Schramke, K. S.; Kortshagen, U. R., Plasmonic Properties of Silicon Nanocrystals Doped with Boron and Phosphorus. *Nano Lett.* **2015**, 15, 5597-603.
36. Adjallah, Y.; Anderson, C.; Kortshagen, U.; Kakalios, J., Structural and Electronic Properties of Dual Plasma Codeposited Mixed-Phase Amorphous/Nanocrystalline Thin Films. *J. Appl. Phys.* **2010**, 107, 043704.
37. Zhou, X.; Uchida, K.; Mizuta, H.; Oda, S., Electron Transport in Surface Oxidized Si Nanocrystal Ensembles with Thin Film Transistor Structure. *J. Appl. Phys.* **2009**, 106, 044511.
38. Priolo, F.; Gregorkiewicz, T.; Galli, M.; Krauss, T. F., Silicon Nanostructures for Photonics and Photovoltaics. *Nat. Nanotechnol.* **2014**, 9, 19-32.
39. Anthony, R. J.; Cheng, K. Y.; Holman, Z. C.; Holmes, R. J.; Kortshagen, U. R., An All-Gas-Phase Approach for the Fabrication of Silicon Nanocrystal Light-Emitting Devices. *Nano Lett.* **2012**, 12, 2822-5.

40. Koshida, N., *Device Applications of Silicon Nanocrystals and Nanostructures*. Springer Science & Business Media: 2008.
41. Cabrera, N.; Mott, N. F., Theory of the Oxidation of Metals. *Rep. Prog. Phys.* **1949**, 12, 163.
42. Nosaka, Y.; Nosaka, A., Understanding Hydroxyl Radical ( $\bullet\text{OH}$ ) Generation Processes in Photocatalysis. *ACS Energy Lett.* **2016**, 1, 356-359.
43. George, S.; Pokhrel, S.; Ji, Z.; Henderson, B. L.; Xia, T.; Li, L.; Zink, J. I.; Nel, A. E.; Madler, L., Role of Fe Doping in Tuning the Band Gap of  $\text{TiO}_2$  for the Photo-Oxidation-Induced Cytotoxicity Paradigm. *J. Am. Chem. Soc.* **2011**, 133, 11270-8.
44. Zhang, H.; Pokhrel, S.; Ji, Z.; Meng, H.; Wang, X.; Lin, S.; Chang, C. H.; Li, L.; Li, R.; Sun, B.; Wang, M.; Liao, Y. P.; Liu, R.; Xia, T.; Madler, L.; Nel, A. E., Pdo Doping Tunes Band-Gap Energy Levels as Well as Oxidative Stress Responses to a  $\text{Co}_3\text{O}_4$  P-Type Semiconductor in Cells and the Lung. *J. Am. Chem. Soc.* **2014**, 136, 6406-20.
45. Sharma, P.; Jha, A. B.; Dubey, R. S.; Pessarakli, M., Reactive Oxygen Species, Oxidative Damage, and Antioxidative Defense Mechanism in Plants under Stressful Conditions. *J. Bot.* **2012**, Article 217037.
46. Choi, O.; Hu, Z., Size Dependent and Reactive Oxygen Species Related Nanosilver Toxicity to Nitrifying Bacteria. *Environ. Sci. Technol.* **2008**, 42, 4583-8.
47. Fredrickson, J. K.; Romine, M. F.; Beliaev, A. S.; Auchtung, J. M.; Driscoll, M. E.; Gardner, T. S.; Nealson, K. H.; Osterman, A. L.; Pinchuk, G.; Reed, J. L.; Rodionov, D. A.; Rodrigues, J. L.; Saffarini, D. A.; Serres, M. H.; Spormann, A. M.; Zhulin, I. B.; Tiedje, J. M., Towards Environmental Systems Biology of *Shewanella*. *Nat. Rev. Microbiol.* **2008**, 6, 592-603.
48. Raven, P. H.; Mason, K. A.; Johnson, G. B.; Losos, J. B.; Singer, S. R., *Biology*. New York, NY: McGraw-Hill: 2011.
49. Shi, L.; Rosso, K. M.; Clarke, T. A.; Richardson, D. J.; Zachara, J. M.; Fredrickson, J. K., Molecular Underpinnings of Fe(III) Oxide Reduction by *Shewanella Oneidensis* Mr-1. *Front. Microbiol.* **2012**, 3, 50.
50. Hang, M. N.; Gunsolus, I. L.; Wayland, H.; Melby, E. S.; Mensch, A. C.; Hurley, K. R.; Pedersen, J. A.; Haynes, C. L.; Hamers, R. J., Impact of Nanoscale Lithium Nickel Manganese Cobalt Oxide (Nmc) on the Bacterium *Shewanella Oneidensis* Mr-1. *Chem. Mater.* **2016**, 28, 1092-1100.
51. Feng, Z. V.; Gunsolus, I. L.; Qiu, T. A.; Hurley, K. R.; Nyberg, L. H.; Frew, H.; Johnson, K. P.; Vartanian, A. M.; Jacob, L. M.; Lohse, S. E.; Torelli, M. D.; Hamers, R. J.; Murphy, C. J.; Haynes, C. L., Impacts of Gold Nanoparticle Charge and Ligand Type on Surface Binding and Toxicity to Gram-Negative and Gram-Positive Bacteria. *Chem. Sci.* **2015**, 6, 5186-5196.

52. Gresback, R.; Kramer, N. J.; Ding, Y.; Chen, T.; Kortshagen, U. R.; Nozaki, T., Controlled Doping of Silicon Nanocrystals Investigated by Solution-Processed Field Effect Transistors. *ACS Nano* **2014**, *8*, 5650-6.
53. Rowe, D. J.; Jeong, J. S.; Mkhoyan, K. A.; Kortshagen, U. R., Phosphorus-Doped Silicon Nanocrystals Exhibiting Mid-Infrared Localized Surface Plasmon Resonance. *Nano Lett.* **2013**, *13*, 1317-22.
54. Holman, Z. C.; Kortshagen, U. R., A Flexible Method for Depositing Dense Nanocrystal Thin Films: Impaction of Germanium Nanocrystals. *Nanotechnology* **2010**, *21*, 335302.
55. Pi, X.; Gresback, R.; Liptak, R.; Campbell, S.; Kortshagen, U., Doping Efficiency, Dopant Location, and Oxidation of Si Nanocrystals. *Appl. Phys. Lett.* **2008**, *92*, 123102.
56. Pi, X. D.; Mangolini, L.; Campbell, S. A.; Kortshagen, U., Room-Temperature Atmospheric Oxidation of Si Nanocrystals after Hf Etching. *Phys. Rev. B* **2007**, *75*, 085423.
57. Stetefeld, J.; McKenna, S. A.; Patel, T. R., Dynamic Light Scattering: A Practical Guide and Applications in Biomedical Sciences. *Biophys. Rev.* **2016**, *8*, 409-427.
58. Zhang, H.; Zhang, R. M.; Schramke, K. S.; Bedford, N. M.; Hunter, K.; Kortshagen, U. R.; Nordlander, P., Doped Silicon Nanocrystal Plasmonics. *ACS Photonics* **2017**, *4*, 963-970.
59. Pi, X. D.; Liptak, R. W.; Nowak, J. D.; Wells, N. P.; Carter, C. B.; Campbell, S. A.; Kortshagen, U., Air-Stable Full-Visible-Spectrum Emission from Silicon Nanocrystals Synthesized by an All-Gas-Phase Plasma Approach. *Nanotechnology* **2008**, *19*, 245603.
60. Spear, W. E.; Lecomber, P. G., Substitutional Doping of Amorphous Silicon. *Solid State Commun.* **1975**, *17*, 1193-1196.
61. Levy, R. A., *Principles of Solid State Physics*. New York, NY : Academic Press: 1968.
62. Lebel, C. P.; Ischiropoulos, H.; Bondy, S. C., Evaluation of the Probe 2',7'-Dichlorofluorescein as an Indicator of Reactive Oxygen Species Formation and Oxidative Stress. *Chem. Res. Toxicol.* **1992**, *5*, 227-231.
63. Imlay, J. A., The Molecular Mechanisms and Physiological Consequences of Oxidative Stress: Lessons from a Model Bacterium. *Nat. Rev. Microbiol.* **2013**, *11*, 443-54.
64. Hazan, R.; Que, Y. A.; Maura, D.; Rahme, L. G., A Method for High Throughput Determination of Viable Bacteria Cell Counts in 96-Well Plates. *BMC Microbiol.* **2012**, *12*, 259.

65. Chen, C.-Y.; Nace, G. W.; Irwin, P. L., A 6×6 Drop Plate Method for Simultaneous Colony Counting and Mpn Enumeration of *Campylobacter* Jejuni, *Listeria* Monocytogenes, and *Escherichia Coli*. *J. Microbiol. Methods* **2003**, *55*, 475-479.
66. Pramanik, S.; Hill, S. K. E.; Zhi, B.; Hudson-Smith, N. V.; Wu, J. J.; White, J. N.; McIntire, E. A.; Kondeti, V. S. S. K.; Lee, A. L.; Bruggeman, P. J.; Kortshagen, U. R.; Haynes, C. L., Comparative Toxicity Assessment of Novel Si Quantum Dots and Their Traditional Cd-Based Counterparts Using Bacteria Models *Shewanella Oneidensis* and *Bacillus Subtilis*. *Environ. Sci.: Nano* **2018**.
67. Verebes, G. S.; Melchiorre, M.; Garcia-Leis, A.; Ferreri, C.; Marzetti, C.; Torreggiani, A., Hyperspectral Enhanced Dark Field Microscopy for Imaging Blood Cells. *J. Biophotonics* **2013**, *6*, 960-7.
68. Gao, L.; Smith, R. T., Optical Hyperspectral Imaging in Microscopy and Spectroscopy—a Review of Data Acquisition. *J. Biophotonics* **2015**, *8*, 441-456.
69. Zamora-Perez, P.; Tsoutsi, D.; Xu, R.; Rivera Gil, P., Hyperspectral-Enhanced Dark Field Microscopy for Single and Collective Nanoparticle Characterization in Biological Environments. *Materials (Basel)* **2018**, *11*, 243.
70. Pena Mdel, P.; Gottipati, A.; Tahiliani, S.; Neu-Baker, N. M.; Frame, M. D.; Friedman, A. J.; Brenner, S. A., Hyperspectral Imaging of Nanoparticles in Biological Samples: Simultaneous Visualization and Elemental Identification. *Microsc. Res. Tech.* **2016**, *79*, 349-58.
71. Pérez-Cruz, C.; Carrión, O.; Delgado, L.; Martinez, G.; López-Iglesias, C.; Mercade, E., New Type of Outer Membrane Vesicle Produced by the Gram-Negative Bacterium *Shewanella Vesiculosa* M7t: Implications for DNA Content. *Appl. Environ. Microbiol.* **2013**, *79*, 1874-1881.
72. Klein, N. D.; Hurley, K. R.; Feng, Z. V.; Haynes, C. L., Dark Field Transmission Electron Microscopy as a Tool for Identifying Inorganic Nanoparticles in Biological Matrices. *Anal. Chem.* **2015**, *87*, 4356-62.

## Chapter Five

1. Ekimov, A. I.; Onushchenko, A. A., Quantum Size Effect in Three-Dimensional Microscopic Semiconductor Crystals. *JETP Lett.* **1981**, *34*, 345-349.
2. Kamat, P. V.; Scholes, G. D., Quantum Dots Continue to Shine Brightly. *J. Phys. Chem. Lett.* **2016**, *7*, 584-585.
3. Xu, G.; Zeng, S.; Zhang, B.; Swihart, M. T.; Yong, K.-T.; Prasad, P. N., New Generation Cadmium-Free Quantum Dots for Biophotonics and Nanomedicine. *Chem. Rev.* **2016**, *116*, 12234-12327.

4. Reiss, P.; Protière, M.; Li, L., Core/Shell Semiconductor Nanocrystals. *Small* **2009**, 5, 154-168.
5. Koh, W.-k.; Dandu, N. K.; Fidler, A. F.; Klimov, V. I.; Pietryga, J. M.; Kilina, S. V., Thickness-Controlled Quasi-Two-Dimensional Colloidal Pbse Nanoplatelets. *J. Am. Chem. Soc.* **2017**, 139, 2152-2155.
6. Zhang, F.; Zhong, H.; Chen, C.; Wu, X. G.; Hu, X.; Huang, H.; Han, J.; Zou, B.; Dong, Y., Brightly Luminescent and Color-Tunable Colloidal  $\text{Ch}_3\text{nh}_3\text{pbx}_3$  (X = Br, I, Cl) Quantum Dots: Potential Alternatives for Display Technology. *ACS Nano* **2015**, 9, 4533-42.
7. Bourzac, K., Quantum Dots Go on Display: Adoption by Tv Makers Could Expand the Market for Light-Emitting Nanocrystals. *Nature* **2013**, 493, 283-284.
8. Semonin, O. E.; Luther, J. M.; Choi, S.; Chen, H.-Y.; Gao, J.; Nozik, A. J.; Beard, M. C., Peak External Photocurrent Quantum Efficiency Exceeding 100% Via Meg in a Quantum Dot Solar Cell. *Science* **2011**, 334, 1530-1533.
9. Galloway, J. F.; Winter, A.; Lee, K. H.; Park, J. H.; Dvoracek, C. M.; Devreotes, P.; Searson, P. C., Quantitative Characterization of the Lipid Encapsulation of Quantum Dots for Biomedical Applications. *Nanomedicine* **2012**, 8, 1190-1199.
10. Lee, S.; Lee, K.; Kim, W. D.; Lee, S.; Shin, D. J.; Lee, D. C., Thin Amorphous  $\text{Tio}_2$  Shell on Cdse Nanocrystal Quantum Dots Enhances Photocatalysis of Hydrogen Evolution from Water. *J. Phys. Chem. C* **2014**, 118, 23627-23634.
11. Pietryga, J. M.; Park, Y.-S.; Lim, J.; Fidler, A. F.; Bae, W. K.; Brovelli, S.; Klimov, V. I., Spectroscopic and Device Aspects of Nanocrystal Quantum Dots. *Chem. Rev.* **2016**, 116, 10513-10622.
12. Pramanik, S.; Hill, S. K. E.; Zhi, B.; Hudson-Smith, N. V.; Wu, J. J.; White, J. N.; McIntire, E. A.; Kondeti, V. S. S. K.; Lee, A. L.; Bruggeman, P. J.; Kortshagen, U. R.; Haynes, C. L., Comparative Toxicity Assessment of Novel Si Quantum Dots and Their Traditional Cd-Based Counterparts Using Bacteria Models *Shewanella Oneidensis* and *Bacillus Subtilis*. *Environ. Sci.: Nano* **2018**, 5, 1890-1901.
13. Gallagher, M. J.; Buchman, J. T.; Qiu, T. A.; Zhi, B.; Lyons, T. Y.; Landy, K. M.; Rosenzweig, Z.; Haynes, C. L.; Fairbrother, D. H., Release, Detection and Toxicity of Fragments Generated During Artificial Accelerated Weathering of Cdse/Zns and Cdse Quantum Dot Polymer Composites. *Environ. Sci.: Nano* **2018**, 5, 1694-1710.
14. Choi, H. S.; Liu, W.; Misra, P.; Tanaka, E.; Zimmer, J. P.; Itty Ipe, B.; Bawendi, M. G.; Frangioni, J. V., Renal Clearance of Quantum Dots. *Nat. Biotechnol.* **2007**, 25, 1165-70.
15. Williams, D. N.; Pramanik, S.; Brown, R. P.; Zhi, B.; McIntire, E.; Hudson-Smith, N. V.; Haynes, C. L.; Rosenzweig, Z., Adverse Interactions of Luminescent

Semiconductor Quantum Dots with Liposomes and *Shewanella Oneidensis*. *ACS Appl. Nano. Mater.* **2018**, 1, 4788-4800.

16. Zhi, B.; Cui, Y.; Wang, S.; Frank, B. P.; Williams, D. N.; Brown, R. P.; Melby, E. S.; Hamers, R. J.; Rosenzweig, Z.; Fairbrother, D. H.; Orr, G.; Haynes, C. L., Malic Acid Carbon Dots: From Super-Resolution Live-Cell Imaging to Highly Efficient Separation. *ACS Nano* **2018**, 12, 5741-5752.

17. Zhi, B.; Gallagher, M. J.; Frank, B. P.; Lyons, T. Y.; Qiu, T. A.; Da, J.; Mensch, A. C.; Hamers, R. J.; Rosenzweig, Z.; Fairbrother, D. H.; Haynes, C. L., Investigation of Phosphorous Doping Effects on Polymeric Carbon Dots: Fluorescence, Photostability, and Environmental Impact. *Carbon* **2018**, 129, 438-449.

18. Zhi, B.; Mishra, S.; Hudson-Smith, N. V.; Kortshagen, U. R.; Haynes, C. L., Toxicity Evaluation of Boron- and Phosphorus-Doped Silicon Nanocrystals toward *Shewanella Oneidensis* Mr-1. *ACS Appl. Nano. Mater.* **2018**, 1, 4884-4893.

19. Slawson, R. M.; Van Dyke, M. I.; Lee, H.; Trevors, J. T., Germanium and Silver Resistance, Accumulation, and Toxicity in Microorganisms. *Plasmid* **1992**, 27, 72-79.

20. Reiss, P.; Carrière, M.; Lincheneau, C.; Vaure, L.; Tamang, S., Synthesis of Semiconductor Nanocrystals, Focusing on Nontoxic and Earth-Abundant Materials. *Chem. Rev.* **2016**, 116, 10731-10819.

21. Wheeler, L. M.; Levij, L. M.; Kortshagen, U. R., Tunable Band Gap Emission and Surface Passivation of Germanium Nanocrystals Synthesized in the Gas Phase. *J. Phys. Chem. Lett.* **2013**, 4, 3392-3396.

22. Kortshagen, U. R.; Sankaran, R. M.; Pereira, R. N.; Girshick, S. L.; Wu, J. J.; Aydil, E. S., Nonthermal Plasma Synthesis of Nanocrystals: Fundamental Principles, Materials, and Applications. *Chem. Rev.* **2016**, 116, 11061-127.

23. Gao, Y.; Pi, X.; Wang, X.; Yuan, T.; Jiang, Q.; Gresback, R.; Lu, J.; Yang, D., Structures, Oxidation, and Charge Transport of Phosphorus-Doped Germanium Nanocrystals. *Part. Part. Syst. Charact.* **2016**, 33, 271-278.

24. Mangolini, L.; Thimsen, E.; Kortshagen, U., High-Yield Plasma Synthesis of Luminescent Silicon Nanocrystals. *Nano Lett.* **2005**, 5, 655-9.

25. Kim, D.; Kang, J.; Wang, T.; Ryu, H. G.; Zuidema, J. M.; Joo, J.; Kim, M.; Huh, Y.; Jung, J.; Ahn, K. H.; Kim, K. H.; Sailor, M. J., Two-Photon in Vivo Imaging with Porous Silicon Nanoparticles. *Adv. Mater.* **2017**, 29, 1703309.

26. Hu, J.; Lu, Q.; Wu, C.; Liu, M.; Li, H.; Zhang, Y.; Yao, S., Synthesis of Fluorescent and Water-Dispersed Germanium Nanoparticles and Their Cellular Imaging Applications. *Langmuir* **2018**, 34, 8932-8938.

27. Li, F.; Wang, J.; Sun, S. Q.; Wang, H.; Tang, Z. Y.; Nie, G. J., Facile Synthesis of Ph-Sensitive Germanium Nanocrystals with High Quantum Yield for Intracellular Acidic Compartment Imaging. *Small* **2015**, 11, 1954-1961.
28. McVey, B. F. P.; Prabakar, S.; Gooding, J. J.; Tilley, R. D., Solution Synthesis, Surface Passivation, Optical Properties, Biomedical Applications, and Cytotoxicity of Silicon and Germanium Nanocrystals. *ChemPlusChem* **2017**, 82, 60-73.
29. Serrano-Ruz, J. A.; Campos-González, E.; Santoyo-Salazar, J.; Arias-Cerón, J. S.; Chávez-Chávez, A.; Gómez-Rosas, G.; Pérez-Centeno, A.; Ceja, I.; Moure-Flores, F. d.; Meléndez-Lira, M.; Hernández-Hernández, A.; Santana-Aranda, M. A.; Quiñones-Galván, J. G., Synthesis of Colloidal Silicon and Germanium Nanoparticles by Laser Ablation of Solid Si and Ge Targets in Ethanol. *Mater. Res. Express* **2018**, 5, 015038.
30. Lehninger, D.; Beyer, J.; Heitmann, J., A Review on Ge Nanocrystals Embedded in SiO<sub>2</sub> and High-K Dielectrics. *Phys. Status Solidi A* **2018**, 215, 1701028.
31. Henderson, E. J.; Hessel, C. M.; Veinot, J. G. C., Synthesis and Photoluminescent Properties of Size-Controlled Germanium Nanocrystals from Phenyl Trichlorogermane-Derived Polymers. *J. Am. Chem. Soc.* **2008**, 130, 3624-3632.
32. Choi, H. C.; Buriak, J. M., Preparation and Functionalization of Hydride Terminated Porous Germanium. *Chem. Commun. (Camb.)* **2000**, 1669-1670.
33. Meghan, N. B.; Youcef, A. B.; David, G. H.; Abderraouf, B.; Christopher, E. V.; Dominique, D.; Richard, A.; Karin, H., Tunable Conductivity in Mesoporous Germanium. *Nanotechnology* **2018**, 29, 215701.
34. Qin, W.; Lu, W.-C.; Zhao, L.-Z.; Ho, K. M.; Wang, C. Z., Optical Absorption Properties of Ge<sub>2-44</sub> and P-Doped Ge Nanoparticles. *Comput. Mater. Sci.* **2017**, 140, 148-158.
35. Pradhan, N.; Das Adhikari, S.; Nag, A.; Sarma, D. D., Luminescence, Plasmonic, and Magnetic Properties of Doped Semiconductor Nanocrystals. *Angew. Chem. Int. Ed. Engl.* **2017**, 56, 7038-7054.
36. Beaulac, R.; Schneider, L.; Archer, P. I.; Bacher, G.; Gamelin, D. R., Light-Induced Spontaneous Magnetization in Doped Colloidal Quantum Dots. *Science* **2009**, 325, 973-976.
37. Meric, Z.; Mehringer, C.; Karpstein, N.; Jank, M. P. M.; Peukert, W.; Frey, L., Tunable Conduction Type of Solution-Processed Germanium Nanoparticle Based Field Effect Transistors and Their Inverter Integration. *Phys. Chem. Chem. Phys.* **2015**, 17, 22106-22114.
38. Selopal, G. S.; Zhao, H.; Liu, G.; Zhang, H.; Tong, X.; Wang, K.; Tang, J.; Sun, X.; Sun, S.; Vidal, F.; Wang, Y.; Wang, Z. M.; Rosei, F., Interfacial Engineering in Colloidal "Giant" Quantum Dots for High-Performance Photovoltaics. *Nano Energy* **2019**, 55, 377-388.

39. Schierning, G.; Theissmann, R.; Stein, N.; Petermann, N.; Becker, A.; Engenhorst, M.; Kessler, V.; Geller, M.; Beckel, A.; Wiggers, H.; Schmechel, R., Role of Oxygen on Microstructure and Thermoelectric Properties of Silicon Nanocomposites. *J. Appl. Phys.* **2011**, 110, 113515.
40. Weiwei, C.; Xiaosheng, T.; Zhigang, Z.; Yue, S.; Zhaoqi, Y.; Juan, D., Tunable Dual Emission in Mn<sup>2+</sup>-Doped CsPbX<sub>3</sub> (X = Cl, Br) Quantum Dots for High Efficiency White Light-Emitting Diodes. *Nanotechnology* **2019**, 30, 075704.
41. Cabrera, N.; Mott, N. F., Theory of the Oxidation of Metals. *Rep. Prog. Phys.* **1949**, 12, 163.
42. Nosaka, Y.; Nosaka, A., Understanding Hydroxyl Radical ( $\bullet$ OH) Generation Processes in Photocatalysis. *ACS Energy Lett.* **2016**, 1, 356-359.
43. Zhang, H.; Pokhrel, S.; Ji, Z.; Meng, H.; Wang, X.; Lin, S.; Chang, C. H.; Li, L.; Li, R.; Sun, B.; Wang, M.; Liao, Y. P.; Liu, R.; Xia, T.; Madler, L.; Nel, A. E., Pdo Doping Tunes Band-Gap Energy Levels as Well as Oxidative Stress Responses to a Co<sub>3</sub>O<sub>4</sub> P-Type Semiconductor in Cells and the Lung. *J. Am. Chem. Soc.* **2014**, 136, 6406-20.
44. George, S.; Pokhrel, S.; Ji, Z.; Henderson, B. L.; Xia, T.; Li, L.; Zink, J. I.; Nel, A. E.; Mädler, L., Role of Fe Doping in Tuning the Band Gap of TiO<sub>2</sub> for the Photo-Oxidation-Induced Cytotoxicity Paradigm. *J. Am. Chem. Soc.* **2011**, 133, 11270-11278.
45. Choi, O.; Hu, Z., Size Dependent and Reactive Oxygen Species Related Nanosilver Toxicity to Nitrifying Bacteria. *Environ. Sci. Technol.* **2008**, 42, 4583-8.
46. Heidelberg, J. F.; Paulsen, I. T.; Nelson, K. E.; Gaidos, E. J.; Nelson, W. C.; Read, T. D.; Eisen, J. A.; Seshadri, R.; Ward, N.; Methe, B.; Clayton, R. A.; Meyer, T.; Tsapin, A.; Scott, J.; Beanan, M.; Brinkac, L.; Daugherty, S.; DeBoy, R. T.; Dodson, R. J.; Durkin, A. S., *et al.*, Genome Sequence of the Dissimilatory Metal Ion-Reducing Bacterium *Shewanella Oneidensis*. *Nat. Biotechnol.* **2002**, 20, 1118.
47. Gresback, R.; Holman, Z.; Kortshagen, U., Nonthermal Plasma Synthesis of Size-Controlled, Monodisperse, Freestanding Germanium Nanocrystals. *Appl. Phys. Lett.* **2007**, 91, 093119.
48. Mohan, T. C.; Jones, A. M. E., Determination of Boron Content Using a Simple and Rapid Miniaturized Curcumin Assay. *Bio-protocol* **2018**, 8, e2703.
49. Murphy, J.; Riley, J. P., A Modified Single Solution Method for the Determination of Phosphate in Natural Waters. *Analytica Chimica Acta* **1962**, 27, 31-36.
50. Setsukinai, K.-i.; Urano, Y.; Kakinuma, K.; Majima, H. J.; Nagano, T., Development of Novel Fluorescence Probes That Can Reliably Detect Reactive Oxygen Species and Distinguish Specific Species. *Journal of Biological Chemistry* **2003**, 278, 3170-3175.

51. Zhao, H.; Kalivendi, S.; Zhang, H.; Joseph, J.; Nithipatikom, K.; Vásquez-Vivar, J.; Kalyanaraman, B., Superoxide Reacts with Hydroethidine but Forms a Fluorescent Product That Is Distinctly Different from Ethidium: Potential Implications in Intracellular Fluorescence Detection of Superoxide. *Free Radical Biology and Medicine* **2003**, 34, 1359-1368.
52. Straumanis, M.; Aka, E., Lattice Parameters, Coefficients of Thermal Expansion, and Atomic Weights of Purest Silicon and Germanium. *J. Appl. Phys.* **1952**, 23, 330-334.
53. Nakagawa, K.; Yoshida, Y.; Miyazaki, S.; Hirose, M., Insights into Surface Reactions During a-SiGe:H Deposition and Hydrogen Plasma Annealing as Obtained from Infrared Attenuated Total Reflection Spectroscopy. *J. Non-Cryst. Solids* **1998**, 227-230, 48-52.
54. Kramer, N. J.; Schramke, K. S.; Kortshagen, U. R., Plasmonic Properties of Silicon Nanocrystals Doped with Boron and Phosphorus. *Nano Lett.* **2015**, 15, 5597-603.
55. Wang, D.; Chang, Y.-L.; Wang, Q.; Cao, J.; Farmer, D. B.; Gordon, R. G.; Dai, H., Surface Chemistry and Electrical Properties of Germanium Nanowires. *J. Am. Chem. Soc.* **2004**, 126, 11602-11611.
56. Ortiz, M. I.; Rodríguez, A.; Sangrador, J.; Rodríguez, T.; Avella, M.; Jiménez, J.; Ballesteros, C., Luminescent Nanostructures Based on Ge Nanoparticles Embedded in an Oxide Matrix. *Nanotechnology* **2005**, 16, S197-S201.
57. Van der Heide, P., *X-Ray Photoelectron Spectroscopy: An Introduction to Principles and Practices*. John Wiley & Sons: 2011.
58. Tanuma, S.; Powell, C. J.; Penn, D. R., Calculations of Electron Inelastic Mean Free Paths. IX. Data for 41 Elemental Solids over the 50 eV to 30 KeV Range. *Surf. Interface Anal.* **2011**, 43, 689-713.
59. Heintzenberg, J., Properties of the Log-Normal Particle Size Distribution. *Aerosol Sci. Technol.* **1994**, 21, 46-48.
60. Stetefeld, J.; McKenna, S. A.; Patel, T. R., Dynamic Light Scattering: A Practical Guide and Applications in Biomedical Sciences. *Biophys. Rev.* **2016**, 8, 409-427.
61. Riddick, T. M., *Control of Colloid Stability through Zeta Potential*. Livingston Wynnewood, PA: 1968.
62. Bondarenko, O.; Ivask, A.; Käkinen, A.; Kurvet, I.; Kahru, A., Particle-Cell Contact Enhances Antibacterial Activity of Silver Nanoparticles. *PLoS ONE* **2013**, 8, e64060.
63. Tu, Y.; Lv, M.; Xiu, P.; Huynh, T.; Zhang, M.; Castelli, M.; Liu, Z.; Huang, Q.; Fan, C.; Fang, H.; Zhou, R., Destructive Extraction of Phospholipids from Escherichia Coli Membranes by Graphene Nanosheets. *Nat. Nanotechnol.* **2013**, 8, 594.

64. Lebel, C. P.; Ischiropoulos, H.; Bondy, S. C., Evaluation of the Probe 2',7'-Dichlorofluorescein as an Indicator of Reactive Oxygen Species Formation and Oxidative Stress. *Chem. Res. Toxicol.* **1992**, 5, 227-231.
65. Imlay, J. A., The Molecular Mechanisms and Physiological Consequences of Oxidative Stress: Lessons from a Model Bacterium. *Nat. Rev. Microbiol.* **2013**, 11, 443-54.
66. Verebes, G. S.; Melchiorre, M.; Garcia-Leis, A.; Ferreri, C.; Marzetti, C.; Torreggiani, A., Hyperspectral Enhanced Dark Field Microscopy for Imaging Blood Cells. *J. Biophotonics* **2013**, 6, 960-7.
67. Gao, L.; Smith, R. T., Optical Hyperspectral Imaging in Microscopy and Spectroscopy—a Review of Data Acquisition. *J. Biophotonics* **2015**, 8, 441-456.
68. Zamora-Perez, P.; Tsoutsi, D.; Xu, R.; Rivera Gil, P., Hyperspectral-Enhanced Dark Field Microscopy for Single and Collective Nanoparticle Characterization in Biological Environments. *Materials (Basel)* **2018**, 11, 243.
69. Zhang, H.; Zhang, R. M.; Schramke, K. S.; Bedford, N. M.; Hunter, K.; Kortshagen, U. R.; Nordlander, P., Doped Silicon Nanocrystal Plasmonics. *ACS Photonics* **2017**, 4, 963-970.
70. Kläui, W., Säure-Base-Konzepte: The Lewis Acid-Base Concepts. An Overview. Von W. B. Jensen. John Wiley & Sons, New York-Chichester-Brisbane-Toronto 1980. Xi, 364 S., Zahlr. Illustr., Geb., £ 20,60. *Nachr. Chem. Tech. Lab.* **1980**, 28, 751-751.

## Chapter Six

1. Xu, X.; Ray, R.; Gu, Y.; Ploehn, H. J.; Gearheart, L.; Raker, K.; Scrivens, W. A., Electrophoretic Analysis and Purification of Fluorescent Single-Walled Carbon Nanotube Fragments. *Journal of the American Chemical Society* **2004**, 126, 12736-12737.
2. Choi, Y.; Choi, Y.; Kwon, O.-H.; Kim, B.-S., Carbon Dots: Bottom-up Syntheses, Properties, and Light-Harvesting Applications. *Chemistry – An Asian Journal* **2018**, 13, 586-598.
3. Mishra, V.; Patil, A.; Thakur, S.; Kesharwani, P., Carbon Dots: Emerging Theranostic Nanoarchitectures. *Drug Discovery Today* **2018**, 23, 1219-1232.
4. Zhi, B.; Gallagher, M. J.; Frank, B. P.; Lyons, T. Y.; Qiu, T. A.; Da, J.; Mensch, A. C.; Hamers, R. J.; Rosenzweig, Z.; Fairbrother, D. H.; Haynes, C. L., Investigation of Phosphorous Doping Effects on Polymeric Carbon Dots: Fluorescence, Photostability, and Environmental Impact. *Carbon* **2018**, 129, 438-449.
5. Yao, B.; Huang, H.; Liu, Y.; Kang, Z., Carbon Dots: A Small Conundrum. *Trends in Chemistry* **2019**.

6. Pirsahab, M.; Mohammadi, S.; Salimi, A.; Payandeh, M., Functionalized Fluorescent Carbon Nanostructures for Targeted Imaging of Cancer Cells: a Review. *Microchimica Acta* **2019**, 186, 231.
7. Hu, C.; Qu, J.; Xiao, Y.; Zhao, S.; Chen, H.; Dai, L., Carbon Nanomaterials for Energy and Biorelated Catalysis: Recent Advances and Looking Forward. *ACS Cent Sci* **2019**, 5, 389-408.
8. Yuan, T.; Meng, T.; He, P.; Shi, Y.; Li, Y.; Li, X.; Fan, L.; Yang, S., Carbon Quantum Dots: An Emerging Material for Optoelectronic Applications. *Journal of Materials Chemistry C* **2019**.
9. Sharma, V.; Singh, S. K.; Mobin, Shaikh M., Bioinspired Carbon Dots: From Rose Petals to Tunable Emissive Nanodots. *Nanoscale Advances* **2019**, 1, 1290-1296.
10. Yuan, F.; Yuan, T.; Sui, L.; Wang, Z.; Xi, Z.; Li, Y.; Li, X.; Fan, L.; Tan, Z. a.; Chen, A.; Jin, M.; Yang, S., Engineering Triangular Carbon Quantum Dots with Unprecedented Narrow Bandwidth Emission for Multicolored Leds. *Nature Communications* **2018**, 9, 2249.
11. Xiao, L.; Sun, H., Novel Properties and Applications of Carbon Nanodots. *Nanoscale Horizons* **2018**, 3, 565-597.
12. Shamsipur, M.; Barati, A.; Taherpour, A. A.; Jamshidi, M., Resolving the Multiple Emission Centers in Carbon Dots: From Fluorophore Molecular States to Aromatic Domain States and Carbon-Core States. *The Journal of Physical Chemistry Letters* **2018**, 9, 4189-4198.
13. Shen, D.; Long, Y.; Wang, J.; Yu, Y.; Pi, J.; Yang, L.; Zheng, H., Tuning the Fluorescence Performance of Carbon Dots with a Reduction Pathway. *Nanoscale* **2019**, 11, 5998-6003.
14. Fanglong, Y.; Zhibin, W.; Xiaohong, L.; Yunchao, L.; Zhan'ao, T.; Louzhen, F.; Shihe, Y., Bright Multicolor Bandgap Fluorescent Carbon Quantum Dots for Electroluminescent Light-Emitting Diodes. *Advanced Materials* **2017**, 29, 1604436.
15. Miao, X.; Qu, D.; Yang, D.; Nie, B.; Zhao, Y.; Fan, H.; Sun, Z., Synthesis of Carbon Dots with Multiple Color Emission by Controlled Graphitization and Surface Functionalization. *Adv. Mater.* **2018**, 30, 1704740.
16. Hola, K.; Sudolska, M.; Kalytchuk, S.; Nachtigallova, D.; Rogach, A. L.; Otyepka, M.; Zboril, R., Graphitic Nitrogen Triggers Red Fluorescence in Carbon Dots. *ACS Nano* **2017**, 11, 12402-12410.
17. Ding, H.; Yu, S. B.; Wei, J. S.; Xiong, H. M., Full-Color Light-Emitting Carbon Dots with a Surface-State-Controlled Luminescence Mechanism. *ACS Nano* **2016**, 10, 484-91.

18. Zhi, B.; Cui, Y.; Wang, S.; Frank, B. P.; Williams, D. N.; Brown, R. P.; Melby, E. S.; Hamers, R. J.; Rosenzweig, Z.; Fairbrother, D. H.; Orr, G.; Haynes, C. L., Malic Acid Carbon Dots: From Super-Resolution Live-Cell Imaging to Highly Efficient Separation. *ACS Nano* **2018**, 12, 5741-5752.
19. Hu, S.; Tian, R.; Dong, Y.; Yang, J.; Liu, J.; Chang, Q., Modulation and Effects of Surface Groups on Photoluminescence and Photocatalytic Activity of Carbon Dots. *Nanoscale* **2013**, 5, 11665-11671.
20. Reckmeier, C.; Schneider, J.; Susha, A.; Rogach, A., Luminescent Colloidal Carbon Dots: Optical Properties and Effects of Doping. *Optics express* **2016**, 24, A312-A340.
21. Jiang, K.; Sun, S.; Zhang, L.; Lu, Y.; Wu, A.; Cai, C.; Lin, H., Red, Green, and Blue Luminescence by Carbon Dots: Full-Color Emission Tuning and Multicolor Cellular Imaging. *Angewandte Chemie International Edition* **2015**, 54, 5360-5363.
22. Bhunia, S. K.; Saha, A.; Maity, A. R.; Ray, S. C.; Jana, N. R., Carbon Nanoparticle-Based Fluorescent Bioimaging Probes. *Scientific reports* **2013**, 3, 1473.
23. Bhattacharya, D.; Mishra, M. K.; De, G., Carbon Dots from a Single Source Exhibiting Tunable Luminescent Colors through the Modification of Surface Functional Groups in Ormosil Films. *The Journal of Physical Chemistry C* **2017**, 121, 28106-28116.
24. Liu, W.; Li, C.; Ren, Y.; Sun, X.; Pan, W.; Li, Y.; Wang, J.; Wang, W., Carbon Dots: Surface Engineering and Applications. *Journal of Materials Chemistry B* **2016**, 4, 5772-5788.
25. Luo, X.; Zhang, W.; Han, Y.; Chen, X.; Zhu, L.; Tang, W.; Wang, J.; Yue, T.; Li, Z., N,S Co-Doped Carbon Dots Based Fluorescent “on-Off-on” Sensor for Determination of Ascorbic Acid in Common Fruits. *Food Chemistry* **2018**, 258, 214-221.
26. Zhi, B.; Cui, Y.; Wang, S.; Frank, B. P.; Williams, D. N.; Brown, R. P.; Melby, E. S.; Hamers, R. J.; Rosenzweig, Z.; Fairbrother, D. H.; Orr, G.; Haynes, C. L., Malic Acid Carbon Dots: From Super-Resolution Live-Cell Imaging to Highly Efficient Separation. *ACS Nano* **2018**.
27. Xu, H.; Ren, D., Lysosomal Physiology. *Annu Rev Physiol* **2015**, 77, 57-80.

## Appendix I: Curriculum Vitae

# Bo Zhi (鄧博)

425 13<sup>th</sup> Ave SE, Minneapolis, MN, 55414 | [zhixx018@umn.edu](mailto:zhixx018@umn.edu) | 612-356-0606

---

### Education

**Ph.D.**, Chemistry, University of Minnesota, Minneapolis, MN Aug. 2019

Thesis: “Group IV elements based luminescent nanoparticles: synthesis, environmental impact evaluation and bio-imaging applications”; Advisor: Dr. Christy L. Haynes

**Master of Science**, Chemistry, University of Minnesota, Minneapolis, MN Jan. 2016

**Master/Bachelor of Science**, Chemistry, Jilin University, China Jun. 2014/Jun. 2011

### Summary of Skills

**Characterization:** transmission electron microscopy (TEM), energy dispersive X-ray spectroscopy (EDS), X-ray photoelectron spectroscopy (XPS), fluorescence spectroscopy, dark-field hyperspectral microscopy, X-ray diffractometer (XRD), dynamic light scattering (DLS), Fourier transform infrared spectroscopy (FTIR), scanning electron microscopy (SEM), atomic force microscopy (AFM), Raman imaging, UV-vis spectrometer, colony counting assay, reactive oxygen species assay, fluorescamine assay

**Synthesis:** microwave synthesizer, muffle oven, high pressure autoclave, CombiFlash chromatography, rotary evaporator, microplate reader, centrifugal evaporator, lyophilizer, cryo-microtoming

**Data analysis:** statistical analyses (*e.g.*, one-way ANOVA and Chi-square tests) and spectroscopic analyses

**Software:** OriginPro 9.0, GraphPad Prism 6, MDI Jade 6.0, ImageJ, CasaXPS, MS Office, EndNote, Chem3D, 3ds Max 2018, Adobe Illustrator, Adobe Photoshop

**Language:** Chinese (native), English (professional), Japanese (JLPT N1 level)

### Research Experience

**Graduate Research Assistant, Christy Haynes Lab** Nov. 2014-Present  
Department of Chemistry, University of Minnesota-Twin Cities Minneapolis, MN

- Synthesized highly photoluminescent polymeric carbon nanodots using microwave-assisted heating method, improved their photostability by phosphorus doping and investigated their environmental impact using *Shewanella oneidensis* MR-1 as model microorganisms (*Carbon* **2018**, 129, 438-449.)

- Developed a high-throughput method to separate carbon nanodot mixtures via C<sub>18</sub> reversed phase column chromatography, characterized the optical properties of representative fractions and investigated how particle size influenced their fluorescence behavior (*ACS Nano* **2018**, *12* (6), 5741-5752.)
- Evaluated the potential bacterial toxicity of boron/phosphorus doped Si/Ge semiconductor nanocrystals by ROS assay and colony counting assay (*ACS Applied Nano Materials* **2018**, *1*, 4884-4893. & *ACS Applied Nano Materials* **2019**. (DOI: 10.1021/acsanm.9b00525))
- Visualized the association behavior of nanoparticles (*e.g.*, quantum dots, Si/Ge semiconductor nanocrystals, and NMC battery materials) with *Shewanella oneidensis* MR-1 cells using enhanced dark-field and hyperspectral microscopy (*ACS Applied Nano Materials* **2018**, *1*, 9, 4788-4800.)
- Constructed calibration curves and quantified the amount of primary amine in a variety of poly(oxo-norbornenes) using fluorescamine assay (*Langmuir* **2018**, *34*, 15, 4614-4625)

#### Graduate Research Assistant, Qisheng Huo Lab

Sept.2010-Jun. 2014

State Key Laboratory of Inorganic Synthesis & Preparative Chemistry Changchun, Jilin

- Utilized vacuum-assisted impregnation method to generate ordered mesoporous MnO<sub>2</sub> and developed Fe<sub>2</sub>O<sub>3</sub>-embedded mesoporous MnO<sub>2</sub> as an effective synergetic adsorbent to remove trace amount of As (III) (as low as 0.3 mg/L) in aquatic environment (*Journal of Materials Chemistry A* **2014**, *2* (7), 2374-2382.)
- Introduced disordered, lamellar, *Pm* $\bar{3}n$  and *p6mm* mesostructures into metal organic frameworks by adjusting surfactant charge density during self-assembly syntheses (*RSC Advances* **2012**, *2*, 5424-5429.)

#### Publications

- **Zhi, B.;** Yang, Y.; Hudson-Smith, N. V.; Kortshagen, U. R.; Haynes, C. L., Bacterial Toxicity of Germanium Nanocrystals Induced by Doping with Boron and Phosphorous. *ACS Applied Nano Materials* **2019**. (DOI: 10.1021/acsanm.9b00525)
- **Zhi, B.;** Mishra, S.; Hudson-Smith, N. V.; Kortshagen, U. R.; Haynes, C. L., Toxicity Evaluation of Boron- and Phosphorus- Doped Silicon Nanocrystals towards *Shewanella oneidensis* MR-1. *ACS Applied Nano Materials* **2018**, *1*, 4884-4893.
- **Zhi, B.;** Cui, Y.; Wang, S.; Frank, B. P.; Williams, D. N.; Brown, R. P.; Melby, E. S.; Hamers, R. J.; Rosenzweig, Z.; Fairbrother, D. H.; Orr, G.; Haynes, C. L., Malic Acid Carbon Dots: From Super-resolution Live-Cell Imaging to Highly Efficient Separation. *ACS Nano* **2018**, *12* (6), 5741-5752.
- **Zhi, B.;** Gallagher, M. J.; Frank, B. P.; Lyons, T.Y.; Qiu, T. A.; Mensch, A. C.; Rosenzweig, Z.; Fairbrother, D. H.; Hamers, R. J.; Haynes, C. L., Investigation of

Phosphorous Doping Effect on Polymeric Carbon Dots: Fluorescence, Photostability and Environmental Impact. *Carbon* **2018**, 129, 438-449.

- **Zhi, B.**; Ding, H.; Wang, D.; Cao, Y.; Zhang, Y.; Wang, X.; Liu, Y.; Huo, Q., Ordered Mesoporous MnO<sub>2</sub> as a Synergetic Adsorbent for Effective Arsenic (III) Removal. *Journal of Materials Chemistry A* **2014**, 2 (7), 2374-2382.
- Zhang, Y.; Tamijani, A. A.; Taylor, M. E.; **Zhi, B.**; Haynes, C. L.; Mason, S. E.; Hamers, R. J., Molecular Surface Functionalization of Carbon Materials via Radical-Induced Grafting of Terminal Alkenes. *Journal of the American Chemical Society* **2019**, 141 (20), 8277-8288.
- Williams, D. N.; Pramanik, S.; Brown, R. P.; **Zhi, B.**; McIntire, E.; Hudson-Smith, N. V.; Haynes, C. L.; Rosenzweig, Z., Adverse Interactions of Luminescent Semiconductor Quantum Dots with Liposomes and *Shewanella oneidensis*. *ACS Applied Nano Materials* **2018**, 1(9), 4788-4800.
- Pramanik, S.; Hill, S. K. E.; **Zhi, B.**; Hudson-Smith, N.; Wu, J.; White, J.; McIntire, E.; Kondeti, V. S. S. K.; Lee, A.; Bruggeman, P.; Kortshagen, U.; Haynes, C., Comparative Toxicity Assessment of Novel Si Quantum Dots and Their Traditional Cd-based Counterparts using Bacteria Models *Shewanella oneidensis* and *Bacillus subtilis*. *Environmental Science: Nano* **2018**, 5(8), 1890-1901.
- Gallagher, M. J.; Buchman, J. T.; Qiu, T. A.; **Zhi, B.**; Lyons, T. Y.; Rosenzweig, Z.; Haynes, C. L.; Fairbrother, D. H., Release and Toxicity of Fragments Generated During the Photodegradation of CdSe/ZnS and CdSe Quantum Dot PMMA Polymer Composites. *Environmental Science: Nano* **2018**, 5 (7), 1694-1710.
- Zheng, Z.; Boschert, D.; **Zhi, B.**; Haynes, C. L.; Murphy, C. J.; Lienkamp, K.; Rosenzweig, Z., Structure-Antimembranal Activity Relationships of Gold Nanoparticle Conjugates of Covalently Linked Poly [Oxo-Norbornenes]. *Langmuir* **2018**, 34 (15), pp 4614-4625
- Pham, S. N.; Kuether, J.; Gallagher, M. J.; Hernandez, R. T.; Williams, D.; **Zhi, B.**; Mensch, A. C.; Hamers, R. J.; Rosenzweig, Z.; Fairbrother, D. H.; Feng, Z. V.; Haynes, C. L., Carbon Dots: A Modular Activity to Teach Fluorescence and Nanotechnology at Multiple Levels. *Journal of Chemical Education* **2017**, 94 (8), pp 1143-1149
- Zhang, Y.; Guan, B.; Tang, D.; Wang, X.; Wang, T.; **Zhi, B.**; Wang, D.; Li, X.; Liu, Y.; Huo, Q., Tailored Synthesis of Hierarchical Spinous Hollow Titania Hexagonal Prisms via a Self-Template Route. *Nanoscale* **2014**, 6 (22), 13915-13920.
- Wang, J.; Luo, J.; **Zhi, B.**; Li, G.; Huo, Q.; Liu, Y., Anion-Templated Assembly of Three Indium–Organic Frameworks with Diverse Topologies. *CrystEngComm* **2014**, 16 (42), 9810-9816.
- Wu, Z.; Wang, Z.; Guan, B.; Wang, X.; Zhang, Y.; Xiao, Y.; **Zhi, B.**; Liu, Y.; Li, Z.; Huo, Q., Improving the Properties of  $\beta$ -Galactosidase from *Aspergillus oryzae* via

Encapsulation in Aggregated Silica Nanoparticles. *New Journal of Chemistry* **2013**, 37 (11), 3793-3797.

- Guo, Y.-N.; Li, Y.; **Zhi, B.**; Zhang, D.; Liu, Y.; Huo, Q., Effect of Cationic Surfactants on Structure and Morphology of Mesostructured MOFs. *RSC Advances* **2012**, 2 (12), 5424-5429.

#### In revision/Submitted/In prep

- **Zhi, B.**; Yao, X.; Cui, Y.; Orr, G.; Haynes, C. L., Syntheses and applications of multicolour carbon-based luminescent dots. *Nanoscale* **2019** (major revision)
- Buchman, J.T.; Bennett, E.A.; Wang, C.; Bennett, J.W.; Hudson, B.G.; Abbaspour Tamijani, A.; Clement, P.L.; **Zhi, B.**; Green, C.M.; Henke, A.H.; Laudadio, E.D.; Mason, S.E.; Hamers, R.J.; Klaper, R.D.; Haynes, C.L. The technologically relevant complex oxide battery material, Ni-enriched NMC, has differential toxicity to *S. oneidensis* MR-1 and *D. magna*. *Environmental Science: Nano* **2019** (major revision)
- Zhang, Z.; Wang, S.; Guan, Y.; Ogden, W.A.; **Zhi, B.**; Haynes, C.L.; Douglas, C.J., Synthesis and characterization of the C70-fragment dibenzo[g,s]rubicene via a tandem Sonogashira cross-coupling and tetra-dehydro-Diels–Alder cycloaddition cascade. **2019** (in revision)
- Duan, P.; **Zhi, B.**; Coburn, L.; Haynes, C.L.; Schmidt-Rohr, K., A molecular fluorophore in citric-acid/ethylenediamine carbon dots identified and quantified by multinuclear solidstate NMR. *Magnetic Resonance in Chemistry* **2019** (submitted)
- **Zhi, B.**; Yao, X.; Cui, Y.; Mensch, A. C.; Wu, M.; Frank, B. P.; Hamers, R. J.; Murphy, C.; Cui, Q.; Fairbrother, D. H.; Orr, G.; Haynes, C. L., The preparation of multicolor carbon dots via an automatic reversed-phase separation. **2019** (in prep)
- Gallagher, M. J.; Zhi, B.; Frank, B. P.; Sigmon, L.; Mensch, A. C.; Robinson, M.; Hamers, R. J.; Haynes, C. L.; Fairbrother, D. H., Fate and properties of carbon dots in aquatic environments. *Environmental Science & Technology* **2019** (in prep)
- Chen, H.; Wang, C.; Kang, H.; **Zhi, B.**; Haynes, C. L.; Aburub, A.; Sun, C.C., Influence of spherical agglomerates microstructure on dissolution and manufacturability. **2019** (in prep)
- Chen, H.; Guo, Y.; Wang, C.; Kang, H.; **Zhi, B.**; Haynes, C. L.; Aburub, A.; Sun, C.C., Cocrystal quasi-emulsion solvent diffusion to improve both manufacturability and dissolution of indomethacin. **2019** (in prep)

#### **Industry Experience**

**Graduate R&D Intern, Analytical Technology Laboratory**      **Mar. 2019-Jun.2019**  
Research and Development Center, Zeon Corporation      Kawasaki, Kanagawa, Japan

- Investigated the distribution of polyvinyl chloride (PVC) components within nitrile butadiene rubber (NBR) composites using AFM, SEM, and Raman imaging techniques
- Visualized the variation of the Young's modulus of polyacrylate (ACM) elastomers via SEM and AFM

## Teaching Experience

- Mentoring junior graduate students and undergraduates and guiding them through professional trainings
- Teaching assistant for Introductory Chemistry: Laboratory (CHEM 1017, Fall 2014) and Chemical Principles II Laboratory (CHEM 1066, Spring 2015) at the University of Minnesota

## Professional Presentations

- **Zhi, B.**, "Toxicity Evaluation of Boron- and Phosphorus- Doped Silicon Nanocrystals towards *Shewanella oneidensis* MR-1", poster presentation for 2018 MRS Fall Meeting, Boston, MA
- **Zhi, B.**, "Malic Acid Carbon Dots: From Super-resolution Live-Cell Imaging to Highly Efficient Separation", poster presentation for 2018 MRS Fall Meeting, Boston, MA
- **Zhi, B.**, "Synthesis of N, P Co-doped Amorphous Carbon Dots and Their Toxicological Impact on *Shewanella oneidensis* MR-1 Bacteria", oral presentation for 253<sup>rd</sup> ACS National Meeting and Exposition, Spring 2017, San Francisco, CA
- **Zhi, B.**, "Synthesis and Bacterial Toxicity of Nitrogen and Phosphorus Co-doped Amorphous Carbon Dots", oral presentation for IPRIME 2017 Annual Meeting, Summer 2017, Minneapolis, MN
- **Zhi, B.**, "Toxicity Evaluation of Boron- and Phosphorous- Doped Si NCs towards *Shewanella oneidensis* MR-1", poster presentation for IPRIME 2018 Annual Meeting, Summer 2018, Minneapolis, MN

## Honors & Awards

- 1st Place at the IEM Annual Conference and Retreat Poster Competition Sept. 2018  
Institute for Engineering in Medicine, University of Minnesota Minneapolis, MN
- NSF Chemistry Highlights Aug. 2018  
*"You may not have heard of carbon dots, but they are opening new paths to imaging cells, even while alive!"*
- Scholarship for Excellent Graduate Students 2011-2013

State Key Laboratory of Inorganic Synthesis & Preparative Chemistry, Jilin University  
Changchun, Jilin

- Scholarship for Excellent Undergraduate Students 2008-2010  
College of Chemistry, Jilin University Changchun, Jilin

### **Volunteer Experience**

- Journal peer-reviewer for *Carbon*, Elsevier 2018-present
- Council of Graduate Students (COGS) Grants Review Committee Mar 2019
- Outreach volunteer:  
West 7th Community Center Outreach, St Paul Jul. 2015, 2016, 2017
- Outreach presenter:  
*"Tuesdays with a Scholar"* @ Osher Lifelong Learning Institute, Edina Jan 2017
- Outreach volunteer:  
*"Energy and U"* @ UMN, Minneapolis May 2016, Jan, 2017
- Blog writer for Center for the Sustainable Nanotechnology:  
*"Nature Under a Microscope: Exploring the Beauty of Nanoscience"* &  
*"Have you ever seen colorful "carbon"?"* Jun 2016, Aug 2018
- Outreach volunteer:  
Kindness Retreat 2019 @ Eisenhower Elementary School & Xinxing Academy,  
Hopkins Jan 2019

### **Certifications**

Certificate for Japanese-Language Proficiency N1 Aug. 2011  
Certificate for Japanese-Language Proficiency N2 Jan. 2011

### **Professional Affiliations**

Materials Research Society 2016-Present  
American Chemical Society 2016-Present